

Effects of Phase Transformations and Dynamic Material
Strength on Hydrodynamic Instability Evolution in

Metals

by

Saul Opie

A Dissertation Presented in Partial Fulfillment
of the Requirements for the Degree
Doctor of Philosophy

Approved May 2017 by the
Graduate Supervisory Committee:

Pedro Peralta, Chair
Eric Loomis
Jay Oswald
Subramaniam Rajan
Kiran Solanki

ARIZONA STATE UNIVERSITY

August 2017

ABSTRACT

Hydrodynamic phenomena such as the Rayleigh-Taylor (RT) and Richtmyer-Meshkov (RM) instabilities can be described by exponential/linear growth of surface perturbations at a bimaterial interface when subjected to constant/impulsive acceleration. A challenge in designing systems to mitigate or exploit these effects is the lack of accurate material models at large dynamic strain rates and pressures. In particular, little stress-strain constitutive information at large strain rates and pressures is available for transient material phases formed at high pressures, and the continuum effect the phase transformation process has on the instability evolution. In this work, a phase-aware isotropic strength model is developed and partially validated with a novel RM-based instability experiment in addition to existing data from the literature. With the validated material model additional simulations are performed to provide insight into to the role that robust material constitutive behavior (e.g., pressure, temperature, rate dependence) has on RM instability and how RM instability experiments can be used to characterize and validated expected material behavior. For phase aware materials, particularly iron in this work, the simulations predict a strong dependence on the Atwood number that single phase materials do not have. At Atwood numbers close to unity, and pressures in the high pressure stability region, the high pressure phase dominates the RM evolution. However, at Atwood numbers close to negative one, the RM evolution is only weakly affected by the high-pressure phase even for shocks well above the phase transformation threshold. In addition to RM evolution this work looks at the closely related shock front perturbation evolution. Existing analytical models for isentropic processes in gases and liquids are modified for metal equation of states and plastic behavior for the first time. It is found that the presence of a volume

collapsing phase transformation with increased pressure causes shock front perturbations to decay sooner, while plastic strength has the opposite effect which is significantly different from the effect viscosity has. These results suggest additional experimental setups to validate material models, or relevant material parameters that can be optimized for system design objectives, e.g., minimize feed through perturbations in inertial confinement fusion capsules.

ACKNOWLEDGMENTS

I would like to sincerely thank my advisor Dr. Pedro Peralta for his time, investment, and guidance through the years when he first took me on selflessly as a part-time student (full-time later), his work ethic will have a lasting influence on me. I would also like to thank my committee for their time and especially Dr. Eric Loomis for all the excellent experimental work he provided and the quick and helpful responses to questions I have had. Sincere thanks to the Boeing Company and my former coworkers there for their support and flexible work hours when I was a part-time student and full/part-time employee. Lastly, I would like to thank my family for their encouragement, and especially my wife Melanie for her support and patience.

This work was supported by the US Department of Energy, Office of Fusion Energy Science under grant #DE-SC0008683. Access to the TRIDENT facility at LANL is gratefully acknowledged as well.

TABLE OF CONTENTS

	Page
LIST OF TABLES	vi
LIST OF FIGURES	vii
CHAPTER	
1. INTRODUCTION	1
1.1. Motivation.....	1
1.2. Hydrodynamic Instabilities	3
1.3. Hydrodynamic Instability Modelling and Experiments	12
1.4. Shock Front Perturbation Models and Experiments.....	21
1.5. Constitutive Modelling for Strength and Phase Transformation.....	26
2. OBJECTIVES	51
3. EXPERIMENTAL PROCEDURES AND TEST DATA ANALYSIS.....	53
3.1. Experimental Procedure.....	53
3.2. Data Post Processing.....	55
4. MODELS	61
4.1. Preston Tonks Wallace Algorithm.....	61
4.2. Isotropic Phase Transformation Algorithm	69
4.3. Crystal Based Phase Transformation Algorithm	76
4.4. Analytical Shock Front Perturbation Evolution for Plastic Materials	86
5. MODEL CALIBRATION, VERIFICATION, AND VALIDATION.....	100
5.1. Calibration and Verification	100
5.2. Preliminary Verification of Phase Aware Crystal Plasticity Model	113

CHAPTER	Page
5.3. Validation with 1-D Experiments	120
5.4. Validation with 2-D Experiments	131
6. DISCUSSION	134
6.1. Shock Front Perturbations	134
6.2. RM Evolution	152
7. CONCLUSIONS	173
8. FUTURE WORK	177
REFERENCES	179
APPENDIX	
A IRON VARIANTS	194
B SHOCK FRONT PERTURBATION EVOLUTION	197

LIST OF TABLES

Table	Page
5.1: EOS Parameters	103
5.2: PTW Parameters for Iron, Cu, and Aluminum	107
5.3: HCP Variant Mass Fraction Results	116
5.4: Mass Fraction Transformation Results	117

LIST OF FIGURES

Figure	Page
1.1: Stability Examples.	4
1.2: Kelvin-Helmholtz Instability.	5
1.3: RT Instability Schematic.	6
1.4: RT Vorticity at Material Interfaces.....	8
1.5: Richtmyer-Meshkov Instability.	9
1.6: Evolution of RM-Like Instability.	11
1.7: Shock Front Evolution.	21
1.8: Sakharov Shock Perturbation Decay Experiment.....	23
1.9: Shorting Pin Shock Perturbation Experiment.	24
1.10: Flyer-Tamper Shock Front Perturbation Study.	25
1.11: General Transient and Steady State Dynamic Wave Structure	27
1.12: PTW Flow Stress	33
1.13: Qualitative Flow Stress Path Experienced by a Material Point	34
1.14: PTW Material Law vs Constant Yield Stress	36
1.15: Transformation Path Schematic.....	49
3.1: Ablation Experimental Schematic.	53
3.2: Optical Profilometer Image of Rippled Sample	55
3.3: Basic Line VISAR Imaging Concept.....	56
3.4: Processing of Line VISAR Images	58
3.5: VISAR Record for Sample s25266.....	58
3.6: Processing of TIDI Image.....	60

Figure	Page
4.1: Schematic of PTW Equations.....	64
4.2: PTW Material Strength for Constant Plastic Strain Values.....	64
4.3: Coordinate System for Shock Perturbation Model.....	87
4.4: Analytical Shock Front Perturbation Evolution.....	99
5.1: EOS Calibration.....	103
5.2: ABAQUS and VUMAT EOS Results.....	105
5.3: Free Surface Velocity Values.....	105
5.4: Verification of State Values for Helmholtz VUMAT for 280 m/s Shock.....	108
5.5: Cu PTW Response.....	109
5.6: Comparison of ABAQUS and VUMAT Material Models for Iron.....	109
5.7: Free Surface Velocity Comparison for Iron EOS Models.....	110
5.8: State Variables from Iron Helmholtz VUMAT.....	111
5.9: PTW Response of Iron for Low and High Pressure Phases.....	112
5.10: Simulation and Experimental Iron Free Surface Response.....	113
5.11: Variant Transformation.....	114
5.12: Barker Shot 5 Experimental Data Versus Crystal Based Simulation.....	120
5.13: Swegle-Grady Law for Cu.....	121
5.14: Swegle Grady Axis Definitions.....	122
5.15: PTW simulation vs. experimental data.....	123
5.16: VISAR results for Cu flat sample s25259.....	124
5.17: VISAR Results for Cu Flat Sample s25481.....	125
5.18: VISAR Results for Cu Flat Sample s25260.....	125

Figure	Page
5.19: VISAR Results for Iron Sample s25490.....	126
5.20: Iron Simulation Results vs Experimental Internal Particle Velocity.....	127
5.21: Simulation and Experimental Data for Iron Sample s25261	128
5.22: Simulation and Experimental Data for Iron Sample s25492	129
5.23: Simulation and Experimental Data for Iron Sample s25283	130
5.24: Evolution of Flat Free Surface as Rippled Shock Front Breaks Out.....	132
5.25: FEM Contours During Perturbation Breakout.....	133
6.1: Analytical Perturbation Shock Front Evolution for Cu	135
6.2: Effect of Strength on Shock Front Perturbation Evolution in Cu.....	136
6.3: Cu Shock Perturbation Evolution for a 300 m/s Boundary Condition	137
6.4: Aluminum Shock Perturbation Evolution.....	137
6.5: Analytical Shock Perturbation Evolution with Strength.....	138
6.6: Stress Distribution Behind Perturbed Shock Front.....	140
6.7: Simulation FEM Contour Results for Perturbed Shock Front.....	141
6.8: Shock Front Evolution in HCP Iron	142
6.9: P-v Hugoniot Comparison	144
6.10: Effect of Fast Relief Waves	146
6.11: Experimental Shock Perturbation Evolution	147
6.12: Shock Front Evolution with Pressure BC	149
6.13: Shock Perturbation Evolution with Flyer BC	151
6.14: Shock Front Perturbation Evolution for Large Amplitudes.....	152
6.15: Single Phase RM Evolution for A=1	155

Figure	Page
6.16: Maximum RM Displacement.....	156
6.17: Simulations at Low Shock Pressure of 12 GPa.	156
6.18: Consolidate PTW RM Results.....	157
6.19: Simulation FEM Contour Results.....	158
6.20: RM PTW Strain Rate Domain.....	159
6.21: Cu RM Evolution for A = -1.....	160
6.22: Simulations at Low Shock Pressure of 12 GPa.	161
6.23: Maximum RM Displacement in Cu RM A = -1 Simulations.....	161
6.24: Maximum RM Deformation Rate.....	162
6.25: Simulation FEM Contour Results.....	163
6.26: Iron RM Evolution for A = 1.....	165
6.27: Maximum RM Displacement for A = 1.....	166
6.28: Simulation FEM Contour Results.....	167
6.29: Iron HCP PTW Response.....	168
6.30: Iron RM Evolution for A = -1.....	169

1. INTRODUCTION

1.1. Motivation

Two hydrodynamic instabilities, the Rayleigh-Taylor (RT) and the Richtmyer-Meshkov (RM), are particularly interesting to researchers working in applications where large sustained or impulse forces act across a dissimilar material interface. In the RT instability a less dense material pushes/supports a denser material, e.g., oil supporting water under regular gravity acceleration or the spherical implosion of a less dense core with a more dense shell. Any perturbation in the interface can lead to exponential perturbation growth as long as the acceleration/force is sustained. The closely related RM instability also results in surface perturbation growth, but evolves only linearly in time and is the result of an impulsive like acceleration, e.g., a shock wave passing through an interface. These two instabilities can have beneficial effects in mixing applications [1] and can be destructive in others such as Inertial Confinement Fusion (ICF) [2,3].

The brief introduction given above for RT and RM instabilities is based primarily on a linear fluid-like analysis of the materials at the interface using perturbation theory [4]. In many applications one or both materials can be solids with significant elastic shear strength that can appreciably alter the perturbation growth evolution from that of a strictly fluid (hydrodynamic) analysis [5,6,7]. Solids also often possess strength anisotropy and rate dependence that can seed perturbations and affect perturbation growth respectively [8]. A relatively unexplored material phenomenon in respect to hydrodynamic instabilities is the effect that phase transformations have on perturbation growth evolution. Many solids under dilatational, e.g., iron, or shear strains, e.g., shape memory alloys, undergo diffusionless “martensitic” phase transformation. In the case of iron the phase change could

have significant effects on the perturbation growth since low pressure iron has body center cubic (BCC) structure while the high pressure phase is hexagonal close packed (HCP); these two structures are known to have significantly different properties [9]. In addition, the existence of a phase change often changes the dynamics of the shock and release waves when compared to a typical single phase material which may lead to other effects on perturbation growth.

Another challenge for instability modeling, and high dynamic strain rates in general, is a lack of experimental data [10]. Typical plate impact and similar shock experiments are inherently one-dimensional and typically become less sensitive to strength effects at higher pressures [11]. Recently there has been increasing interest in using RT [12] and RM [13] instability experiments for material strength model calibration and validation. In these experiments, modern dynamic diagnostic tools such as proton radiography [14] and x-ray radiography [13] have typically been used to capture the surface evolution. However, the sensitivity of these diagnostics is limited and not ideal for low opacity materials and small displacements (~ 1 micron) [73].

Currently in development at ASU and LANL is a feed-thru RM experiment where surface perturbations at the incident shocked surface of a sample produces a perturbed shock front that is “fed-thru” the sample to a flat free surface. The flat free surface subsequently develops a perturbed surface as the perturbed shock front breaks out. The advantage of this technique with respect to others is that the evolution of the free surface can be tracked more accurately with transient imaging displacement interferometry (TIDI) [15-18], which provides discrete transient displacement data for material model validation. Continuous Line VISAR [19] diagnostics monitoring the same free surface also provide

data on shock front perturbation evolution which provides more data for material model validation.

The aim of the proposed work then is to utilize the recently developed ASU/LANL RM instability experiments, in addition to published data and traditional data acquisition methods, to validate material models that account for high strain rates and phase transformation phenomena. With these models we can then predict the influence that deviatoric behavior has on hydrodynamic instabilities, and what experimental setups and diagnostic requirements are ideal for further characterizing the relevant material behavior. The specific materials to be studied are copper and iron, as the latter experiences a martensitic phase transformation around 13 GPa from BCC alpha (α) to HCP epsilon (ϵ) [20]. To date little work is available on characterizing the strength of high pressure solid phases.

1.2. Hydrodynamic Instabilities

1.2.1. Stability

The stability of a dynamic system refers to the ability of the system to remain near an equilibrium point when perturbed from it [21], and asymptotic stability refers to the ability of the system to return exactly to the equilibrium point [21]. For example, a mass-spring system, a mass-spring-damper system, and a mass-spring-damper with friction are stable (although often called marginally stable), asymptotically stable, and stable respectively. The last being only stable because it will not generally return to the original equilibrium point. More precisely, a system of states x_i (e.g., position and velocity), defined by the system $\dot{x}_i = f_{ij}(x_j)$, at an equilibrium point $x_i = 0$, is stable when perturbed if

$x_i f_{ij}(x_j) \leq 0$, asymptotically stable if $x_i f_{ij}(x_{kj}) < 0$, and unstable if $x_i f_{ij}(x_j) > 0$.

Typically, the system is stable or asymptotically stable for some perturbed neighborhood $\|x_i\| < \delta$ near an equilibrium point. This is shown graphically in Figure 1.1 [21].

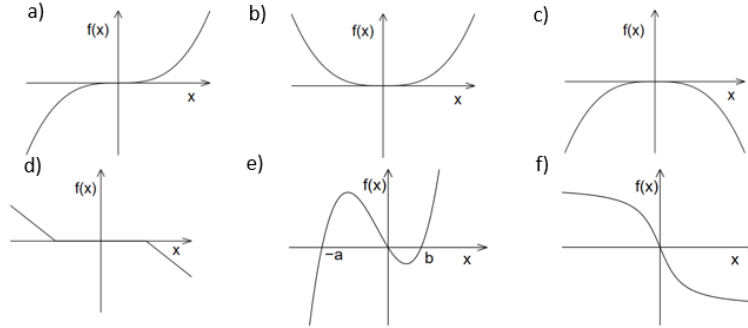


Figure 1.1: Stability Examples. a) unstable, b) unstable, c) unstable, d) stable, e) asymptotically stable for $x \in [-a, b]$, f) asymptotically stable (globally).

1.2.2. Hydrodynamic Instabilities

Hydrodynamic instabilities typically occur at a bimaterial perturbed interface. In solids the Rayleigh-Taylor (RT), Richtmyer-Meshkov (RM), and Kelvin-Helmholtz (KH) instabilities are often encountered. The KH instability however usually occurs in the late highly non-linear stages of the RT or RM instabilities and is mentioned only briefly here. It is characterized by two counter streaming (relative difference in velocity) materials, Figure 1.2, that meet at an interface. If the fluids are approximated as incompressible and inviscid then the interface is called a vortex sheet (irrotational flow in bulk of fluid with vortices trapped at interface). Small geometric perturbations in the sheet lead to pressure perturbations due to high velocity on one side and low velocity flow on the other (e.g. Bernoulli's equation). These pressure perturbations further deform the interface, leading to larger pressure perturbations, and as a result the perturbation growth becomes exponential.

Another way to visualize the KHI is with the vortices trapped at the interface, which can be seen to slow fluid under the peaks while accelerating fluid above as shown in Figure 1.2

. In the nonlinear regime the perturbations start to curl.

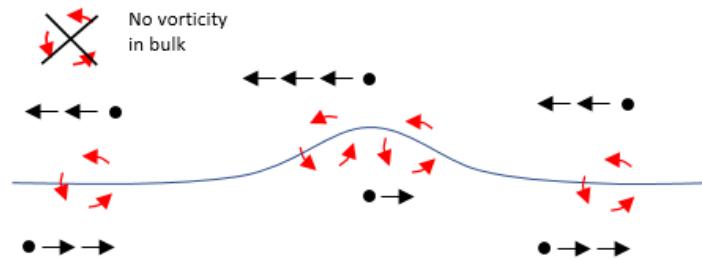


Figure 1.2: Kelvin-Helmholtz Instability. Two counter streaming flows that meet at an interface with different tangential velocities (i.e. a vortex sheet). Vortices at interface accelerate fluid above peaks and slow fluid under.

1.2.3. Rayleigh Taylor (RT) Instability

The RT instability requires opposing pressure and density gradients at a perturbed material interface. An intuitive example of a RT instability is oil (light) supporting water (heavy) under regular gravity. If the interface between the oil and water is perfectly flat the water will remain at top, however if a perturbation exists at the interface then the water sinks irreversibly and deforms the interface further from its equilibrium position, hence the system is unstable. This can be seen with an intuitive one degree of freedom model [22] that agrees well with more complicated models based on conservation equations [23]. Consider Figure 1.3 and the force balance of particles that share a surface with the interface, say we consider an element whose lower surface is on the interface, then

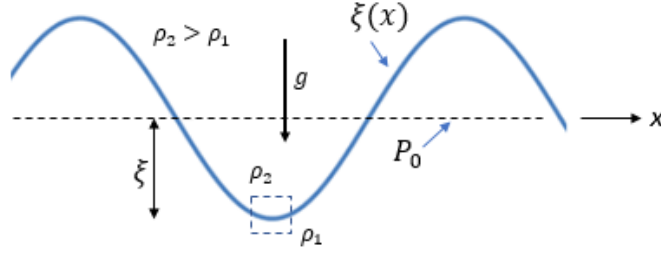


Figure 1.3: RT instability schematic.

$$F_{upper} = A \left(P_0 + \frac{\rho_2 \xi g}{A} \right), \quad F_{lower} = A \left(P_0 + \frac{\rho_1 \xi g}{A} \right) \quad (1.1)$$

where A is the particle area on either the top or bottom, ρ_i are the densities, P_0 is the mean pressure at the interface, g is the acceleration due to gravity in this example, and ξ is the amplitude of the interface perturbation. Applying Newton's second law the particles acceleration is

$$m \ddot{\xi} = F_{lower} - F_{upper} = A(\rho_1 - \rho_2) \xi g \quad (1.2)$$

where m is mass. Assuming both fluids are incompressible the particle cannot move freely, i.e., the fluid around it will accelerate also. Therefore the model uses a characteristic mass

$$m = m_1 + m_2 = \rho_1 \frac{A}{k} + \rho_2 \frac{A}{k} \quad (1.3)$$

where $k = 2\pi/\lambda$ is the wavenumber and λ is the perturbation wavelength. Solving for the perturbation acceleration $\ddot{\xi}$ and the perturbation evolution ξ yields

$$\ddot{\xi} = A_T k g \xi_0 \Rightarrow \xi(t) = \xi_0 \exp(\sigma t), \quad \sigma = \sqrt{A_T k g} \quad \text{where } A_T = \frac{\rho_2 - \rho_1}{\rho_2 + \rho_1} \quad (1.4)$$

where ξ_0 is the initial perturbation amplitude, and σ is the growth rate. Equation (1.4) shows that in the absence of other forces the perturbations will grow exponentially in the linear regime (i.e., $\xi k \ll 1$) for which Eq. (1.4) is approximately valid [23]. Outside this range nonlinear effects become important and the growth is approximately linear [23]. If

effects such as surface tension, viscosity, elastic strength, etc. are considered then stabilizing effects are present but stability is not assured [22,24]. These additional forces can be added to the RHS of Eq. (1.2) to derive a modified growth rate [22].

Another way to visualize the Rayleigh-Taylor instability is in terms of vorticity. Vorticity, \mathbf{w} , is the curl of the velocity, $\nabla \times \mathbf{u}$, or equally it is the vector formed from the components of the spin tensor (antisymmetric part of velocity gradient). In plain terms, it is a measure of local rotation rate. Note that an absence of vorticity is not an absence of shear. The vorticity equation (curl of linear momentum) for the bulk material is given by [26]

$$\frac{D\mathbf{w}}{Dt} = (\mathbf{w} \cdot \nabla)\mathbf{u} - \mathbf{w}(\nabla \cdot \mathbf{u}) + \frac{1}{\rho^2} \nabla\rho \times \nabla P + \nabla \times \left(\frac{\nabla \cdot \mathbf{S}}{\rho} \right) + \nabla \times \left(\frac{\mathbf{B}}{\rho} \right) \quad (1.5)$$

where P is pressure, \mathbf{S} is the deviatoric stress, \mathbf{B} is a body force, and $\frac{D}{Dt}$ is the material derivative (i.e., total derivative). The second and third terms are zero for incompressible fluids and is usually approximately true for other materials (i.e., $\nabla\rho$ will usually be small for most materials and pressure gradients) [23], the first term is zero if the flow is two dimensional, and the last term is zero if the body forces are conservative (e.g., gravity). If the RHS of Eq. (1.5) is zero the flow is irrotational and any vorticity deposited at the interface (i.e. vortex sheet), stays at the interface as shown in Figure 1.4.

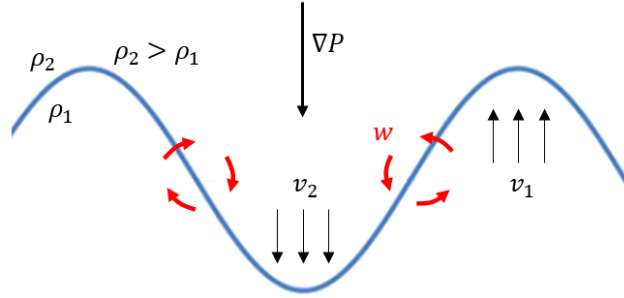


Figure 1.4: RT vorticity at material interfaces. For an incompressible and inviscid material the vorticity at the interface increases exponentially in the linear regime, viscous or elastic effects however can reduce the vorticity growth or eliminate it with shear waves.

At the interface the vorticity can be seen to increase because as the particles accelerate down in the valleys and up in the peaks, due to the pressure gradient, the vorticity at the interfaces (i.e., a vortex sheet) will increase due to the increase in relative motion at the interface. As a result, we can visualize the perturbations growing exponentially due to the growing vorticities. The presence of elastic or viscous forces ($\nabla \cdot \mathbf{S}$ is no longer zero in Eq. (1.5)) allows the vorticity at the interface to be carried away (reduced) into the bulk with shear waves [26] and the exponential growth is decreased.

1.2.4. Richtmyer-Meshkov (RM) Instability

The RM instability is similar to the RT instability but does not require a pressure gradient, and perturbation growth is only linear with time after an initial transient period [28]. It is formed by the passage of a shock front through a perturbed interface of two different materials. The perturbed interface imprints a perturbation to the transmitted shock front as it passes through the second material, and a perturbed reflected shock passes through the first material (unless a rarefaction wave is formed in the first material because its acoustic impedance is larger than the second material) as shown in Figure 1.5.

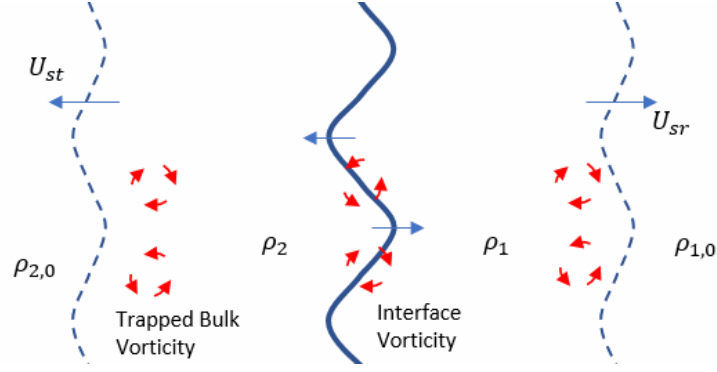


Figure 1.5: Richtmyer-Meshkov Instability. Shock passes through interface as a rippled transmitted shock U_{st} , and a rippled reflected U_{rs} shock for a low impedance to high impedance impact (e.g. air to solid). Pressure perturbations generated behind rippled shocks develop vorticity at rippled interface and for strong shocks significant bulk vortices. After a brief transient period, and in the absence of deviatoric stress terms (e.g., inviscid fluid), vortices are trapped and constant producing a linear perturbation growth rate [33, 27].

Transient pressure perturbations generated by the perturbed shock fronts evolve the interface vortices with time. Also these pressure perturbations, particularly near the shock front where pressure perturbations are strong, generate bulk vortices because the baroclinic term $\nabla\rho\times\nabla P$ in Eq. (1.5) is no longer zero for real materials and strong shocks [27,28]. Eventually the pressure perturbations completely decay, and therefore the area near the interface becomes incompressible, and constant interface and bulk vortices are established [27]. The resulting perturbation growth rate after this transient period can be approximated by the so called impulsive model [29]

$$\dot{\xi} = A_T k v_i \xi_0; \quad A_T = \frac{\rho_{af} - \rho_{bf}}{\rho_{af} + \rho_{bf}} \quad (1.6)$$

where ρ_{af} and ρ_{bf} are the final densities in the transmitted and reflected materials respectively, v_i is the mean fluid velocity after shock passage, and A_T is the Atwood number. Equation (1.6) is an approximation and overpredicts the perturbation growth rate for large shocks (the bulk vortices oppose the interface vortices) [27,30]. The trapped bulk

vortices are generally spread throughout the material but reach a maximum strength at a distance that decreases with shock strength [27]. Also the magnitude of the bulk vorticity increases with shock strength. For weak shocks the bulk vortices are of second order and the perturbation evolution can be visualized with the interface vortex only; however, for strong shocks both the bulk and interface vortices must be used to properly visualize the perturbation growth. Analytical expressions for the resulting linear growth rate to replace Eq. (1.6) can be found in [27,31,32]. Finally, as in the RT instability, deviatoric stresses reduce the interface and bulk vortices in time. In the linear regime deviatoric stresses eliminate the growth rate and the interface is stable, if the perturbations increase too much nonlinear growth ensues, so called bubbles and spikes form and stability is no longer possible.

1.2.5. Feed-In/Out Perturbations and RM-Like Instabilities

As has already been discussed when a shock interacts with a perturbed surface a perturbed shock front is created that can carry perturbations to the opposite surface. This process has been modeled analytically for an inviscid fluid by [34] and coined a “feed-in” [35,36] perturbation. When the perturbed shock front is supported at the originating surface containing the perturbation (e.g. a rigid piston with constant velocity) as in [34] the growth of the perturbations imprinted by the shock front at the initially flat surface has also been called an “RM-Like” instability [28]. With the supported perturbed boundary the breakout ripple at the originally flat free surface is shown to grow in a damped oscillatory manner about a mean growth rate, as shown in Figure 1.6 [34], with a maximum mean rate dependent on the perturbed shock velocity of the perturbed shock front at shock impact. That is a large perturbed shock front may not create the largest perturbation at the initially

flat surface, but rather a small shock front perturbation with large relative velocities could cause more growth. This would be the case for a perturbed shock front near inversion, see Figure 1.6. The asymptotic perturbation growth rate for an inviscid fluid at the initially flat free surface is [34]

$$\langle \dot{a}_c \rangle = D \frac{u_c}{u_s} \dot{a}_s(t_0) \quad (1.7)$$

where $\langle \dot{a}_c \rangle$ is the asymptotic growth rate (i.e., steady state) of the perturbation imprinted by the perturbed shock front at the initially flat surface, $\dot{a}_s(t_0)$ is the perturbed shock front velocity at the time t_0 the shock reaches the flat surface, u_c is the mean contact surface velocity (e.g., $2U_p$ for a vacuum interface), u_s is the shock velocity, and D is a constant equal to about 0.66 [34].

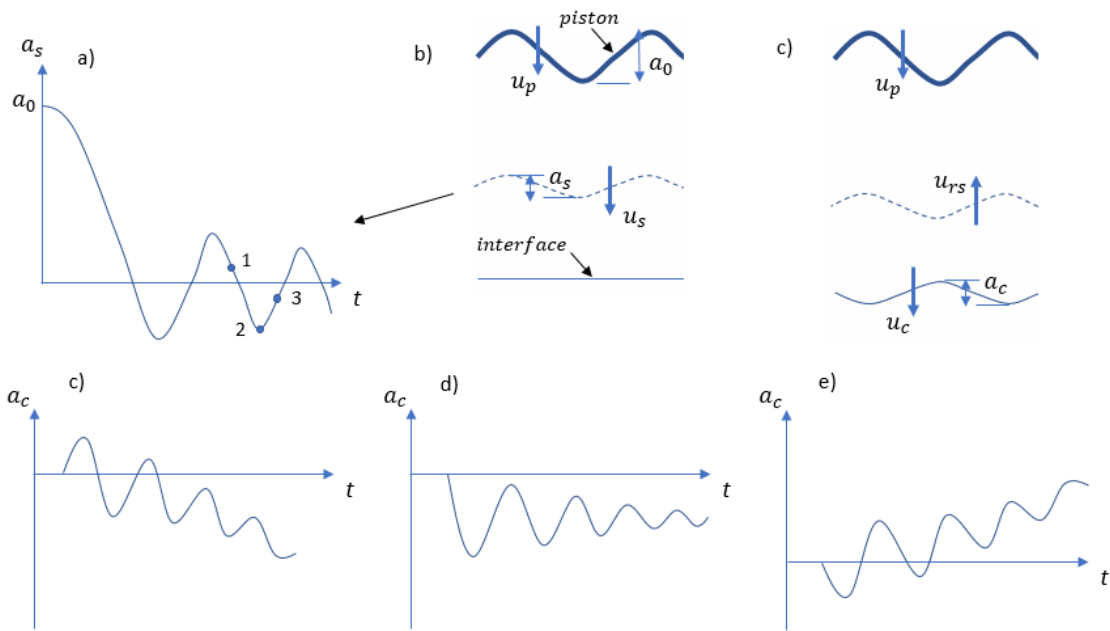


Figure 1.6: Evolution of RM-Like instability. Feed-in perturbation at interface created by perturbed shock front originating at rigid piston moving with constant velocity u_p . a) and b) Shock front perturbation a_s decreases with time towards zero. c) Shock front has reflected off interface as a rarefaction wave (if below interface is a vacuum) and has

imprinted the initial flat surface with a perturbation that oscillates with time approaching an asymptotic perturbation velocity. Perturbation at interface evolves as in c), d), or e) depending on the shock front perturbation amplitude at impact (at time t_0), i.e., positions 1, 2, or 3 in a) respectively. For an ideal inviscid fluid the perturbation mean growth rate is constant in time, for a viscous or material with strength growth rate will be reduced substantially towards zero.

Another similar phenomenon is “feed-out”, where a flat shock travels into a material, reaches a perturbed interface and carries that perturbation back to the originally flat surface [35,37]. These feed-in, feed-out, and RM-Like instabilities can all seed RT stabilities in processes such as ICF [38]. None of the feed-in or feed-out experiments or models appeared to consider the effect strength plays on the breakout perturbation evolution.

1.3. Hydrodynamic Instability Modelling and Experiments

1.3.1. RM Models (without strength) and Experiments

One of the earliest RM analytical model formulations is attributed to Richtmyer [29] for inviscid (no shear stress) compressible mediums using a general equation of state. Richtmyer developed the boundary and initial conditions just after the reflected and transmitted shock fronts formed for the two shock fronts and the interface. He solved the resulting linear initial boundary value problem (IBVP) with numerical methods using an isentropic compression gas equation of state (although any EOS could have been used). Yang [30] formulated the very similar problem of a rarefaction wave (rather than the reflected shock wave of Richtmyer) and solved it numerically also. Velikovich [39,40] and Wouchuk [27] solved the same IBVPs but analytically with power and Bessel series respectively. All of these solutions confirmed the same results that for an inviscid medium

an asymptotic interface perturbation velocity (i.e., $\dot{\xi}$ is constant) is reached after the transmitted and reflected shock waves had traveled several wavelengths into the materials. Nonlinear perturbation models as well as several analytical models based on ideal gas EOS are reviewed in [28] for RM instability.

The first verification of the RM instability was performed by Meshkov [41], using shock tubes, who confirmed a quasi-linear initial perturbation growth rate, similar studies have been performed by others [42,43] and experimental difficulties (e.g. boundary layer effects) are noted in [44]. A review of shock tube fabrication and diagnostics tailored for RM experiments is given in [45]. Dimonte [46] and others [47], were able to overcome many of the limitations of shock tubes with an ablative generated shock, where a Hohlraum was used to uniformly radiate a sample launching a shock wave from a flat surface of the first material into the perturbed interface of the second material. For small amplitude to wavelength ratios, linear growth rates were confirmed via face-on and side-on radiography diagnostics. Other novel approaches to initiate a shock for RM instability creation have been undertaken, such as a high-powered linear electric motor [48].

Ablative RM instability is very similar to the classical RM instability except the RM instability occurs directly at the perturbed surface that is being ablated [49]. The ablative process reduces or stabilizes the RM growth, which has been verified experimentally by [50]. As the peaks grow they essentially get ablated faster (temperature differentials increase) and a restoring velocity pushes them towards the valleys. In contrast as the valleys move away, towards the cold interior of the sample, they see weaker temperature gradients and are ablated less [38,49,50]. As a result, the RM growth rate can be eliminated.

1.3.2. Hydrodynamic Instabilities, Modelling and Experiments with Strength

Hydrodynamic instabilities have received a significant amount of attention in the Inertial Confinement Fusion (ICF) community. In this application perturbations from a wide array of origins (e.g., loading, geometry, material anisotropy, etc.) seed Rayleigh Taylor instabilities preventing efficient implosion of the fuel capsule [23]. Understanding material properties that have an effect on seeding the RT instabilities is important in the design stage to delay the quasi exponential growth of the RT instability as long as possible. It is also known that RT growth can be reduced to zero after an initial transient period for a region of driving forces, material, and geometry conditions [51]. The following sections review some of the modelling and experimental efforts to date.

1.3.2.1. RT Models and Experiments with Strength

Material strength is one property that has been shown to affect the seeding and growth of the RT instability, in conjunction with many others. Some of the earliest experiments for metallic materials were performed by Barnes where a perturbed aluminum plate was accelerated by expansion of detonation products [52,53]. This study showed that perturbation growth was arrested if initial perturbation amplitudes fell below a certain value [54] and strength estimates could be made from perturbation growth results. Later Swegle [51,55] showed through a series of nonlinear simulations that the stability limit depended on several factors with increasing wavelength or amplitude both causing increasing growth rate. For small wavelength to thickness ratios the relationship was nearly independent of wavelength and a critical amplitude can be estimated as a function of shock pressure, material strength, and density [7,53,51,56,57]. At large wavelength to thickness

ratios stability becomes independent of amplitude and a critical wavelength emerges as a function of only shock pressure and density [51]. These numerical and analytical prediction have been supported with some experimental results [52,53,59,60]. Many other factors (e.g. pressure BC rise time) are considered in the simulations of [51] showing that actual RT growth is not generally prescribed easily due to transient effects, and strength determination using RT type experiments can be complicated as a result of several variables that may be difficult to know with great certainty (e.g. pressure ramp history). An interesting result of [51] is that the ideal RT setup is realized physically only after a series on transient shock and release waves have reverberated through the sample, these reverberations establish initial conditions at the time that ideal RT conditions (i.e. constant mean acceleration) are established. These ICs are dependent on a series of factors and can affect the subsequent RT evolution substantially.

Recent RT experiments include laser generated plasma reservoirs [12,60] that send a plasma across a vacuum gap and that eventually stagnates on the target and gradually accelerates it (in contrast to direct ablation of the target sample that would launch a shock wave at the surface and an approximate step change in velocity). This loading scheme is often referred to as quasi-isentropic compression loading (ICE) and has allowed for exploring material pressures and strain rates in thermodynamic states inaccessible with gas gun or shock methods [61,62].

Models accounting for strength have ranged from simple constant yield [51] that appear to bound variable strength models (i.e. low and high yield strength simulations bound the results expected from a variable strength model that at any time is within the constant upper and lower limit) to complicated dislocation density formulations [63,64].

Barton [63] has used an isotropic multiscale model where molecular dynamic results are used to determine parameters in a dislocation based strength law that is pressure, temperature, and strain rate sensitive; a similar crystal plasticity model was also developed by [65].

1.3.2.2. RM Models and Experiments with Strength

Richtmyer-Meshkov experiments are similar to RT experiments, but a shock wave passes through the interface, that after a short time establishes a quasi-constant growth rate. In experiments the growth rate is reduced with time due to nonlinear effects and deviatoric stresses. Dimonte [66] used a high explosive experiment, similar to [42], with radiography to monitor the spike growth of copper perturbations in a metal to gas interface (Atwood number of negative one). He found a copper effective dynamic yield stress ranging from 0.4 to 1.5 GPa that appears to agree with [67], and an empirical model similar to [68] was developed. Later detailed numerical simulations with more complex flow stress laws were performed by [69] showing results similar to [66,68], i.e., that at the strain rates seen in RM instability experiments flow stress can be represented as a constant effective flow stress (although this value may change when comparing large shock experiments to smaller shocks). Recently [70,71,72] performed RM experiments on copper with explosives and highly accurate radiography, showing some perturbation growth prediction differences between a simple elastic-plastic material law and a more capable PTW law. An interesting observation of [71] is that the large amount of deformation in the perturbations generates a significant amount of plastic strain and therefore temperature rise (e.g. his experiments showed a ~100K shock release increase due to a 36 GPa shock but an additional ~900K

increase due to plastic deformation of $\sim 700\%$). This should be a consideration when designing experiments to calibrate material laws, large deformations are generally good to reduce signal to noise ratios, but it may push the material out of the temperature range of interest. Peralta [73] constrained the RM growth of a free surface with a PMMA window to obtain an experimental data point for material strength determination on textured copper discs at low shock pressures. Jensen [74] performed RM experiments with cerium, which has a solid-solid phase change when shocked, using a copper flyer to impart a shock wave on the flat portion of a cerium target that had a rippled interface at a free surface. Because of the free surface the low pressure strength was only measured. Finally, RM instabilities with strength were modeled for converging geometries (spheres) in [75].

Piriz [68] developed a simple and intuitive semi-analytical model for 2-D planar geometries, calibrated to simulations, that captures the basic effect material strength has on RM growth in the situation of a solid interfacing with a vacuum. The model predictions have also been independently verified with detailed numerical solutions using more complicated material models [69]. The RM growth is idealized as a one dimensional system as Eq. (1.8)

$$m\ddot{\xi} = -S_y \quad (1.8)$$

where ξ is the surface perturbation amplitude, m is a characteristic mass per unit area, and S_y is the deviatoric traction in the direction of the perturbation (e.g., $Y/\sqrt{3}$ for a plastically deforming material). Piriz assumed the velocity field was [68]

$$v_y = \dot{\xi} \exp(qy) \cos(kx), \quad q = k/\alpha, \quad k = 2\pi/\lambda \quad (1.9)$$

where y is the parallel to the perturbation motion (zero at the perturbation and increasing away from it), x is the transverse direction, k is the wavenumber, and α is a fitting factor

that is adjusted to match simulation results. Returning to Eq. (1.8) the deviatoric term S_y , if the material is plastically deforming, is

$$S_y = \frac{Y}{\sqrt{3}} \text{ if plastically deforming} \quad (1.10)$$

where Y is the material yield stress. If the material has not yielded then S_y is equal to

$$S_y = \int_{t_n}^t \dot{S}_{yy} dt, \quad \dot{S}_{yy} = 2GD_{yy}|_{x=0,y=0} = 2G \frac{k}{\alpha} \dot{\xi} \quad \Rightarrow \quad S_y = 2G \frac{k}{\alpha} (\xi(t) - \bar{\xi}(t_n)) \quad (1.11)$$

where $\bar{\xi}(t_n)$ is the mean perturbation amplitude that the surface oscillates about. The last piece needed are the characteristic mass per unit area, assumed to be

$$m = \rho \frac{\alpha}{k} \quad (1.12)$$

where ρ is the compressed density (i.e., post shock density). Then the perturbation evolution while the material is plastically deforming is

$$\int_{t_0}^t \dot{\xi} dt = - \int_{t_0}^t \frac{k}{\alpha\rho\sqrt{3}} dt \quad \Rightarrow \quad (\dot{\xi} - \dot{\xi}_0) = - \frac{k}{\alpha\rho\sqrt{3}} (t - t_0) \quad (1.13)$$

integrating once more yields

$$\xi - \xi_0 = \dot{\xi}_0(t - t_0) - \frac{k}{\alpha\rho\sqrt{3}} (t - t_0)^2 \quad (1.14)$$

where t_0 is the time at which the shock has traveled a couple perturbation wavelengths into the material. At this point the pressure perturbations have been eliminated and the perturbation interface has an asymptotic velocity $\dot{\xi}_0$ that a no strength fluid would have [27,31,32]. For a weak shock $\dot{\xi}_0$ can be approximated with Richtmyers impulse approximation

$$\dot{\xi}_0 = k\xi_i U_p \quad (1.15)$$

where U_p is the shocked material particle velocity, and ξ_i is the initial perturbation velocity. For stronger shocks an asymptotic velocity is still reached but the expression is more complicated [27,31].

We are interested in the maximum perturbation amplitude ξ_m . Setting $\dot{\xi}$ to zero in Eq. (13) and solving for the time t_m yields

$$(t_m - t_0) = \frac{\alpha\rho\sqrt{3}}{kY} \dot{\xi}_0 \quad (1.16)$$

Using Eq. (1.16) in Eq. (1.14) yields

$$(\xi_m - \xi_0) = \frac{\alpha\sqrt{3}}{2} \frac{\rho}{kY} \dot{\xi}_0^2 = 0.29 \frac{\rho}{kY} \dot{\xi}_0^2 \quad (1.17)$$

where Piriz found a fitting constant of $\alpha=0.335$ matches simulation predictions very well. Eq. (1.17) applies to a shock travelling from a light to heavy material, when the shock travels from a heavy to light material the constant in Eq. (1.17) changes from 0.29 to ~ 0.23 [66,69]. Often ξ_0 is estimated as ξ_i or even zero for large shocks.

At times greater than t_m the material oscillates elastically about a mean $\bar{\xi}$

$$\frac{Y}{\sqrt{3}} \cong \frac{2k}{\alpha} G(\xi_m - \bar{\xi}) \quad (1.18)$$

where ξ_m is given by Eq. (1.17), but in Eq. (1.18) $\alpha=1.90$. The oscillation frequency w can be found with Eq. (1.8,1.11,1.12)

$$\ddot{\xi} = -\frac{2k^2}{\rho\alpha^2} G(\xi - \bar{\xi}) \quad (1.19)$$

Solving Eq. (1.19) gives

$$\xi = \bar{\xi} + (\xi - \bar{\xi})\cos(\omega t), \quad \omega = 2\pi/T = \frac{k}{\alpha} \sqrt{\frac{2G}{\rho}} \Rightarrow T = \frac{2\pi\alpha}{k} \sqrt{\frac{\rho}{2G}} \quad (1.20)$$

where T is the oscillation period, and the fitting factor is $\alpha=2.35$. Numerous simulations using Eqs. (1.16) through (1.20) can be found in [68] for small (<0.004) amplitude over wavelength ratios.

Alternatively, instead of using a characteristic mass as in Eq. (1.12), the derivation can start by looking at the change in linear momentum of a material point near the free surface of a perturbation

$$\frac{dv_i}{dt} = \frac{\partial v_i}{\partial t} + \frac{\partial v_i}{\partial x_j} v_j = \frac{1}{\rho} \frac{\partial \sigma_{ij}}{\partial x_j} + \frac{1}{\rho} b_i = \frac{1}{\rho} \frac{\partial P}{\partial x_i} + \frac{1}{\rho} \frac{\partial S_{ij}}{\partial x_j} + \frac{1}{\rho} b_i \quad (1.21)$$

where b_i is a body force, P is pressure, and S is the deviatoric stress. If we consider a path that passes through a peak or valley of the perturbation, ignore body forces, wait a short period for pressure perturbations to vanish [27], and finally, assume all perturbed quantities (the deviatoric stress) in the lateral direction x vary as $\exp(ikx)$ we have

$$\frac{dv_y}{dt} = \frac{1}{\rho} \frac{\partial S_{yx}}{\partial x} + \frac{1}{\rho} \frac{\partial S_{yy}}{\partial y} = \frac{k}{\rho \sqrt{3}} \frac{Y}{\rho} \beta + \frac{k}{\rho \sqrt{3}} \frac{Y}{\rho} \gamma \quad (1.22)$$

where Y is the material yield stress, β and γ are fitting constants, and we assumed that the longitudinal y gradient is still dependent on the wave number k which is reasonable based on geometry scaling arguments similar to Eq. (1.9). If we pick a point just inside the free surface then $\frac{dv_y}{dt} \cong \ddot{\xi}$, and therefore

$$\ddot{\xi} = \frac{k}{\rho \sqrt{3}} \frac{Y}{\rho} \beta + \frac{k}{\rho \sqrt{3}} \frac{Y}{\rho} \gamma = \frac{k}{\alpha \rho \sqrt{3}} \frac{Y}{\rho} \quad (1.23)$$

which is identical to Eq. (1.8) and (1.12). A similar derivation can be used for the elastic case. Equation (1.23) also shows why the fitting parameter α likely changes depending on

the stress regime (plastic or elastic) since it is actually a function of the effective (i.e., average) shear and longitudinal stress gradients that will change as the loading evolves.

1.4. Shock Front Perturbation Models and Experiments

As has been mentioned previously when a flat shock passes through a perturbed interface separating dissimilar materials a perturbed shock front forms as shown in Figure 1.7. The evolution of the perturbed shock is analyzed in the inviscid RM solutions [27,31-33] since it is an evolving boundary condition in those problems. The pressure perturbations left behind and created by the passage of the shock fronts are responsible for establishing the linear RM growth [31,32]. This general approach is used by [76-78], and [79,80] for strongly ablated materials, for calculation of the perturbed shock front evolution.

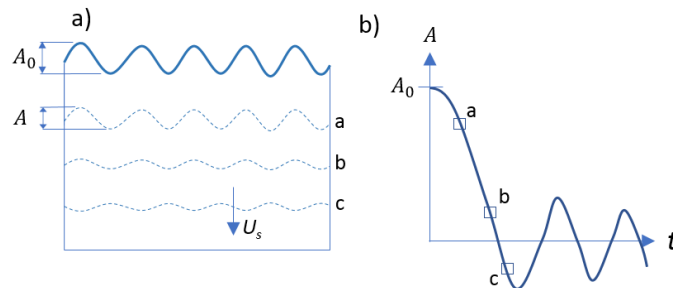


Figure 1.7: Shock front evolution. a) Shock front evolution after shock passes through a perturbed surface. b) Amplitude, A , evolution of shock front.

In most materials and moderate shock pressures the perturbed shock front decays with time [80-82] and is asymptotically stable; however, for certain equations of state the shock front may only be marginally stable, i.e., it oscillates, this is discussed by D'yakov [83] and Kontorovich [84]. Subsequent studies of this oscillation, with general equation of

states, are discussed in [82,85,78]. It turns out this oscillation develops only when pressure perturbations are able to reflect off the interface, after being generated at the shock front, and reach the perturbed shock front from behind. In these instances, the shock front perturbation decay should consider the interface boundary conditions [78]. The ability of the pressure perturbations to reach the interface and come back to the shock front is unlikely for most material equations of state, intuitively, and as shown by [78, 82], it would require the sound speed in the compressed material to significantly exceed the shock speed (in general the compressed sound speed is larger than the shock speed, but usually not significantly enough to reach the shock due to oblique reflection at the bimaterial interface boundary [86,78]).

In some cases, the material interface that the flat shock passes through could reasonably be replaced with a constant velocity or pressure boundary condition (for small perturbations) and the RM evolution neglected at the interface. This would reduce the complexity of the analysis for the shock front perturbation [87,88,78]. For instance, the RM growth at an interface could be minor and ultimately stable if the materials possess strength. In the case of a weak or moderate ablative shock the interface can move at a nearly constant velocity; however, strong ablative shocks tend to reduce the rate of shock perturbation decay (see for instance Fig. 5 of [80]). If the interface boundary can be approximated as moving at a nearly constant velocity, e.g., a rigid piston, and the compressed sound speed is significantly small (as has been the case experimentally [82]), then the interface boundary condition can be neglected and only the boundary conditions at the shock need to be considered [87,88]. None of these models consider solid material strength or a typical metal EOS.

Experiments to validate shock front perturbation decay models (at least qualitatively) have been performed primarily with materials that lack significant elastic strength, such as water [77], metals above the melting temperature [89,87,90], or laser irradiated plastics [91]. A setup developed by Russian researchers [92,89] is shown in Figure 1.8. In this setup an explosive launches, ideally, a supported shock wave into a flat portion of material 1 of the apparatus whose opposite end is perturbed and interfaces with a material 2, the sample of interest. The perturbed interface launches a perturbed shock wave into the sample whose evolution is monitored by noting shock breakout times at a wedge shaped free surface. In theory with one sample an entire shock front evolution can be captured.

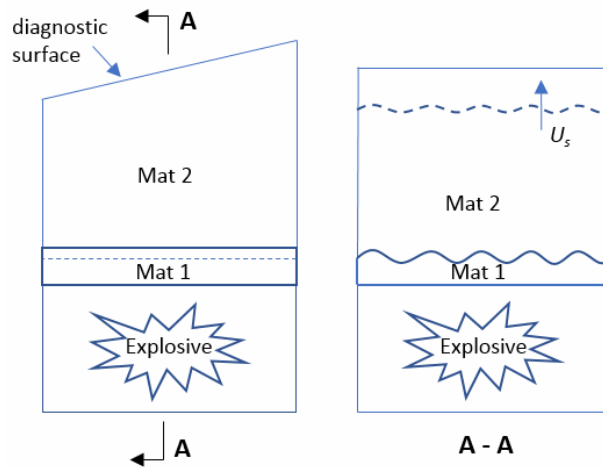


Figure 1.8: Sakharov shock perturbation decay experiment [92]. Explosive launches a sustained shock into material 1 which initiates a perturbed shock into typically a lower impedance material 2 whose high pressure viscosity we want to measure. The diagnostic surface contains some type of time-stamped photography to capture the evolution of the shock front.

These experiments were used primarily to determine the viscosity of shock melted metals or an effective viscosity of plastically deforming shocked solids [93, 94,89]. The viscosity was determined by using the experimental data and the approximate viscous

analysis of [87]. In these experiments and analysis, the elastic-plastic strength of the solids was considered irrelevant provided the shock was strong enough; it was assumed any changes in perturbation decay were due to viscous effects [87]

A similar but different experimental setup, Figure 1.9, was developed by [95]. In this setup, the explosive is replaced by a flat flyer plate impacting a perturbed interface of the sample of interest. The opposite end of the sample is wedge shaped and shock breakout was monitored with shorting pins.

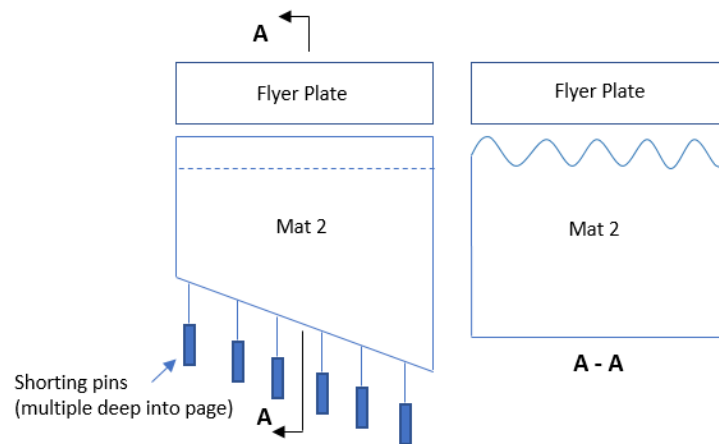


Figure 1.9: Shorting pin shock perturbation experiment. Flyer plate hits perturbations placed into solid material whose viscosity (or strength) we want to measure. Shorting pins placed below peaks and valleys of perturbations monitor shock front perturbation evolution at breakout at the wedged free surface [95].

A significant problem with this setup is that the perturbed shock front will not initially have the shape of the initial interface, since the shock speed is faster than the flyer plate. They initially used a linear perturbation solution [88] to estimate an effective viscosity, values were estimated to be around 500 Pa-s for aluminum at 42 GPa [95]. Subsequent efforts used numerical simulations to model the impact and geometry details more accurately and capture nonlinear effects. Surprisingly for shock pressures from 42-

101 GPa they noted an increase in shear viscosity from 1500 to 3500 Pa-s [96]. Which differs from other published data [89]. Additional numerical simulations considered a viscoelastic material with pressure dependent yield strength at a shock pressure of 101 GPa [97]; however, an elastic model at this pressure may be inappropriate since aluminum would be close to melting. The results from this analysis are not discussed in detail in [97].

Another recent experimental setup has been designed by [98,99] for porous materials, Figure 1.10. In this setup a driver plate and the porous material share a perturbed interface. The driver plate is then impacted with a much thicker flyer plate of the same material. This is a good setup that approximates the ideal analytical setup of a constant velocity boundary condition. Shock perturbation decay is monitored with shock breakout times via Line VISAR. Unfortunately, with this setup many samples are needed to capture the perturbation decay evolution since only one data point is captured per sample.

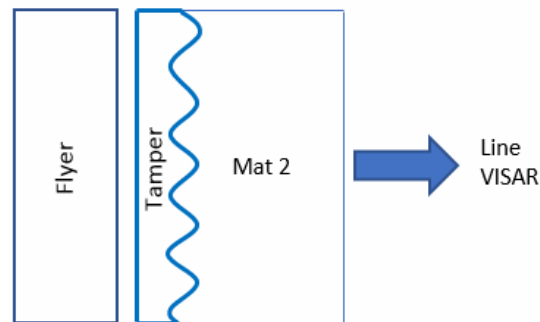


Figure 1.10: Flyer-Tamper shock front perturbation study. Flyer plate impacts perturbed tamper launching a perturbed shock front into the material viscosity or strength we want to measure which is typically has a much lower impedance than the tamper [98]. Line VISAR monitors shock breakout. This setup most closely matches the ideal piston BC that analytical and simulations model [87,88]. Unfortunately, only one data point is generated per experiment unlike Figure 1.8 and Figure 1.9, which get multiple data points per experiment. Reference [99] discusses future improvements.

Vogler [98], unlike prior researchers, was interested in strength models (i.e., not viscosity). His numerous continuum simulations showed that shock front perturbation decay was decreased (i.e., the rippled front lasted longer) by increasing yield strength and perturbation wavelength, and perturbations decayed faster with increasing initial perturbation amplitude. This geometry relationship is the opposite seen in the viscous models (i.e., perturbation decay increase with wavelength increase, and no dependence on initial amplitude [88]).

1.5. Constitutive Modelling for Strength and Phase Transformation

1.5.1. General Shock Wave

When a material is compressed at rates large enough to no longer be considered quasistatic, i.e., inertial effects are no longer negligible, a large range of dynamic material properties can be observed. Figure 1.11 shows a schematic of a velocity impact boundary condition on a solid whose material can be described with rate-dependent plasticity and a martensitic (diffusionless) phase transformation constitutive model. At impact, and assuming nearly uniaxial strain, a large elastic wave instantaneously breaks into three waves: an elastic wave and two plastic waves. Each wave typically has a different velocity denoted here as C_0 , C_1 , and C_2 respectively. If given sufficient time ($\sim 1 \mu\text{sec}$) with respect to the wave velocities, the three waves reach an equilibrium level before reaching the other surface of the target. Assuming the wave is not overdriven (i.e. $C_0 > C_1 > C_2$ is not overdriven) the first wave to arrive is an elastic wave at a stress state that produces a plastic strain rate of nearly zero [64]. The component of the stress in the direction of the wave propagation is the Hugoniot Elastic Limit (HEL) [100]. The next wave to arrive is a plastic

wave traveling at a speed determined by an equation of state (EOS), and whose stress state is nearly hydrostatic; the large effective bulk modulus, which increases with the compression, prevents significant uniaxial strain and therefore significant plastic deformation (although under severe impacts large strains can occur) [100]. The stress level at the first plastic wave is limited by the velocity boundary condition, or in this case, the equilibrium pressure level at which a martensitic phase change occurs [101]. Plastic wave two finally reaches the target surface at a speed that is determined by a second EOS specific to the material phase at high pressure, and at a stress level determined by the velocity boundary condition and EOS [102,103]. This last stress level would represent a point on the shock Hugoniot [100].

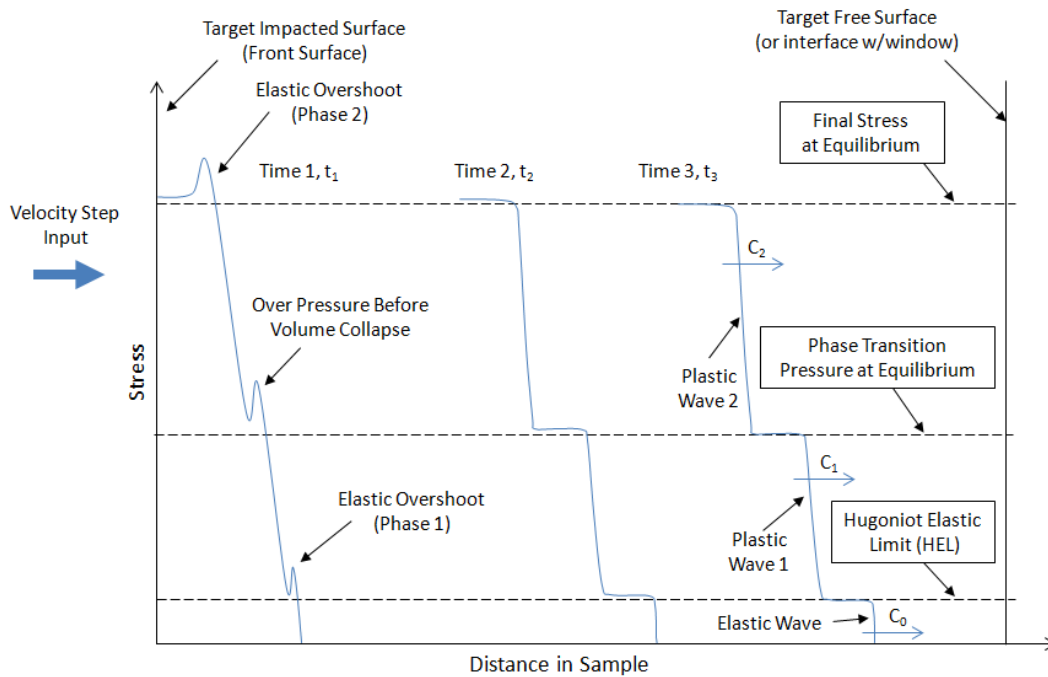


Figure 1.11: General transient and steady state dynamic wave structure (adapted from [101]).

The slopes (or more generally, the shock front structure) of the two plastic shock waves in the simplest theories would be infinite, i.e., a discontinuity in stress, density and velocity; however, in real materials rate-dependent plasticity leads to a finite rise time to the wave plateau [104-106]. Empirically the rise time, and hence the rate-dependent plasticity, can be roughly characterized with the Swegle-Grady fourth power law [107]. In numerical codes artificial viscosity is often utilized to further widen this rise time to prevent instabilities, particularly if the code neglects material strength (e.g. hydrocodes) [100,108]. Midway through the sample (time t_2) the shock front has reached a pseudo-equilibrium form; however, the stress plateaus are generally falling with distance travelled. This can be seen by shocking samples of varying thickness at the same impact level and recording the free surface velocity, which is related to the stress [102,103]. The falling stress levels at the elastic wave front and second plastic wave front can be attributed to rate-dependent plasticity [64,109], while the falling stress level at the first plastic wave front is related to phase transformation kinetics [110,111].

Recent experimental data supports the qualitative shock front schematic shown at time t_1 in Figure 1.11 [109,111,112]. The first elastic “overshoot” is believed to be a result of rate-dependent plasticity and a lack of mobile dislocations [64,113,109,114]. Rapid dislocation generation at the peak and behind the front leads to a sharp stress drop and a release wave that quickly drops the overshoot to the level seen at time t_2 . This same explanation can also be used for the overshoot and subsequent fall of the elastic overshoot in the second plastic wave. The overshoot in the first plastic wave is a result of nucleation and phase transformation kinetics [110,111]. At the first plastic wave peak there is a volume collapse due to a rapid phase transformation, this leads to a release wave and a

subsequent drop of the peak stress to an equilibrium level (often a metastable state) in accord with the transformation kinetics [110]. In the next section plasticity and strength models are reviewed.

1.5.2. Strength Models (Crystal Plasticity)

Nearly all metals are modeled with a rate-dependent plasticity model when shock waves are expected. With a rate-independent plasticity model [115] the plastic shock front would evolve into a discontinuity and numerical instability would result [104]; hence, artificial viscosity in this case would always be a necessity.

1.5.2.1. Creep Power Law

The rate-dependent empirical power law given in Eq. (1.24) is the one of the most common approaches taken in numerical codes for crystal plasticity [116,117].

$$D^P = \sum_{\alpha} \dot{\gamma}^{\alpha} P_s^{\alpha} \quad \text{where} \quad \dot{\gamma}^{\alpha} = \dot{\gamma}_0 \left| \frac{\tau_r^{\alpha}}{g^{\alpha}} \right|^{1/m} \text{sgn}(\tau_r^{\alpha}) \quad (1.24)$$

where D^P is the plastic deformation rate, $\dot{\gamma}^{\alpha}$ is the slip rates per slip system α , and P_s^{α} is the symmetric Schmid tensor per slip system. The slip rates are calculated with the empirical power law expression, where τ_r^{α} is the resolved shear stress, g^{α} is evolving critical strength, while $\dot{\gamma}_0$ and m are fitting constants. For quasi-static and low strain rates ($\sim < 10^4 \text{ s}^{-1}$) manipulation of the power law parameters in conjunction with various strength evolution models [116,118-120] for $g^{\alpha} = g^{\alpha}(\gamma^{\beta}, \dot{\gamma}^{\beta}, T, \dots)$ can simulate experimental results well; however, the agreement is limited to conditions near the empirical fit. Artificial viscosity is usually retained for stability also. Numerically, for low strain rates, Eq. (1.24) with appropriate parameter values can be made qualitatively similar to the

isotropic Johnson-Cook strength model, yet be capable of accounting for crystal texture evolution at large strains.

1.5.2.2. Dislocation Based Models

Dislocation based crystal plasticity models typically start with the Orowan relationship, Equation (1.25). For low strain rates where dislocation nucleation is not significant

$$\dot{\gamma}^{\alpha} = b^{\alpha} N_m^{\alpha} \bar{v}^{\alpha} \quad (1.25)$$

where b^{α} is the burgers vector magnitude, N_m^{α} is the mobile dislocation density, and \bar{v}^{α} is the average dislocation velocity. When dislocation nucleation dominates

$$\dot{\gamma}^{\alpha} = b^{\alpha} \dot{N}^{\alpha} \bar{x}^{\alpha} \quad (1.26)$$

where \dot{N}^{α} is the rate of dislocation generation (mobile and immobile) and \bar{x}^{α} is the average distance swept out by new dislocations [64,121,122]. The separation of the total dislocation density, N , into mobile, N_m , and immobile, N_{im} , dislocations was recently done in [123] with interesting results. A generalized Orowan relation has also been used, as shown in Eq. (1.27) [64,124,121].

$$\dot{\gamma}^{\alpha} = b^{\alpha} N_m^{\alpha} \bar{v}^{\alpha} + b^{\alpha} \dot{N}^{\alpha} \bar{x}^{\alpha} \quad (1.27)$$

The average dislocation velocity, \bar{v}^{α} , is usually expressed as [40]

$$\bar{v}^{\alpha} = \bar{L}^{\alpha} / (t_r^{\alpha} + t_w^{\alpha}) \quad (1.28)$$

where \bar{L}^{α} is the average distance between obstacles and t_r^{α} is the running time between obstacles. The dislocation waiting time, t_w^{α} , is controlled by thermal activation, typically an Arrhenius type relation is used resulting in [125]

$$t_w^\alpha = \frac{1}{\omega_0} \left[\exp\left(\frac{\Delta G^\alpha}{kT}\right) - 1 \right] \quad (1.29)$$

where ω_0 is the attempt frequency to move past the barrier, ΔG^α is the energy barrier to dislocation movement, k is Boltzmann's constant, and T is the temperature. Alternatively, other relationships have been used for the thermal activation term, for instance [63] used a multiscale modeling approach to determine a different empirical form. In Eq. (1.29) the ΔG^α resulting from dislocation forests (e.g., FCC materials) and/or Peierls-Nabarro forces (e.g., BCC materials) is often expressed as [124,126]

$$\Delta G^\alpha = \Delta G_0^\alpha \left\{ 1 - \left(\frac{|\tau_r^\alpha| - \tau_a^\alpha}{\tau_{th}^\alpha} \right)^p \right\}^q \quad (1.30)$$

For a FCC material [124] modeled the athermal long range term, τ_a^α , as the stress needed to pass parallel dislocations, while the stress that can be statistically overcome with thermal vibrations, τ_{th}^α , is modeled with dislocation forests. Both are quantified with a Taylor hardening form.

$$\tau_{th}^\alpha = \zeta_{th} G_0^\alpha b^\alpha \sqrt{N_p^\alpha} \quad \text{and} \quad \tau_a^\alpha = \zeta_a G^\alpha b^\alpha \sqrt{N_f^\alpha} \quad (1.31)$$

where ζ is a material constant, G_0^α is the shear modulus at 0 K, N_p^α is a measure of the density of dislocations that belong to a given slip plane α , N_f^α is a measure of the density of dislocations that pierce a given slip plane α , and G^α is a pressure/temperature dependent shear modulus. The cold activation barrier, ΔG_0^α , is typically influenced by the pressure/temperature dependent shear modulus [123,127].

The running time, t_r^α , spent between thermal barriers is usually modeled as phonon drag, typically as

$$t_r^\alpha = \frac{\bar{L}^\alpha}{v_r^\alpha} \text{ where } v_r^\alpha = \frac{b^\alpha(|\tau_r^\alpha| - |\tau_a^\alpha|)}{B^\alpha} \quad (1.32)$$

The damping term, B^α , is written as

$$B^\alpha = \frac{B_0}{1 - (v_r^\alpha/c_s)^2} \quad (1.33)$$

where B_0 is a damping constant and c_s is the shear wave speed [40]. Equation (1.33) prevents the dislocation velocity from exceeding the shear wave speed.

Equations (1.25) through (1.33) are a basic framework to model strain rates from nearly quasistatic to rates around 10^8 s^{-1} [64]. All of the equations should be tailored for the particular crystal symmetry and other specific material associated phenomena. Recent data from [109] provides support for a thermal to phonon drag transition. For BCC materials with twinning it is suggested that twinning actually delays this transition to higher strain rates [109].

1.5.3. Isotropic Strength Models

A large number of relevant isotropic strength models exist in the literature; however, here only a select few are referenced that were evaluated or are analogs to similar crystal plasticity models. Recently Austin [64,123] developed a dislocation-based model, utilizing mobile and immobile dislocations, that is the isotropic analog to Eqs. (1.25) – (1.33). Barton [5,63] developed a dislocation-based strength model from multi-scale simulations and showed that predictions were often better than existing popular strength models (e.g. Steinberg-Guinan (SG) [128], Steinberg-Lund (SL) [129], and Preston-Tonks-Wallace (PTW) [67]. Barton's dislocation model was also used in a multiphase sample [130]. Finally, Belof [131] made a slight modification to the PTW [67] model for

multiphase iron; simulations showed the multiphase strength model captured experimental Rayleigh-Taylor instability data reasonably well.

Before moving on the PTW model should be reviewed in more detail since it is the primary strength model used in this work. The PTW model is specifically designed to model thermal activation (strain rates below $\sim 10^5 \text{ s}^{-1}$) and phonon drag well (strain rates above $\sim 10^8 \text{ s}^{-1}$), while interpolating the transition between these two regimes [67]. Figure 1.12 shows the PTW response for copper with the parameters given in [67] at room temperature and ambient pressure. An increase in pressure would cause this family of curves to shift up, while an increase in temperature would have the opposite effect. The PTW model contains all the basic levers to capture the effects of strain rate, temperature, pressure, and work hardening [67]. It does, however, lack some kinetic phenomenon that are present in dislocation based models [64,124].

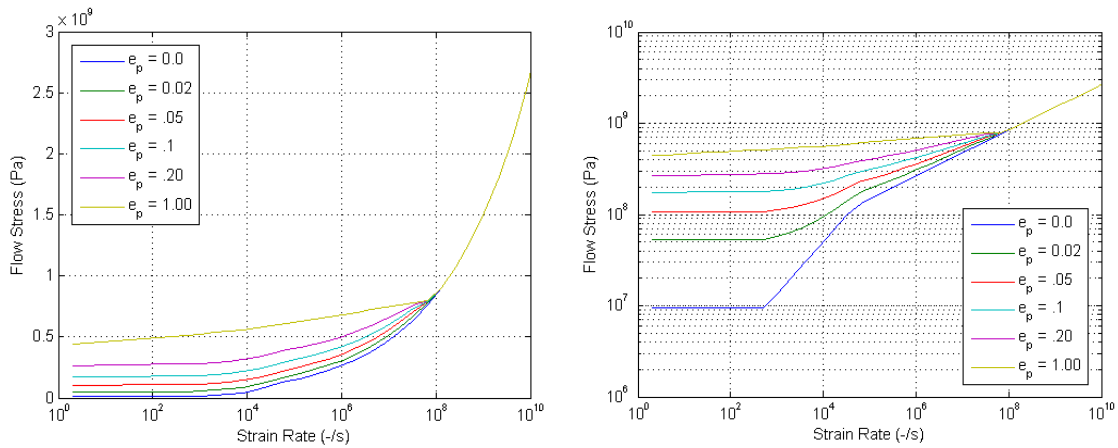


Figure 1.12: PTW flow stress vs plastic strain rate at different levels of cumulative plastic strain. Both plots are identical except one uses a linear vertical scale while the other is logarithmic.

Figure 1.13 shows (qualitatively) the flow stress (using a PTW strength law) a material point would experience as a shock front passes through it. Notice how (for many

metals) the stress, except at the shock front, changes weakly with strain rate until strain rates enter the drag regime ($\sim > 10^8 \text{ s}^{-1}$). In contrast the stress for a viscous material would change by a large amount. Fitting a viscous model to any one of the points in Figure 1.13 would produce large errors at other points. A simple compromise could be reached by approximating the low stress thermal activation regime with a constant yield stress, however this model would under predict the stress briefly in the shock front resulting in a very narrow shock front. In a simulation a significant amount of artificial viscosity may be needed to keep the numerical solution stable.

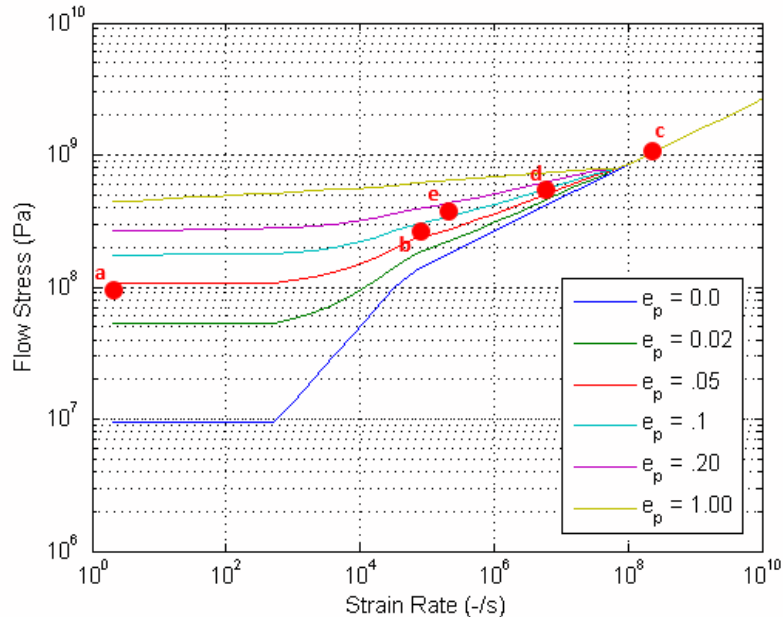


Figure 1.13: Qualitative flow stress path experienced by a material point as a shock front reaches and passes it for a PTW material. a) material starts off with some amount of prior quasi-static work hardening. b) Elastic precursor, or foot of shock wave, reaches material point. c) Material point is in the shock front, large strain rates experienced. d) Material point is experiencing moderately large strain rates due to pressure perturbations or other transient effects (e.g., elastic overshoot) immediately behind shock front. e) Material point is far away from shock front and experiences low to moderate strain rates and has accumulated a moderate amount of work hardening.

If a viscosity type model is used, the viscosity relationship would have to be strain rate dependent (decreasing with increased strain rate). This can be seen by looking at the log-log transformation of the pure viscous material law

$$y = \eta \dot{\epsilon}_p \Rightarrow Y = \log(\eta) + X \quad (1.34)$$

where $Y = \log(y)$ is the log of the flow stress, X is the log of the plastic strain rate, and η is the viscosity. Equation (1.34) would obviously not be a good fit for the behavior in Figure 1.13. Now consider a nonlinear viscous relationship with a constant yield stress term added

$$\begin{aligned} \text{yield, } y &= S_y + \eta \dot{\epsilon}_p^{\frac{1}{4}} \Rightarrow \\ \log(y) &\cong \begin{cases} \log(S_y) \equiv S, & \text{at low strain rates} \\ \log(\eta) + \frac{1}{4} \log(\dot{\epsilon}) \equiv A + \frac{1}{4} X, & \text{at high strain rates} \end{cases} \end{aligned} \quad (1.35)$$

where the upper approximation holds for low strain rates, and the second approximation holds at high strain rates. Equation (1.35) is shown in Figure 1.14. Note that Eq. (1.35) could be improved by adding pressure, temperature, and hardening sensitivity to the results, this is essentially what the PTW law does, at high strain rates it simplifies to the bottom approximation in Eq. (1.35), although the viscosity η in Eq. (1.35) scales with temperature and pressure [67]. Despite the above comments several researchers have tried to use an effective viscosity (i.e., $\eta_{eff} \dot{\epsilon}_p$) for materials [12,132]. Such an approach is likely only valid for a particular set of experimental data that is dominated by a very narrow range of strain rates.

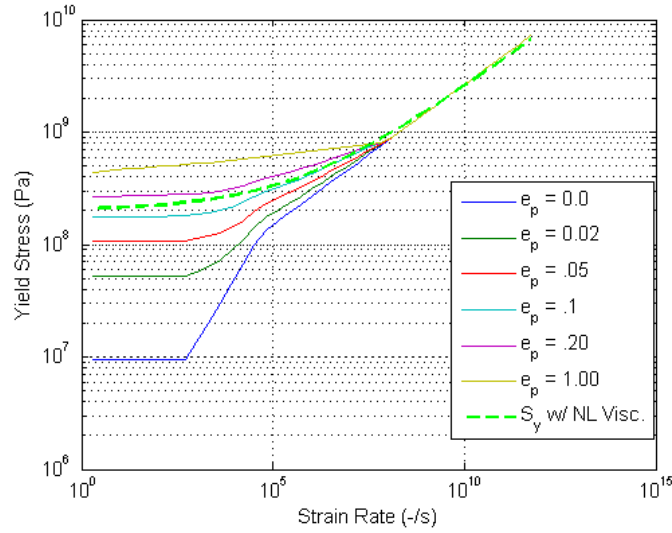


Figure 1.14: PTW material law vs constant yield stress incorporating a nonlinear viscosity strain rate relationship where $S_y = 200\text{MPa}$ and $\eta=7.5e6 \text{ Pa}\cdot\text{s}$. The nonlinear strain rate relationship is equivalent to the Swegle-Grady (SG) power law [107].

In the following sections material behavior dominated by the volumetric response is discussed, that with the deviatoric response just reviewed, completes the material constitutive behavior. First, thermodynamic equations of state typical for metals are reviewed. Then phase transformation kinetics and kinematics are reviewed. The phase transformation is found to be driven by the Gibbs free energy which can be derived from the equations of state [101].

1.5.4. Mie-Grüneisen Equation of State

The Mie-Grüneisen equation of state (MG-EOS) is the most commonly used EOS in shock simulations, and is typically included in commercial FEM packages that have an explicit solver. The MG-EOS can be derived in several ways [133,100,101], for moderate shocks the most common expression for pressure is

$$P(v, U) = \frac{\Gamma}{v}(U - U_H(v)) + P_H(v) \quad (1.36)$$

where Γ is the Gruneisen material parameter. From Eq. (1.36) the first partial with respect to temperature gives

$$\frac{\partial P}{\partial T} \cong K(v)\alpha(v) \cong \frac{\Gamma}{v} \frac{\partial U}{\partial T} = \frac{\Gamma}{v} C_v \cong \text{constant} \quad (1.37)$$

where the common assumption is that the quantity $\frac{\Gamma}{v} = \frac{\Gamma_0}{v_0}$ is approximately constant. The reference terms U_H and P_H in Eq. (1.36) are found with an appropriate relations representing appropriate material behavior, and are calculated at the same v as the pressure of interest. Several relationships can be used, such as those representing the shock velocity as a linear function of particle velocity (i.e. $C_s \cong C_0 + SC_p$), which, when combined with the conservation equations describing the jump conditions across the shock front, lead to [100]

$$P_H(v) = \frac{\rho_0 C_0^2 \eta}{(1-S\eta)^2}; \quad \eta = \left(1 - \frac{v}{v_0}\right); \quad U_H(v) = v_0 P_H \eta \quad (1.38)$$

or an explicit EOS can be used for U_H such as a Birch-Murnaghan potential [134], P_H is then the partial of U_H with respect to v along a Hugoniot path. In this regard, Equations (1.38) are a fit to a materials P - v (or equally U - v) Hugoniot, an intrinsic property of the material for a given reference point. In Eq. (1.38) the reference point is at zero pressure. The MG-EOS, Equation (1.36), then allows one to calculate a pressure for a material state, i.e. a (U, v) pair, that is off the known Hugoniot described by Eq. (1.38). The MG-EOS typically assumes material parameters (e.g. C_v , $\frac{\Gamma}{v}$, K) to be constant or temperature independent. When temperature changes are large this can obviously introduce issues. Finally, the MG-EOS has a bounded (U, v) range for which it is valid, see [101, p. 136] and

[135] to correct some errors in [101] (e.g., assuming $\gamma_0/v_0 = \gamma/v$, is more stable than $\gamma \equiv \text{constant}$ and is not developed correctly in [101]).

1.5.5. Multiphase Equation of State

A Multiphase EOS in the dynamic material literature typically refers to a highly tailored Helmholtz potential, $F(v, T)$, in terms of two state variables such as specific volume and temperature for each material phase, e.g., the α (BCC) and ϵ (HCP) phases of iron. When constructed properly a multiphase EOS describes a material better over a wider range of independent variable values than a typical Mie-Gruneisen EOS developed for each phase. A common Helmholtz potential is

$$F(v, T) = F_{cold}(v) + F_{vib}(v, T) + F_{el}(v, T) \quad (1.39)$$

where F_{cold} is the cold energy (i.e. lattice potential, no vibration), F_{vib} is the energy associated with lattice vibration (also known as the quasi-harmonic term [133, p.60]), and F_{el} is the energy associated with thermal vibrations of electrons [136]. The exact form of each term varies slightly between authors but typically follows the form described in [136, p.208]. Regardless of the exact form used, the usefulness of Eq. (1.39) is determined by how well it predicts material states (first partials of Eq. (1.39)) and material properties (second partials of Eq. (1.39)) such as shock Hugoniot. Fitting the parameters in Eq. (1.39) is typically based on experimental data; however, experimental data has been recently complemented with first principle numerical calculations such as Density Functional Theory (DFT) to provide additional data points often beyond experimental capabilities [137]. An iron multi-phase EOS is given in [138].

The next sections review the basic kinematic and kinetic principles of phase transformation. Each phase is governed by its own EOS and deviatoric behavior. The stability of a phase relative to another is determined by a thermodynamic transformation driving force which is a function of the material EOS, deviatoric behavior is also seen to be important in the phase transformation kinematics where certain phase variants (same crystal structure, but different orientation) are favored more than others due to the stress-strain conjugate term in the driving force.

1.5.6. Phase Transformation

1.5.6.1. Driving Force

The thermodynamic force that motivates a phase change is known as the driving force, f [139]. Following [140] consider a bounded region, D , with normal n_i . The rate of entropy production, Γ_D , associated with D is defined to be the excess entropy supplied to D over the amount supplied by heat flux, q , and heat supply, r , that is

$$\Gamma_D = \int_D \rho \dot{s} dV - \int_{\partial D} \frac{q_i n_i}{T} dA - \int_D \frac{\rho r}{T} dV \quad (1.40)$$

where s is entropy per unit mass, T is a piecewise continuous temperature, and ρ is a piecewise continuous density. Now consider a surface discontinuity, S_t , that intersects D , and breaks Eq. (1.40) into the sum of two parts

$$\Gamma_D = \Gamma_D^{bulk} + \Gamma_D^{jump} \quad (1.41)$$

where Γ_D^{bulk} is the bulk rate of entropy production [141], and Γ_D^{jump} is the rate of entropy production associated with the surface discontinuity.

$$\Gamma_D^{bulk} = \int_D \left(\rho \dot{s} - q_{i,i}/T - \rho r/T \right) dV \quad (1.42)$$

$$\Gamma_D^{jump} = - \int_{S_t \cap D} \left(\rho \llbracket s \rrbracket v_n + \llbracket q_i n_i / T \rrbracket \right) dA \quad (1.43)$$

where $\llbracket x \rrbracket = x^+ - x^-$ represents the difference or jump in a quantity, x , just ahead, x^+ , and just behind, x^- , the moving surface discontinuity. The derivation in Eqs. (1.42) and (1.43) uses the divergence theorem. The discontinuity moves in the direction of the normal with a velocity v_n . By using the balance of linear momentum/energy and piecewise continuity of displacement across S_t it can be shown [140, p.109] that the second term of Eq. (1.43) is

$$\llbracket q_i n_i / T \rrbracket = - \frac{1}{\langle T \rangle} \left(\rho \llbracket U \rrbracket - \sigma_{ij} \llbracket E_{ij} \rrbracket \right) v_n + \left(\langle 1/T \rangle - 1/\langle T \rangle \right) \llbracket q_i n_i \rrbracket + \llbracket 1/T \rrbracket \langle q_i n_i \rangle \quad (1.44)$$

where $\langle x \rangle = 1/2(x^+ + x^-)$ represents the average of a quantity across a boundary, U is the internal potential, and E is the work conjugate to the stress measure σ . Assuming adiabatic ($q_i = 0$) conditions or continuity of temperature across S_t , Eq. (1.44) reduces to

$$\llbracket q_i n_i / T \rrbracket = - \frac{1}{\langle T \rangle} \left(\rho \llbracket U \rrbracket - \sigma_{ij} \llbracket E_{ij} \rrbracket \right) v_n \quad (1.45)$$

Eq. (1.43) can now be written as

$$\Gamma_D^{jump} = \int_{S_t \cap D} \frac{v_n}{\langle T \rangle} \left(\llbracket \rho U \rrbracket - \langle \sigma_{ij} \rangle \llbracket E_{ij} \rrbracket - \langle T \rangle \llbracket \rho s \rrbracket \right) dA \quad (1.46)$$

Equation (1.46) can be written in terms of the Helmholtz potential, φ , as

$$\Gamma_D^{jump} = \int_{S_t \cap D} \frac{v_n}{\langle T \rangle} (\llbracket \rho \varphi \rrbracket - \langle \sigma_{ij} \rangle \llbracket E_{ij} \rrbracket + \langle \rho s \rangle \llbracket T \rrbracket) dA \quad (1.47)$$

$$f \equiv (\llbracket \rho U \rrbracket - \langle \sigma_{ij} \rangle \llbracket E_{ij} \rrbracket - \langle T \rangle \llbracket \rho s \rrbracket) = (\llbracket \rho \varphi \rrbracket - \langle \sigma_{ij} \rangle \llbracket E_{ij} \rrbracket + \langle \rho s \rangle \llbracket T \rrbracket) \quad (1.48)$$

The term in parenthesis in both Eqs. (1.46) and (1.48) is defined as the driving force, f , and has just been shown to be related to the increase in entropy across a phase boundary. Therefore, intuitively, and by the second law of thermodynamics, it appears to be a reasonable quantity for the formulation of phase transformation nucleation and kinetic equations.

In martensitic phase transformations a common assumption is that the stress ahead and behind the phase boundary is the same [137,134,142]. It is also common to make the assumption that the temperature ahead and behind the phase boundary is equal. With these assumptions, and Eq. (1.48), the driving force can be written as the difference in the Gibbs ($G = \varphi - \sigma_{ij} E_{ij}$) energy potential and for equal stress and temperature f becomes

$$\Rightarrow f = \llbracket \rho \varphi \rrbracket - \llbracket \sigma_{ij} E_{ij} \rrbracket = \llbracket G \rrbracket \quad (1.49)$$

1.5.6.2. Nucleation

In the previous section a moving discontinuity, S_t , was introduced, in this section the source or nucleation of the discontinuity is reviewed. Nucleation is typically explained in terms of either homogeneous or heterogeneous nucleation [143]. Qualitatively, homogeneous nucleation is described as a material inherently having a given distribution of embryos of certain sizes as determined by statistical fluctuations. For a given driving force all embryos of a minimum size or larger grow [144,111,101,145], embryos that grow

are said to have nucleated and further growth is determined by a kinetic model [111,110]. In almost all homogeneous cases a nonzero driving force is needed for nucleation to overcome the added surface energy produced by the nucleating embryo [101].

In heterogeneous nucleation, nucleation sites are supposed to exist at defects in the crystal structure. It is well accepted in the literature that polycrystalline and shocked materials are controlled by heterogeneous nucleation [110,144]. Some authors describe a pseudo nucleation period where heterogeneous sites begin to “nucleate” once the pressure and temperature are near the phase equilibrium value (i.e. driving force of zero). These sites continue to grow, along with the pressure (now a non zero driving force is present), until they reach a critical volume at which rapid growth ensues. This time until rapid growth has been described by some as nucleation [111, 144] while others include this pseudo nucleation time in the growth (kinetic) phase [110]. In either case the phenomenological models produce similar quantitative results. Finally, it is noted that the above references do not model nucleation/growth at individual boundaries, but instead an implied homogenization is used. For examples of nucleation and growth modeling at individual boundaries, see [146] and references therein.

1.5.6.3. Kinetics

Once a phase boundary is present the growth of the boundary (or speed) is described with a kinetic relation between the driving force and phase growth. Early phenomenological laws for shock-induced transitions observed that a simple time constant described the perceived transition rate [102,103],

$$\frac{d\lambda}{dt} = \frac{\lambda_{eq} - \lambda}{\tau} \quad (1.50)$$

where λ_{eq} is the equilibrium volume fraction for a given set of thermodynamic variables, λ is the evolving volume fraction, and τ is the time constant estimated to be around 180 ns for the iron martensitic BCC to HCP transformation. However these early experiments were limited in that only the non-driven surface velocity profiles could be observed, rates were inferred by observing a decrease in the surface velocity at transition with respect to an increase in specimen thickness, with sufficient thickness the surface velocity reaches an equilibrium value (e.g., Figure 1.11).

Boettger and Wallace [138] reexamined this experimental data and proposed models to account for metastable states and the effect of driving force. First the experimental Hugoniot was accurately described with the aid of

$$\lambda_m = 1 - \exp\left(\frac{(A - \Delta G(v, T))}{B}\right) \quad (1.51)$$

where λ_m is the metastable phase fraction of a transformed phase for a given set of thermodynamic variables (i.e. v and T), A is an activation energy (often modeled as zero), ΔG is the driving force, B is essentially a fitting constant, and a transition proceeds if the argument of the exponential in Eq. (1.51) is less than zero. Equation (1.51) combined with the typical conservation laws and phase specific EOS accurately reproduced the experimental Hugoniot [138]. A reverse transformation, nearly identical in form to Eq. (1.51), is also provided. Boettger and Wallace also revised the relation in Eq. (1.50) with a continuously varying time constant dependent on λ_m . The new time constant formulation shows that the time constant falls linearly (range of 30 to 50 ns) with the peak shock stress

at the phase transition plateau, simulations showed a much better agreement with available experimental data at the time.

More recent experimental data has shown that the time constant or rate of transformation is much more complicated than previously estimated, e.g., see [111,147]. Jensen [147] used a front surface impact experiment setup where the target was accelerated into a window. With this setup the phase transformation kinetics of the directly loaded surface could be observed. Results showed that the time constant is as low as ~ 1 ns at pressures 5 GPa above the equilibrium pressure, and time constants as high as 250 ns near the equilibrium pressure. Further work by Smith [111], showed interestingly that the transformation rate was better modeled with an analogy to dislocation based plasticity. At transformation rates below 10^6 s⁻¹ the driving force was well represented by

$$\Delta G_{peak} = 10.8 + 0.55 \ln(\dot{\lambda}) \quad (1.52)$$

while at transformation rates above that level the driving force was better captured as

$$\Delta G_{peak} = 1.15 \dot{\lambda}^{0.18} \quad (1.53)$$

where ΔG_{peak} is the driving force just before phase growth is indicated in the velocity profiles [111]. When plotted, Eqs. (1.52) and (1.53) qualitatively looked similar to plasticity limited at first by thermal activation and then at higher rates being limited by phonon drag. Smith used these results to hypothesize that phase growth is controlled by similar mechanisms to plasticity. This is a convenient result since it supports using crystal plasticity numerical constructs for phase transformation kinetics [142,148].

One final note is that earlier experiments, where transmitted wave velocities were recorded at the non impacted window surface of a relatively thick sample (>1 mm) [e.g. 102,103], missed a key observation of velocity pull back immediately after the first signs

of phase transformation in the velocity records that are witnessed in front surface impact experiments [104] and quasi-isentropic experiments where the sample thickness is relatively small (~30 microns) [111]. These experiments show dynamics that are missed with the older experiments. The cause of the velocity pull back is attributed to a rapid volume collapse due to the high initial driving force for transformation. As the wave propagates into the sample the driving force decreases via a release wave from the volume collapse so that velocity pullback eventually disappears as the driving force approaches a slowly changing value as observed in thicker samples [111,110].

1.5.6.4. Kinematics

Several methods have been used to account for phase transformation kinematics. The simplest continuum approach is to model each phase as an isotropic material where mass is simply passed to and from phases/phase variants, accounting kinematically only for the volume change [102,138,149]. Others have used isotropic material models but attempted to account for crystal orientation and transformation effects on kinematics with phenomenological expressions, e.g., potentials or expressions that result in additions to the plastic strain [150,151].

Borrowing from shape memory alloys (SMA) and transformation induced plasticity (TRIP) literature a wealth of information can be found on how to deal with diffusionless (martensitic) transformations at the crystal level [152]. The essential concept to capture is the geometric relation between the transforming phase and the phase it is transforming to. More specifically, for displacement continuity for all vectors l parallel to the phase

boundary normal n the deformation gradient in front F^+ and behind F^- the phase boundary must differ by only by a rank-1 tensor, i.e. ($a_i n_j$)

$$F_{ij}^+ l_j = F_{ij}^- l_j \Rightarrow F_{ij}^+ = F_{ij}^- + a_i n_j \quad (1.54)$$

this imposes constraints on the crystal structure and orientation on each side of the phase boundary leading to the end result that a crystal can only transform into certain ‘phase variants’ determined by n and the growth vector a_i that is generally not perpendicular to phase boundary normal n (also known as the habit plane) [140]. If F^- is the reference configuration (i.e. I_{ij}), then the right hand side in Eq. (1.54) is the transformation deformation gradient, F_{tr}^* , from a reference configuration. Alternatively, $a_i n_j$ can viewed as the transformation strain. The transformation strain has been used in infinitesimal strain algorithms [153].

Others have used a multiplicative decomposition framework utilizing F_{tr}^* for finite strains [154]

$$F = F_e F_{tr} \Rightarrow L = \dot{F} F^{-1} = \dot{F}_e F_e^{-1} + F_e \dot{F}_{tr} F_{tr}^{-1} F_e^{-1} \quad (1.55)$$

where the transformation velocity gradient, \tilde{L}_{tr} , in the reference configuration is

$$\tilde{L}_{tr} = \dot{F}_{tr} F_{tr}^{-1} = \sum_i^n \zeta^i \gamma_T^i b^i \otimes m^i \quad (1.56)$$

$$F_{tr} = \zeta_1 F_{tr,1}^* + \zeta_2 F_{tr,2}^* + \dots + \zeta_n F_{tr,n}^* = I + \sum_i^n \zeta^i \gamma_T^i b^i \otimes m^i \quad (1.57)$$

$$1 = \sum_i^n \zeta^i, \quad F_{tr,i}^* = I + \gamma_T^i b^i \otimes m^i \quad (1.58)$$

where ζ^i is the volume fraction of phase/variant i , b^i is a unit vector of the growth direction, m^i is a unit vector of the habit plane, and γ_T^i is the transformation magnitude.

Implied in Eq. (1.55) is the assumption that the elastic stretch and rotation in all the phases (variants) is the same. Assuming that the phases (variants) in a small neighborhood

share the same rotation appears reasonable since the geometric constraints imposed by Eq. (1.54) (i.e. constraints on lattice parameters) would require that the transformed grains rotate closely with the parent. However, assuming that the elastic stretch is the same in all the constituents is generally not appropriate if the transformed elastic properties are significantly different from the parent.

Another issue with Eq. (1.55) is that crystal plasticity is not accounted for. An obvious attempt to account for this would be a form such as $F = F_e F_{tr} F_p$, however the expression for F_p is not clear, unless one assumes the plastic strain in all the phases (variants) is the same [146]. To address the assumptions used in F_e and F_p Barton [142] took a slightly different approach starting with the requirement that the volume average of the velocity gradient has to equal the macro velocity gradient, L ,

$$L = \dot{F}F^{-1} = \langle L \rangle \equiv L^X + \sum_i^n \zeta^i L^i \quad (1.59)$$

$$L^i = \dot{F}_{e(i)}F_{e(i)}^{-1} + F_{e(i)}\dot{F}_{P(i)}F_{P(i)}^{-1}F_{e(i)}^{-1} \quad (1.60)$$

where L^i represents the velocity gradient of a phase (variant) constituent in the typical form used in crystal plasticity, and L^X is used to account for kinematics introduced by the phase transformations. The transformation velocity gradient, L^X , is shown below.

$$L^X = \sum_i^p L_X^i \quad (1.61)$$

$$L_X^i = \dot{m}_{(i)} \left[F_{e(i)to} G_{(i)} F_{e(i)from}^{-1} + \left(F_{e(i)to} F_{e(i)from}^{-1} - I \right) \right] \quad (1.62)$$

$$G_{(i)} = (F_{tr(i)to}^* - F_{tr(i)from}^*) F_{tr}^{-1} \quad (1.63)$$

Equation (1.63), when multiplied by $\dot{m}_{(i)}$, represents the velocity gradient produced by a mass transforming from a parent to variant or a variant to variant transformation, all with respect to the reference configuration. The first term in Eq. (1.62) then performs the appropriate elastic pull-back and push-forward operations. That is, an elastic pull-back with the transforming constituent deformation gradient ($F_{e(i)from}^{-1}$), and an elastic push-forward with the elastic deformation gradient of the resulting constituent ($F_{e(i)to}$), see Figure 1.15. This procedure is analogous to the pull-back and push-forward procedure performed on the reference configuration plastic velocity gradient in crystal plasticity. The second term in Eq. (1.62), when multiplied by $\dot{m}_{(i)}$, accounts for any elastic deformation differences in the transforming constituents, particularly in the case if transformation deformation gradients ($F_{tr(i)to}^*$ and $F_{tr(i)from}^*$ in Eq. (1.63)) are close or equal yet the elastic deformation gradients differ significantly. An interesting observation of Eq. (1.59) is that it simplifies to Eq. (1.55) in the limiting case where there is no plastic deformation and all the elastic deformation gradients among the constituents are the same. Barton's kinematic description reproduced experimental diamond anvil compression (DAC) texture plots [155,156]. The texture in the DAC experiments is a result of preferred variants growing at the expense of others due to the deformation bias of the uniaxial compression. The texture is not a result of plasticity as is the case in rolling, forming, stretching, etc.

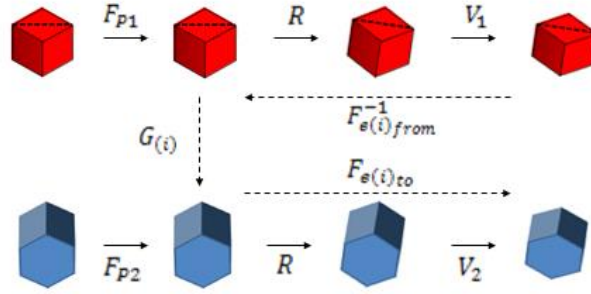


Figure 1.15: Transformation path schematic from one phase/variant to another (adapted from [142]). Transforming phase is pulled back elastically to reference configuration (reference variant), transformed to the new variant with the transformation gradient $G_{(i)}$, and then pushed forward elastically to current configuration.

Finally, it should be mentioned that DAC experiments have shown that the phase transformation of iron can be sensitive to shear stress [e.g. 157]. Caspersen, using a continuum model developed by [158] with parameters fitted to DFT calculations, was able to capture this dependence reasonably well [159].

The literature review provided above shows that evolution of hydrodynamic instabilities is well understood in the absence of deviatoric strength and phase transformations. Numerous analytical solutions exist, as previously reviewed, for RT and RM instabilities. In addition, analytical solutions exist separately for the evolution of shock front perturbations that initializes the RM instability hydrodynamic growth rate and carries perturbations to other interfaces. However, the above solutions have been primarily for isentropic processes in gases or liquids, and none of these solutions have discussed the effect of phase transformations.

The role of deviatoric stresses produced by viscous processes has been explained qualitatively well when introduced into the above analytical frameworks, and recently, semi-analytical solutions for simple elastic perfectly-plastic deviatoric strength (i.e., elastic

origins) have been developed that quantitatively capture simulation results well for RT and RM instabilities. There are still, however, underlying questions of how these instabilities behave under more complicated material models that model the dependence of strength and phase on variables such as pressure, temperature, work hardening, deformation rate, and other state variables, and how these instabilities can be used in turn to characterize material properties in these loading regimes.

2. OBJECTIVES

The objective of this work is to help expand our understanding of how more general deviatoric behavior may affect shock front perturbations and RM evolution and additional behavior introduced by phase transformations. As part of this exploratory work potential experimental setups to confirm or invalidate predicted behavior will be discussed. To meet these broad objectives the following subtasks/objectives are performed:

1. Gather and post process experimental data in a loading regime, and with materials that possess general deviatoric behavior and phase transformations, representative of RM instability evolution loading.
 - This will be accomplished with ablative loading of copper and iron samples, where the iron samples are loaded above the martensitic phase transformation. Diagnostics are used to capture dynamic data useful for model verification and validation. This experimental data is not exhaustive, but when complimented with existing data provides a good material model validation foundation for the exploratory simulations that follow.
2. Develop continuum material model subroutines for numerical simulations, and modification of existing analytical techniques, such that state variable effects in RM evolution can be studied.
 - The PTW material model is used here via a ABAQUSTM/Explicit user defined subroutine (VUMAT). The subroutine allows for two coexisting phases, each with their own state variables and deviatoric behavior. Furthermore an analytical solution for shock front perturbation evolution originally developed for viscous liquids and melted solids is modified for

solid phase metallic materials with elastic-plastic strength; the analytical solution agrees well with numerical simulations, validating general behavior.

3. Calibrate, verify, and validate material models and numerical implementation with analytical solutions and available experimental data.
4. Use the developed numerical and analytical tools to predict the effect phase transformations and general deviatoric behavior, expected from metals, has on shock front perturbation and RM evolution. This simulated behavior also provides insight into effective experimental setups that can be used to characterize and confirm material behavior at high pressure and high strain rate loading regimes.
 - Shock front perturbation evolution in solids with elastic-plastic strength and phase transformations is studied analytically and numerically for the first time.
 - RM evolution simulations are performed with copper in upper and lower bound pressure scenarios (e.g., Atwood number of 1 and -1 respectively).
 - RM evolution simulations with iron are performed in the same scenarios as copper. These results point to effective experimental setups to confirm the high-pressure phase deviatoric behavior.

3. EXPERIMENTAL PROCEDURES AND TEST DATA ANALYSIS

3.1. Experimental Procedure

The primary experimental data used in this work was produced at the Trident Laser Facility at Los Alamos National Laboratory [160]. Figure 3.1 shows the basic experimental setup. A direct laser ablation technique was used where the sample surface was irradiated with a square 10 – 30 J pulse over 5 ns. The energy was concentrated onto a 1 mm x 1 mm area (producing laser intensities around $2\text{-}6 \times 10^{11} \text{ W/cm}^2$) of the rippled side of a target with a wavelength to amplitude ratio of 25 or greater, hence irradiation of the surface was nearly uniform.

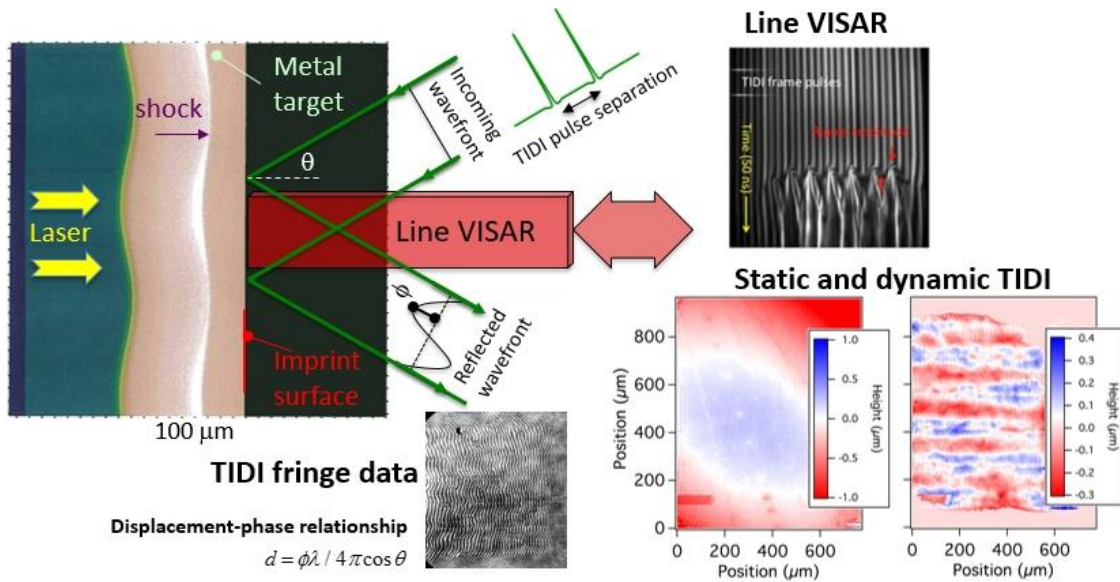


Figure 3.1: Ablation experimental schematic. High energy laser is concentrated on a 1mm x 1mm square spot on rippled target surface. Ablation of surface launches a perturbed shock wave into the material whose breakout at the opposite, initially flat, free surface is monitored with velocity (Line VISAR) and displacement (TIDI) measurements in real-time. Velocity records are continuous while displacement measurements are made discretely, but with known relation to velocity records.

At these power levels a small layer of the surface (< 1 micron [161]) is ablated launching a perturbed shock front into the sample in a way similar to a pressure boundary condition analogous to a rigid piston for a sustained ablation rate [80], although at very high laser intensities the boundary condition becomes more complicated [80,49]. The opposite free surface of the sample was monitored with laser interferometry techniques. Specifically Line VISAR [19] was used to monitor the velocity continuously of the opposite unloaded free surface and Transient Imaging Displacement Interferometry (TIDI) [15-18,162] to monitor displacement at discrete time instances keyed to the VISAR velocity record. TIDI measurements were limited to the number of fast frame CCD cameras available, in these experiments two cameras allowed two dynamic images per laser shot. Further details of the experimental setup are given in [163].

Flat and rippled samples were made from either Half-hard Oxygen-free high conductivity (OFHC) Cu or 99.99% pure iron procured in rod form. The flat and rippled samples were typically about 100 microns in thickness (all dimensions were measured prior to testing), which is the same direction as the shock. Rippled samples were made with a photolithography process, where a columnar mask with a wavelength of 80 or 150 μm was applied to the side to be rippled. A solution of 30% iron (III) chloride, 3-4% hydrochloric acid, and DI water was used as the etchant. Optical profilometry was used to measure ripple amplitude with peak to valley depths of 9 to 12 μm (i.e., amplitudes of 4.5 to 6 μm). Figure 3.2 shows a profilometer image of a typical specimen.

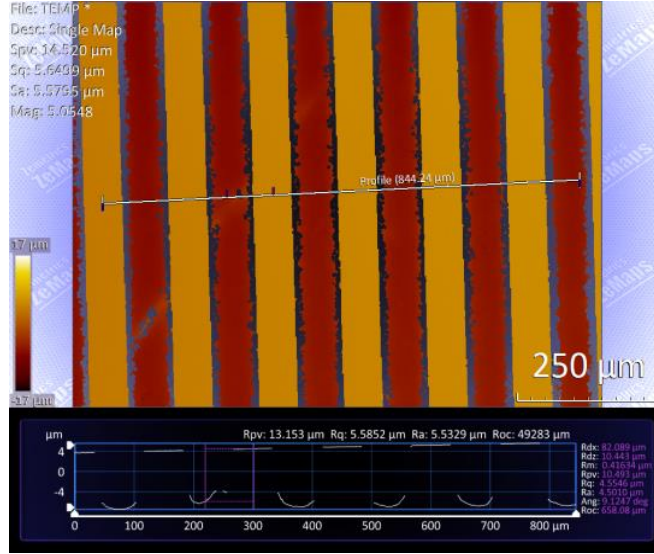


Figure 3.2: Optical profilometer image of rippled sample made with photolithography process.

3.2. Data Post Processing

The Line VISAR images are interferograms produced by splitting a laser beam source (reflected off a sample) to a delay leg and then recombining it, which forms an analog differentiation operation, so that accuracy is determined primarily by the recording source and noise. Figure 3.3 shows the basic concept [164] and is explained in more detail in [19]. Line VISAR allows for the velocity along a line to be monitored continuously for every point along that line. A simple explanation and procedure for post processing interferograms in general is given in [165]. Briefly at a given time t on the interferogram the intensity is given by [165]

$$g(x, t) = a(x, t) + b(x, t)\cos(2\pi f_0 x + \theta(x, t)) \quad (3.1)$$

where $a(x, t)$ is a DC offset that can be ignored or filtered out, $b(x, t)$ is an intensity variation that ideally would be equal to one, f_0 is the nominal frequency of the fringe pattern, and $\theta(x, t)$ is the phase angle (proportional to velocity) we want to find.

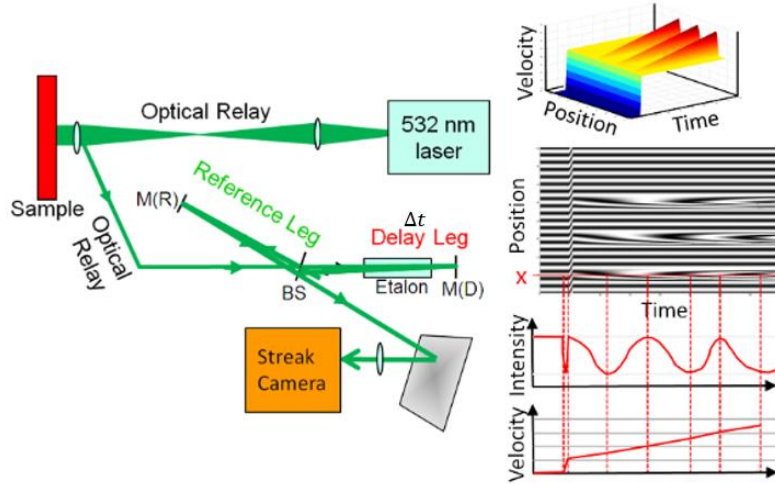


Figure 3.3: Basic Line VISAR imaging concept, reproduced from [164]. Relative laser path difference at (t) and $(t - \Delta t)$ creates a line on the interferogram for a given time (i.e., a line oscillating between strong and weak intensities). If the path difference is constant with respect to time then that point of the sample is moving with constant velocity (i.e., $vel = (x(t) - x(t - \Delta t))/\Delta t$ where x is the laser path length). If, however, a point on the sample (that is illuminated by the line VISAR) accelerates the path difference will change and the interferogram will change with the change in velocity of the point on the sample.

For a 1-D sample and impact θ would only be a function of time, for velocity variations

along the line, however, it is dependent on x . Using Euler's identity ($\cos\beta = \frac{1}{2}(e^{i\beta} +$

$e^{-i\beta})$) Eq. (3.1) can be rewritten and Fourier Transformed \mathcal{F} as

$$g(x, t) = a + \left(\frac{b}{2}e^{i\theta}\right)e^{i2\pi f_0 x} + \left(\frac{b}{2}e^{-i\theta}\right)e^{-i2\pi f_0 x} = a + c(x, t)e^{i2\pi f_0 x} + c^*(x, t)e^{-i2\pi f_0 x} \quad (3.2)$$

$$g(x) \xrightarrow{\mathcal{F}} G(f) \Rightarrow G(f, t) = A(f, t) + C(f - f_0) + C^*(f - f_0) \quad (3.3)$$

where Eq. (3.3) uses the Fourier Transform identity $f(x)e^{iw_0 x} \xrightarrow{\mathcal{F}} F(w - w_0)$. Using Eq.

(3.3) $A(f, t)$ can be ignored (i.e., filtered) while either $C(f - f_0)$ or $C^*(f - f_0)$ can be shifted

to the origin by f_0 in the frequency domain so that $C(f - f_0) \xrightarrow{shift} C(f)$. Then the inverse

Fourier Transformation and simple trigonometry gives the phase angle we want

$$C(f) \xrightarrow{\mathcal{F}^{-1}} \frac{b(x,t)}{2} e^{i\theta(x,t)} = Re(x,t) + Im(x,t) \Rightarrow \theta(x,t) = atan\left(\frac{Im}{Re}\right) \quad (3.4)$$

Given $\theta(x,t)$ the velocity is determined by multiplying θ with a factor (vpf , velocity per fringe) determined from $vpf = \lambda/2\tau$ where λ is the laser wavelength and τ is the delay in the interferometer (Figure 3.3) [19].

A couple practical issues arise while unwrapping the 2π jumps in $\theta(x,t)$. In this effort a 2D algorithm developed by [166] was used, which is applied to the 2D image of the $\theta(x,t)$ values. Also a finite impulse response (FIR) bandpass [167] filter centered at f_0 was applied to each row (i.e., t held constant) of the raw interferogram before any line by line FFTs were applied (i.e., before Eq. (3.3)), this helps to eliminate some noise such as $a(x,t)$ and other spurious data that can give the unwrapping algorithm a hard time. Figure 3.4 shows the general steps to produce a velocity signal at a point on the line illuminated by the Line VISAR. A caveat with filtering the image is that some good data could be lost. The same filter settings used to produce Figure 3.4 (Fe sample s25266) were also used on Figure 3.5 (Fe sample s25261) which showed an interesting elastic overshoot on the elastic precursor for an Fe sample [102].

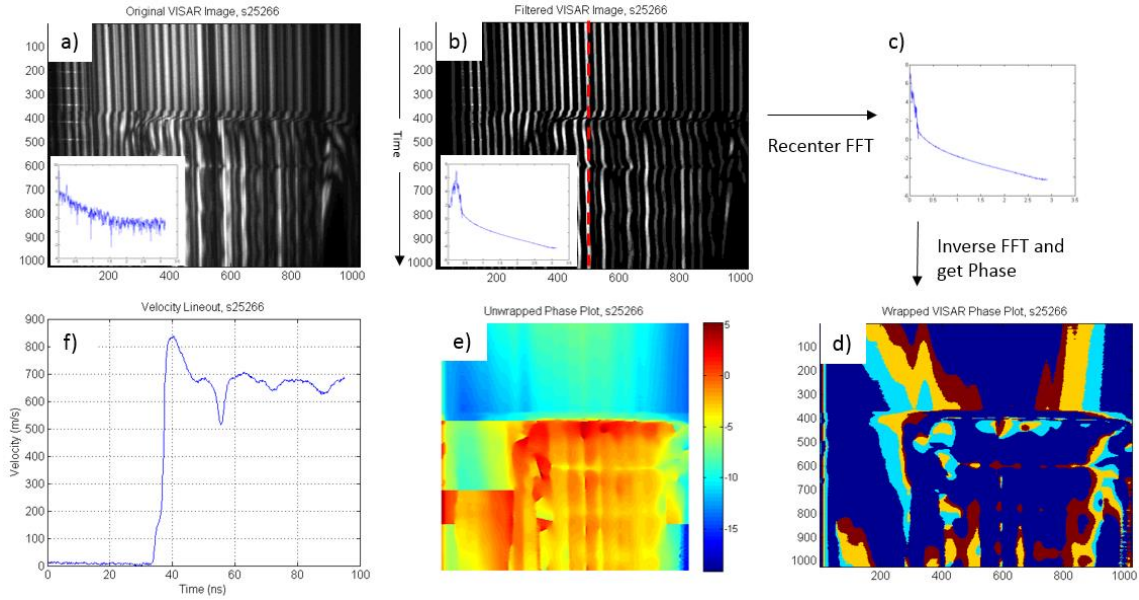


Figure 3.4: Processing of Line VISAR images. a) Original image with FFT Spectrum (of a single horizontal line, i.e., t fixed) shown in inset is filtered to produce image b) and the corresponding spectrum. In c) the filtered spectrum is shifted by f_0 to the origin. d) The phase angle $\theta(x, t)$ map found after taken the inverse FFT of c). A phase unwrapper to remove 2π jumps in d) is applied to produce image e). Finally, a lineout (dashed red line in b)) is taken from e) and multiplied by the velocity per fringe factor (vpf) to get the velocity at a point illuminated by the Line VISAR. Time, x-axis, in lineout is determined by fiducial marks (bright horizontal lines in top left corner of figure a)). Pixels between fiducials is 6.5 ns.

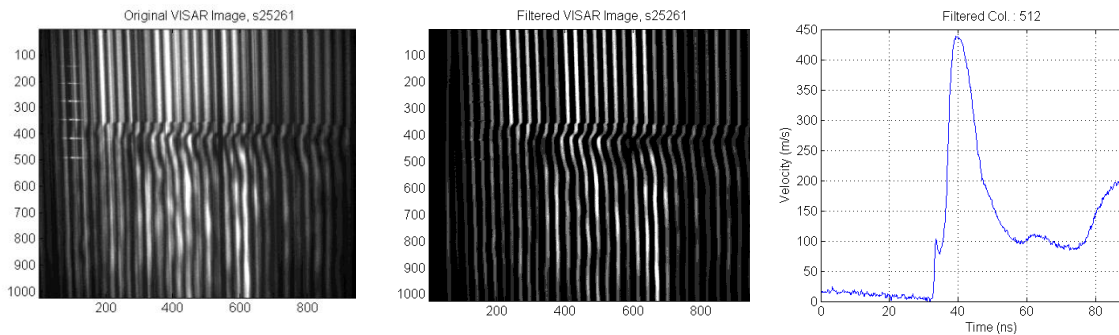


Figure 3.5: VISAR record for sample s25266. Original (left) and filtered (middle) Line VISAR image for iron sample s25266. Possible elastic overshoot on elastic precursor shown in velocity lineout (right).

The TIDI images are the result of a Mach-Zehnder interferometer [15,162], where a diagnostic beam is split into two equal beams. One beam reflects off the sample while the second beam travels a nearly equal length. When the two beams recombine an interferogram is created. This interferogram mathematically is handled identically as in the Line VISAR case, except now the phase values $\theta(x, y)$ are a measure of out-of-plane displacement for a point (x, y) in the area monitored by the beam, with interference variations representative of local displacements illuminated by the diagnostic beam. Displacement cannot be monitored continuously in time (if possible it would be a stack of 2D images, essentially a movie), but displacements (a single 2D image) can be time stamped with a tolerance of about 50 ps [162]. In this effort the TIDI interferograms were post processed slightly differently than in the Line VISAR case, however, the same phase unwrapper is used on the 2D wrapped image of $\theta(x, y)$.

For the TIDI images the images were first transformed with a 2D FFT, filtered and shifted in the frequency domain, and then the 2D inverse taken and the phase angles found $\theta(x, y)$. All of these operations are easily done with Matlab built-in functions. The Line VISAR post processing technique would have worked with the TIDI images as well, but the filtering in that approach (i.e., line by line filtering) tended to be too aggressive and better results were found with the 2D filtering method. One final note is that a ~DC or slowly varying displacement was often superimposed on the TIDI images due to macro deformation of the sample (e.g., bowing). This displacement was fitted to a polynomial and subtracted out in some cases. The unwrapped phase plot is then converted to displacement units with the displacement-phase relationship $d = \theta\lambda / (4\pi\cos\phi)$ where θ is the unwrapped phase, λ is the TIDI beam wavelength (527 nm), and ϕ is the angle of incidence

the TIDI beam forms with the sample ($\sim 28^\circ$, see Figure 3.1 [8]). Figure 3.6 shows the post processing steps.

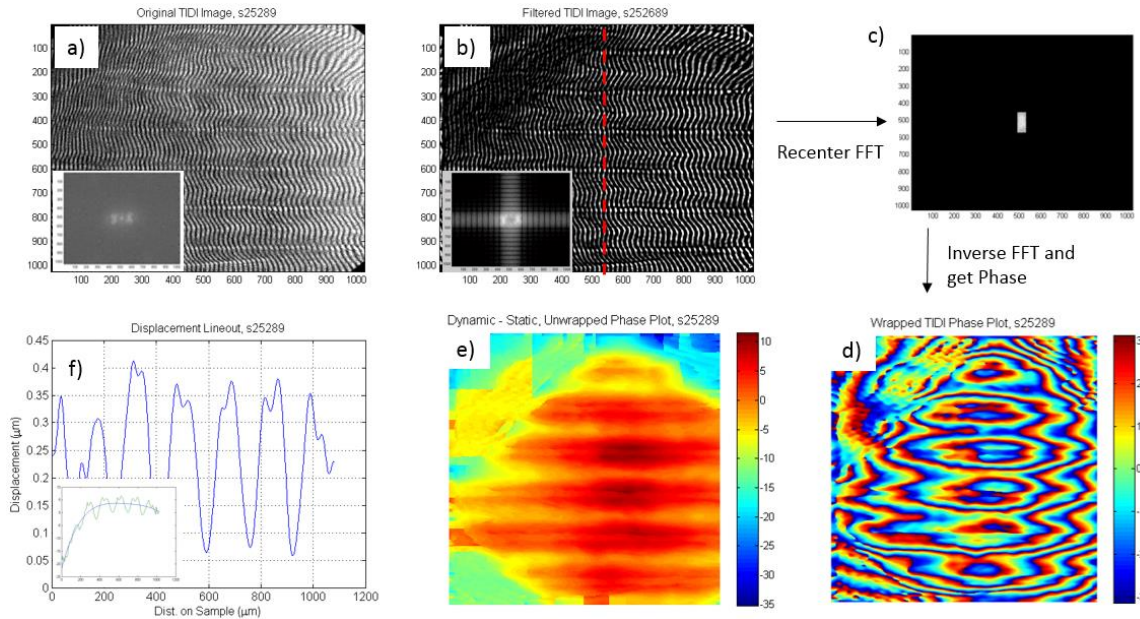


Figure 3.6: Processing of a TIDI image to obtain displacement at a point (x,y) illuminated by the TIDI beam. a) Original image with FFT Spectrum shown in inset is filtered to produce image b) and the corresponding spectrum. In c) the filtered spectrum is shifted by f_0 to the origin. d) The phase angle $\theta(x,y)$ map found after taking the inverse FFT of c). A phase unwrapper to remove 2π jumps in d) is applied to produce image e). Finally, a lineout (dashed red line in b)) is taken from e) and multiplied by the displacement per fringe factor (dpf) to get the displacement along a line illuminated by the TIDI beam f). Note in f) some bowing in the sample was removed with the polynomial fit shown in the inset.

4. MODELS

In this section several analytical and numerical models will be outlined that will later be used to describe expected or experimental results in the Results and Discussion Sections.

4.1. Preston Tonks Wallace Algorithm

The Preston-Tonks-Wallace (PTW) model was designed to provide an accurate strength model (deviatoric response) for metals across a wide range of temperatures, pressures, work hardening, and strain rates [67]. The following subsections review the model briefly and the numerical approach used. This model has been coded into an ABAQUSTM/Explicit subroutine for 2D and 3D problems.

4.1.1. Preston Tonks Wallace Strength Model

The following is a summary of [67]. Let the shear flow stress τ be one half the von Mises stress, $\dot{\phi}$ the plastic strain rate such that $\mathbf{D}_p = \dot{\phi} \partial f / \partial \boldsymbol{\sigma}$, where \mathbf{D}_p is the plastic rate of deformation, f the yield surface, and $\boldsymbol{\sigma}$ the stress tensor. Consider three non-dimensional variables

$$\hat{\tau} = \frac{\tau}{G(P,T)}, \quad \hat{T} = \frac{T}{T_m}, \quad \hat{\varepsilon} = \dot{\phi} / \dot{\xi} \quad (4.1)$$

where T_m is the melting temperature, G is the pressure and temperature dependent shear modulus, and $\dot{\xi}$ is a parameter that changes slowly with pressure and temperature (see Eq. (2) in [67]). For plastic strain rates less than $\sim 10^4 \text{ s}^{-1}$ [67] assumed thermal activation was the phenomena controlling the flow stress

$$\dot{\phi} = \phi_0 \exp(-\Delta\phi/k_B T) \quad (4.2)$$

where $\Delta\phi$ is the activation energy that decreases with applied stress so that Eq. (4.2) increases with applied stress or with an increase in temperature, and k_B and ϕ_0 are constants. Or we can say the flow stress decreases with

$$\frac{1}{\tau} \propto k_B T \ln(\phi_0/\dot{\phi}) \Rightarrow \text{analogous to } \frac{1}{\tau} \propto \kappa \hat{T} \ln(\gamma \dot{\xi}/\dot{\phi}) \quad (4.3)$$

where γ and κ are constants. Equation (4.3) needs to be merged with a work hardening expression. Preston did this with a Voce approach [168]

$$\frac{d\hat{\tau}}{d\varepsilon} = \theta \frac{\hat{\tau}_s - \hat{\tau}}{\hat{\tau}_s - \hat{\tau}_y} \quad (4.4)$$

where θ is the initial hardening slope and

$$\hat{\tau}_s = s_0 - (s_0 - s_\infty) \operatorname{erf}\left(\kappa \hat{T} \ln(\gamma \dot{\xi}/\dot{\phi})\right), \quad s_0 \geq s_\infty, \quad \dot{\phi} > 0 \quad (4.5)$$

$$\hat{\tau}_y = y_0 - (y_0 - y_\infty) \operatorname{erf}\left(\kappa \hat{T} \ln(\gamma \dot{\xi}/\dot{\phi})\right), \quad y_0 \geq y_\infty, \quad s_0 > y_0, \quad \dot{\phi} > 0 \quad (4.6)$$

where we see the saturation stress $\hat{\tau}_s$ approaches s_∞ as T becomes large or for small $\dot{\phi}$. The same relations hold for the initial yield stress $\hat{\tau}_y$. Equation (4.4) is made a little more flexible by introducing another parameter p

$$\frac{d\hat{\tau}}{d\varepsilon} = \theta \frac{\exp\left[p \frac{\hat{\tau}_s - \hat{\tau}}{s_0 - \hat{\tau}_y}\right] - 1}{\exp\left[p \frac{\hat{\tau}_s - \hat{\tau}_y}{s_0 - \hat{\tau}_y}\right] - 1} \quad (4.7)$$

Equation (4.7) becomes Eq. (4.6) for small p (e.g., apply L'Hospital's Rule). Increasing p slows the decay of Eq. (4.7), i.e., the stress-strain curve hardens longer for larger plastic strains with p increased. Integrating Eq. (4.7) with $\dot{\phi}$ held constant yields

$$\hat{\tau} = \hat{\tau}_s + \frac{1}{\rho}(s_0 - \hat{\tau}_y) \ln \left[1 - \left[1 - \exp \left(-p \frac{\hat{\tau}_s - \hat{\tau}_y}{s_0 - \hat{\tau}_y} \right) \right] \exp \left\{ - \frac{p\theta\phi}{(s_0 - \hat{\tau}_y) \left[\exp \left(p \frac{\hat{\tau}_s - \hat{\tau}_y}{s_0 - \hat{\tau}_y} \right) - 1 \right]} \right\} \right] \quad (4.8)$$

so that Eqs. (4.5), (4.6), and (4.8) are the necessary equations for plastic strain rates around or less than $\sim 10^4 \text{ s}^{-1}$ (note that the strain rates that Eq. (4.8) applies to depends on $\gamma\dot{\xi}$).

For large plastic strain rates $> \sim 10^7 \text{ s}^{-1}$ (e.g., rates you would see in the shock front) a phonon drag model is used

$$\hat{\tau}_s = \hat{\tau}_y = \omega(\dot{\phi}/\gamma\dot{\xi})^\beta \Rightarrow \hat{\tau} = \omega(\dot{\phi}/\gamma\dot{\xi})^\beta \quad (4.9)$$

where typically $\beta \approx 0.25$ which obeys the Swegle-Grady fourth power law [107], and ω is another parameter [131] set to s_0 by [67] so that no extra parameters are added.

In the intermediate region $\sim 10^4 \text{ s}^{-1} < \dot{\phi} < \sim 10^7 \text{ s}^{-1}$ [67] used a fitting technique to tie the transition from Eq. (4.8) to Eq. (4.9) together

$$\hat{\tau}_s = \max\{\text{Eq. (4.5), Eq. (4.9)}\} \quad (4.10)$$

$$\hat{\tau}_y = \max\left\{\text{Eq. (4.6), } \min\left[y_1(\dot{\phi}/\gamma\dot{\xi})^{y_2}, \text{Eq. (4.9)}\right]\right\} \quad (4.11)$$

where y_1 and y_2 are two new additional parameters. Figure 4.1 shows how Eqs. (4.5), (4.6), and (4.8) and (4.11) effect the flow stress $\hat{\tau}$ versus strain rate $\dot{\phi}$, and Figure 4.2 is a constant pressure and temperature plot for copper.

Finally to get the actual flow stress τ (Eq. (4.1)) we need an expression for the pressure and temperature dependent shear modulus.

$$G(P, T) = (G_0(P_0) + \alpha_P (P - P_0))(1 - \alpha_T \hat{T}) \quad (4.12)$$

where α_T and α_P are typically assumed to be constants. Therefore the flow stress Y is

$$Y = 2G\hat{\tau} \quad (4.13)$$

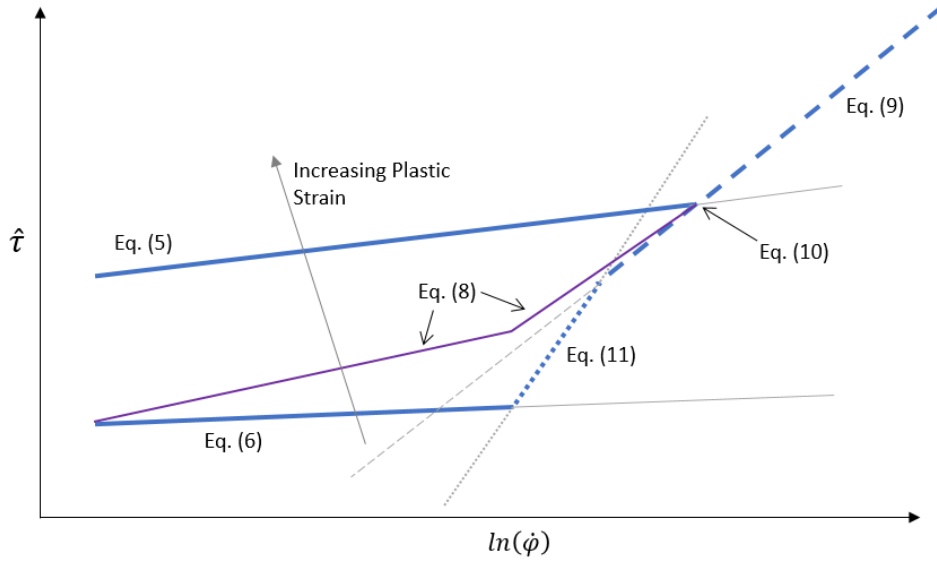


Figure 4.1: Schematic of PTW equations. Dark thick blue lines show approximate upper and lower limits determined by the indicated equations. Purple curve is the actual normalized flow stress (not unique) as it evolves with work hardening and plastic strain rate.

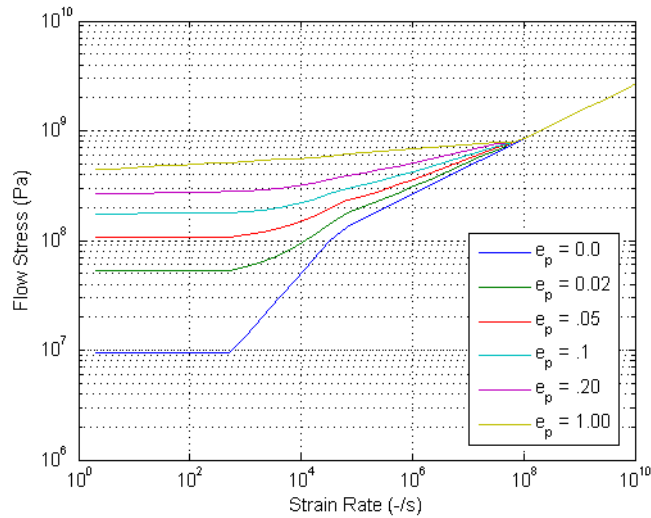


Figure 4.2: PTW material strength for constant plastic strain values at a fixed pressure and temperature (generated with C_u values from [67]).

4.1.2. PTW Algorithm

The PTW equations outlined above were implemented into an ABAQUS Explicit User Subroutine (VUMAT). The kinematic framework is in a corotated system, where ABAQUS provides the corotated strain increment and the VUMAT passes back a corotated stress $\hat{\boldsymbol{\sigma}}$

$$\hat{\boldsymbol{\sigma}}_{t+\Delta t} = \hat{\boldsymbol{\sigma}}_t + \Delta \hat{\boldsymbol{\sigma}}_{t+\Delta t} = \hat{\boldsymbol{\sigma}}_t + \left(\hat{\mathbf{S}} - \mathbf{I}\dot{P} \right) dt = \hat{\mathbf{S}}_t + \hat{\mathbf{S}}_{t+\Delta t} dt - \mathbf{I}P_{t+\Delta t} \quad (4.14)$$

where the pressure $P_{t+\Delta t}$ is calculated with an EOS that is decoupled from the deviatoric response. The deviatoric stress rate $\hat{\mathbf{S}}_{t+\Delta t}$ is what we need to calculate with the PTW strength model. For convenience we drop the carrot on the corotated terms and the deviatoric stress rate becomes

$$\dot{\mathbf{S}}_{t+\Delta t} = 2\dot{G}_{t+\Delta t}\mathbf{E}_t^e + 2G\mathbf{D}_{t+\Delta t}^{e,dev} \quad (4.15)$$

where \mathbf{E}_t^e is the corotated deviatoric elastic strain, $\mathbf{D}_{t+\Delta t}^{e,dev}$ is the corotated deelastic deformation rate that we need to find, and G is the pressure and temperature dependent shear modulus. Rather than find the elastic deformation rate directly we use an elastic predictor and plastic corrector

$$\mathbf{S}_{t+\Delta t} = \mathbf{S}_t + \left(2\Delta G\mathbf{E}_t^e + 2G\mathbf{D}_{t+\Delta t}^{dev} dt \right) - 2G\mathbf{D}_{t+\Delta t}^p dt = \mathbf{S}'_{t+\Delta t} - 2G\mathbf{D}_{t+\Delta t}^p dt \quad (4.16)$$

where $\mathbf{D}_{t+\Delta t}^{dev} dt$ is the total deviatoric corotated strain increment passed in, and

$$\mathbf{D}_{t+\Delta t}^p dt = \Delta\gamma_{t+\Delta t}\mathbf{r}, \quad \mathbf{r} = \frac{\partial f}{\partial \hat{\boldsymbol{\sigma}}} = \frac{3}{2} \frac{\mathbf{S}_t}{\sigma_{vm,t}}, \quad \Delta\gamma_{t+\Delta t} = \dot{\gamma} dt \quad (4.17)$$

$$\mathbf{S}'_{t+\Delta t} = \mathbf{S}_t + \left(2\Delta G\mathbf{E}_t^e + 2G\mathbf{D}_{t+\Delta t}^{dev} dt \right) = \mathbf{S}'_{t+\Delta t} + 2\Delta G\mathbf{E}_t^e \quad (4.18)$$

where $\Delta\gamma \geq 0$ is the plastic strain increment, and \mathbf{r} is the normal to the flow stress surface f . We need to find $\dot{\gamma}$, consider the flow stress surface at the end of the time increment

$$f_{t+\Delta t} = \sigma_{Y,t+\Delta t}(P + \Delta P, T + \Delta T, \dot{\gamma}, \gamma + \dot{\gamma}dt) - \sigma_{vm,t+\Delta t} \leq 0 \quad (4.19)$$

where σ_Y is the yield stress calculated with the PTW equations. If f is less than zero for $\dot{\gamma} = 0$ the problem is elastic and Eq. (4.16) is the solution with no plastic strain, otherwise Eq. (4.18) is a nonlinear equation that has to be solved for the unknown plastic strain rate (or equally plastic strain increment). To do that we need σ_{vm} as a function of the plastic strain increment (rate)

$$\mathbf{S} = \mathbf{S}^{tr} - 2G\Delta\gamma\mathbf{r} = \mathbf{S}^{tr} - 2G\Delta\gamma\frac{3}{2}\frac{\mathbf{S}}{\sigma_{vm}} \quad (4.20)$$

After some algebra [169] with Eq. (4.20) we can write

$$\sigma_{vm,t+\Delta t} = \sigma_{vm,t+\Delta t}^{tr} - 3G\Delta\gamma = \sigma_{vm,t+\Delta t}^{tr} - 3G\dot{\gamma}dt \quad (4.21)$$

Equations (4.19), (4.21), and the PTW Equations (4.5), (4.6), (4.8) through (4.11) can be used in a Newton-Raphson solver to find $\dot{\gamma}$ assuming ΔG is given. Typically $\Delta G = G_{,T}\Delta T + G_{,P}\Delta P$ is known from the $G=G(T,P)$ behavior and the known temperature and pressure deltas determined with the volumetric equation of state (i.e., deviatoric influence is neglected). The decoupling between the volumetric and deviatoric response is not necessary with a little more effort. We can show this with the following, consider the change in specific volume

$$\dot{v} = \frac{\partial v}{\partial P}\dot{P} + \frac{\partial v}{\partial T}\dot{T} + \frac{\partial v}{\partial E_{dev}}:\mathbf{D}_{dev} \Rightarrow \frac{\Delta v}{v} = -\frac{1}{B}\Delta P + \alpha\Delta T + 0 \quad (4.22)$$

where B is the temperature and density dependent bulk modulus, and α the temperature and density dependent coefficient of thermal expansion, both are found with the volumetric term of the Helmholtz free energy $F_v(v, T)$

$$B(v, T) = v\frac{\partial^2 F_v}{\partial v^2}, \quad \alpha(v, T) = -\frac{1}{B}\frac{\partial^2 F_v}{\partial T\partial v} \quad (4.23)$$

where v is the specific volume. Next consider the internal energy rate \dot{E}

$$\dot{E} - v\mathbf{S}:\mathbf{D}^e = \frac{\partial E_v}{\partial v}\dot{v} + \frac{\partial E_v}{\partial T}\dot{T} \quad (4.24)$$

where $\dot{E} = v\boldsymbol{\sigma}:\mathbf{D}$ and the volumetric internal energy E_v is

$$E_v = F_v + sT = F_v - \frac{\partial F_v}{\partial T}T \quad (4.25)$$

After some algebra and using Eq. (4.22) \dot{E} becomes

$$\dot{E} - v\mathbf{S}:\mathbf{D}^e = \left(\frac{v^P}{B} - T\alpha v\right)\dot{P} + (-Pv\alpha + Tv\alpha^2B + C_v)\dot{T} \quad (4.26)$$

where $C_v = -T \partial^2 F_v / \partial T^2$ is the specific heat. Equation (4.26) can be simplified with

$$\begin{aligned} \dot{E} - v\mathbf{S}:\mathbf{D}^e &= v\boldsymbol{\sigma}:\mathbf{D} - v\mathbf{S}:\mathbf{D}^e = \left\{v\left(-P\frac{\dot{v}}{v}\right) + v\mathbf{S}:(\mathbf{D}^p + \mathbf{D}^e)\right\} - v\mathbf{S}:\mathbf{D}^e \\ &= -IP\dot{v} + v\mathbf{S}:\mathbf{D}^p \end{aligned} \quad (4.27)$$

and the plastic deformation rate \mathbf{D}^p term can be simplified more

$$v\mathbf{S}:\mathbf{D}^p = v\mathbf{S}:\left(\frac{3}{2}\frac{\mathbf{S}}{\sigma_{vm}}\dot{\gamma}\right) = v\sigma_{vm}\dot{\gamma} \quad (4.28)$$

From Eq. (4.26) through (4.28) we have

$$-IP\dot{v} = \left(\frac{v^P}{B} - T\alpha v\right)\dot{P} + (-Pv\alpha + Tv\alpha^2B + C_v)\dot{T} - v\sigma_{vm}\dot{\gamma} \quad (4.29)$$

$$-IP\Delta v = \left(\frac{v^P}{B} - T\alpha v\right)\Delta P + (-Pv\alpha + Tv\alpha^2B + C_v)\Delta T - v\sigma_{vm}\dot{\gamma}dt \quad (4.30)$$

Equations (4.22) and (4.30) have three unknowns ΔP , ΔT , and $\dot{\gamma}$ and shows how the deviatoric behavior of the material is coupled with the volumetric behavior in the above hypoelastic formulation. Equation (4.19) provides the third equation and is generally dependent on all three unknowns. A multi-variate Newton-Raphson (NR) solver can be used in this case, although in most cases due to the weak deviatoric/volumetric coupling the solution will likely not differ much from the approximate decoupled solution. Before moving on it is helpful to simplify Eq. (4.19) a little more. The deviatoric stress is

$$\mathbf{S} = \mathbf{S}_t + 2G\mathbf{D}_{dev}^e \Delta t + 2\Delta G\mathbf{E}_{dev} = \mathbf{S}^{tr} - 2Gr\Delta\gamma + 2\Delta G\mathbf{E}_{dev} \quad (4.31)$$

where

$$\mathbf{S}^{tr} = \mathbf{S}_t + 2G\mathbf{D}_{dev}\Delta t, \quad \mathbf{r} = \frac{3}{2}\frac{\mathbf{S}}{\sigma_{vm}}, \quad \mathbf{E}_{dev} = \frac{\mathbf{S}}{2G}, \quad \mathbf{D}_{dev} = \mathbf{D}_{dev}^e + 2Gr\Delta\gamma \quad (4.32)$$

Using Eq. (4.31) and (4.32) we have

$$\mathbf{S} = \mathbf{S}^{tr} - 3G\frac{\mathbf{S}}{\sigma_{vm}}\Delta\gamma + \frac{\Delta G}{G}\mathbf{S} \Rightarrow \left(1 - \frac{\Delta G}{G} + 3\frac{\Delta\gamma}{\sigma_{vm}}G\right)\mathbf{S} = \mathbf{S}^{tr} \quad (4.33)$$

Squaring both sides of Eq. (4.33), multiplying by 3/2, and using the definition of the von Mises stress

$$\left(1 - \frac{\Delta G}{G} + 3\frac{\Delta\gamma}{\sigma_{vm}}G\right)\sigma_{vm} = \sigma_{vm}^{tr} \Rightarrow \sigma_{vm} = (\sigma_{vm}^{tr} - 3G\Delta\gamma)\left(1 - \frac{\Delta G}{G}\right)^{-1} \quad (4.34)$$

For small changes in the shear modulus ΔG Eq. (4.34) becomes

$$\begin{aligned} \sigma_{vm} &\cong (\sigma_{vm}^{tr} - 3G\Delta\gamma)\left(1 + \frac{\Delta G}{G}\right) \cong \sigma_{vm}^{tr} + \frac{\sigma_{vm}^{tr}}{G}\Delta G - 3G\Delta\gamma \\ &= \sigma_{vm}^{tr} + \frac{\sigma_{vm}^{tr}}{G}G_{,T}\Delta T + \frac{\sigma_{vm}^{tr}}{G}G_{,P}\Delta P - 3G\dot{\gamma}dt \end{aligned} \quad (4.35)$$

where $G_{,T} = \partial G/\partial T$ and $G_{,P} = \partial G/\partial P$. Then Eq. (4.19) becomes

$$\begin{aligned} f = \sigma_y - \sigma_{vm} = 0 &\Rightarrow f = \sigma_y(P + \Delta P, T + \Delta T, \dot{\gamma}, \gamma + \dot{\gamma}dt) \\ &- \left(\sigma_{vm}^{tr} + \frac{\sigma_{vm}^{tr}}{G}G_{,T}\Delta T + \frac{\sigma_{vm}^{tr}}{G}G_{,P}\Delta P - 3G\dot{\gamma}dt\right) = 0 \end{aligned} \quad (4.36)$$

Now Eq. (4.36) replaces Eq. (4.19) so that the only numerical derivative (if needed at all) is for the material strength law that defines $\sigma_y(P, T, \dot{\gamma}, states)$. Therefore the equations to solve (assuming yielding is occurring) are

$$\begin{aligned} y_1 &= -\frac{1}{B}\Delta P + \alpha\Delta T - \frac{\Delta v}{v} = 0 \\ y_2 &= \left(\frac{vP}{B} - T\alpha v\right)\Delta P + (-Pv\alpha + Tv\alpha^2 B + C_v)\Delta T - v\sigma_{vm}\dot{\gamma}dt + IP\Delta v = 0 \end{aligned}$$

$$y_3 = \sigma_y(P + \Delta P, T + \Delta T, \dot{\gamma}, \gamma + \dot{\gamma}dt) - \left(\sigma_{vm}^{tr} + \frac{\sigma_{vm}^{tr}}{G} G_{,T} \Delta T + \frac{\sigma_{vm}^{tr}}{G} G_{,P} \Delta P - 3G\dot{\gamma}dt \right) = 0$$

which becomes the Newton-Raphson (NR) problem (with the constraint $\dot{\gamma} > 0$)

$$\mathbf{y}_n + \mathbf{A}_n(\mathbf{x}_{n+1} - \mathbf{x}_n) = 0 \Rightarrow \mathbf{x}_{n+1} = \mathbf{A}_n^{-1}(-\mathbf{y}_n) + \mathbf{x}_n, \text{ where } \mathbf{y}_n = \mathbf{y}(\mathbf{x}_n)$$

$$\begin{bmatrix} y_1 \\ y_2 \\ y_3 \end{bmatrix}_n +$$

$$\begin{bmatrix} -\frac{1}{B} & \alpha & 0 \\ \left(\frac{vP}{B} - T\alpha v\right) & (-Pv\alpha + Tv\alpha^2 B + C_v) & -v\sigma_{vm}dt \\ \frac{\partial \sigma_y}{\partial P} - \frac{\sigma_{vm}^{tr}}{G} G_{,P} & \frac{\partial \sigma_y}{\partial T} - \frac{\sigma_{vm}^{tr}}{G} G_{,T} & \frac{\partial \sigma_y}{\partial \dot{\gamma}} + dt \frac{\partial \sigma_y}{\partial \gamma} + 3G \end{bmatrix}_n \begin{bmatrix} (\Delta P_{n+1} - \Delta P_n) \\ (\Delta T_{n+1} - \Delta T_n) \\ (\dot{\gamma}_{n+1} - \dot{\gamma}_n) \end{bmatrix}_{n+1} = 0$$

$$residual \equiv \sqrt{\mathbf{y}^T(\mathbf{x}_{n+1})\mathbf{W}\mathbf{y}(\mathbf{x}_{n+1})} \quad (4.37)$$

where the subscript n is the NR iteration count within a time increment, and the matrix \mathbf{W} is a diagonal matrix of weighting coefficients (set to identity by default). The initial guess when entering the NR loop is $\mathbf{x}_0 = [0 \ 0 \ \dot{\gamma}_{old}]^T$. Typically a solution is found after only one or two NR iterations.

4.2. Isotropic Phase Transformation Algorithm

In this section an algorithm is developed, similar to those in [149,171], for materials that undergo phase changes at high pressure/temperature conditions. We also assume each phase has its own strength behavior modeled with a different set of PTW parameters for each of them.

4.2.1. Volume

As in a single-phase material we start with the increment (rate) of the volume

$$v = \sum_k \xi_k v_k \Rightarrow \dot{v} = \sum_k (\dot{\xi}_k v_k + \xi_k \dot{v}_k) \quad (4.38)$$

where ξ_k is the mass fraction of phase k . We assume that the mass fraction rate is known from the previous time step via a kinetics relation (i.e., it is calculated explicitly). The volume rate for phase k is known from Eq. (4.22), so that Eq. (4.38) becomes

$$\frac{\dot{v}}{v} = \frac{1}{v} \sum_k \left(\dot{\xi}_k v_k - \frac{\xi_k v_k}{B_k} \dot{P} + \xi_k v_k \alpha_k \dot{T} \right) \Rightarrow \frac{\dot{v}}{v} = -\frac{1}{B} \dot{P} + \alpha \dot{T} + \sum_k \frac{\dot{\xi}_k v_k}{v} \quad (4.39)$$

where the effective bulk modulus B and thermal expansion coefficient α are

$$B = \left[\sum_k \frac{\zeta_k}{B_k} \right]^{-1}, \quad \alpha = \sum_k \zeta_k \alpha_k, \quad \zeta_k = \xi_k v_k / v \quad (4.40)$$

and ζ_k is the phase volume fraction.

4.2.2. Energy

The increment in energy E is

$$E = \sum_k \xi_k E_k \Rightarrow \dot{E} = \sum_k (\dot{\xi}_k E_k + \xi_k \dot{E}_k) \quad (4.41)$$

where

$$\dot{E}_k = \left(\frac{v_k P}{B_k} - T \alpha_k v_k \right) \dot{P} + (-P v_k \alpha_k + C_k) \dot{T} + v_k \mathbf{S}_k : \mathbf{D}^e, \quad \text{where } C_k = T v_k \alpha_k^2 B_k + C_{v_k} \quad (4.42)$$

so that Eq. (4.41) becomes

$$\dot{E} = \sum_k \dot{\xi}_k E_k + v \left[\left(\frac{1}{B} P - \alpha T \right) \dot{P} + \left(-\alpha P + \frac{1}{v} C_p \right) \dot{T} \right] + \sum_k \boldsymbol{\sigma}_k : \mathbf{D}_k^{e,dev} \xi_k v_k \quad (4.43)$$

$$C_p = \sum_k \xi_k C_k \quad (4.44)$$

and E_k is

$$E_k = E_{v_k} + E_{dev_k}, \quad E_{dev_k} = E_{dev_k} + \Delta E_{dev_k} \quad (4.45)$$

so that

$$dt\dot{\xi}_k E_{dev_k} = dt\dot{\xi}_k (E_{dev_k} + \Delta E_{dev_k}) \cong dt\dot{\xi}_k E_{dev_k} \quad (4.46)$$

where E_{dev_k} (as well as E_{v_k}) is the energy updated at the end of the previous time step.

Using Eq. (4.26) and (4.43) we have

$$-P\dot{v} - \sum_k \dot{\xi}_k E_k = v \left(\frac{1}{B} P - \alpha T \right) \dot{P} + v \left(-P\alpha + \frac{1}{v} C_p \right) \dot{T} - v \sum_k \sigma_{vm_k} \zeta_k \dot{\gamma}_k \quad (4.47)$$

At this point we make a homogenization assumption with respect to the deviatoric stress \mathbf{S}

and assume all phases are at the same deviatoric stress $\mathbf{S} = \mathbf{S}_k$. Then Eq. (42) becomes

$$-P\dot{v} - \sum_k \dot{\xi}_k E_k = v \left(\frac{1}{B} P - \alpha T \right) \dot{P} + v \left(-P\alpha + \frac{1}{v} C_p \right) \dot{T} - v \sigma_{vm} \sum_k \zeta_k \dot{\gamma}_k \quad (4.48)$$

where

$$\sigma_{vm} \dot{\gamma}_k dt = (\sigma_{vm} + \dot{\sigma}_{vm} dt) \dot{\gamma}_k dt \cong \sigma_{vm} \dot{\gamma}_k dt \quad (4.49)$$

4.2.3. Deviatoric

Start with the total deviatoric strain rate \mathbf{D}^{dev}

$$\mathbf{D}^{dev} = \sum_k \dot{\zeta}_k \mathbf{E}_k^{e,dev} + \sum_k \zeta_k (\mathbf{D}_k^{e,dev} + \mathbf{D}_k^{p,dev}) \quad (4.50)$$

where $\mathbf{E}_k^{e,dev}$ is the elastic deviatoric strain in phase k. Using the assumption that the deviatoric stress \mathbf{S} is the same in all the phases Eq. (4.50) becomes

$$\mathbf{D}^{dev} = \mathbf{S} \sum_k \dot{\zeta}_k \frac{1}{2G_k} + \sum_k \zeta_k (\mathbf{D}_k^{e,dev} + \mathbf{D}_k^{p,dev}) \quad (4.51)$$

and also

$$\dot{\mathbf{S}} = 2\dot{G}_k \mathbf{E}_k^{e,dev} + 2G_k \mathbf{D}_k^{e,dev} \Rightarrow \mathbf{D}_k^{e,dev} = \frac{\dot{\mathbf{S}}}{2G_k} - \frac{\dot{G}_k}{G_k} \frac{\mathbf{S}}{2G_k} \quad (4.52)$$

Combining Eq. (4.51) and (4.52) gives

$$\mathbf{D}^{dev} = \sum_k \zeta_k \left(\frac{\dot{\mathbf{S}}}{2G_k} - \frac{\dot{G}_k}{G_k} \frac{\mathbf{S}}{2G_k} + \mathbf{D}_k^{p,dev} \right) + \mathbf{S} \sum_k \dot{\zeta}_k \frac{1}{2G_k} \quad (4.53)$$

Using

$$\mathbf{D}_k^{p,dev} = \frac{3}{2} \frac{\mathbf{S}}{\sigma_{vm}} \dot{\gamma}_k, \quad G = \left[\sum_k \frac{\zeta_k}{G_k} \right]^{-1} \quad (4.54)$$

Equation (4.53) gives

$$\dot{\mathbf{S}} = 2G\mathbf{D}^{dev} - 2G \left[\mathbf{S} \sum_k \dot{\zeta}_k \frac{1}{2G_k} + \mathbf{S} \sum_k \frac{3}{2} \frac{\zeta_k}{\sigma_{vm}} \dot{\gamma}_k - \mathbf{S} \sum_k \frac{\dot{G}_k}{G_k} \frac{\zeta_k}{2G_k} \right] \quad (4.55)$$

or

$$\mathbf{S} = \mathbf{S}_{old} + \dot{\mathbf{S}}dt = \mathbf{S}^{tr} - 2G \left[\mathbf{S} \sum_k \Delta\zeta_k \frac{1}{2G_k} + \mathbf{S} \sum_k \frac{3}{2} \frac{\zeta_k}{\sigma_{vm}} \Delta\gamma_k - \mathbf{S} \sum_k \frac{\Delta G_k}{G_k} \frac{\zeta_k}{2G_k} \right] \quad (4.56)$$

where \mathbf{S}^{tr}

$$\mathbf{S}^{tr} = \mathbf{S}_{old} + 2G\mathbf{D}^{dev} \quad (4.57)$$

Rearranging Eq. (4.56) yields

$$\mathbf{S} \left(1 + G \sum_k \Delta\zeta_k \frac{1}{G_k} + 3G \sum_k \frac{\zeta_k}{\sigma_{vm}} \Delta\gamma_k - G \sum_k \frac{\zeta_k \Delta G_k}{G_k^2} \right) = \mathbf{S}^{tr} \quad (4.58)$$

If the volumetric and deviatoric response are approximated as being decoupled then all terms in the parenthesis in Eq. (4.58) are known except for the increments in the plastic slip $\Delta\gamma_k$

Equation (4.58) introduces k additional unknowns $\dot{\gamma}_k$ (i.e., in addition to \dot{P} and \dot{T}). The k additional equations come from the flow surface f_k

$$f_k = \sigma_{y_k}(P + \Delta P, T + \Delta T, \dot{\gamma}_k, \gamma_k + \dot{\gamma}_k dt) - \sigma_{vm} = 0 \quad (4.59)$$

where the flow stress σ_y is the same as in the single phase problem.

The von Mises stress σ_{vm} in Eq. (4.59) can be found by squaring Eq. (4.58), multiplying by 3/2 and using the definition of σ_{vm} (i.e., $\sigma_{vm}^2 = \frac{3}{2} \mathbf{S} : \mathbf{S}$) yields

$$\sigma_{vm} \left(1 + G \sum_k \Delta\zeta_k \frac{1}{G_k} + 3G \sum_k \frac{\zeta_k}{\sigma_{vm}} \Delta\gamma_k - G \sum_k \frac{\zeta_k \Delta G_k}{G_k^2} \right) = \sigma_{vm}^{tr} \quad (4.60)$$

which gives

$$\sigma_{vm} = \sigma_{vm}^{tr} \left(1 + G \sum_k \Delta\zeta_k \frac{1}{G_k} - G \sum_k \frac{\zeta_k \Delta G_k}{G_k^2} \right)^{-1} - 3G \sum_k \zeta_k \Delta\gamma_k \quad (4.61)$$

which can be expanded, by ignoring second order terms, as

$$\sigma_{vm} = \sigma_{vm}^{tr} - G \sigma_{vm}^{tr} \sum_k \Delta\zeta_k \frac{1}{G_k} + G \sigma_{vm}^{tr} \sum_k \frac{\zeta_k \Delta G_k}{G_k^2} - 3G \sum_k \zeta_k \Delta\gamma_k \quad (4.62)$$

For just two phases (i.e., $k=2$), and expanding out ΔG_k , gives

$$\begin{aligned} \sigma_{vm} = & \left[1 - G \left(\frac{\Delta\zeta_1}{G_1} + \frac{\Delta\zeta_2}{G_2} \right) \right] \sigma_{vm}^{tr} + \left[\sigma_{vm}^{tr} \frac{G\zeta_1}{G_1^2} G_{1,T} + \sigma_{vm}^{tr} \frac{G\zeta_2}{G_2^2} G_{2,T} \right] \Delta T \\ & + \left[\sigma_{vm}^{tr} \frac{G\zeta_1}{G_1^2} G_{1,P} + \sigma_{vm}^{tr} \frac{G\zeta_2}{G_2^2} G_{2,P} \right] \Delta P - [3G\zeta_1] \dot{\gamma}_1 dt - [3G\zeta_2] \dot{\gamma}_2 dt \end{aligned} \quad (4.63)$$

which is similar to the single phase expression, and recall we calculate the mass/volume fraction increments $\Delta\zeta_k$ explicitly so they are known in Eq. (4.63).

4.2.4. Solution

Equations (4.39), (4.48), and (4.59) have at most $2 + k$ unknowns if all the material phases are yielding. The equations are

$$y_1 = \frac{1}{B} \Delta P + \alpha \Delta T + \sum_k \frac{\Delta \xi_k v_k}{v} - \frac{\Delta v}{v} = 0$$

$$y_2 = v \left(\frac{1}{B} P - \alpha T \right) \Delta P + v \left(-P \alpha \frac{1}{v} C_p \right) \Delta T - v \sigma_{vm} \sum_k \zeta_k \dot{\gamma}_k dt + P \Delta v + \sum_k \Delta \xi_k E_k = 0$$

$$y_k = f_k = \sigma_y(P + \Delta P, T + \Delta T, \gamma_{k+} \dot{\gamma}_k dt, \dot{\gamma}_k)$$

$$\begin{aligned} & - \left\{ \begin{aligned} & \left[1 - G \left(\frac{\Delta\zeta_1}{G_1} + \frac{\Delta\zeta_2}{G_2} \right) \right] \sigma_{vm}^{tr} + \left[\sigma_{vm}^{tr} \frac{G\zeta_1}{G_1^2} G_{1,T} + \sigma_{vm}^{tr} \frac{G\zeta_2}{G_2^2} G_{2,T} \right] \Delta T \\ & + \left[\sigma_{vm}^{tr} \frac{G\zeta_1}{G_1^2} G_{1,P} + \sigma_{vm}^{tr} \frac{G\zeta_2}{G_2^2} G_{2,P} \right] \Delta P - [3G\zeta_1] \dot{\gamma}_1 dt - [3G\zeta_2] \dot{\gamma}_2 dt \end{aligned} \right\} \\ & = 0 \end{aligned}$$

which forms the NR problem (for a two phase system)

$$\begin{bmatrix} y_1 \\ y_2 \\ y_3 \\ y_4 \end{bmatrix}_n + \begin{bmatrix} -\frac{1}{B} & \alpha & 0 & 0 \\ \left(\frac{\nu P}{B} - T\alpha\nu\right) & (-P\nu\alpha + C_p) & (-\nu\sigma_{vm}\zeta_1 dt) & (-\nu\sigma_{vm}\zeta_2 dt) \\ \left(\frac{\partial\sigma_{y_1}}{\partial P} - \frac{\sigma_{vm}^r G\zeta_1}{G_1^2} G_{1,P} - \frac{\sigma_{vm}^r G\zeta_2}{G_2^2} G_{2,P}\right) & \left(\frac{\partial\sigma_{y_1}}{\partial T} - \frac{\sigma_{vm}^r G\zeta_1}{G_1^2} G_{1,T} - \frac{\sigma_{vm}^r G\zeta_2}{G_2^2} G_{2,T}\right) & \left(\frac{\partial\sigma_{y_1}}{\partial\dot{\gamma}_1} + \frac{\partial\sigma_{y_1}}{\partial\gamma_1} dt + 3G\zeta_1 dt\right) & (3G\zeta_2 dt) \\ \left(\frac{\partial\sigma_{y_2}}{\partial P} - \frac{\sigma_{vm}^r G\zeta_1}{G_1^2} G_{1,P} - \frac{\sigma_{vm}^r G\zeta_2}{G_2^2} G_{2,P}\right) & \left(\frac{\partial\sigma_{y_2}}{\partial T} - \frac{\sigma_{vm}^r G\zeta_1}{G_1^2} G_{1,T} - \frac{\sigma_{vm}^r G\zeta_2}{G_2^2} G_{2,T}\right) & (3G\zeta_1 dt) & \left(\frac{\partial\sigma_{y_2}}{\partial\dot{\gamma}_2} + \frac{\partial\sigma_{y_2}}{\partial\gamma_2} dt + 3G\zeta_2 dt\right) \end{bmatrix}_n \begin{bmatrix} \Delta P_{n+1} - \Delta P_n \\ \Delta T_{n+1} - \Delta T_n \\ \dot{\gamma}_{1,n+1} - \dot{\gamma}_{1n} \\ \dot{\gamma}_{2,n+1} - \dot{\gamma}_{2n} \end{bmatrix}_{n+1} = 0 \quad (4.64)$$

Equation (4.64) will be reduced to three or two equations if only one or no phases are yielding. The NR loop typically converges in one or two iterations. For most metals the 4x4 partial matrix, A , in Eq. (4.64) could be decoupled since the $A(1:2,1:2)$ dominates the first two rows, and $A(3,3)$ and $A(4,4)$ dominate the last two rows.

4.2.5. Mass (Phase) Fraction Update and Helmholtz Potential

The phase mass fractions, ξ_k , are updated explicitly after the new pressure, temperature, and slip rates are calculated. The driving force, f , for the transformation is calculated with the difference in the Gibbs Free Energy, G , between the two phases as discussed in Section 1.5.6.1. , where G can be calculated from the volumetric Helmholtz potential, F_v , as

$$G_k(v_k, T) \cong F_{v_k}(v_k, T) + v_k P = F_{v_k}(v_k, T) + v_k \left(-\frac{1}{v_k} \frac{\partial F_{v_k}}{\partial v_k} \right) \quad (4.65)$$

the typical assumption to ignore the small contribution of the deviatoric component to the Gibbs Energy has been made in Eq. (4.65). The mass fraction ‘‘conversion’’ rate, $\dot{\xi}_{ij}$, from phase j to i is calculated with an empirical equation [149]

$$\dot{\xi}_{ij} = \xi_j \frac{G_j - G_i}{G_0 \tau} \quad (4.66)$$

where τ is a time constant, and G_0 is energy barrier. An option for an additional equation is available [149,172]

$$\dot{\xi}_{ij} = \xi_j \dot{\xi}_0 \frac{G_j - G_i}{b} \left\{ \exp\left(\frac{G_j - G_i}{b}\right) \right\}^2 \quad (4.67)$$

where b represents an energy barrier and $\dot{\xi}_0$ is a reference rate.

Numerous options are available for the Helmholtz potential F_v [138,111,173,174].

We used a simple form from [175]

$$F_v(v, T) = E_k(v) + C_{v0}(T - T_0)\varepsilon(v) - T \left[s_0 + C_{v0} \ln\left(\frac{T}{T_0}\right) \right]$$

$$E_k(v) = E_0 + \frac{9K_0}{16\rho_0} (x^2 - 1)^2 [2 + (N_0 - 4)(x^2 - 1)] \quad (4.68)$$

$$\varepsilon(v) = 1 + \Gamma_0(1 - \rho_0 v), \quad x(v) = (\rho_0 v)^{-1/3}$$

where $C_v \equiv \frac{\partial E}{\partial T} = T \left(\frac{\partial S}{\partial T} \right) = T \left(-\frac{\partial^2 F}{\partial T^2} \right) = C_{v0}$ is a constant specific heat, T_0 is a reference temperature, v_0 is a reference specific volume, and K_0 , s_0 , and Γ_0 are the reference bulk modulus, entropy, and Mie-Gruneisen constants at the reference temperature and specific volume. Equation (4.68) assumes $\frac{\Gamma_0}{v_0} = \frac{\Gamma}{v}$ where $\frac{\Gamma}{v} \equiv \frac{\partial P}{\partial E} = \frac{1}{C_v} \left(\frac{\partial P}{\partial T} \right) = \frac{1}{C_v} \left(-\frac{\partial^2 F}{\partial T \partial v} \right) = \frac{\Gamma_0}{v_0}$.

Finally, N_0 is the derivative of the bulk modulus with respect to pressure, i.e., $N \equiv$

$$\left(\frac{\partial K}{\partial P} \right)_{T_0, v_0} = v \left(\frac{\partial^3 F}{\partial v^3} \right) \left(-\frac{\partial^2 F}{\partial v^2} \right)^{-1} = v \left[\left(\frac{\partial^3 E_k}{\partial v^3} \right) \left(-\frac{\partial^2 E_k}{\partial v^2} \right)^{-1} \right]_{v_0} = N_0.$$

We assume cumulative plastic strain is transferred to the new phase j from the transforming phase i as [142]

$$\gamma_{j,new} = \gamma_j + \Delta\gamma_j = \frac{\zeta_j\gamma_j + \Delta\zeta_j\gamma_i}{\zeta_j + \Delta\zeta_j} \quad (4.69)$$

Equation (4.69) is a simple assumption; the evolution of a particular dislocation upon phase transformation is not known but experimental data [100,203] suggests shock loading generally leads to hardening and Eq. (4.69) assumes cumulative plastic strain has an effect on the microstructure of the new phase. More data is needed to confirm the validity of Eq. (4.69).

The shear modulus is assumed to vary with pressure and temperature as

$$G(P, T) = (G_0 + \alpha_p P) \left(1 - \alpha_T \frac{T}{T_m}\right) \quad (4.70)$$

where G_0 is a reference shear modulus, T_m is the melt temperature, and α_p and α_T are constant pressure and temperature factors.

4.3. Crystal Based Phase Transformation Algorithm

The following subsection describes a crystal plasticity approach to model phase transformation, where each phase can be subdivided into variants (i.e., orientations).

4.3.1. Spatial Hyperelastic Rate

The isotropic model in the previous section is a hypoelastic material model for the deviatoric response, and is implemented in a Fortran subroutine with ABAQUSTM/Explicit built in corotational framework, specifically the Green-Naghdi stress rate [176]. It is well documented that hypoelastic material models are not accurate at large elastic shear (deviatoric) strains, and can produce significant integration errors for a large number of stress cycles [177-180]. However, for metals, elastic shear strains are small [65,181], and large dilatational strains/stress are handled with an EOS that is typically independent of the

deviatoric part of the corotational stress rate. Simulations of the isotropic material model developed in this work showed no noticeable errors for the magnitude of elastic shear strains seen throughout most of the simulations. The benefit of using a hypoelastic material model is that a hyperelastic material model would require a complex (slow) nonlinear solving routine in this phase aware application, e.g., [68,29]. Also note that for large strains there are some numerical issues with the Green-Naghdi stress rate, so the corotational rate passed into the Fortran subroutine by ABAQUS would have to be corrected if large elastic shear strains were present [182,135].

If the problem details stray too far from the small elastic shear strain assumption, a spatial hyperelastic rate formulation [182] can be used that is valid at large elastic strains but still has some of the benefits of the rate formulation in [149]. This spatial hyperelastic formulation will be described in the following section.

Assuming a $S = C^*(P, T): E_e$ material constitutive relation the spatial rate form is related to the Second Piola Kirchoff Stress (PK2) rate, \dot{S} , with an elastic push forward operation

$$\dot{S} = \dot{C}^*(P, T): E_e + C^*(P, T): \dot{E}_e \quad (4.71)$$

$$\text{LHS Push Forward} \Rightarrow \sigma^\nabla = J^{-1} F_e \dot{S} F_e^T = \dot{\sigma} - L_e \sigma - \sigma L_e^T + \text{tr}(L_e) \sigma \equiv \text{Truesdell Rate} \quad (4.72)$$

$$\text{RHS Push Forward} \Rightarrow J^{-1} F_e (\dot{C}^*(P, T): E_e + C^*(P, T): \dot{E}_e) F_e^T = C_T \dot{T} + C_P \dot{P} + C: D_e \quad (4.73)$$

where

$$F_e^T D_e F_e = \dot{E}_e \quad (4.74)$$

and

$$\begin{aligned}
C_T &= \left\{ J^{-1} F_e \left(\frac{\partial C^*}{\partial T} : E_e \right) F_e^T \right\} \\
C_P &= \left\{ J^{-1} F_e \left(\frac{\partial C^*}{\partial P} : E_e \right) F_e^T \right\} \\
C_{qzpn} &= \left(J^{-1} F_{qi}^e F_{zj}^e F_{pk}^e F_{nl}^e C_{ijkl}^* \right)
\end{aligned} \tag{4.75}$$

where E_e is the elastic Green Strain, C^* is a pressure and temperature dependent material elasticity tensor, F_e is the elastic deformation gradient, $J = \det(F_e)$ is a measure of volume change, σ is the Cauchy stress, and D_e is the spatial deformation rate or equally the kinematic push forward of \dot{E}_e . Note that the first two terms on the RHS of Eq. (4.73) drop out if the material elasticity tensor is independent of pressure and temperature (not a valid assumption for large shocks).

The typical source of error in the hypoelastic algorithms is the small elastic strain assumption

$$\left(J^{1/3} F_{qi}^{dev} F_{zj}^{dev} F_{pk}^{dev} F_{nl}^{dev} C_{ijkl}^* \right) D_{pn}^e \cong \left(R_{qi} R_{zj} R_{pk} R_{nl} C_{ijkl}^* \right) D_{pn}^e \xrightarrow{\text{if isotropic}} C_{qzpn}^* D_{pn}^e \tag{4.76}$$

where

$$J = \det(F_e) \text{ and } F_e = J^{1/3} F_{dev} \Rightarrow \det(F_{dev}) = 1 \tag{4.77}$$

This leads to the general hypoelastic relation for an isotropic material (assuming no pressure and temperature dependence)

$$\sigma^\nabla \cong C^* : D_e \tag{4.78}$$

The objective stress rate (LHS of Eq. (4.78)), σ^∇ , can be replaced by any number of objective stress rates [177-179]; however, stating that one is better than the other is suspect if the approximation in Eq. (4.76) is used [180]. Without the approximation, the Truesdell objective rate as given in Eq. (4.72) is the correct expression for σ^∇ [182].

4.3.2. Crystal Plasticity

The multiplicative decomposition of each phase and phase variant is

$$F_i = F^e F^P \quad (4.79)$$

where F_i is the total deformation gradient for the particular crystal (variant), F^e is the thermoelastic deformation and F^P is the plastic deformation from dislocation slip [10,141,142]. The plastic deformation is derived from the plastic velocity gradient, \tilde{L}_t^P ,

$$\tilde{L}_t^P = \sum_{k=1}^n \dot{\gamma}_t^k P_s^k \quad (4.80)$$

$$F_{t+\Delta t}^P \cong \exp(\tilde{L}_t^P \Delta t) F_t^P \cong F_t^P + \Delta t \tilde{L}_t^P F_t^P \quad (4.81)$$

where P_s^k is the symmetric Schmid tensor (in a reference frame fixed to the rotating crystal) for the given slip system k , and $\dot{\gamma}^k$ is the slip rate for the given slip system. The slip rates are calculated explicitly with a power law (rate-dependent) approach [10], and a Voce hardening law is used.

4.3.3. Phase Transformation and Linking Assumptions

To use Eq. (4.79) the crystal deformation gradient, F_i , must be known, which is assumed to not be equal amongst all the phases and twins. Rather than calculate F_i directly we use the macroscopic velocity gradient and the kinematic framework of [142] which was reviewed in Section 1.5.6.4. . Starting with the macro velocity gradient, \check{L} , passed into the material subroutine we subtract the velocity gradient due to phase transformations.

$$\langle L_i \rangle_{t+\Delta t} \cong \check{L}_{t+\Delta t} - L_t^X \quad (4.82)$$

where L^X is the deformation associated with phase transformation (and twinning if modeled), and $\langle L_i = \dot{F}_i F_i^{-1} \rangle$ is the velocity gradient volume average of all the phases. An explicit routine will always be used for L^X so at the beginning of every time step it is known.

Concentrating on a particular phase, the elastic push forward of the PK2 stress rate, \dot{S} , gives the Truesdell rate, σ^∇

$$\sigma^\nabla \equiv J^{-1} F_e(\dot{S}) F_e^T = \dot{\sigma} - L_e \sigma - \sigma L_e^T + \text{tr}(L_e) \sigma = [C_T \dot{T} + C_P \dot{P} + C : D_e] \quad (4.83)$$

where $\dot{\sigma}$ is the Cauchy stress rate, L_e is the elastic velocity gradient, and D_e is the elastic deformation rate (symmetric part of L_e). The constitutive assumptions in square brackets were defined in Section 4.3.1. .

For cubic or isotropic materials Eq. (4.83) can be broken up into hydrostatic and deviatoric parts and solved for with a Reuss Average approach [142,149], but HCP phases couple deviatoric/dilatational strain with pressure/deviatoric stress, so we leave the equations coupled and write out the expression for hydrostatic and deviatoric stress rates

$$I \dot{P}_{t+\Delta t} = C_T^h \dot{T}_{t+\Delta t} + C_P^h \dot{P}_{t+\Delta t} + C^h : D_{e,t+\Delta t} - \left(\frac{\dot{v}}{v_{t+\Delta t}} \sigma_{t+\Delta t} \right)^h + \{(D_e \sigma + \sigma D_e)^h\}_t \quad (4.84)$$

$$\dot{\sigma}_{t+\Delta t}^d = C_T^d \dot{T}_{t+\Delta t} + C_P^d \dot{P}_{t+\Delta t} + C^d : D_{e,t+\Delta t} - \left(\frac{\dot{v}}{v_{t+\Delta t}} \sigma_{t+\Delta t} \right)^d + \{(D_e \sigma + \sigma D_e)^d + (W_e \sigma - \sigma W_e)\}_t \quad (4.85)$$

where C^h and C^d are the hydrostatic and deviatoric decomposition of the elasticity tensor C and W_e is the elastic spin. Values in curly brackets are updated explicitly. Superscripts d and h signify deviatoric and hydrostatic parts.

Since we are dealing with large pressures and temperatures, Eq. (4.84) is modified by removing the first two terms and the volumetric dependence in the $C^h:D_e$ term (leaving only $C^h:D_e$) and replacing those terms with an EOS, a similar approach is taken by [10,142].

$$I\dot{P} = I\dot{P}_{EOS}(\dot{v}, \dot{T}) + C^h:D_e + \left(\frac{\dot{v}}{v}\sigma\right)^h + \{(D_e\sigma + \sigma D_e)^h\} \quad (4.86)$$

where $\dot{P}_{EOS}(\dot{v}, \dot{T})$ is derived from a EOS with independent variables of specific volume rate, \dot{v} , and temperature rate, \dot{T} . Equations (4.85) and (4.86) are complemented with an additional equation for total energy rate, \dot{E} , in a particular phase

$$\dot{E} = (P + K_{EOS}\alpha_{EOS}T)\dot{v} + C_v\dot{T} + v\sigma:D_e^d \quad (4.87)$$

where C_v is a constant specific heat, and K_{EOS} and α_{EOS} are the isothermal bulk modulus and coefficient of volumetric thermal expansion calculated with a Helmholtz potential. Note that a thermal stress is included in the \dot{P}_{EOS} term, this is the equivalent of a thermal expansion term at constant pressure [10]. Still missing from Eq. (4.85) is an equivalent anisotropic thermal stress term that is present in low symmetry structures, however this term has been neglected in similar efforts [142,65]. After some algebra Eqs. (4.85-4.87) are rewritten with Voigt notation as

$$A_{8 \times 8} \begin{bmatrix} \dot{T} \\ \dot{P} \\ \dot{\sigma}^d \end{bmatrix} = \begin{bmatrix} \dot{E} \\ \dot{v} \\ v \end{bmatrix} - (\text{explicitly updated values})_{8 \times 1} \quad (4.88)$$

where $A_{8 \times 8}$ is a singular matrix due to the decomposition of the elasticity tensor. To remove the singularity a change of basis is used [184]

$$\sigma = [\sigma_{11}, \sigma_{22}, \sigma_{33}, \sigma_{23}, \sigma_{13}, \sigma_{12}]^T \rightarrow$$

$$\sigma^\lambda = \left[\frac{2\sigma_{33} - \sigma_{11} - \sigma_{22}}{\sqrt{6}}, \frac{\sigma_{22} - \sigma_{11}}{\sqrt{2}}, \sqrt{2}\sigma_{23}, \sqrt{2}\sigma_{13}, \sqrt{2}\sigma_{12}, \frac{\sigma_{33} + \sigma_{11} + \sigma_{22}}{\sqrt{3}} \right]^T \quad (4.89)$$

then

$$\sigma_{6x1}^d, D_{e\ 6x1}^d \rightarrow \sigma_{5x1}^\lambda, D_{e\ 5x1}^\lambda \quad (4.90)$$

so that

$$A^\lambda_{7x7} \begin{bmatrix} \dot{T} \\ \dot{P} \\ \dot{\sigma}_{5x1}^\lambda \end{bmatrix} = \begin{bmatrix} \dot{E} \\ \dot{v} \\ D_{e\ 5x1}^\lambda \end{bmatrix} - (\text{explicitly updated values})_{7x1}^\lambda \quad (4.91)$$

Equation (4.91) is for an individual phase. Several linking assumptions need to be made now to proceed to a macroscopic response. First we make the logical assumption that all phases are at the same pressure and temperature, which is typical of the thermodynamics of phase transformations. Next a slightly weaker assumption is that all the phases rotate together; therefore, all spins, W_e , are equal, which is reasonable since the phase boundaries should approximate the conditions in Section 1.5.6.4. [139]. The last assumption used, which can be altered in subsequent derivations for different homogenization approaches, is that all the phases have the same deviatoric stress. With these assumptions a Reuss average is appropriate leading to

$$A^{\lambda}_{R.Avg} \begin{bmatrix} \dot{T} \\ \dot{P} \\ \dot{\sigma}_{5x1}^{\lambda} \end{bmatrix} = \begin{bmatrix} \dot{E} - \sum \dot{m}_i E_i \\ \langle \frac{\dot{v}}{v} \rangle \\ \langle D_e^{\lambda} \rangle_{5x1} \end{bmatrix} - (\text{explicitly updated values})_{R.Avg}^{\lambda}$$

$$\text{RHS is Known} \Rightarrow \begin{bmatrix} \dot{T} \\ \dot{P} \\ \dot{\sigma}_{5x1}^{\lambda} \end{bmatrix}_{t+\Delta t} = A^{\lambda^{-1}} \text{RHS} \quad (4.92)$$

where E_i is the energy in variant i , and \dot{m}_i is the mass fraction of a transforming variant. Using Eq. (4.92) the temperature, pressure, and deviatoric stress increments can be solved for. Where the first term of the RHS of the first line of Eq. (4.92) is:

$$\begin{bmatrix} \dot{E} - \sum (\dot{m}_i E_i)_t = v \check{D}_{t+\Delta t} : \sigma_t - \sum (\dot{m}_i E_i)_t \\ \langle \frac{\dot{v}}{v} \rangle_{t+\Delta t} \\ \langle D_e^{\lambda} \rangle_{5x1} = (\langle D^{\lambda} \rangle_{5x1})_{t+\Delta t} - (\langle D_p^{\lambda} \rangle_{5x1})_{t+\Delta t} \end{bmatrix} \quad (4.93)$$

All the terms in (4.93) are provided by the explicit integration performed internally in ABAQUSTM, except for the mass fraction calculation ($\check{D}_{t+\Delta t}$ is the total deformation rate). The solution sensitivity is typically dominated by the kinematic inputs $\langle \frac{\dot{v}}{v} \rangle_{t+\Delta t}$ and $(\langle D^{\lambda} \rangle_{5x1})_{t+\Delta t}$. Once the new temperature, pressure, and deviatoric stress rates are known the kinematic variables for each phase can be solved with Eq. (4.91).

Keeping with the assumption that all phases rotate together, there exists a coordinate system that is related to the global coordinate system by a rotation, $R_{t+\Delta t}$, [185, p.560-561]

$$R_{t+\Delta t} \cong \Delta t W_{t+\Delta t}^t R_t + R_t \quad (4.94)$$

where all phases rotate with this common phase coordinate system. The rotation matrix $R_{t+\Delta t}$ maps a vector from the common phase lattice system to the global coordinate system.

Each phase will then be oriented relative to this common system with a static rotation. The updated rotation in Eq. (4.94) could also be found with the polar decomposition of the macro elastic deformation gradient.

$$F_e = FF_p^{-1} \quad (4.95)$$

The elastic deformation gradient for each phase can be calculated with

$$F_i^e = \exp((D_i^e + W^e)\Delta t) F_i^e \quad (4.96)$$

One final detail is that the stress passed from the Fortran subroutine to ABAQUS is the corotated stress, $\hat{\sigma}$

$$\hat{\sigma} = R_c^T (\sigma_{t+\Delta t}) R_c \quad (4.97)$$

where R_c is found from the polar decomposition of the total deformation gradient passed into the VUMAT from ABAQUS.

4.3.4. Phase Transformation Kinetics

Phase transformations are possible with iron under the right conditions. For each phase transformation path, i , an approach close to [142, 172] is used

$$\dot{m}_i = \dot{m}_{i_0} \left(\frac{f_i - t_i}{g_i} \right)^{p_i} \quad \text{for } f_i - t_i \geq 0 \quad \text{else } \dot{m}_i = 0 \quad (4.98)$$

where \dot{m}_i is the mass rate of transformation, t_i is similar to an activation energy [20] or energy barrier [139], g_i evolves with state variables to increase the resistance to phase transformation, p_i affects the rate of transformation, and \dot{m}_{i_0} is a fitting constant. Equation (4.98) should be valid if the phase transformation kinetics is quantitatively similar to thermal activation (see Section 1.5.6.3.). The last parameter in Eq. (4.98) is the driving force, f_i ,

$$f_i = G_{fr} - G_{to} \cong (\varphi_{fr} - \varphi_{to}) + \tau_{fr} : P_i \quad (4.99)$$

$$P_i = \text{sym}(\ln(F_i)) \text{ where } F_i = V_{to} F_{to}^* F_{fr}^{*-1} V_{fr}^{-1} \quad (4.100)$$

where G is the Gibbs free energy potential, which is appropriate if we assume all phases are at the same Cauchy stress (see Section 1.5.6.1.), V is the left stretch tensor from the elastic deformation gradient of each phase, F^* is the transformation gradient from a reference configuration to the respective phase, τ_{fr} is the Kirchhoff stress of the transforming phase, and φ is the Helmholtz potential. Equation (4.100) comes from [142], and is a pull-back from the transforming “from” phase and a push forward to the transforming “to” phase as discussed earlier.

4.3.5. Equation of State

The intensive properties are found with a Helmholtz potential, φ_i , used for each phase

$$\varphi_i = \varphi_{v_i} + \varphi_{d_i} \quad (4.101)$$

$$\varphi_{d_i} = \frac{1}{2} E' : C_i : E' \quad (4.102)$$

where E' is the deviatoric part of the Green strain, C is the material elasticity tensor, and φ_{v_i} is the volumetric component similar to that used in [175] or [20].

The above sections concluded the constitutive models that were implemented numerically in ABAQUSTM. In the next chapter we will verify and calibrate the models. In the next section, however, an analytical solution for the shock front perturbation evolution is developed. This solution provides some insight into the effect material parameters, both deviatoric and EOS, have on the shock front evolution. The analytical solution also

provides a means to validate the post processing of the numerical models (e.g., calculating the shock front evolution via Python scripts and ABAQUS™ results).

4.4. Analytical Shock Front Perturbation Evolution for Plastic Materials

Zaidel [87] and later Miller [88] developed a simple approach to model shock front perturbation decay as discussed in Section 1.4. . In these two works the perturbation was developed for inviscid and weakly viscous materials [87,88]. The approach involved two boundary conditions, at one end a rigid piston moving at a constant velocity imparts a shock wave to a fluid initially at rest, at the other end the boundary conditions are those present in a shock front, i.e., the Rankine-Hugoniot jump conditions [100]. In this section we review the derivation in [88] and make the changes necessary to model a material with plastic strength up to about shock front perturbation inversion. The analysis shows that the perturbation decay has a material and geometry dependent scaling factor that agrees well with numerical solutions. The following derivation is also useful because it points out explicitly where the procedure in [87,88] would need to be modified for general equations of state (EOS). Code for the solution is included in the Appendix.

4.4.1. Boundary conditions

Three boundary conditions on mass and linear momentum (x and y), can be written at the perturbed shock front due to the Rankine-Hugoniot (RH) jump conditions. To use the RH conditions at the perturbed shock front we need expressions for the normal and tangential velocities and stresses. Following [87,88], consider a coordinate system that travels with the nominal shock velocity U_{s0} as shown in Figure 4.3

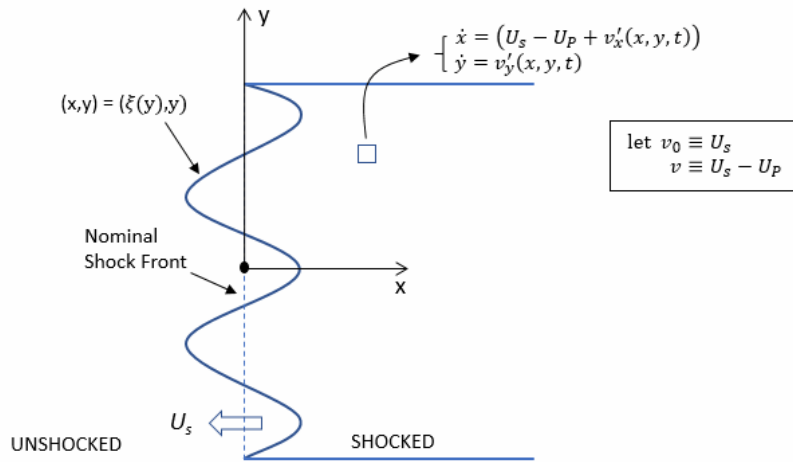


Figure 4.3: Coordinate system for shock perturbation model, from [88].

The coordinates and velocity at the shock front are

$$\vec{x}_S = \xi(y)\hat{i} + y\hat{j} \quad (4.103)$$

$$\dot{\vec{x}}_S = \dot{\xi}(y)\hat{i} \quad (4.104)$$

with normal and tangent vectors of

$$\hat{t} = \frac{\partial \vec{x}_S / \partial y}{|\partial \vec{x}_S / \partial y|} = \frac{\xi_{,y}\hat{i} + \hat{j}}{\sqrt{1 + \xi_{,y}^2}} \quad (4.105)$$

$$\hat{n} = \frac{\hat{i} - \xi_{,y}\hat{j}}{\sqrt{1 + \xi_{,y}^2}} \quad (4.106)$$

where $\xi_{,y} = \partial \xi / \partial y$. The tangential and normal velocity at the shock front are then

$$\dot{x}_{St} = \dot{\vec{x}}_S \cdot \hat{t} = \frac{\dot{\xi}}{\sqrt{1+\xi_{,y}^2}} \quad (4.107)$$

$$\dot{x}_{Sn} = \dot{\vec{x}}_S \cdot \hat{n} = \frac{\xi_{,y}\dot{\xi}}{\sqrt{1+\xi_{,y}^2}} \quad (4.108)$$

Similar expressions for the tangential and normal velocity of material just ahead of the shock (+) (unshocked) and behind the shock (-) can easily be found

$$\vec{x}_+ = (x + v_0 t)\hat{i} + y\hat{j}, \quad \dot{\vec{x}}_+ = v_0\hat{i} \quad (4.109)$$

$$\dot{\vec{x}}_{+n} = \frac{v_0}{\sqrt{1+\xi_{,y}^2}} \quad (4.110)$$

$$\dot{\vec{x}}_{+t} = \frac{\xi_{,y}v_0}{\sqrt{1+\xi_{,y}^2}} \quad (4.111)$$

$$\vec{x}_- = (x + vt + v_x't)\hat{i} + (y + v_y't)\hat{j}, \quad \dot{\vec{x}}_- = v_0\hat{i} \quad (4.112)$$

$$\dot{\vec{x}}_{-n} = \frac{v + v_x' - v_y'\xi_{,y}}{\sqrt{1+\xi_{,y}^2}} \quad (4.113)$$

$$\dot{\vec{x}}_{-t} = \frac{v_y' + \xi_{,y}(v + v_x')}{\sqrt{1+\xi_{,y}^2}} \quad (4.114)$$

where we define $v_0 = U_s$ and $v = U_s - U_P$. The stress jump at the shock boundary for an elastic-perfectly plastic material is

$$\sigma_{xx} = -P + S_{xx} \cong -P - 2Y/3 \quad (4.115)$$

$$\sigma_{yy} = \sigma_{zz} = -P + S_{yy} \cong -P + Y/3 \quad (4.116)$$

$$\sigma_{xy} = S_{xy} \cong 0 \quad (4.117)$$

where P is the pressure (which contains a perturbed term), S_{ij} is the deviatoric stress, and Y is the material yield stress. We have assumed the shear stress term S_{xy} to be approximately

zero for small perturbations, i.e., S_{ij} in the shock front will be dominated by the longitudinal term (uniaxial strain) accelerating the material from zero to the particle velocity behind the shock front.

The RH condition for mass (e.g., mass in = mass out) is

$$\rho_0 (\dot{x}_{+n} - \dot{x}_{Sn}) = \rho (\dot{x}_{-n} - \dot{x}_{Sn}) \quad (4.118)$$

which gives

$$\text{BC: } \rho_0 (v_0 + \dot{\xi}) = \rho (\dot{\xi} - v - v'_x + v'_y \xi_{,y}) \quad (4.119)$$

The RH condition for linear momentum in the normal direction is (e.g., jump in force = jump in momentum)

$$\begin{aligned} \sigma_{+nn} - \sigma_{-nn} &= \rho_0 (\dot{x}_{+n} - \dot{x}_{Sn}) (\dot{x}_{+n} - \dot{x}_{Sn}) - \rho (\dot{x}_{-n} - \dot{x}_{Sn}) (\dot{x}_{-n} - \dot{x}_{Sn}) \\ \Rightarrow 0 - \sigma_{-nn} &= \rho_0 (\dot{x}_{+n} - \dot{x}_{Sn}) (\dot{x}_{+n} - \dot{x}_{-n}) \end{aligned} \quad (4.120)$$

where σ_{nn} is the normal stress given by

$$\sigma_{nn} \equiv \sigma_{ij} n_j n_i \quad (4.121)$$

Therefore Eq. (4.120) and (4.121), and using the prior definitions, gives

$$\text{BC: } P(1 + \xi_{,y}^2) + (2 - \xi_{,y}^2) \frac{S_y}{3} + \rho_0 (\dot{\xi} - v_0) (v_0 - v - v'_x + v'_y \xi_{,y}) = 0 \quad (4.122)$$

The last RH boundary condition for the tangential momentum is

$$\begin{aligned} \sigma_{+nt} - \sigma_{-nt} &= \rho_0 (\dot{x}_{+n} - \dot{x}_{Sn}) (\dot{x}_{+t} - \dot{x}_{St}) - \rho (\dot{x}_{-t} - \dot{x}_{St}) (\dot{x}_{-t} - \dot{x}_{St}) \\ \Rightarrow 0 - \sigma_{-nt} &= \rho_0 (\dot{x}_{+n} - \dot{x}_{Sn}) (\dot{x}_{+t} - \dot{x}_{-t}), \quad \sigma_{nt} \equiv \sigma_{ij} n_j t_i \end{aligned} \quad (4.123)$$

which gives

$$\text{BC: } \xi_{,y} Y + \rho_0 (\dot{\xi} - v_0) [\xi_{,y} v_0 - \xi_{,y} (v + v'_x) - v'_y] = 0 \quad (4.124)$$

The boundary conditions Eq. (4.119), (4.122), and (4.124) can be linearized by letting

$$P = P_\emptyset + P' \quad (4.125)$$

where P_\emptyset is the nominal unperturbed pressure behind the front, and P' is the perturbed quantity. The density ρ can be linearized as

$$\rho = \rho_\emptyset + \rho', \quad \rho = V^{-1} \Rightarrow \rho' = -V_\emptyset^{-2} V' = -\rho_\emptyset^2 V' \quad (4.126)$$

$$V' = \left. \frac{\partial V}{\partial P} \right|_{P_\emptyset} P' \quad (4.127)$$

$$\rho' = -\rho_\emptyset^2 \left. \frac{\partial V}{\partial P} \right|_{P_\emptyset} P' = \rho_\emptyset^2 \frac{P' \delta}{v_0^2 \rho_0^2}; \quad \text{where } \delta \equiv -\left. \frac{\partial V}{\partial P} \right|_{P_\emptyset} v_0^2 \rho_0^2 \quad (4.128)$$

where X_\emptyset is the zero order (nominal) value, i.e., the value of quantity X for a 1-D shock, V is the specific volume, and δ is evaluated (i.e., the $\partial V/\partial P$ term) on the P - V Hugoniot at the nominal pressure P_\emptyset and is given by (for a linear $U_s - U_P$ material)

$$\text{let } P = \rho_0 U_P U_s \Rightarrow \delta = -\left(\frac{\partial P}{\partial U_P} \frac{\partial U_P}{\partial V} \right)^{-1} \Big|_{P_\emptyset} v_0^2 \rho_0^2 = \frac{U_s - s U_P}{U_s + s U_P} \quad (4.129)$$

where $U_p = U_s(1 - V/V_0)$. Combining Eq. (4.119), (4.125), (4.126), and (4.129) gives

$$\rho_0(v_0 + \dot{\xi}) = (\rho_\emptyset + \rho')(\dot{\xi} - v - v'_x + v'_y \xi_{,y}) \quad (4.130)$$

which gives the following zero order and first order perturbed terms (higher order terms are approximately zero for small perturbations)

$$\text{Zero Order: } \rho_0 v_0 = \rho_\emptyset v \quad (4.131)$$

$$\text{First Order: } \rho_0 \dot{\xi} = \rho_\emptyset(\dot{\xi} - v'_x) - \rho' v \Rightarrow v'_x - \left(\frac{\sigma - 1}{\sigma} \right) \dot{\xi} + \frac{P' \delta}{v \rho_\emptyset} = 0 \quad (4.132)$$

where in Eq. (4.132) we used Eq. (4.129) and Eq. (4.131) with the definition $\sigma \equiv \rho_\emptyset/\rho_0 = v_0/v$.

Similarly, Eq. (4.122) and (4.125) give

$$\text{Zero Order: } P_0 + 2Y/3 = \rho_0(v_0 - v)v_0 = \rho_0 U_P U_S \quad (4.133)$$

$$\text{First Order: } P' + \rho_0 v_0 \dot{\xi} - \rho_0 v \dot{\xi} + \rho_0 v_0 v'_x = 0 \Rightarrow v'_x + \frac{P'}{\rho_0 v} + \left(\frac{\sigma-1}{\sigma}\right) \dot{\xi} = 0 \quad (4.134)$$

and lastly, Eq. (4.124) gives

$$\text{Zero Order: } 0 \quad (4.135)$$

$$\begin{aligned} \text{First Order: } \xi_{,y} Y - \rho_0 v_0^2 \xi_{,y} + \rho_0 v_0 \xi_{,y} v + \rho_0 v_0 v'_y &= 0 \\ \Rightarrow v'_y - v(\sigma - 1) \xi_{,y} &= \frac{-\xi_{,y} Y}{\rho_0 v} \end{aligned} \quad (4.136)$$

The boundary conditions for the first order plastic perturbed problem are given by Eq. (4.132), (4.134), and (4.136) and make no assumption about the EOS, which enters the equations through δ (i.e., Eq. (4.129)).

4.4.2. Continuum Equations Behind Shock Front

Conservation of linear momentum behind the shock front is

$$\frac{\partial v_x}{\partial t} + v_x \frac{\partial v_x}{\partial x} + v_y \frac{\partial v_x}{\partial y} = \frac{-1}{\rho} \frac{\partial P}{\partial x} + \frac{1}{\rho} \left(\frac{\partial S_{xx}}{\partial x} + \frac{\partial S_{xy}}{\partial y} \right) \quad (4.137)$$

$$\frac{\partial v_y}{\partial t} + v_x \frac{\partial v_y}{\partial x} + v_y \frac{\partial v_y}{\partial y} = \frac{-1}{\rho} \frac{\partial P}{\partial y} + \frac{1}{\rho} \left(\frac{\partial S_{yx}}{\partial x} + \frac{\partial S_{yy}}{\partial y} \right) \quad (4.138)$$

where the velocity terms (as well as the stress terms) have a zero order and perturbed component, e.g.,

$$v_x = v + v'_x \text{ and } v_y = 0 + v'_y \quad (4.139)$$

and the non-perturbed (zero order) components have spatial and time derivatives of zero. We assume near the shock front that the material has yielded, the longitudinal components are approximately constant (i.e., $\partial S_{ix}/\partial x \cong 0$), and the components of the deviatoric tensor S_{ij} are periodic with the lateral variable y . This should be reasonable until the shock

front approaches inversion, and far away from the shock front the actual values of the deviatoric components should not affect the shock front perturbation evolution [78]. Therefore, the deviatoric components, perturbed pressure P' , and perturbed velocity components near the shock front are

$$S_{xx} \propto \frac{Y}{\sqrt{3}} \cos(ky) \quad (4.140)$$

$$S_{yy} \propto \frac{Y}{\sqrt{3}} \cos(ky + \pi) \Rightarrow \frac{\partial S_{yy}}{\partial y} \propto \frac{-ikY}{\sqrt{3}} \exp(iky) \quad (4.141)$$

$$S_{xy} \propto \frac{Y}{\sqrt{3}} \cos\left(ky - \frac{\pi}{2}\right) \Rightarrow \frac{\partial S_{xy}}{\partial y} \propto \frac{kY}{\sqrt{3}} \exp(iky) \quad (4.142)$$

$$P' = P'(x, t) \exp(iky) = P' \exp(iky) \quad (4.143)$$

$$v'_i = v'_i(x, t) \exp(iky) = v'_i \exp(iky) \quad (4.144)$$

where it is stressed Eqs. (4.140) through (4.142) are approximations meant to only capture the general effect of the plastic deviatoric behavior, they are not meant to be exact.

The momentum Eqs. (4.137) and (4.138), using Eqs. (4.139) through (4.144), and eliminating second order perturbed terms, become

$$\frac{\partial v'_x}{\partial t} + v \frac{\partial v'_x}{\partial x} + \frac{1}{\rho_\phi} \frac{\partial P'}{\partial x} = \frac{1}{\rho_\phi} \frac{C_x k Y}{\sqrt{3}} \quad (4.145)$$

$$\frac{\partial v'_y}{\partial t} + v \frac{\partial v'_y}{\partial x} + \frac{1}{\rho_\phi} ikP' = -\frac{i}{\rho_\phi} \frac{C_y k Y}{\sqrt{3}} \quad (4.146)$$

where the sinusoidal factor $\exp(iky)$ has been divided out since all perturbed terms depend on the lateral coordinate y with the same factor and we added two fitting constants C_x and C_y ($C_x \approx 2$ and $C_y \approx 1$ work well) to compensate for nonlinearities and other deviations from the assumptions. For instance, $\frac{\partial S_{yx}}{\partial x}$ is not zero very close to the shock front where S_{yx} rises from approximately zero at the shock front (i.e., the boundary condition for uniaxial

strain) to $Y/\sqrt{3}$ behind the shock front, resulting in $\max \left| \frac{\partial S_{yx}}{\partial x} \right| \cong \left| 10 \frac{kY}{\sqrt{3}} \right|$ (as measured in ABAQUS™ simulations). Similarly, for S_{xx} , the BC at the shock front is uniaxial strain; however, at the peak of the shock front the material temporarily stops yielding as it reaches a peak particle velocity before decelerating (i.e., the pressure perturbation peaks at the shock front then decreases behind the front slowing the particle velocity). As a result, S_{xx} rapidly changes signs resulting in $\max \left| \frac{\partial S_{xx}}{\partial x} \right| \cong \left| 10 \frac{kY}{\sqrt{3}} \right|$. The fitting constants C_x and C_y are well less than 10 because these steep gradients last only until the material yields.

Equations (4.140) through (4.142) appear to imply that S_{zz} is zero behind the shock front; this is generally not true. When the velocity gradient perturbations (i. e., $L'_{ij} = \frac{\partial v'_i}{\partial x_j}$) just behind the shock front are such that the lateral and longitudinal deformation rates are equal in magnitude (i. e., $D'_{xx} = -D'_{yy}$) then S_{zz} becomes zero, this happens early in the shock front evolution as the pressure perturbations increase from zero while the lateral velocity perturbations are large compared to the longitudinal perturbations. However, for a larger part of the shock front evolution (before inversion) $|D'_{xx}|$ is greater than $|D'_{yy}|$ just behind the shock front and uniaxial strain conditions are approached again and $|S_{zz}|$ approaches $Y/3$. As a result, the ranges for the stress component amplitudes just behind the shock front (before inversion) are $Y/3 \leq |S_{yy}| \leq Y/\sqrt{3}$, $Y/\sqrt{3} \leq |S_{xx}| \leq 2Y/3$, $0 \leq |S_{zz}| \leq Y/3$, and $|S_{xy}| \cong Y/\sqrt{3}$; where of course the yield constraint must be met $Y = \sqrt{2/3 (S_{xx}^2 + S_{yy}^2 + S_{zz}^2 + 2S_{xy}^2)}$. The fitting constants C_x and C_y are then approximations to produce an effective equivalent average stress gradient near the shock front.

Returning to the solution, there are three unknowns v'_x , v'_y , and P' . We need one more equation that comes from mass conservation

$$\frac{\partial \rho}{\partial t} + \frac{\partial}{\partial x}(\rho v_x) + \frac{\partial}{\partial y}(\rho v_y) = 0 \quad (4.147)$$

that can be written in first order terms as

$$\frac{\partial \rho'}{\partial t} + v \frac{\partial \rho'}{\partial x} + \rho_\phi \left(\frac{\partial v'_x}{\partial x} + \frac{\partial v'_y}{\partial y} \right) = 0 \quad (4.148)$$

The density perturbation ρ' has a different form than in the shock front Eq. (4.128). We still assume small perturbations, as in the shock front, but behind the shock front we assume perturbations are isentropic and relate density and pressure perturbations with the isentropic relation [186, p. 7]

$$\rho' = \left(\frac{\partial \rho}{\partial P} \right)_s \Big|_{P_\phi = P_H} P' = \frac{1}{c_s^2} P' \quad (4.149)$$

where c_s is the isentropic sound speed at the nominal shock pressure, and is calculated from an isentrope passing through the Hugoniot point [101, p. 111] at the nominal shock pressure P_ϕ . For a material with a linear $U_s = C_0 + sU_P$ Hugoniot, it can be calculated with [101, p. 111] (or experimental data could be used [88])

$$c_s^2 = \frac{(1-\eta)^2}{(1-s\eta)^3} C_0^2 [1 + s\eta(1 - \gamma\eta)] \quad (4.150)$$

where

$$\eta = 1 - \frac{\rho_0}{\rho_\phi} = \frac{U_P}{U_s} \quad (4.151)$$

and γ is the Grüneisen parameter. Therefore Eq. (4.148) becomes

$$\frac{\partial P'}{\partial t} + v \frac{\partial P'}{\partial x} + c_s^2 \rho_\phi \left(\frac{\partial v'_x}{\partial x} + \frac{\partial v'_y}{\partial y} \right) = 0 \quad (4.152)$$

4.4.3. Laplace Transform of BCs and Continuum Equations, and Final Solution

The Laplace Transform of the first order perturbed portion of the BCs, Eqs. (4.132,4.134,4.136), gives

$$\hat{v}_x + \frac{\hat{P}\delta}{\rho_\emptyset v} - \frac{\sigma-1}{\sigma}(\hat{\xi}s - \xi_0) = 0 \quad (4.153)$$

$$\hat{v}_x + \frac{\hat{P}}{\rho_\emptyset v} + \frac{\sigma-1}{\sigma}(\hat{\xi}s - \xi_0) = 0 \quad (4.154)$$

$$\hat{v}_y - v(\sigma-1)ik\hat{\xi} = -\frac{ik\hat{\xi}Y}{\rho_\emptyset v} \quad (4.155)$$

where $\hat{f}(s)$ is the Laplace Transform of $f(t)$, s is the Laplace variable, and ξ_0 is the initial perturbation amplitude. We also assumed all perturbations (i.e., variables denoted with primes) depend on the lateral coordinate y with $exp(iky)$. Simple algebra with Eqs. (4.153) – (4.155) gives

$$\vec{u}_{x=0} \equiv \begin{bmatrix} \hat{v}_x \\ i\hat{v}_y \\ \hat{P}/\rho_\emptyset v \end{bmatrix}_{x=0} = \begin{bmatrix} -\frac{(\sigma-1)(1+\delta)}{\sigma(1-\delta)}(\xi_0 - s\hat{\xi}) \\ -kv(\sigma-1)\hat{\xi} + \frac{Yk}{\rho_\emptyset v}\hat{\xi} \\ \frac{2(\sigma-1)}{\sigma(1-\delta)}(\xi_0 - s\hat{\xi}) \end{bmatrix}_{x=0} \quad (4.156)$$

Next we transform the continuum Eqs. (4.145,4.146,4.152)

$$(\hat{v}_x s - v'_{x0}) + v \frac{\partial \hat{v}_x}{\partial x} + \frac{1}{\rho_\emptyset} \frac{\partial \hat{P}}{\partial x} = \frac{1}{\rho_\emptyset} \frac{C_x k Y}{\sqrt{3}} \frac{1}{s} \quad (4.157)$$

$$(\hat{v}_y s - v'_{y0}) + v \frac{\partial \hat{v}_y}{\partial x} + \frac{1}{\rho_\emptyset} ik\hat{P} = -\frac{i}{\rho_\emptyset} \frac{C_y k Y}{\sqrt{3}} \frac{1}{s} \quad (4.158)$$

$$(\hat{P}s - P'_0) + v \frac{\partial \hat{P}}{\partial x} + \rho_\emptyset c_s^2 \left(\frac{\partial \hat{v}_x}{\partial x} + ik\hat{v}_y \right) = 0 \quad (4.159)$$

where we neglect the initial perturbations at $t=0$, i.e., $v'_{x0} = v'_{y0} = P'_0 \cong 0$ (for small ξ_0/λ [88, p. 936]). Simple algebra with Eqs. (4.157)-(4.159) give

$$\frac{\partial \vec{u}}{\partial x} = \mathbf{A}\vec{u} + \vec{g} \quad (4.160)$$

where

$$\mathbf{A} \equiv \begin{bmatrix} \frac{\beta^2 kz}{1-\beta^2} & \frac{-k}{1-\beta^2} & \frac{-\beta^2 kz}{1-\beta^2} \\ 0 & -kz & k \\ \frac{-kz}{1-\beta^2} & \frac{k}{1-\beta^2} & \frac{\beta^2 kz}{1-\beta^2} \end{bmatrix} \quad (4.161)$$

$$\vec{g} \equiv \begin{bmatrix} -\frac{1}{\rho_0 v} \frac{\beta^2}{1-\beta^2} \frac{1}{s} \frac{C_x Y k}{\sqrt{3}} = -\frac{1}{\rho_0 v^2} \frac{\beta^2}{1-\beta^2} \frac{1}{z} \frac{C_x Y}{\sqrt{3}} \\ \frac{1}{\rho_0 v} \frac{1}{s} \frac{C_y Y k}{\sqrt{3}} = \frac{1}{\rho_0 v^2} \frac{1}{z} \frac{C_y Y}{\sqrt{3}} \\ \frac{1}{\rho_0 v} \frac{1}{1-\beta^2} \frac{1}{s} \frac{C_x Y k}{\sqrt{3}} = \frac{1}{\rho_0 v^2} \frac{1}{1-\beta^2} \frac{1}{z} \frac{C_x Y}{\sqrt{3}} \end{bmatrix} \quad (4.162)$$

where $\beta = v/c_s$ and $z = s/kv$.

To find the solution of Eq. (4.160) it is useful to expand \mathbf{A} in terms of its eigenvalues and left eigenvectors (row vector) [88]

$$\mathbf{A} = \mathbf{S}^{-1} \mathbf{\Lambda} \mathbf{S} \quad (4.163)$$

$$\mathbf{S} = \begin{bmatrix} -1 & z & -1 \\ z & -1 & w \\ z & -1 & -1 \end{bmatrix}, \quad \mathbf{\Lambda} = \begin{bmatrix} -zk & 0 & 0 \\ 0 & \frac{k(\beta^2 z - w)}{1-\beta^2} & 0 \\ 0 & 0 & \frac{k(\beta^2 z + w)}{1-\beta^2} \end{bmatrix} = \begin{bmatrix} \lambda_1 & 0 & 0 \\ 0 & \lambda_2 & 0 \\ 0 & 0 & \lambda_3 \end{bmatrix} \quad (4.164)$$

where $w = \sqrt{\beta^2 z^2 + 1 - \beta^2}$. Then Eq. (4.160) becomes (\mathbf{S} is independent of x)

$$\mathbf{S} \frac{\partial \vec{u}}{\partial x} = \mathbf{\Lambda} \mathbf{S} \vec{u} + \vec{g} \Rightarrow \frac{\partial (\mathbf{S} \vec{u})}{\partial x} = \mathbf{\Lambda} (\mathbf{S} \vec{u}) + \mathbf{S} \vec{g} \quad (4.165)$$

multiplying through by the homogeneous solution yields

$$\exp(-\Lambda x) \frac{\partial(\mathbf{S}\vec{u})}{\partial x} - \exp(-\Lambda x) \Lambda(\mathbf{S}\vec{u}) = \exp(-\Lambda x) \mathbf{S}\vec{g} \quad (4.166)$$

$$\Rightarrow \exp(-\Lambda x) \frac{\partial(\mathbf{S}\vec{u})}{\partial x} - \Lambda \exp(-\Lambda x) (\mathbf{S}\vec{u}) = \exp(-\Lambda x) \mathbf{S}\vec{g} \quad (4.167)$$

$$\Rightarrow \int_0^x \frac{\partial\{\exp(-\Lambda x) \mathbf{S}\vec{u}\}}{\partial x} \partial x = \int_0^x \exp(-\Lambda x) \mathbf{S}\vec{g} \partial x \quad (4.168)$$

$$\Rightarrow \exp(-\Lambda x) \mathbf{S}\vec{u} - \mathbf{S}\vec{u}_{x=0} = \int_0^x \exp(-\Lambda x) \mathbf{S}\vec{g} \partial x \quad (4.169)$$

$$\Rightarrow \vec{u} = \mathbf{S}^{-1} \exp(\Lambda x) [\mathbf{S}\vec{u}_{x=0} + \int_0^x \exp(-\Lambda x) \mathbf{S}\vec{g} \partial x] \quad (4.170)$$

The integral in Eq. (4.170) becomes (since \vec{g} is independent of x in this problem when assuming constant strength)

$$\int_0^x \exp(-\Lambda x) \mathbf{S}\vec{g} \partial x = \Lambda^{-1} (\mathbf{I} - \exp(-\Lambda x)) \mathbf{S}\vec{g} \quad (4.171)$$

Equation (4.170) still has an unknown, the shock perturbation amplitude $\hat{\xi}(s)$ so that we need one more equation, and is given by Zaidel. Zaidel [87] noted that for the solution, Eq. (4.170), to be bounded the third component of the term in brackets in Eq. (4.170) has to be zero as x gets large (i.e., as the shock gets further away from the rigid piston boundary) since the third eigenvalue is positive.

$$\text{third term of } \{\mathbf{S}\vec{u}_{x=0} + \int_0^{x \rightarrow \infty} \exp(-\Lambda x) \mathbf{S}\vec{g} \partial x\} = 0 \quad (4.172)$$

$$\Rightarrow \text{third term of } \{\mathbf{S}\vec{u}_{x=0} + \Lambda^{-1} \mathbf{S}\vec{g}\} = 0 \quad (4.173)$$

Equation (4.173) amounts to neglecting the boundary at the rigid piston for times greater than zero. This has been shown to be valid by subsequent authors for known real equation of states [78, 82]. Simple algebra with Eq. (4.173) gives an expression for $\hat{\xi}(s)$ (we do the algebra in a symbolic package), which can then be transformed back to the time domain with the inverse Laplace Transform. The inverse Laplace transform is complicated analytically (and results in a final integral that has to be solved numerically anyhow) so we

do the inversion numerically; however, application of the Final Value Theorem can easily be done to $\hat{\xi}(s)$ resulting in

$$\lim_{t \rightarrow \infty} \frac{\xi(t)}{\xi_0} = \lim_{s \rightarrow 0} s \frac{\hat{\xi}(s)}{\xi_0} \cong \frac{Y}{k\xi_0} \frac{(C_x + C_y \sqrt{1 - \beta^2})}{\sqrt{3}P_0} =$$

$$\frac{Y}{k\xi_0} \frac{\left(C_x + C_y \sqrt{1 - \left(\frac{U_s - U_P}{c_s} \right)^2} \right)}{\sqrt{3}\rho_0 U_s U_P} \Rightarrow \sim \frac{Y}{k\xi_0} \frac{C_x}{\sqrt{3}\rho_0 U_s U_P} \text{ for weak shocks} \quad (4.174)$$

This qualitatively matches FEM simulations well, and the approximation is used because the deviatoric contribution to the boundary condition (middle row of Eq. (4.156)) at the shock front has a very minor contribution to Eq. (4.174) that we have neglected. Equation (4.174) is not strictly valid since the assumptions used in the continuum momentum Eqs. (4.140) – (4.142) are approximately valid only until the shock front nears inversion, at which point the deviatoric stress may become elastic and possibly change signs. However, Eq. (4.174) is an upper bound of the maximum steady state shock front perturbation amplitude.

Figure 4.4 shows the solution for shock front perturbation using the same fluid parameters as [88] for the inviscid case (i.e., $Y=0$), and matches the results in [88] exactly.

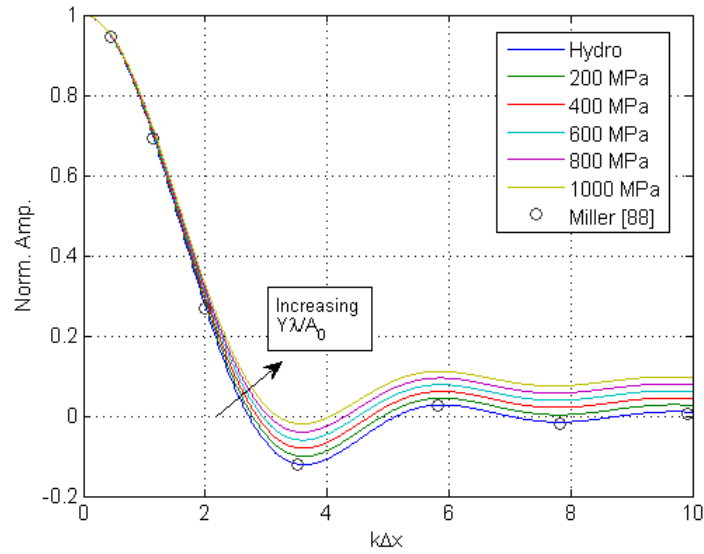


Figure 4.4: Analytical shock front perturbation evolution for water using the parameters from Table 1 in [88]. Solution matches results from [88] exactly. Plot also shows effect of adding strength.

This concludes the numerical and analytical models. The next chapter will verify and validate the numerical models that were implemented via user subroutines into ABAQUS™/Explicit. The analytical shock front perturbation solution will be revisited in the Discussion Chapter.

5. MODEL CALIBRATION, VERIFICATION, AND VALIDATION

This section provides steps taken to calibrate and validate the material models, particularly the parameters in the Helmholtz potential, to published data.

5.1. Calibration and Verification

5.1.1. Helmholtz Parameters

At first glance the Helmholtz Equation (5.1), used in the isotropic and crystal plasticity models,

$$F_v(v, T) = E_k(v) + C_{v0}(T - T_0)\varepsilon(v) - T \left[s_0 + C_{v0} \ln \left(\frac{T}{T_0} \right) \right] \quad (5.1)$$

$$E_k(v) = E_0 + \frac{9K_0}{16\rho_0} (x^2 - 1)^2 [2 + (N_0 - 4)(x^2 - 1)]$$

$$\varepsilon(v) = 1 + \Gamma_0(1 - \rho_0 v), \quad x(v) = (\rho_0 v)^{-1/3}$$

contains several unknowns,

$$C_{v0k}, s_{0k}, E_{0k}, \rho_{0k}, N_{0k}, \Gamma_{0k}, K_{0k}$$

where the subscript k is for each phase, and $T_{0k} = 300K$ and $P_{0k} = 0$; however, many of them are known or are just reference values. For the low pressure iron phase we let $s_{0_1} = E_{0_1} = 0$, and use the room temperature value of $C_{v0_1} = 450 J/(kg.K)$ [201]. Arbitrarily we also set the high pressure specific heat to the same value as the low pressure. The specific heat does not have much of an influence on the P - v Hugoniot or the Temperature-Pressure phase diagram; however, it does have a significant effect on the temperature rise due to the shock passage. The reference density and bulk modulus for the low pressure phase are easily known $\rho_{0_1} = 7873 kg/m^3$ and $K_{0_1} = 176 GPa$ [20,201]. The bulk

modulus pressure derivatives (N_{0_1}, N_{0_2}) and the Mie-Grüneisen parameters ($\Gamma_{0_1}, \Gamma_{0_2}$) are taken from a range of similar Helmholtz equations and are only adjusted slightly to fit the known P - v Hugoniot. This leaves only four remaining parameters for the high pressure iron phase $s_{0_2}, E_{0_2}, \rho_{0_2}, K_{0_2}$. These four remaining parameters (and small changes to N_{0_2}) are used to fit experimental P - v Hugoniot data and pressure-temperature phase diagrams for the low (BCC) and high pressure (HCP) phases [111,20,170]. The final parameters are in the range of similar Helmholtz functions [138,111,173,174,187].

For a single phase material Eq. (5.1) and energy conservation at the shock front

$$E(v, T) - E_0(v_0, T_0) = -\frac{1}{2}(P(v, T) - P_0(v_0, T_0))(v - v_0) \quad (5.2)$$

along with the definitions

$$P(v, T) = -\frac{\partial F(v, T)}{\partial v}, \quad E(v, T) = F(v, T) - \frac{\partial F}{\partial T} T \quad (5.3)$$

allow for the P - v Hugoniot to be plotted for a given specific volume v (i.e., compression), either analytically [101, p. 126] for certain Helmholtz functions or numerically by minimizing the objective function below for a given v (and using the definitions in Eq. (5.3))

$$J = \left\{ (E(v, T) - E_0) - \left[-\frac{1}{2}(P(v, T) - P_0)(v - v_0) \right] \right\}^2 \quad (5.4)$$

whose solution results in the correct temperature, which can be substituted back into Eq. (5.3) to find the pressure on the P - v Hugoniot.

For a two phase system a similar approach is used except that the work term in square brackets in Eq. (5.4), becomes one of three equations depending on where we are on the theoretical P - v Hugoniot

$$-\frac{1}{2}(P - P_0)(v - v_0) \quad (5.5)$$

$$-\frac{1}{2}(P_{1'} - P_0)(v_{1'} - v_0) - P_{1'}(v - v_{1'}) \quad (5.6)$$

$$\max \left\{ -\frac{1}{2}(P_{1'} - P_0)(v_{1'} - v_0) - \frac{1}{2}(P + P_{1'})(v - v_{1'}), -\frac{1}{2}(P - P_0)(v - v_0) \right\} \quad (5.7)$$

and

$$E = \lambda E(v_1, T) + (1 - \lambda)E(v_2, T) \quad (5.8)$$

$$v = \lambda v_1 + (1 - \lambda)v_2 \quad (5.9)$$

where $(v_{1'}, P_{1'})$ is the known P - v pair where the phase transformation starts, and the first term in Eq. (5.7) is for the case the second shock is not overdriven. To create the P - v Hugoniot then for a two-phase system we start with Equations (5.4) and (5.6, 5.8, 5.9), assuming a two-phase mixture for a given v , with additional constraints added to Eq. (5.4) that the Gibbs free energy of the two phases is equivalent as well as the pressure. The solution to this problem produces a v_2, v_1, T, λ set of data, for a given v , where λ is the mass fraction of phase 1 (low pressure phase). If $0 < \lambda < 1$ our guess was correct and we are done, if $\lambda > 1$ then we resolve the problem with the same v but using only Eq. (5.4) and (5.5), similarly if $\lambda < 0$ we resolve the problem with the same v but using only Eq. (5.4) and (5.7). Boettger and Wallace [20] explicitly accounted for metastable states (incomplete or very slow transformations when driving force is low) present for shock pressures below ~ 18 GPa. The metastable states in this work relied on an empirical kinetics equation to slow transformations that were near the ~ 13 GPa transition for iron [142,111].

Finally the P - T temperature phase diagrams can be plotted by simply calculating the Gibbs free energy for both phases for an assortment of (v, T) points, calculating the pressure, and comparing the Gibbs values of both phases for a given P - T point; with the

stable phase being the phase with the lower Gibbs energy. Results from the P - v Hugoniot and P - T phase diagram fits are shown in Table 5.1 and Figure 5.1.

Table 5.1: EOS Parameters using the Helmholtz function given in Eq. (5.1) [175,20,111].

		Fe BCC	Fe HCP	Cu	Alum
Reference Temp. , T_0 (K)		300	300	300	300
Reference Density , ρ_0 (kg/m ³)		7873	8342	8960	2700
Specific Heat, C_p (J/kg-K)		450	450	386	900
Mie Gruneisen Constant, γ (-)		1.82	2.80	1.99	2.00
Reference Bulk Modulus, K_0 (Pa)		176.64e9	187.27e9	140.0e9	76.0e9
Press. Derivative of Bulk Mod., N_0 (-)		4.70	5.47	4.50	3.86
Reference Energy, E_0 (J/kg)		0.0	1.0186e5	0.0	0.0
Reference Entropy, S_0 (J/kg-K)		0.0	46.25	0.0	0.0
Opt. 1	Phase Trans. Time Const., τ (s)	1e-9		-	-
	Trans. Barrier, G_0 (J/kg)	3500		-	-
Opt. 2	Reference Rate, ξ_0 (1/s)	1e5		-	-
	Energy Barrier, b (J/kg)	688		-	-

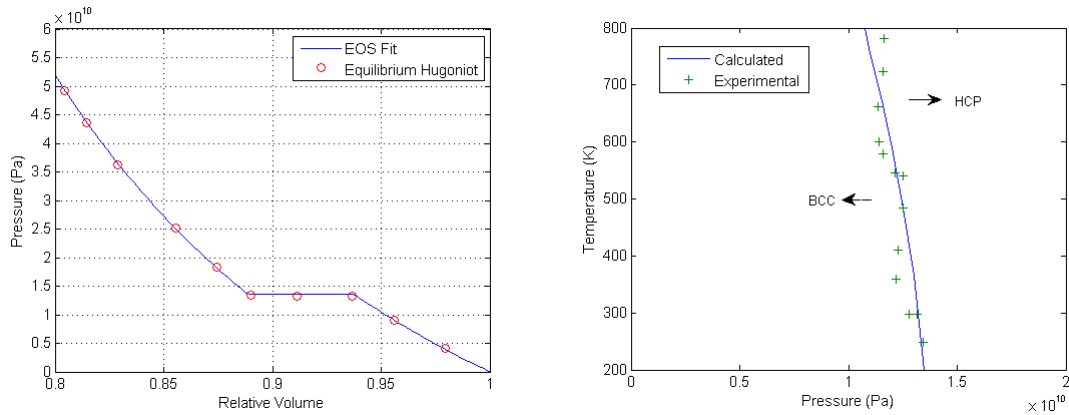


Figure 5.1: EOS calibration. (left) Hugoniot formed with parameters in Table 5.1 compared to theoretical Hugoniot [20]. (right) Temperature-Pressure phase diagram formed with EOS parameters from Table 5.1, experimental values are from [20,170].

Qualitatively, increasing E_{0_2} raises the pressure for the transformation, increasing ρ_{0_2} increases the transformation volume change, increasing K_{0_2} steepens the second phase Hugoniot, and changes in s_{0_2} does not affect the P - v Hugoniot much, but do affect the P -

T diagram. The final values obtained are within a few percent of similar Helmholtz equations given in [20, 111]. Table 5.1 also lists parameters for pure copper and aluminum with this Helmholtz function.

5.1.2. Verification

5.1.2.1. Copper

To verify the the correct formulation coding of the isotropic single and two-phase models and insure EOS parameters provide appropriate solutions a series of 2-D plane strain problems were solved in ABAQUS using built-in material models, i.e., it is assumed that the ABAQUS solutions are mathematically and numerically correct and can be used as appropriate baselines. The model is a $100\ \mu\text{m}$ thick flat sample with symmetry conditions on the sides, a 0.25 micron mesh, a fixed time step of $1\text{e-}12$, and a Mie-Grüneisen EOS with copper parameters: $\rho_0 = 8960\ \text{kg}/\text{m}^3$, $G = 48\ \text{GPa}$, $Y = 500\ \text{MPa}$, $C = 3933\ \text{m}/\text{s}$, $s = 1.5$, $\gamma = 1.99$ [100]. Two ABAQUS subroutines (VUMATs) were run, one used the coupled deviatoric-hydrodynamic formulation outlined in Section 4.1.2. with the Helmholtz parameters in Table 5.1, and the other used a decoupled formulation with a Mie-Grüneisen EOS (same formulation as ABAQUS) and the a deviatoric model identical to the first VUMAT (i.e., a PTW strength model).

Figure 5.2 shows pressure profiles through the thickness of the sample when the shock wave is about halfway through the specimen (at a time of 12 ns) at various BC velocities. In the figure ABAQUS (AB) results are compared to the subroutine Mie-Grüneisen (MG) results and Helmholtz (F) model. Figure 5.3 shows velocity results at the opposite free surface. As can be seen in the figures all models show similar results with the

biggest difference in the shape of the shock front at lower shock pressures, which is to be expected due to the difference in the deviatoric models [104]. All simulations used the same amount of artificial viscosity (linear term = 0.06, quadratic term = 1.2).

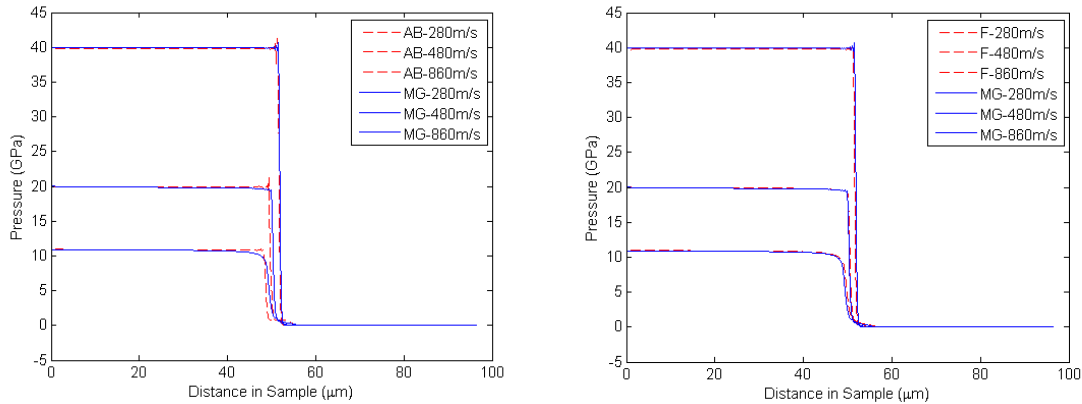


Figure 5.2: ABAQUS and VUMAT EOS results. (left) Comparison of ABAQUS (AB) built-in Mie-Grüneisen EOS with a Fortran subroutine (MG) using an identical EOS but with a PTW strength law. (right) same results but with Helmholtz function (F) and parameters in Table 5.1. BC velocities are given in legend. Note: x-axis is true distance, i.e., distance in compressed sample, not reference state.

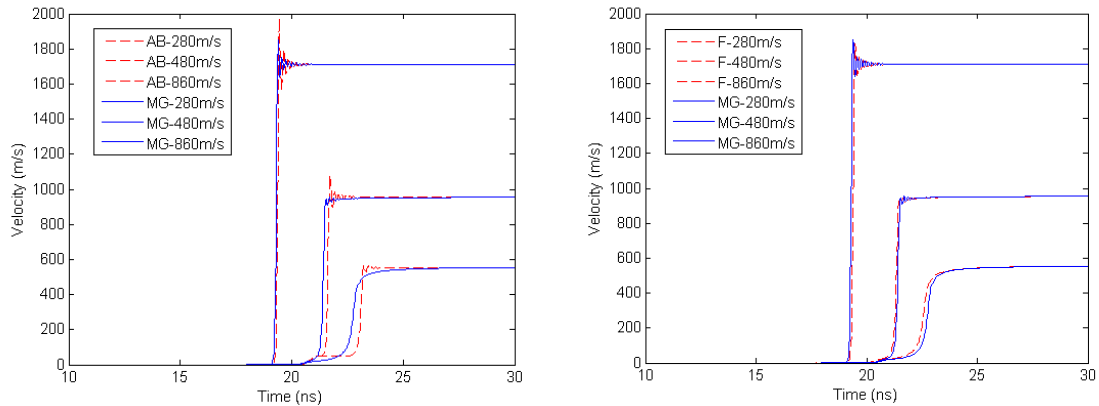


Figure 5.3: Free surface velocity values of ABAQUS (AB) built-in Mie-Grüneisen EOS and Fortran subroutines (MG) and (F). Numerical oscillations at higher velocities are expected for materials with weak deviatoric responses at high strain rates. The shock slope on the AB models is limited by the artificial viscosity, while the MG and F model slope is influenced by the PTW nonlinear strain rate response.

To verify the PTW calculations in the models a series of plots were made for the 280 m/s BC for the Helmholtz (F) VUMAT, using the PTW parameters in Table 5.2. At random integration points the flow stress, plastic rate dy/dt , plastic strain γ , pressure, and temperature were obtained and compared to the PTW equation. As can be seen in Figure 5.4 and Figure 5.5 the Fortran subroutine correctly calculates the PTW values. Figure 5.4 shows the state values at 12 ns (when the shock wave is about halfway through the sample), and Figure 5.5 shows the PTW response at a pressure of 10.86 GPa (equivalent to 280 m/s BC) and temperature of 350 K (approximate temperature behind shock front).

5.1.2.2. Iron

Similar to the copper simulations a set of simulations was performed for iron to confirm the code was producing reasonable results. However because iron has two phases there is no convenient way to perform a direct comparison with built-in ABAQUS models, particularly for medium shock pressures above the phase transition (~ 13 GPa) and below the overdriven pressures of ~ 40 and ~ 60 GPa for the first plastic wave and elastic wave respectively [102]. Figure 5.6 shows a comparison of an ABAQUS material with properties of $\rho_0 = 7860 \text{ kg/m}^3$, $G = 82 \text{ GPa}$, $Y = 1.0 \text{ GPa}$, $C = 4630 \text{ m/s}$, $s = 1.33$, $\gamma = 1.70$ for a pressure below 13 GPa [102], to a similar subroutine, but with a PTW strength law with the Phase 1 (BCC) parameters in Table 5.2, and a phase aware subroutine with the PTW parameters in Table 5.2. Figure 5.6 also shows the results for pressure above the phase transition for an ABAQUS material with parameters of $\rho_0 = 7860 \text{ kg/m}^3$, $G = 82 \text{ GPa}$, $Y = 1.0 \text{ GPa}$, $C = 3570 \text{ m/s}$, $s = 1.92$, $\gamma = 1.80$ [100], to a similar subroutine but with the Phase 2 (HCP) PTW parameters in Table 5.2, and finally the phase aware subroutine.

Table 5.2: PTW Parameters for Iron, Cu, and Aluminum [67, 131].

	Phase 1 BCC	Phase HCP	Cu	Alum (ref)
Temp. Constant, κ (-)	3.50e-1	3.00e-1	0.11	0.494
Strain Rate Parameter, γ (-)	1.00e-5	1.00e-5	1.0e-5	1.52e-4
Strain Hard. Parameter, θ (-)	1.50e-2	1.50e-2	2.5e-2	5.29e-2
Strain Hard. Parameter, p (-)	3.00	3.00	2.0	3.0
Sat. Stress Factor, s_0 (-)	1.75e-2	2.1875e-2	8.5e-3	3.2e-2
Sat. Stress Factor, s_{inf} (-)	4.375e-3	4.375e-3	5.5e-4	7.91e-3
Yield Stress Factor, y_0 (-)	6.625e-3	1.1594e-2	1.0e-3	9.42e-3
Yield Stress Factor, y_{inf} (-)	1.1594e-4	1.3125e-3	1.0e-5	5.66e-3
Med. Strain Rate Const., y_1 (-)	1.75e-2	5.25e-2	9.4e-2	1.42e-2
Med. Strain Rate Exp., y_2 (-)	2.65e-1	2.50e-1	0.25	0.4
Exponent in Drag, β (-)	0.265	0.25	0.25	0.23
Melt Temperature, T_m (K)	1810	2050	1357	930
Ref. Shear Modulus, G_0 (Pa)	87.2e9	87.2e9	51.8e9	26.0e9
Press. Derivative of G , α_P (-)	1.40	1.4	1.36	1.98
G_0 Temp. Parameter, α_T (-)	0.23	0.23	0.43	0.23

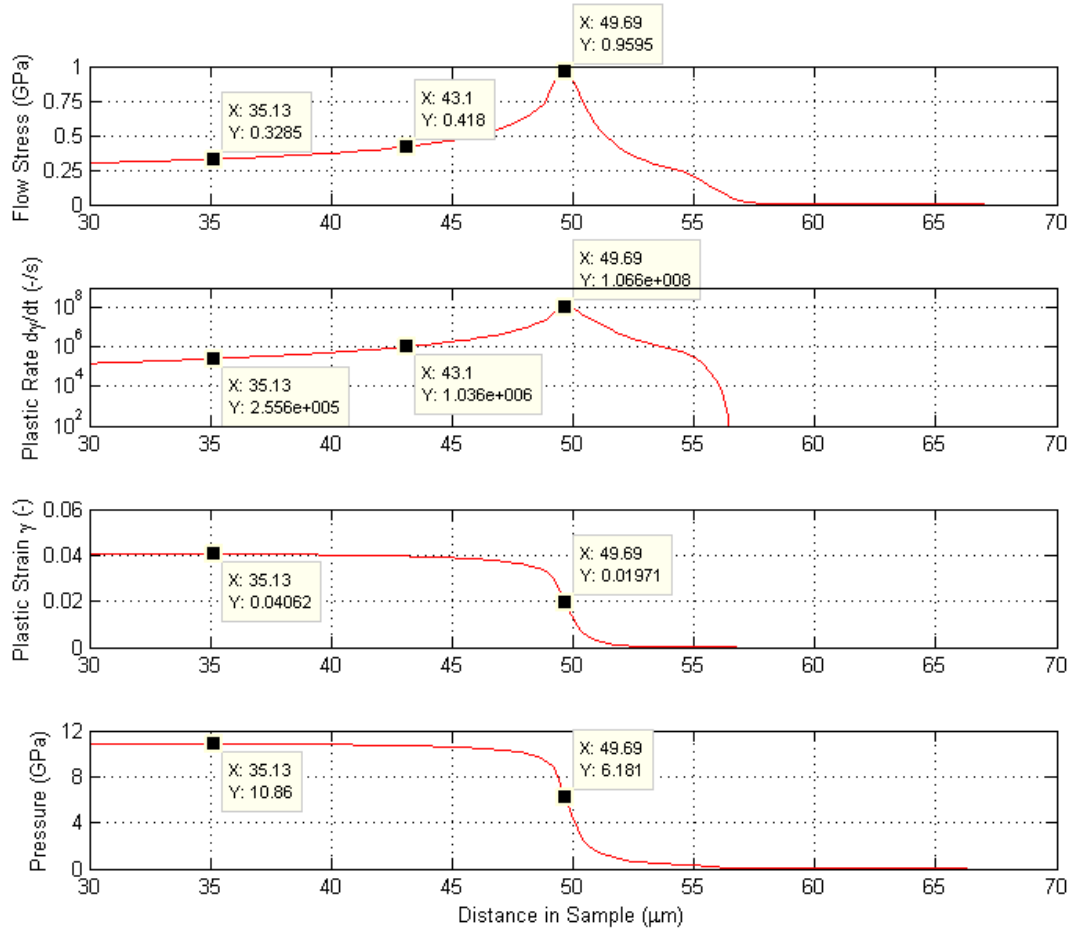


Figure 5.4: Verification of state values for Helmholtz VUMAT for 280 m/s shock front is about halfway through the sample. Note flow stress in Figure 5.5 agrees with highlighted points above except at the peak strain rate point, and is only slightly off at that point because Figure 5.5 is for a pressure higher than marker point above in the shock front (i.e., higher than 6.18 GPa).

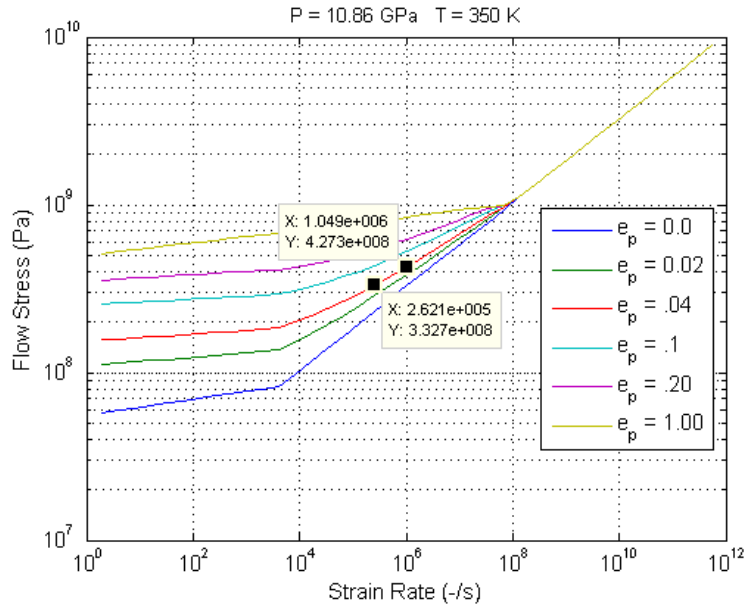


Figure 5.5: Cu PTW response at a pressure of 10.86 GPa and a temperature of 350 K, for the PTW parameters of Table 5.2.

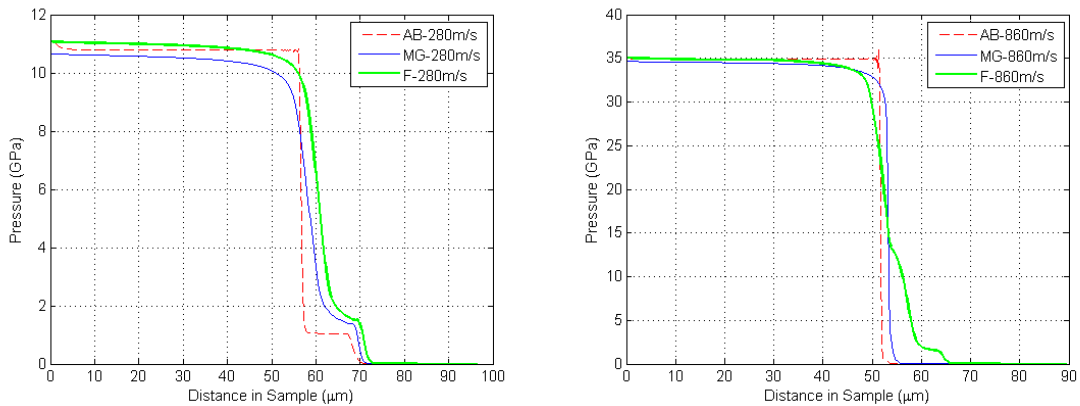


Figure 5.6: Comparison of ABAQUS and VUMAT material models for iron for pressures below (left) and above (right) the phase transformation threshold. MG VUMAT uses an EOS identical to the one in ABAQUS while the Helmholtz (F) VUMAT uses a phase aware EOS. Both VUMATs use a PTW strength law. BC velocities are given in legend Notice how much different the Helmholtz (F) routine response is due to more accurately capturing properties ahead of the shock front. Note: x-axis is true distance (i.e., distance in compressed sample, not reference state).

Figure 5.7 shows the velocity response at the free surface 100 microns away from the impact surface. Several interesting observations can be made from these plots.

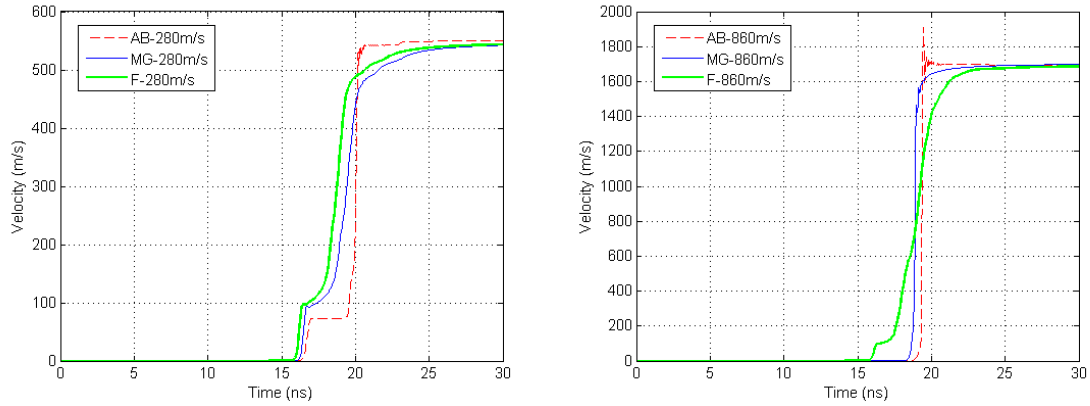


Figure 5.7: Free surface velocity comparison for iron EOS models. BC velocities are given in legend. Note: x-axis is true distance (i.e., distance in compressed sample, not reference state). Notice how much different Helmholtz (F) routine response is due to accurately capturing properties ahead of shock front. Note: x-axis is true distance (i.e., distance in compressed sample, not reference state).

First for the low-pressure shock all the models are similar except for some differences due to the deviatoric models. However, for the higher pressure shock the phase aware model is the only one capable of accurately reproducing the elastic precursor and general plastic wave shapes. The Mie-Grüneisen EOS cannot reproduce the elastic precursor accurately because the elastic longitudinal wave speed is dependent on not only the shear modulus, but also on the low pressure bulk modulus, which is not accurately reproduced by the high pressure EOS parameters. Figure 5.8 shows plastic strain rates and deviatoric stress for the phase aware subroutine for the high speed impact and Figure 5.9 shows the PTW response at the indicated points in Figure 5.8. As can be seen in the plots the deviatoric stress is being calculated as expected.

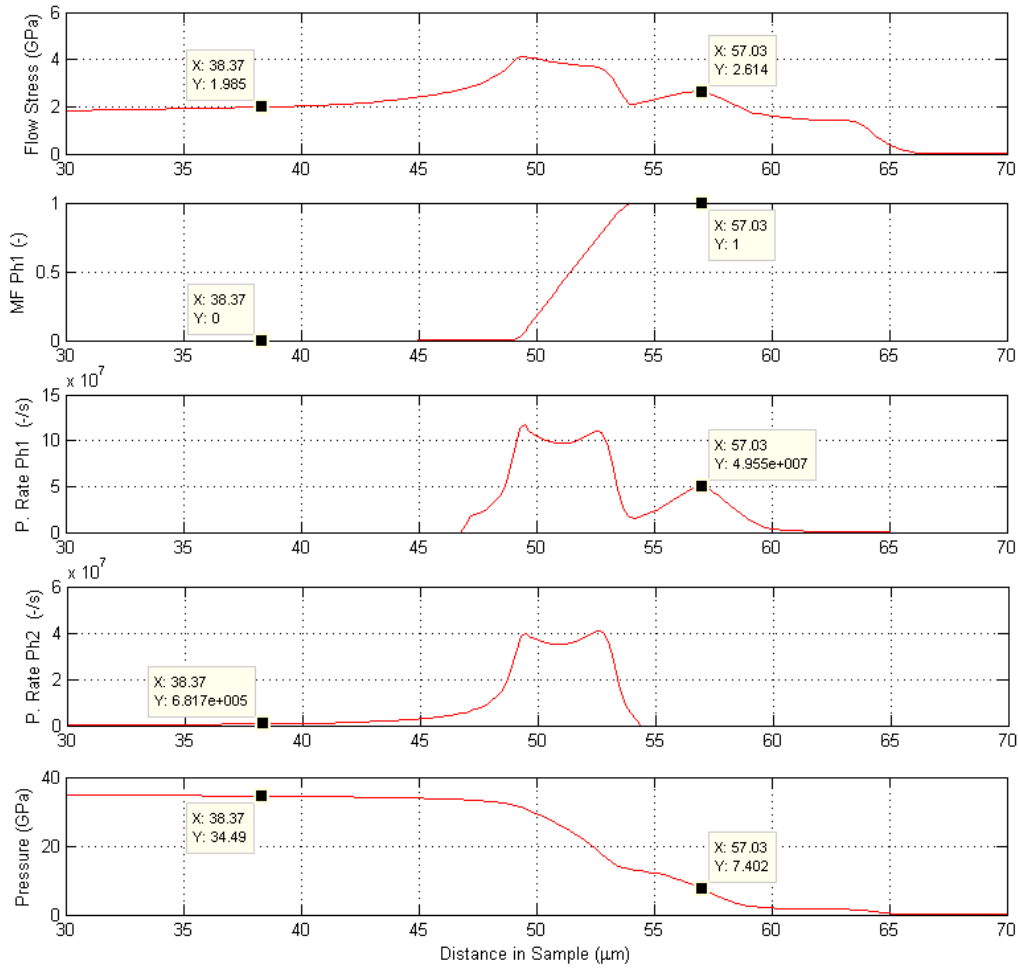


Figure 5.8: State variables from iron Helmholtz VUMAT when the 860 m/s BC shock front is about halfway through the sample. At the indicated material points the plastic strain and temperature is (0.10, 600 K) and (0.01, 375 K) from left to right. Second figure from top is mass fraction of low pressure phase (BCC). Figure 5.9 shows the PTW response for each phase at the indicated pressure and temperatures. Note: x-axis is true distance (i.e., distance in compressed sample, not reference state).

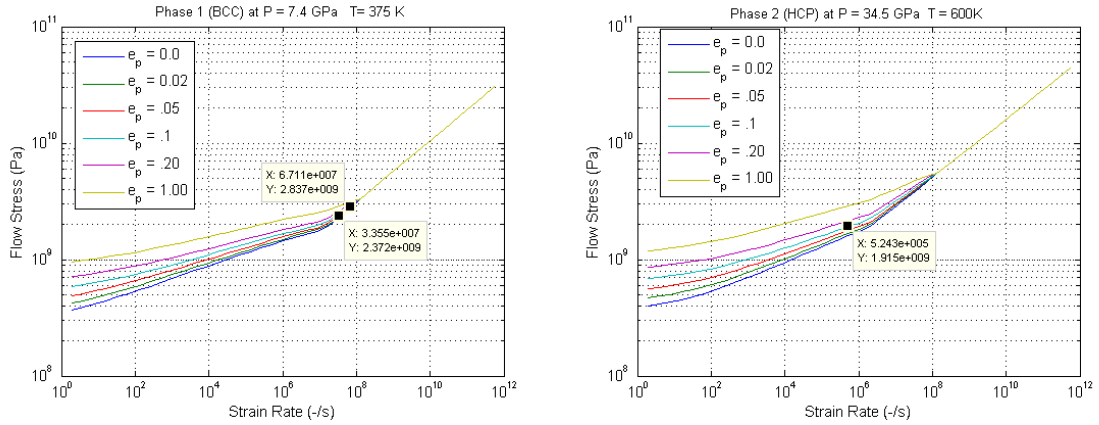


Figure 5.9: PTW response of iron for low and high pressure phases. PTW parameters are given in Table 5.2. (left) Data point marker in figure bound the indicated BCC material point in Figure 5.8. (right) Data point marker in figure is for HCP marker in Figure 5.8.

As a final verification of the code, Shot 5 from Barkers experiments [102] was simulated without any attempt to fitting the data. The phase aware code was used with the same EOS and PTW parameters as all previous plots shown thus far. Figure 5.10 shows the results. Barker’s shot 5 was a plate on plate impact, with an equal target and flyer thickness of 6.314 mm at a flyer velocity of 1292 m/s (i.e., $1292/2 = 646$ m/s BC velocity).

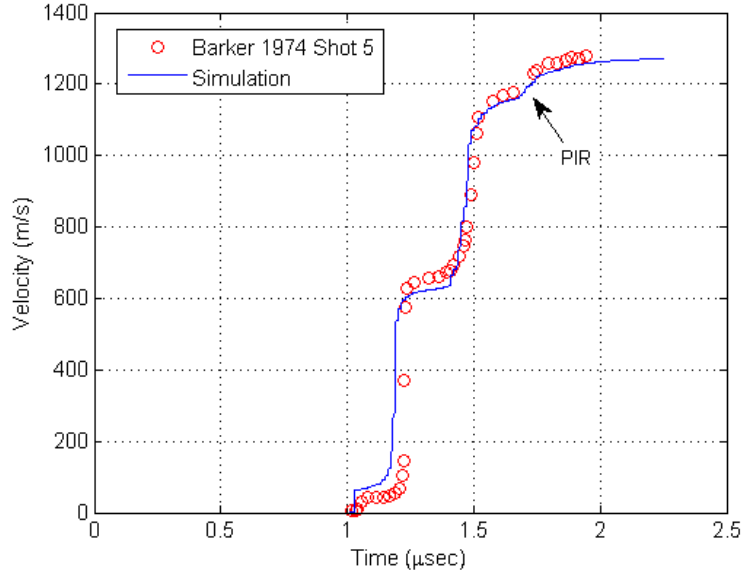


Figure 5.10: Simulation and experimental iron free surface response [102] Shot 5. Shot 5 was an impact velocity of 1292 m/s (velocity BC of $1292/2 = 646$ m/s) on a 6.314 mm target, peak stress is ~ 23.6 GPa. The phase interface reflection (PIR) wave is a result of the release wave of the second shock front interacting and partially reflecting at a metastable HCP-BCC phase boundary within the material (i.e., an impedance mismatch), see Barker [102] for more details.

5.2. Preliminary Verification of Phase Aware Crystal Plasticity Model

A primary feature of the phase aware crystal model is its capability of tracking variants. Starting with a single BCC variant six possible HCP variants are possible through the transformation gradient \mathbf{F}_i^{tr} [188, p. 60]

$$\mathbf{F}_i^{tr} = \mathbf{G}_i \mathbf{U} \mathbf{G}_i^T \quad (5.10)$$

where \mathbf{U} is compression along [001] and an extension along $[\bar{1}10]$ given by [189]

$$\mathbf{U} = \begin{bmatrix} \frac{\alpha}{2} + \frac{3}{4\sqrt{2}} & \frac{\alpha}{2} - \frac{3}{4\sqrt{2}} & 0 \\ \frac{\alpha}{2} - \frac{3}{4\sqrt{2}} & \frac{\alpha}{2} + \frac{3}{4\sqrt{2}} & 0 \\ 0 & 0 & \frac{\sqrt{3}}{2} \end{bmatrix}, \quad \alpha = (c/a)\sqrt{3/8} \quad (5.11)$$

where c/a is the ratio of the HCP cell height to side length. Then $\mathbf{G}_i(\cdot)\mathbf{G}_i^T$ is a rotation to the six different HCP variants (i.e., the six different ways you can compress and extend the starting BCC cell to a HCP cell (see [188, p. 60] for more details). For the reference BCC variant $\mathbf{G}_i = \mathbf{I}$ and \mathbf{U} creates a HCP variant with the c-axis in the $[1\ 1\ 0]$ direction. To get the 13 BCC variants (12 if you do not count the starting unit cell) we use the 6-fold rotational property of the HCP structure, i.e., a starting BCC cell can transform to 1 of 6 HCP cells and each one of those 6 HCP cells can transform back to the reference BCC cell or 2 other BCC variants (who share the same HCP variants as the starting cell) that differ slightly because of the 6-fold symmetry, see Figure 5.11.

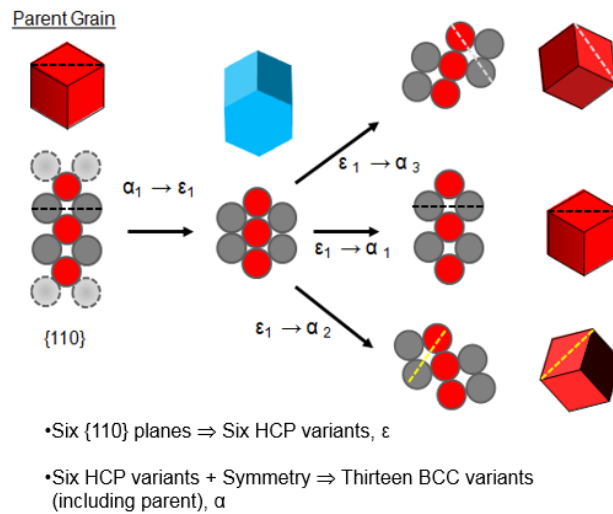


Figure 5.11: Variant transformation. The reference BCC variant is transformed to HCP variant “1” with \mathbf{U} . This HCP variant can then transform back to the reference BCC variant or one of two other variants related by the HCP 6-fold symmetry. Dashed line represents intersection of HCP basal plane with BCC cell.

The BCC variant transformation is

$$\mathbf{F}_j^{tr} = (\mathbf{H}_j \mathbf{G}_i \mathbf{U}^{-1} \mathbf{G}_i^T \mathbf{H}_j^T) (\mathbf{G}_i \mathbf{U} \mathbf{G}_i^T) \quad (5.12)$$

where $\mathbf{H}_j(\cdot)\mathbf{H}_j^T$ performs the 6-fold rotation. Essentially Eq. (5.12) starts with the reference BCC variant transforms to one of the 6 HCP cells, applies a + or -60° rotation (or no rotation at all) about the c axis of the HCP variant and then reverses the HCP transformation. The Appendix lists the transforms for all 19 variants. Also, recall the transformation path from one variant to another is $\mathbf{F}_{to}^e \mathbf{F}_{to}^{tr} \mathbf{F}_{fr}^{tr^{-1}} \mathbf{F}_{fr}^{e^{-1}}$ so that the starting BCC variant is the reference state.

Some simple one-element tests were performed with somewhat intuitive results to verify the phase transformation variant selection. Table 5.3 shows the resulting HCP variants of a single block element unconstrained with a constant velocity applied to the face normal to the y -axis ($[0\ 1\ 0]$ direction). Table 5.3 also shows the results for a uniaxial strain (the element was constrained on all sides).

As you might expect the HCP variants whose c -axis is perpendicular to the compression axis (the y -axis) is the preferred variant (since the maximum deformation on transformation is the compression perpendicular to the c -axis) in both cases with the unconstrained element preferring those variants more than the others. In the unconstrained case those two variants, 16 and 17, are preferred even more since there is no constraint penalizing the expansion (c -axis of HCP) of the reference BCC cell in the direction normal to the compression.

Table 5.3: HCP variant mass fraction results from single element tests for a BCC compression along the y-axis for uniaxial strain and unconstrained strain. Dashed line signifies the intersection of the HCP Basal plane with the reference BCC unit cell (Variant No. 1).


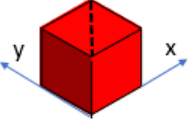

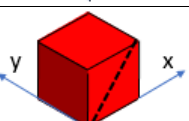
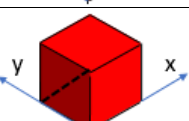
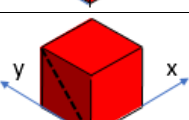
Variant No.	HCP Variant	Uniaxial Compression	Unconstrained Compression
14		0.118	0.087
15		0.118	0.087
16		0.259	0.327
17		0.259	0.327
18		0.118	0.087
19		0.118	0.087

Table 5.4 shows a second set of simulations where a long slender rod was compressed and released and then compressed again in uniaxial strain. The results are not as intuitive in this case. In Table 5.4 a transformation empirical parameter θ was also added to the ABAQUS subroutine. This parameter ranges from 0 to 1 (Table 5.3 used a value of 1), when 1 the transformation velocity gradient L^X is as derived in Section 1.5.6.4. , when 0 the transformation velocity gradient is only volumetric as would be found in the isotropic model. This parameter was added due to the observation that for $\theta = 1$ a compression and release (e.g., BCC to HCP to BCC) does not return to a normalized volume of 1. This is a

result of the fact

$$\det(\sum m_i F_i^{tr}) \neq \sum \det(m_i F_i^{tr}) = 1 \text{ for } \det(F_i^{tr}) = 1 \quad (5.13)$$

where m_i is the BCC mass fraction of BCC variant i , and the LHS of Eq. (5.13) is the situation of the current model, and produces macro volumes about 1 to 2 % greater than the normalized volume (starting volume). In fact, upon returning to the BCC phase for more than one BCC variant the normalized volume is always greater than 1 for $\theta > 0$.

The drawback to setting $\theta = 0$ is that you lose the feedback of the deviatoric portion of the transformation deformation, however the variant selection is still reasonable and without more experimental data it is difficult to know what the practical penalty to using $\theta = 0$ is. The results in Table 5.4 show that with $\theta = 1$ the variant selection is not intuitive after the first compression, but with $\theta = 0.25$ the results are more so. Reference [142], which the kinematics of the current subroutine are based on for $\theta = 1$, did not discuss variant selection on release or the non conservative volume issue in Eq. (9). Experimental texture results for shock loading are given in [190-192] where the original BCC orientation was preferred after a BCC to HCP to BCC transformation for iron during shock loading.

Table 5.4: Mass fraction transformation results from a uniaxial compression-release-compression cycle in the format (Start ,Compression, Release, Compression), where load is applied in y direction. When $\theta = 1$ the transformation velocity gradient deviatoric portion is completely used, for $\theta = 0$ only the volumetric portion is. Dashed line signifies the intersection of the HCP Basal plane with the reference BCC unit cell (Variant No. 1).


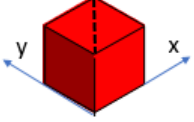

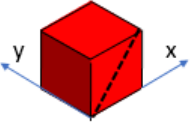
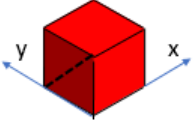
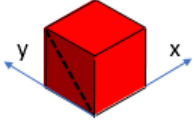
Variant No.	Variant	Uniaxial Compression ($\theta = 1$)	Uniaxial Compression ($\theta = 0.25$)	Uniaxial Compression ($\theta = 0$)
1	Reference BCC	(1,0,0.367,0)	(1,0,0.34,0)	(1,0,0,0)
2	From +60 rot. of HCP 14	(0,0,0.087,0)	(0,0,0.083,0)	(0,0,0.238,0)
3	From -60 rot. of HCP 14	(0,0,0.087,0)	(0,0,0.083,0)	(0,0,0.238,0)
4	From +60 rot. of HCP 15	(0,0,0.032,0)	(0,0,0.083,0)	(0,0,0.238,0)
5	From -60 rot. of HCP 15	(0,0,0.032,0)	(0,0,0.083,0)	(0,0,0.238,0)
6	From +60 rot. of HCP 16	(0,0,0.051,0)	(0,0,0,0)	(0,0,0,0)
7	From -60 rot. of HCP 16	(0,0,0.051,0)	(0,0,0,0)	(0,0,0,0)
8	From +60 rot. of HCP 17	(0,0,0.051,0)	(0,0,0,0)	(0,0,0,0)
9	From -60 rot. of HCP 17	(0,0,0.051,0)	(0,0,0,0)	(0,0,0,0)
10	From +60 rot. of HCP 18	(0,0,0.048,0)	(0,0,0.083,0)	(0,0,0.012,0)
11	From -60 rot. of HCP 18	(0,0,0.048,0)	(0,0,0.083,0)	(0,0,0.012,0)
12	From +60 rot. of HCP 19	(0,0,0.048,0)	(0,0,0.083,0)	(0,0,0.012,0)
13	From -60 rot. of HCP 19	(0,0,0.048,0)	(0,0,0.083,0)	(0,0,0.012,0)
14		(0,0.12,0,0)	(0,0,0,0)	(0,0,0,0)
15		(0,0.12,0,0.40)	(0,0,0,0)	(0,0,0,0)
16		(0,0.26,0,0.15)	(0,0.5,0,0.5)	(0,0.5,0,0.5)
17		(0,0.26,0,0.32)	(0,0.5,0,0.5)	(0,0.5,0,0.5)
18		(0,0.12,0,0.09)	(0,0,0,0)	(0,0,0,0)
19		(0,0.12,0,0.04)	(0,0,0,0)	(0,0,0,0)

Figure 5.12 shows the results of Barker's shot 5 [102] with the current crystal plasticity model and with $\theta = 0.5$. A power law hardening model was used with a critical shear stress of 400 MPa and an exponent of 50. The EOS used for the volumetric response is the same as that used in the isotropic model (Table 5.1), and the load was applied in the $\langle 100 \rangle$ BCC direction. As can be seen in Figure 5.12 the velocity profiles are similar with the biggest difference in the late arrival of the elastic precursor which is a result of a BCC crystal having more compliance in the $\langle 100 \rangle$ direction than any other direction, hence a slower elastic wave speed [194].

In summary, the crystal plasticity formulation appears to satisfy some intuitive results, but has some issues such as not conserving volume on the HCP to BCC transformation. This could possibly be rationalized by grain boundaries and increased dislocations causing a residual volume change but 1 to 2 % volume change is likely too large for such an explanation. The empirical parameter θ might be a reasonable compromise, but more data is necessary to confirm its validity.

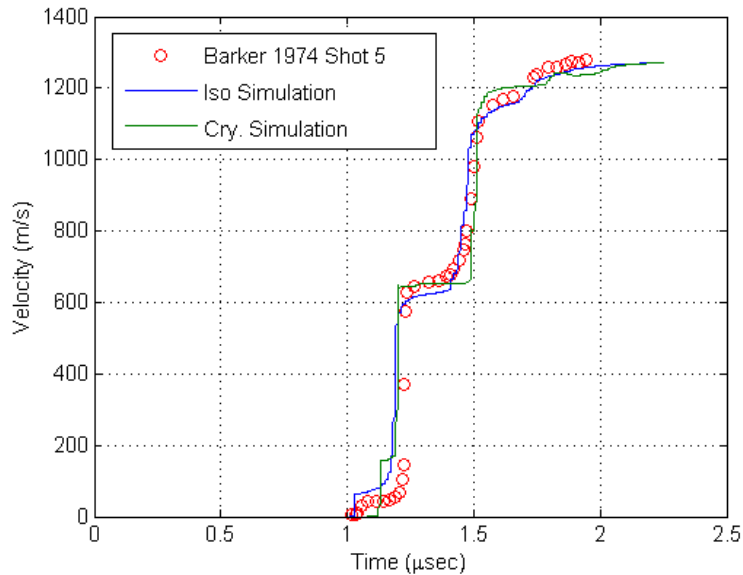


Figure 5.12: Barker shot 5 experimental data versus crystal based simulation and isotropic simulation (shock direction in $\langle 100 \rangle$ direction of reference BCC cell). Crystal and isotropic simulations use the same EOS for the volumetric response, but the crystal simulation uses a weakly strain rate dependent deviatoric model. Note that the elastic wave arrives later in the crystal based model, as expected, since the $\langle 100 \rangle$ direction is most compliant (i.e., for Fe $\sim 5380 < C_{long.} < \sim 6369$ m/s for [100] and [111] directions respectively).

5.3. Validation with 1-D Experiments

5.3.1. Copper

5.3.1.1. High Strain Rate

The high strain rate deviatoric behavior of the isotropic models can be calibrated and validated partly with experimental shock front profiles obtained from flat samples [104]. In uniaxial strain conditions it can be shown that a steady non vertical shock front is controlled by irreversible effects such as rate dependent plasticity [104] and heat transport [194,195]. For moderate shocks heat transport can be neglected and Molinari [104] showed that rate dependent plasticity explains the steady state shock front well and reproduces the experimentally observed Swegle-Grady one-fourth power law for steady state shock fronts,

i.e., that the stress jump at a well-established shock front is proportional to the maximum strain rate (or maximum plastic strain rate) to the one-fourth power [107, 104, 64,123]

$$\Delta\sigma_{11} \propto \left(\max(\dot{\gamma}_p)\right)^{1/4} \quad (5.14)$$

where $\dot{\gamma}_p$ is the effective plastic strain rate, and $\Delta\sigma_{11}$ is the stress jump in the shock direction. Figure 5.13 compares Eq. (5.14) with PTW simulation results for copper at impact pressures of 5.2, 10.9, and 20.0 GPa (impact velocities of 140, 280, and 480 m/s respectively).

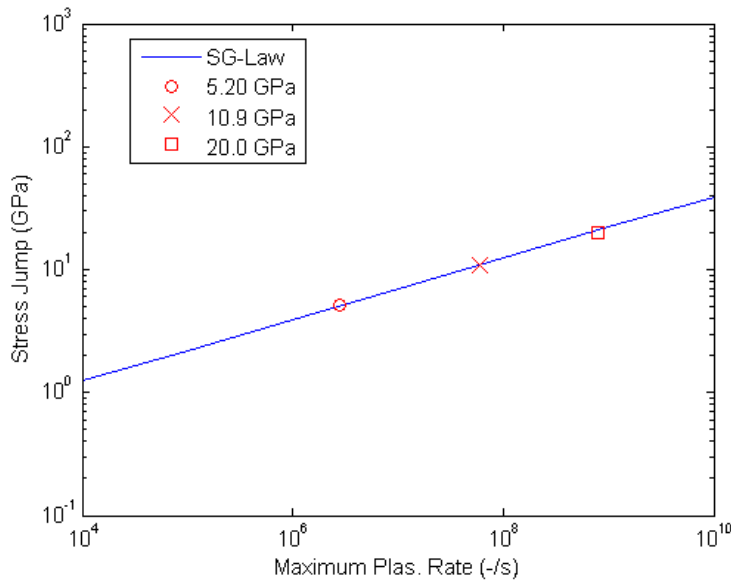


Figure 5.13: Swegle-Grady Law for Cu. Linear fit $\Delta\sigma = 0.124 \left(\max(\dot{\gamma}_p)\right)^{1/4}$ (GPa) and three simulation points (5.20, 10.9, and 20.0 GPa) for Copper using PTW strength law. Results are nearly identical to [64].

As can be seen in the figure the simulations agree well with the experimentally observed one-fourth power law. In these plots it is critical to make sure the sample is long enough that the plastic strain rate has reached a near steady-state value, which takes the longest for the weakest shock of 5.2 GPa and was about 1 mm. An analytical approximation for the

necessary sample thickness to develop a steady shock front is given in [104]. For stresses much more above 20 GPa the shock front is nearly vertical (as can be seen in the numerical “ringing” in the free surface plots of Figure 5.3) and the simulations deviate from the one-fourth power law due to artificial viscosity dominating the dissipative behavior. At the plastic rates in Figure 5.14 the shock front is in the phonon drag or transition region of the PTW law and the drag exponent β (which is 0.25), Eq. (4.9), dominates the flow stress behavior. Finally Figure 5.15 compares copper PTW simulations to experimental data [64,107].

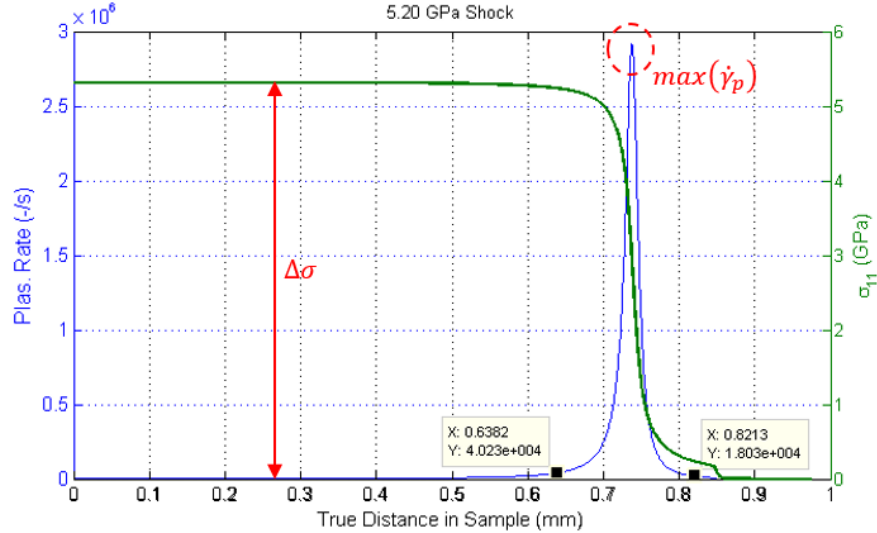


Figure 5.14: Swegle Grady axis definitions. Plastic strain rate and longitudinal stress in 1-D shock front for a 5.20 GPa shock. Note nearly all of shock front is in the region dominated by the phonon drag mechanism or transition region of the PTW strength law, since strain rates are $\sim > 10^4 \text{ s}^{-1}$. Figure also shows values (in red) used for the axes in Figure 5.13, i.e., the Swegle-Grady power law [107].

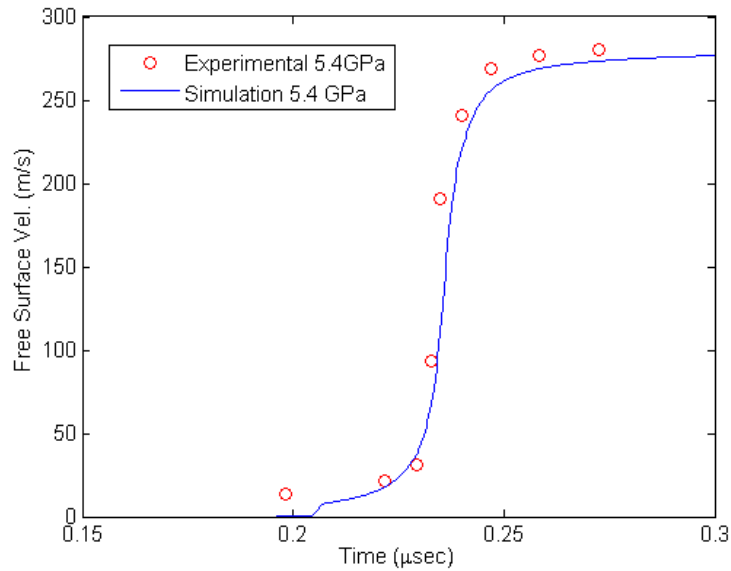


Figure 5.15: PTW simulation vs. experimental data. Comparison of [107] data to PTW strength law simulation for BC equivalent to 5.4 GPa and a sample thickness sufficient for a nearly steady shock front.

5.3.1.2. Low Strain Rate

To obtain low strain rate and initial yield properties the y_0 and y_1 parameters (see Table 5.2) were changed slightly from those given in Preston [67] to match the elastic precursor seen in our flat sample experiments. This is reasonable since our sample had some initial hardening while Preston’s parameters were for pure soft copper (ours were half-hard). Some of the hardening parameters that establish τ_s on the PTW law cannot be fitted to any of our experimental data since they control a regime outside our data (i.e., large plastic strains); therefore, we assumed Preston’s parameters are sufficient.

With these PTW parameters a temporal pressure boundary condition for the 5 ns laser pulse was created to match the free velocity signal in sample s25259. The temporal profile (ramp up 0 to 1 ns, hold 1 to 5 ns, ramp down 5 to 10 ns) was then considered a

constant and only the magnitude of the profile (peak hold pressure) changed with laser energy according to Eq. (5.15)

$$P_{peak} = K \left(\frac{I}{\lambda} \right)^{2/3} \text{ (GPa)} \quad (5.15)$$

which is taken from [196], with a laser wavelength of $\lambda = 523e - 9 \text{ m}$, a constant $K = 3.3e-5 \pm 5\% \text{ Pa}^{1/3}$ and a laser intensity I of $\frac{\text{Energy}}{\text{Area} \cdot \Delta t} \left(\frac{\text{W}}{\text{m}^2} \right)$ where here the area is 0.01 cm^2 and Δt is 5 ns , which gives similar results to [197]. This temporal pressure profile, laser to pressure transformation, and PTW parameters matched the majority of our flat sample data well as can be seen in Figure 5.16 to 5.18.

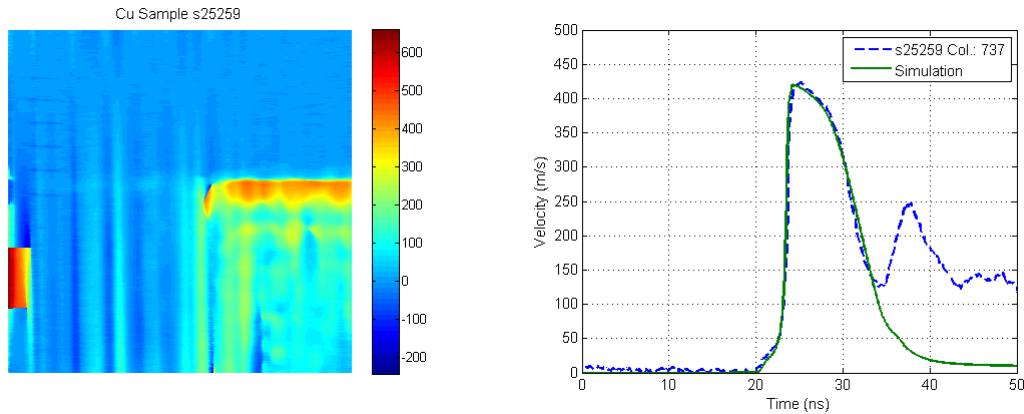


Figure 5.16: VISAR results for Cu flat sample s25259. (left) VISAR contour showing that peak velocity is about $400 \pm 5\%$ m/s (confirmed with lineouts). (right) PTW strength law where y_l and y_0 values were increased slightly relative to [Preston] to fit elastic precursor in the data. Simulation used a peak pressure BC of 9 to 10 GPa to fit data with a temporal profile of ramp up 0 to 1 ns, hold 1 to 5 ns, ramp down 5 to 10 ns. Sample thickness is 100 microns and laser energy was 13.0 joules. Simulations used a 0.5 micron mesh (no difference in velocity results seen below this, and shock front had ~ 10 nodes).

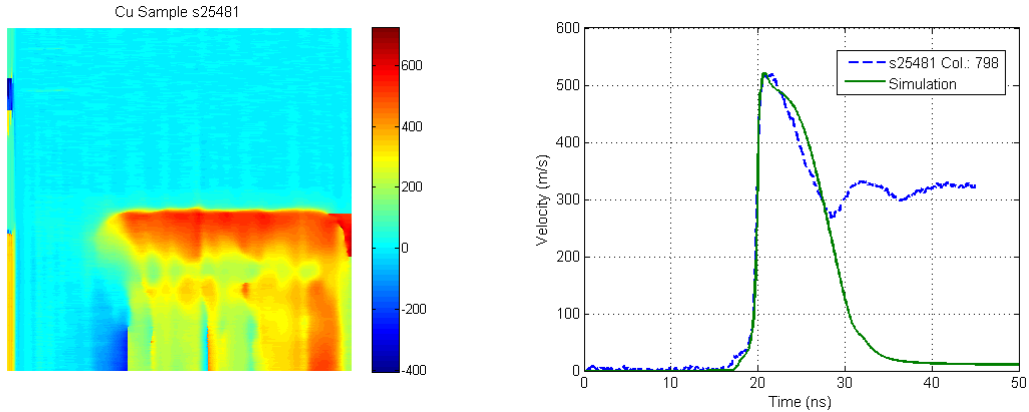


Figure 5.17: VISAR results for Cu flat sample s25481. (left) VISAR contour showing that peak velocity is about $500 \pm 5\%$ m/s (confirmed with lineouts). (right) Comparison of PTW simulation with lineout. Simulation used a peak pressure BC of 11 to 12 GPa to fit data with a temporal profile of ramp up 0 to 1 ns, hold 1 to 5 ns, ramp down 5 to 10 ns. Sample thickness is 86 microns and laser energy was 16.3 joules.

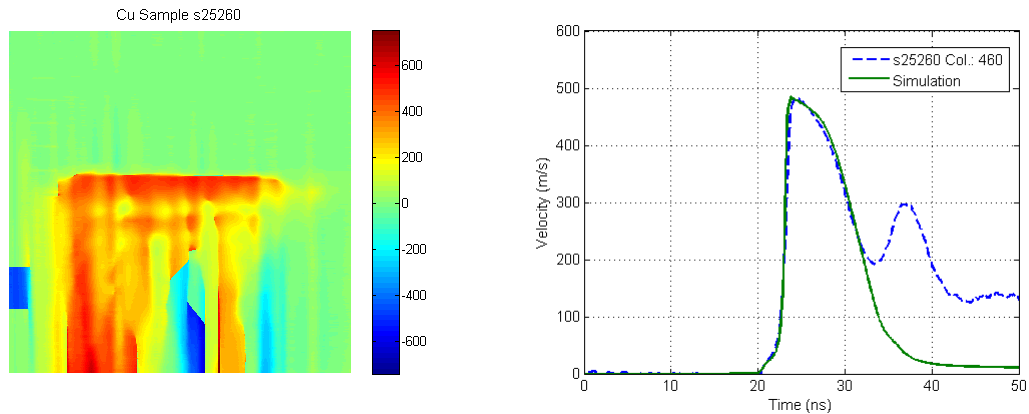


Figure 5.18: VISAR results for Cu flat sample s25260. (left) VISAR contour showing that peak velocity is about $500 \pm 5\%$ m/s (confirmed with lineouts). (right) Comparison of PTW simulation with lineout. Simulation used a peak pressure BC of 11 to 11.5 GPa to fit data with a temporal profile of ramp up 0 to 1 ns, hold 1 to 5 ns, ramp down 5 to 10 ns. Sample thickness is 100 microns and laser energy was 16.0 joules.

5.3.2. Iron

The PTW parameters for iron are more difficult to fit than copper primarily due to the large elastic deviatoric strength in compression and an apparent lack of elastic strength on unloading, which has been noticed by several other researchers [102]. The steady elastic

and plastic compression waves [102] shown in Figure 5.10 are fitted reasonably well with the parameters in Table 5.1 and Table 5.2 and are similar to the models given in [138,111,173,174,187]. A better fit to the compression waves given in Barkers data [102] can be obtained if the reference bulk modulus for the BCC phase is reduced by about 5% (i.e., to a value of 167.2 GPa) from the ambient pressure value of 176.6 GPa. With this change the first plastic wave shock (P1) front (i.e., low pressure phase) fits Barker's shock front data well and some of our flat sample data better also. The magnitude of the plastic precursor is at least twice as large in our flat sample data, when compared to Barkers data, ranging from about 1 to 2 GPa, as shown in Figure 5.19, this apparent increase or variable elastic strength has been noticed by others and has been attributed to time dependent phenomena (e.g., dislocation nucleation) [64,5] that the PTW model cannot capture.

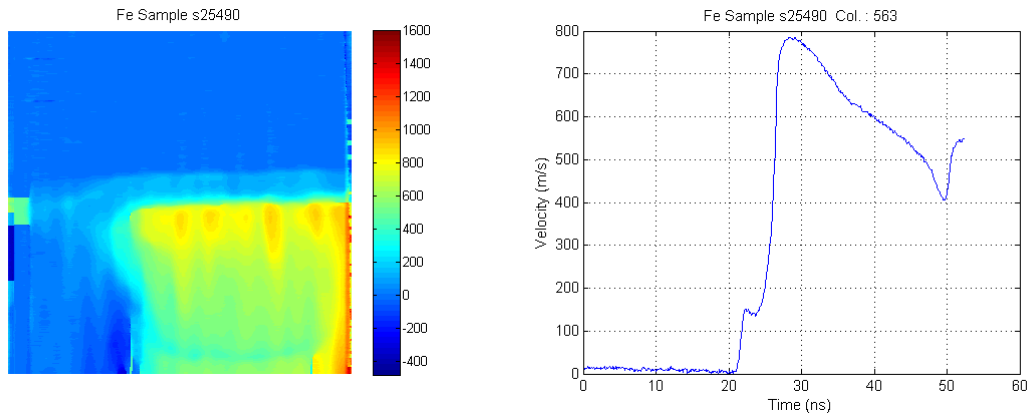


Figure 5.19: VISAR results for iron sample s25490 (132 microns thick, 85.9 J shot). Sample shows an elastic overshoot (~1.7 GPa), and a lack of a two plastic wave structure expected from phase transformation.

Barker's shock release wave data (e.g., shot 15) shows a lack of an elastic release, a feature that our flat sample data also seemed to possess. Figure 5.20 compares Barkers Shot 15 [102] to the PTW model calibrated for his P1 data (i.e., PTW parameters from [131] to match smaller elastic precursor, and 167.2 GPa reference bulk modulus).

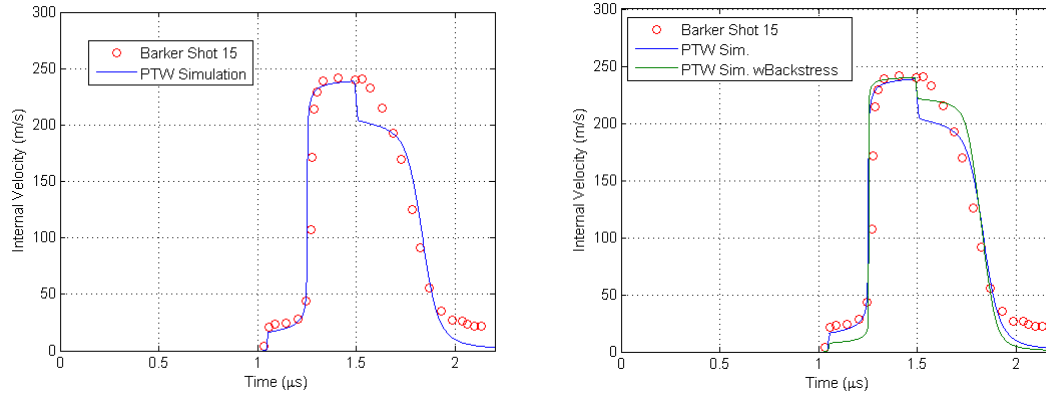


Figure 5.20: Iron simulation results vs experimental internal particle velocity of Barker Shot 15 (used an \sim equal impedance sapphire window) [102]. (left) Experimental data vs Simulation using EOS parameters from Table 5.1, but with the reference bulk modulus of Phase 1 reduced to 167.2 GPa and PTW parameters from [131]. (right) same comparison but with reduced thermal activation PTW model parameters where s_0 , s_{inf} , y_0 , y_{inf} , and y_1 values of [131] reduced by half (a loss of \sim 200 MPa in elastic precursor) and 75 MPa of backstress via Armstrong-Frederick [199] kinematic hardening was added to the model. Backstress model matches release slightly better but does a poorer job on elastic precursor, this is because kinematic hardening occurs in the plastic wave not the elastic precursor (i.e., elastic precursor is set by initial yield point). Dislocation models of [64,63] may do a better job of matching elastic precursor and having a weak elastic release in combination with a backstress model.

The experimental release wave suggests a lack of an elastic release, i.e., that the release wave is entirely plastic. Barker was able to fit a simulation to Shot 15 but he used an ad hoc model that used a decreasing yield strength, backstress, and increasing Poisson's ratio with increasing pressure, and no rate dependence. Figure 5.20 shows the results of adding backstress to the PTW model as suggested in [198], a slightly better fit is obtained on the release but a poorer elastic precursor fit, this is due to kinematic hardening occurring in the plastic wave (P1) and not the elastic precursor, so no amount of kinematic hardening would fix this. Our flat sample data appeared to share this same fully plastic release behavior; however, in our data it is difficult to tell due to uncertainties in the pressure boundary condition produced by the laser. Figure 5.21 shows VISAR data for sample

s25261, which was loaded below the transformation pressure. Simulations for this sample show an elastic release, but the test data appears not to.

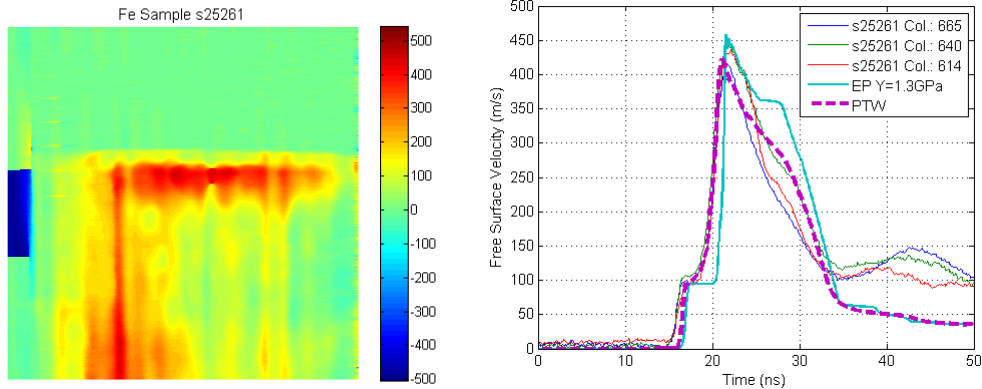


Figure 5.21: Simulation and experimental data for iron sample s25261 (100 microns thick, 20 J shot ~ 12 GPa) to PTW and Elastic-Plastic (EP) simulation. PTW simulation used parameters from Table 5.2, while EP simulation uses linear U_s-U_P EOS from [102] with a EP yield of 1.3 GPa. Both simulations (and all other iron simulations) use the same BC temporal profile as copper and a peak pressure of 11.5 GPa. A K of $3.1e-5 \pm 5\% Pa^{1/3}$ was used for all the iron simulations. Notice that the PTW model shows a pronounced elastic release, and the EP more so, while the data shows little to no elastic release as was also found in Barkers data [102].

The second plastic wave (P2) is where phase transformation occurs as well as a large increase in pressure; therefore, two processes form the plastic wave shape, a good review of the processes in the steady profile shape is given in [101, p.210]. Wallace [20] assumed this shape was dominated by the phase transformation kinetics and proposed a transition time constant of about 30 ns for a P2 peak pressure of ~ 20 GPa, which would increase slightly with a decrease in the P2 peak pressure. Later Jensen [112] used a front surface VISAR setup where an iron sample impacts a sapphire window (similar impedance) so that the phase transformation, and therefore kinetics, can be monitored directly rather than indirectly with free surface measurements of a thick iron sample as in Barkers experiments. Jensen found that at shock pressures near ~ 20 GPa the phase transformation time constant is about 1 ns or less at the monitored impact boundary, and

longer (in a nonlinear relationship) for impact pressures below this. This fast rate of transformation would suggest the P2 wave shape (i.e., rise time) is influenced by rate dependent plasticity (at least for pressure near and above 20 GPa) as well as transformation kinetics. Our samples did not show clear signatures of a phase transformation at first glance, but interestingly many of the simulations using the same copper BC temporal profile (i.e., 1 ns ramp up, hold for 4 ns, ramp down for 5 ns) showed phase transformations and matched the experimental free velocity measurements reasonably well. Figure 5.22 and Figure 5.23 show the VISAR results for flat samples s25492 (92 microns thick, 109.5 J) and s25283 (100 microns thick, 119 J), where a pressure BC of 36.5 GPa and 40.0 GPa was used which corresponds to $K = 3.1e-5 \pm 5\% Pa^{1/3}$ (this constant was used for all the iron simulations).

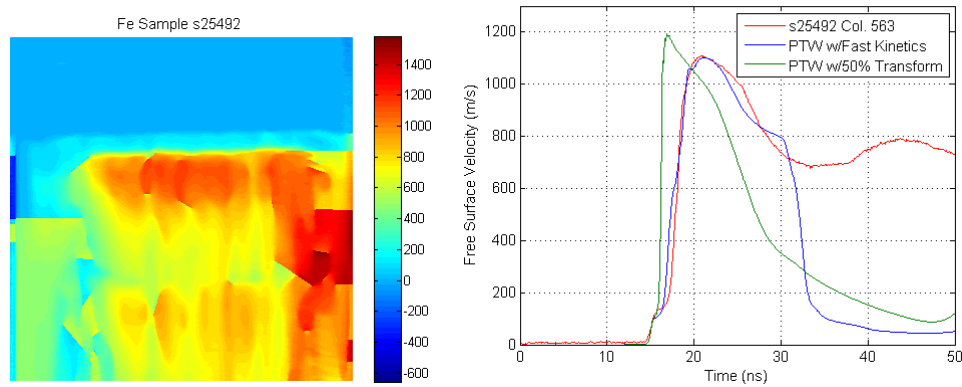


Figure 5.22: Simulation and experimental data for iron sample s25492 (92 microns thick, 109.5 J shot) with simulations where phase transformation kinetics are varied. Fast kinetics simulation occurs quickly so that all material points, except near the free surface, experience 100 % transformation to the HCP structure. Slow kinetics model only allows about a 50% transformation, for the same material points, to the HCP structure. Simulations suggest a full phase transformation may have occurred. Material parameters used are given in Table 5.1 and Table 5.2, except that the slow kinetics uses a τ of $800e-9 s^{-1}$. Where simulation and data diverge may be related to spall.

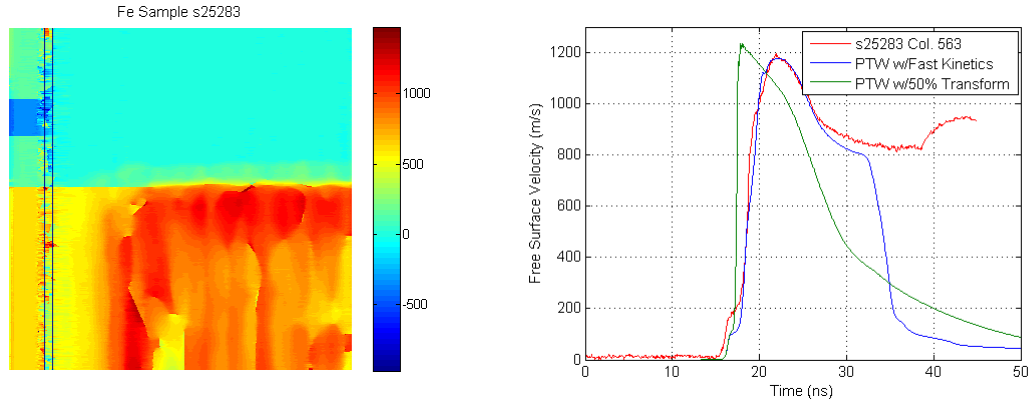


Figure 5.23: Simulation and experimental data for iron sample s25283 (100 microns thick, 119 J shot) with simulations where phase transformation kinetics are varied. Fast kinetics simulation occurs quickly so that all materials points, except near free surface, experience 100 % transformation to HCP structure. Slow kinetics model only allows about a 50% transformation, for the same material points, to the HCP structure. Simulations suggest a full phase transformation may have occurred. Material parameters used are given in Table 5.1 and Table 5.2, except that the slow kinetics uses a τ of $800e-9 \text{ s}^{-1}$. Where simulation and data diverge may be related to a sharp spall caused by a rarefaction shock [101 p. 344, 186 p. 757]; a rarefaction shock, as shown in the right figure, is seen in the simulation.

The ‘fast kinetics’ simulation uses the parameters in Table 5.1, while the ‘50% transformation’ simulation uses the same parameters but with τ increased significantly to $800e-9 \text{ s}^{-1}$ which resulted in about a 50% transformation of the BCC phase to HCP (i.e., no material point completely transformed), this would create an effective time constant closer to what Wallace found in Barkers data. What is interesting in these two figures is that the simulations suggest a complete phase transformation did occur in these two samples, since the slow kinetics simulation is significantly different than the VISAR data. It is difficult to say with certainty that the phase transformation occurred since there is some ambiguity in the pressure BC applied in the simulation and the suspect elastic release issue (although at higher pressures this should be less of an issue), but Figure 5.22 and Figure 5.23 do provide

compelling evidence. This data should be revisited once a more validated strength and transformation kinetics model is available.

5.4. Validation with 2-D Experiments

In this section we look at the Transient Imaging Displacement Interferometry (TIDI) data collected in the rippled samples. In these tests TIDI frame captures of the initially flat surface were ‘time-stamped’ to continuous Line VISAR data of the same surface so that the time of the TIDI frame was known in relation to shock breakout (via the Line VISAR record). Three TIDI images were made of each rippled, a static image and two dynamic images (images taken after the rippled shock breaks out at the initially flat free surface). The static image was used to remove bias from the dynamic images.

Unfortunately most of the TIDI images were taken after signs of spall making it difficult to validate simulations to the data. However, for the samples that had TIDI data before spall the simulations typically matched up well. Figure 5.24 compares the first TIDI frame of Samples s25288 and s25289 to a PTW simulation using the PTW parameters in Table 5.2 and a Mie-Grüneisen EOS ($\rho_0 = 8960 \frac{kg}{m^3}$, $G = 51.8 GPa$, $C_0 = 3940 \frac{m}{s}$, $s = 1.49$, $\gamma = 2.0$), with the same temporal BC as previous simulations and a peak pressure of 12.0 GPa. These two samples had about the same geometry (120 and 118 μm thickness respectively, 6 μm amplitude, and 150 μm wavelength) and similar laser energies, 19.3 and 20.25 J, respectively. An interesting observation is that not only does the simulation match the TIDI points well in Figure 5.24a but the shape of the ripple agrees well as shown in Figure 5.24e-g, where a smaller ‘higher harmonic’ ripple appears due to interactions with the release wave. Spall effects are unlikely affecting the data in these TIDI frames since

they were taken 6.2 to 7 ns, respectively, after shock breakout and the flat samples showed no signs of spall in this time range (see Figures 5.16-5.18).

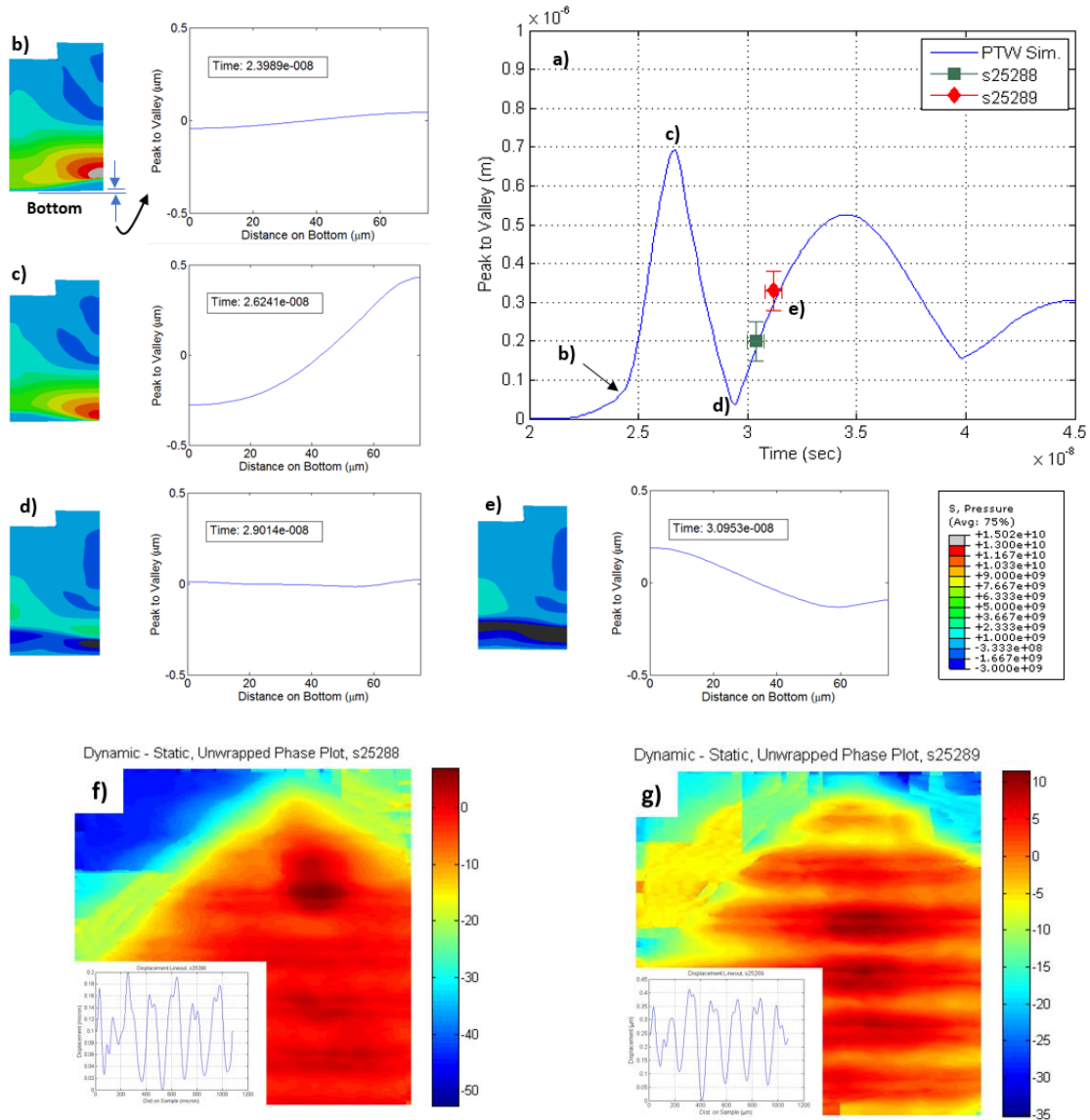


Figure 5.24: Evolution of flat free surface as rippled shock front breaks out. a) First dynamic TIDI frame for Cu samples s25288 and s25289, and PTW simulation. b-e) Pressure contours and displacement of free surface from PTW simulations. f,g) TIDI contour plots for samples s25288 and s25289. Note how the TIDI data and PTW simulation agree well as shown in a), and also that the smaller ‘higher harmonic’ ripple seen in f) and g) also show up in the PTW simulations in e) (simulations show same higher harmonic at other TIDI frame also). FEM contours are of pressure, and peak slightly near 14 GPa and are negative (tension) where black.

Figure 5.25 shows plastic strain rate and shear stress σ_{12} near point d) in Figure 5.24. The shear stress is shown because it gives an estimate of the deviatoric stresses due to the perturbation growth at the free surface rather than the deviatoric stresses due to the release waves.

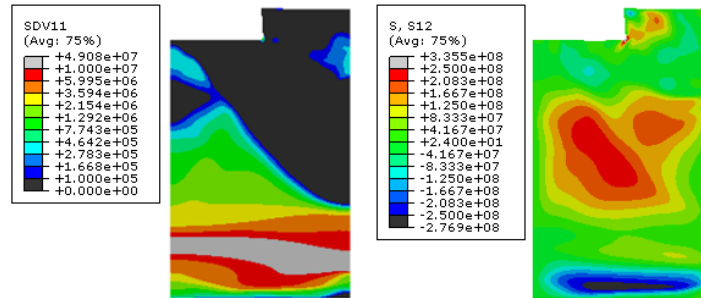


Figure 5.25: FEM contours during perturbation breakout. (left) Plastic strain rate and (right) shear stresses near points d) and e) in Figure 5.24. Large (grey and red) strain rates above bottom surface are due to release waves; however, rates near the bottom free surface are due to perturbation growth and are around $1e6 \text{ s}^{-1}$. The effective deviatoric stress due to perturbation deformation is around 500 MPa (i.e., $\sigma_y = 500 \cong s_{12}\sqrt{3}$ MPa).

As can be seen in Figure 5.25 the plastic strain rates near the bottom free surface are around $1e6 \text{ s}^{-1}$ (large rates above that are from release waves) while the shear stresses are near 280 MPa (or equivalently an effective yield stress of about 500 MPa, i.e., $\sigma_y = 280\sqrt{3}$ MPa).

6. DISCUSSION

This section uses the material models from the previous sections to draw some conclusions about the effect strength and phase transformation have on hydrodynamic instabilities discussed in the literature review. We also compare results from modern strength models (e.g., PTW) to simple elastic-plastic and traditional linear viscous deviatoric behaviors that have often been used in the literature in conjunction with a hydrodynamic EOS as a simple way to account for effect of shear stresses under loading conditions leading to high triaxialities [132].

6.1. Shock Front Perturbations

6.1.1. Single Phase Materials

Shock front perturbations, as discussed in Section 1.4. , form as a shock passes through a perturbed interface between dissimilar materials or through inhomogeneities (e.g., density fluctuations, material anisotropy) in the material, or similarly if a perturbed loading launches a perturbed shock into a material. An understanding of how material properties affect the shock front evolution is important in applications such as inertial confinement fusion (ICF) where perturbations at the ablator surface can feed-in, via the perturbed shock fronts, to inner layers seeding RT instabilities. Additionally, as will be shown next, shock front evolution experiments can be used as a tool for validating deviatoric strength models for materials in the post shock state, i.e., behind the shock front.

Figure 6.1 compares the hydrodynamic solutions (no deviatoric stress) obtained with the analytical solution derived in Section 4.4. , and ABAQUS numerical solutions (all used a mesh of 1/10 the initial perturbation amplitude or less, larger meshes would

cause plot phase shifts). A constant velocity in the longitudinal direction is applied on the perturbed surface as the boundary condition, no lateral movement is allowed simulating a rigid piston boundary condition. The simulations and the analytical form use the same EOS material parameters ($C_0 = 3940 \frac{m}{s}$, $s = 1.49$, $\gamma = 2.0$, $\rho_0 = 8960 \frac{kg}{m^3}$). In the numerical solution the shock front perturbation is determined by finding the spatial difference between the leading and trailing front at the same particle velocity (via a Python and Matlab script), chosen here as twice the elastic precursor seen in the experiments (~ 50 m/s); however the evolution is not sensitive to this choice (e.g., a threshold of three times the elastic precursor velocity would produce the same results).

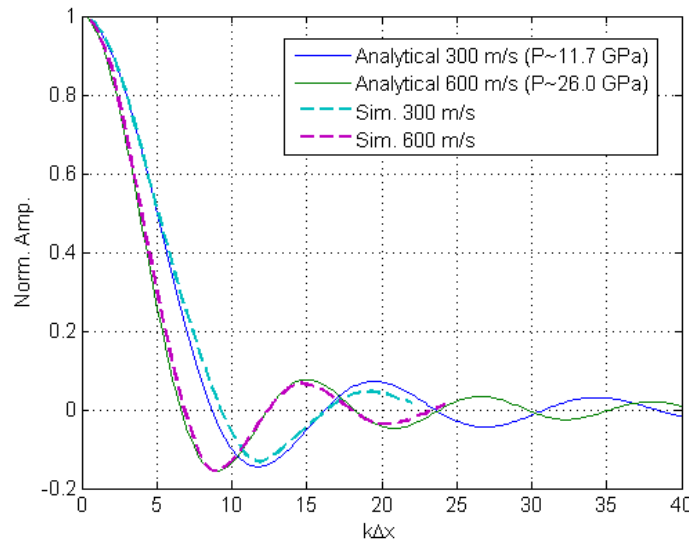


Figure 6.1: Analytical perturbation shock front evolution under pure hydrodynamic behavior for Cu versus numerical simulation for an initial amplitude of $6 \mu\text{m}$ and wavelength of $150 \mu\text{m}$, with a BC of 300 and 600 m/s (or equally a pressure of 11.7 and 26.0 GPa). The analytical solution was derived in Section 4.4. . In general, numerical simulations matched analytical simulations well provided the amplitude to wavelength ratio was less than about 0.05 which is an assumption of the analytical solution (i.e., small perturbations so that linearization is applicable).

In Figure 6.1 the initial perturbation to wavelength is kept below 0.05 to assure we remain in a pseudo linear regime where the analytical prediction should be valid. Figure 6.1 also shows that increasing the driving pressure decreases the time to shock front inversion although it is not a linear relationship. In this pseudo linear regime the hydrodynamic solutions (simulations and analytically) evolve independently of perturbation wavelength and amplitude, and are only affected by the material EOS and the driving pressure at the boundary condition.

Next we look simulations where deviatoric strength is added and geometry changes are made. Figure 6.2 and Figure 6.3 compares simulations for a 600 m/s and 300 m/s shock using the Cu PTW material model from Section 5.1.2. Table 5.2 and an elastic-plastic (EP) model. Figure 6.4 shows a similar plot but with aluminum ($C_0 = 5452 \frac{m}{s}$, $s = 1.26$, $\gamma = 2.14$, $\rho_0 = 2712 \frac{kg}{m^3}$).

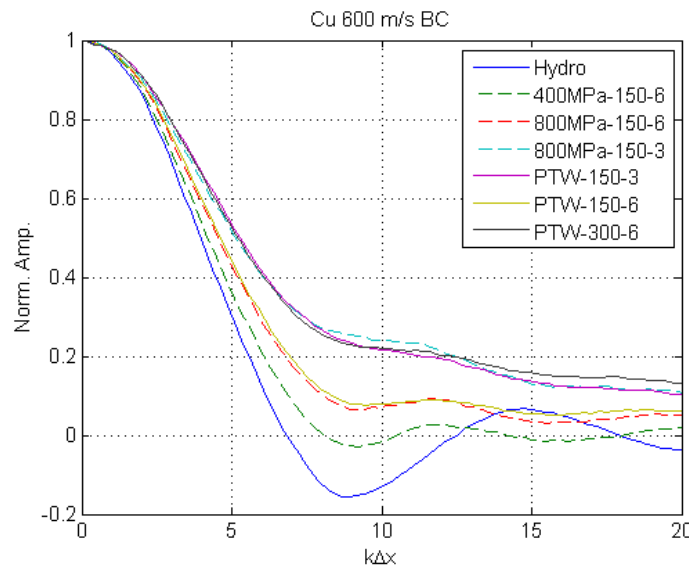


Figure 6.2: Effect of strength on shock front perturbation evolution in Cu for a 600 m/s ($P=26.0$ GPa) boundary condition. Legend shows elastic-plastic strength of model (or PTW) followed by initial perturbation wavelength and initial amplitude. PTW model shows an effective yield stress of about 800 MPa.

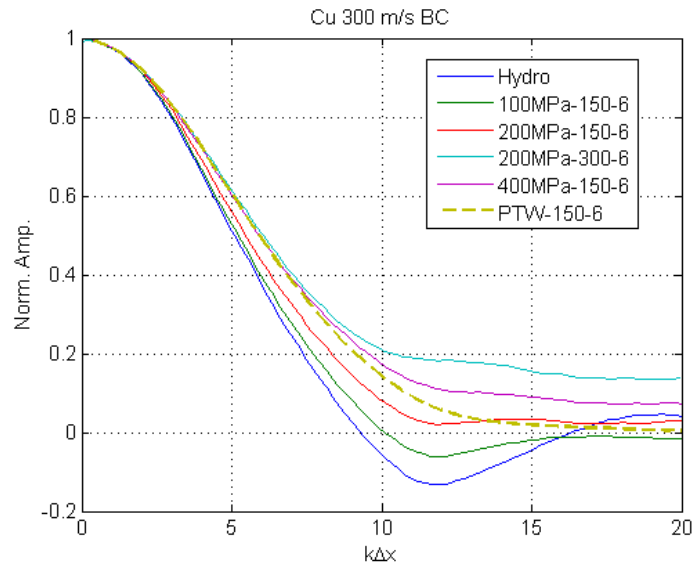


Figure 6.3: Cu shock perturbation evolution for a 300 m/s boundary condition ($P=11.7$ GPa). Note in this case the PTW model has an effective strength of ~ 400 MPa behind the shock front initially, but as the pressure perturbations decrease, and hence strain rates, the PTW flow stress decreases.

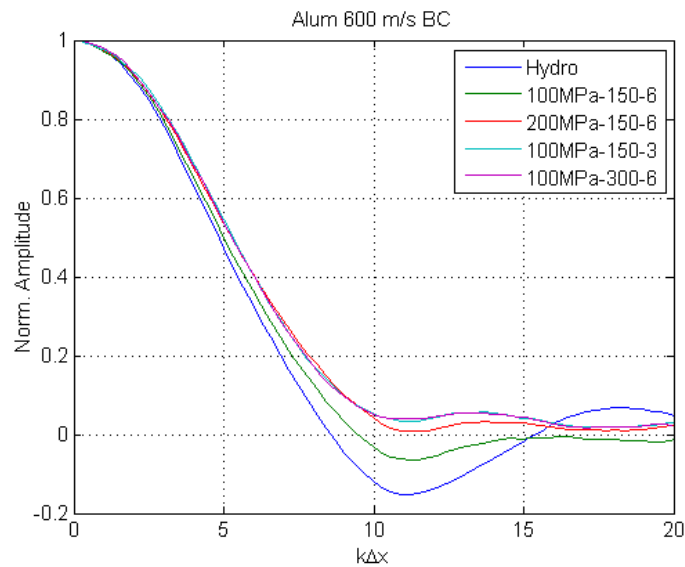


Figure 6.4: Aluminum shock perturbation evolution for a 600 m/s ($P=10.1$ GPa) boundary condition. Legend shows elastic-plastic strength followed by initial perturbation wavelength and initial amplitude.

What can be seen in these figures is that the normalized shock front amplitude $A \equiv \xi(t)/\xi_0$ in the models with elastic-plastic strength generally differ from the models without strength (the hydrodynamics models) by an amount that scales with

$$(A_{EP} - A_{hydro}) \propto \lambda Y / \xi_0 \quad (6.1)$$

where A_{EP} and A_{hydro} are the normalized shock front amplitudes of the models with and without strength, λ is the perturbation wavelength, Y is the yield strength of the material, and ξ_0 is the initial perturbation shock front amplitude. The PTW models also scale as

$$(A_{PTW} - A_{hydro}) \propto \lambda / \xi_0 \quad (6.2)$$

and generally as the PTW strength is increased (e.g., increased material parameters or increased strain rate and/or pressure) the difference becomes larger as in Eq. (6.1).

The general behavior in Equations (6.1) and (6.2) is predicted by the analytical model, with strength, see Section 4.4. , as can be seen in Figure 6.5.

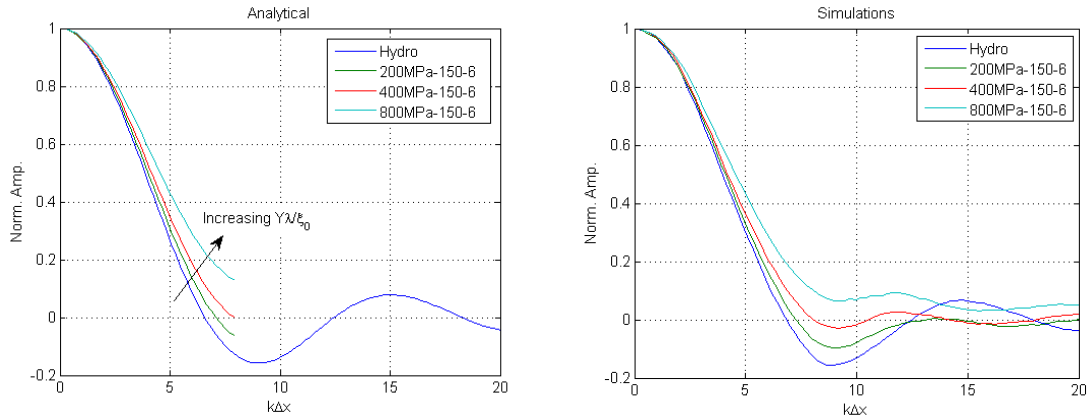


Figure 6.5: Analytical shock perturbation evolution with strength versus numerical simulations for a Cu material and a 600 m/s (~26 GPa pressure) boundary condition. Analytical simulations with strength are accurate up to ~shock inversion at which point material near shock front is no longer yielding and deviatoric stresses eventually change signs. Analytical and simulations solutions with strength differ from the hydrodynamic solution by an amount that scales with yield strength times perturbation wavelength over initial perturbation amplitude (i.e., $Y\lambda/\xi_0$) when plotted on the normalized distance axis (distance shock has traveled in the material Δx multiplied by wavenumber k).

The development of the analytical model was based on the observation that before shock front perturbation inversion the material is yielding approximately in a constant manner due to the pressure perturbations near the shock front, this can be seen in Figure 6.6. Figure 6.6 shows the deviatoric stresses alternate with a wavenumber of $k = 2\pi/\lambda$ and an average amplitude proportional to $\frac{Y}{\sqrt{3}}$ (i.e., $s_{yx} \propto \frac{Y}{\sqrt{3}} \sin(kx)$, $s_{xx} \propto \frac{Y}{\sqrt{3}} \cos(kx)$, $s_{yy} \propto \frac{-Y}{\sqrt{3}} \cos(kx)$), so that the gradients that enter the momentum equation near the shock front have an effective constant amplitude term proportional to $\frac{Yk}{\sqrt{3}}$ and constant sign. The s_{yy} and s_{yx} terms have nearly no deviatoric gradient in the shock direction (y-direction) since they are saturated. Near shock front inversion however, the pressure perturbations become smaller, yielding near the shock front ceases, and the problem becomes elastic. The analytical solution is accurate up to shock front inversion, after which the assumptions as discussed above in the analytical solution with strength are no longer reasonable. Verification with simulations show the scaling factor in Eq. (6.1) holds if the approximate limits are met

$$\frac{\xi_0}{\lambda} < \sim 0.05 \quad (6.3)$$

$$\frac{P\xi_0}{\lambda} > \sim Y \quad (6.4)$$

where P is the nominal shock pressure (e.g., $P = \rho_0 U_p U_s$). Equation (6.3) is a geometry requirement that the perturbations are small in comparison to the wavelength so that second order effects can be neglected, and Eq. (6.4) reflects that the pressure perturbations need to be large enough that the material is yielding for most of the shock front evolution up to

shock front inversion. Outside these limits the scaling factor $\lambda Y/\xi_0$ (Eq. (6.1)) typically holds but is not as accurate.

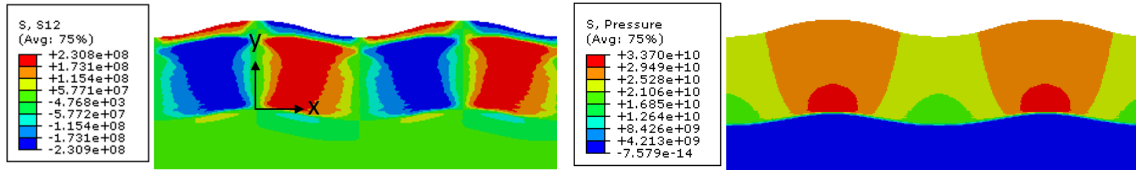


Figure 6.6: Stress distribution behind perturbed shock front in Cu for a 600 m/s (~ 26 GPa pressure) boundary condition, and a yield stress of 400 MPa. (left) Shear stresses, s_{xy} , (and similarly deviatoric stress s_{xx} and) are periodic with respect to the horizontal (lateral) coordinate with an amplitude proportional to $\frac{Y}{\sqrt{3}}$. Near the shock front, before inversion, the spatial deviatoric gradient near the shock front is approximately constant with an amplitude proportional to $\frac{Yk}{\sqrt{3}}$ which enters the momentum equation (i.e., Newtons law). (right) Alternating pressure perturbations near the shock front drive the deviatoric stresses.

Finally, Figure 6.7 shows FEM contours of plastic strain rate, von Mises stress, and cumulative plastic strain behind the perturbed shock front at a $k\Delta x$ of ~ 5 for the PTW strength model. As can be seen in these contours the average (or effective) yield strength behind the shock front matches the value predicted by the perturbation evolution simulations.

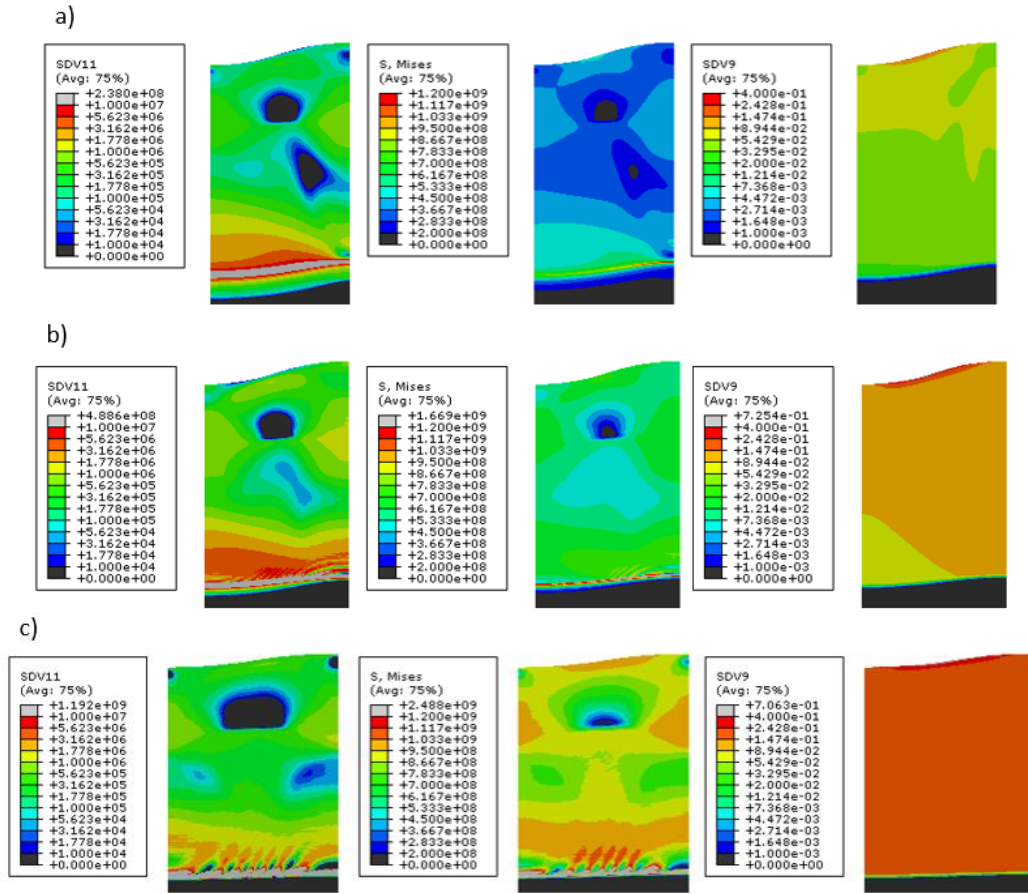


Figure 6.7: Simulation FEM contour results for perturbed shock front. Plastic strain rate, Von Mises, and plastic strain contours at a $k\lambda x$ of ~ 5 for the PTW simulations. a) V300-150-6 (BC velocity-wavelength-amplitude), b) V600-150-6, and c) V1175-150-3.

6.1.2. Materials with Phase Transformation

Intuitively a material that undergoes a phase transformation should not behave any differently, in regards to strength effects on shock front perturbation evolution, provided the high pressure phase is overdriven such that a single shock forms. Figure 6.8 shows the results from a series of iron simulations for a boundary condition of 1000 m/s (43.2 GPa pressure), and shows that the general behavior (i.e., Eq. (6.1) and (6.2)) observed in the single phase material holds. Figure 6.8 also shows that Eq. (6.1) holds only qualitatively

for the 3000 MPa Elastic-Plastic (EP) simulation since a Y of 3.0 GPa violates Eq. (6.4)

(i.e., $\frac{P\xi_0}{\lambda} = 1.73 \not\approx 3.0 \text{ GPa}$).

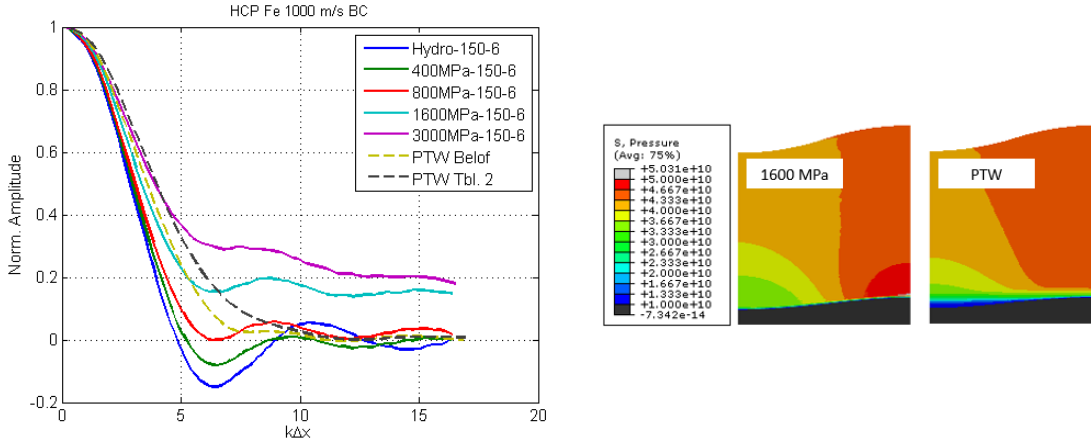


Figure 6.8: Shock front evolution in HCP iron. (left) Shock front evolution simulations for a 1000 m/s BC (e.g., a shock of ~ 43.2 GPa). Elastic-Plastic (EP) materials are compared to PTW material using parameters from Table 5.2. These parameters are essentially the thermal activation region of [131] shifted up by a factor of 1.75. Note how ‘PTW Tbl. 2’ fits the 3000 MPa curve well while ‘PTW Belof’ fits the 1600 MPa curve well, where $1.75 \times 1600 \approx 3000$ MPa. The 3000 MPa simulation violates Eq. (6.4) so the relation given in Eq. (1) holds only qualitatively. (right) Comparison of pressure perturbations in EP 1600 MPa simulation and ‘PTW Belof’ simulation at $k\Delta x \approx 6$ where the shock front evolution curves start to deviate as a result of smaller pressure perturbations in the PTW model and hence smaller deviatoric strain rate and stresses.

The deviation of the PTW curves from the EP curves is a result of a drop in pressure perturbations in the former, resulting in a lack of stress gradients to drive the deviatoric stresses. For this pressure, similar to the Cu curves in Figure 6.3, the shock front gets affected by the relatively strong deviatoric stresses and rate dependence, causing it to deviate from the EP behavior which in theory does not affect the shock front (i.e., no rate dependence). The fact that the high pressure phase dominates the shock front evolution makes it a good experimental setup candidate for characterizing the deviatoric behavior of materials with high pressure phases. Traditional shock front rise times (i.e., shock front

shapes) are not good candidates for this because phase transformation kinetics play a large role in the plastic wave shape, making it difficult to separate the two effects. In the shock front perturbation evolution the phase transformation occurs in the plastic wave (or equally the BC of the analytical solution) which does not have much of an effect on the perturbation evolution provided the phase transformation kinetics are fast, which for a overdriven shock they are.

There is an interesting feature, however, of materials that have a phase transformation such as iron in comparison to a typical single phase metal EOS due the relatively low high pressure phase shock velocity to sound speed ratio present in materials with a negative volume change in transformation. Neglecting strength for a moment the shock front perturbation evolution curve oscillates with a frequency of approximately [88]

$$\begin{aligned} \text{approximate shock perturbation oscillation freq.} &= kv\mu \text{ (units of } s^{-1}\text{)} \\ \text{or equally a period of} &= \frac{2\pi}{kv\mu} \text{ (units of } s\text{)} \end{aligned} \quad (6.5)$$

where $v = U_s - U_p$ and

$$\mu = \sqrt{\frac{1 - \left(\frac{v}{c_s}\right)^2}{\left(\frac{v}{c_s}\right)^2}} \quad (6.6)$$

where c_s is the sound velocity behind the shock front. Equation (6.5) shows the intuitive result that for weak shocks the oscillation period approaches zero (i.e., no shock inversion), since $\frac{v}{c_s} \rightarrow 1$ for weak shocks. For strong shocks the oscillation frequency approaches infinity (i.e., rapid shock front inversion), since $\frac{v}{c_s} \rightarrow 0$ for strong shocks; however, this limit is not realistically approached (e.g., for HCP iron $\frac{v}{c_s}$ at 0.62 and 0.50 corresponds to a pressure of 116 and 354 GPa respectively). To approach shock front inversion as fast as

possible (for a given v), which could be helpful to limit feed-in perturbations that seed damaging RT instabilities in applications such as ICF [200,38], a beneficial characteristic of the material EOS is for it to have as small a $\frac{v}{c_s}$ ratio as possible in the domain that the EOS is valid [135]. Two approaches to this come to mind. The first is a shallow P - v Hugoniot, since the shock speed is proportional to the Rayleigh line and the sound speed for a metal can be approximated as the tangent to the Hugoniot (or see Eq. (4.150)), see Figure 6.9.

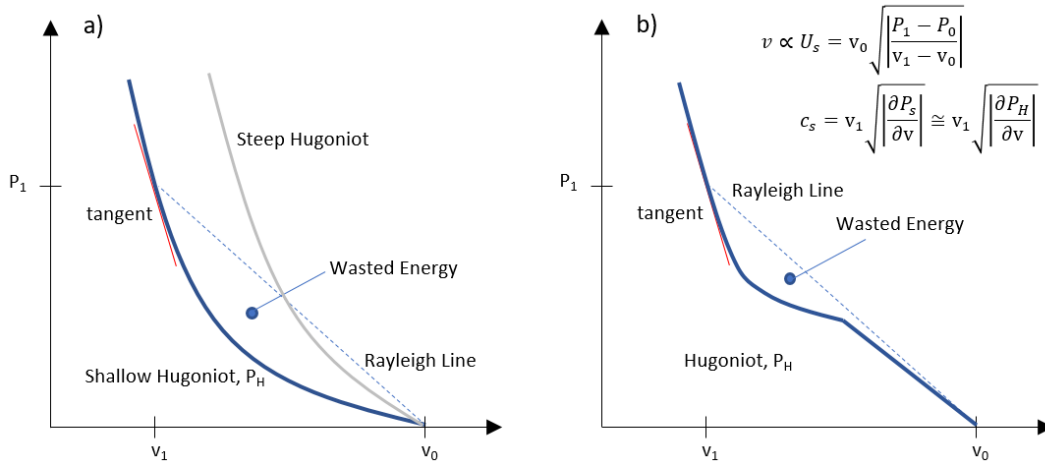


Figure 6.9: P - v Hugoniot comparison. a) A shallow P - v Hugoniot and has a small v/c_s ratio but wastes a significant amount of energy. b) P - v Hugoniot that contains a phase transformation has the same v/c_s ratio but converts less energy to heat (same total energy, but part of the energy is stored used for the phase transformation). A better calculation for the compressed sound speed is given in Eq. (4.150) where the isentrope is calculated exactly, the Hugoniot tangent approximation is for illustrative purposes.

However, shallow P - v Hugoniots produce a large amount of heat which may or may not be beneficial. Typically for minimizing instabilities this is not good since heat tends to weaken strength properties that limit instability growth. The second way to obtain a small $\frac{v}{c_s}$ ratio is with a phase change. In this case the same $\frac{v}{c_s}$ ratio can be obtained but not as much heat is generated on compression since the area below the Rayleigh line and above

the P - v Hugoniot is smaller as shown graphically in Figure 6.9 (same amount of work, but energy is stored used for the phase transformation instead of heat). Additionally there may be materials with a large volume collapse and a steep Hugoniot in the second phase which would be ideal to minimizing the $\frac{v}{c_s}$ ratio.

A draw back of a rapid path to inversion is large perturbation velocities, that can lead to growth of feed-in perturbations (see Section 1.2.5.). However, if a material has even a small amount of strength these perturbation velocities should dampen out quickly. Figure 6.10 shows the analytical shock front perturbation for BCC and HCP iron at a Pressure of about 45 GPa (1000 m/s BC) with no strength.

Figure 6.10 shows the k normalized oscillation wavelength versus pressure which may be relevant for some applications (e.g., ICF), where, notice, a small oscillation wavelength implies the shock front perturbation dies off close to the surface of the applied pressure/velocity boundary. The oscillation wavelength on the normalized $kU_s t = k\Delta x$ axis is given by

$$\text{approximate shock perturbation oscillation wavelength (norm. by } k) = \frac{U_s 2\pi}{v\mu} \text{ (units -)} \quad (6.7)$$

so that the general conclusions from the oscillation frequency still apply, i.e., a small $\frac{v}{c_s}$ ratio leads to the shock front perturbations decaying sooner – closer to the shock origin surface which in most cases is ideal.

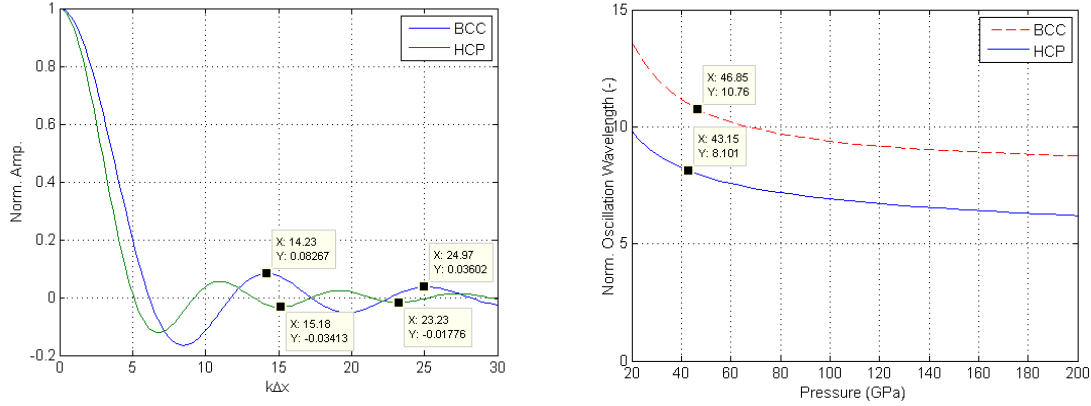


Figure 6.10: Effect of fast relief waves. (left) Shock front perturbation plots for BCC (low pressure) and HCP (high pressure) iron at the same pressure of 45 GPa. BCC is not stable at this pressure so figure is only illustrative. Plot shows the effect of a steep P-v Hugoniot (BCC) vs a shallow Hugoniot (HCP) (see Figure 6.9a for these definitions). Shallow Hugoniot (or material with phase change) has a smaller v/c_s ratio leading to a smaller oscillation wavelength and faster decay. (right) Normalized oscillation wavelength (Eq. (6.7)) versus shock pressure. Note that approximate oscillation wavelength figure (right), matches well with (left) figure as markers show.

6.1.3. Viscous Effects on Shock Perturbations

It is worth reviewing Millers [88] and Zaidel [87] work on viscous effect on shock front perturbations. Miller showed that viscosity affects perturbation evolution as

$$(A_{viscous} - A_{hydro}) \propto \eta/\lambda \quad (6.8)$$

where η is the kinematic viscosity, so that an increase in viscosity pushes the evolution curve up relative to the hydrodynamic solution, and an increase in perturbation wavelength pushes the viscous curve closer towards the hydrodynamic solution, which is of course insensitive to geometry changes in the linear regime, while changes in initial amplitude have no effect. This behavior is much different than the behavior elastic strength has shown in Eq. (6.1). This suggests changes in geometry (while staying in the \sim linear regime) should help to determine what deviatoric behavior, either strength or viscosity, is dominant in the material behind the shock front.

Figure 6.11 shows the results of five experiments at similar shock conditions (~ 12 GPa and $150 \mu\text{m}$ wavelength), where target thickness Δx was varied. The error bars are determined by the temporal resolution and noise in the VISAR data.

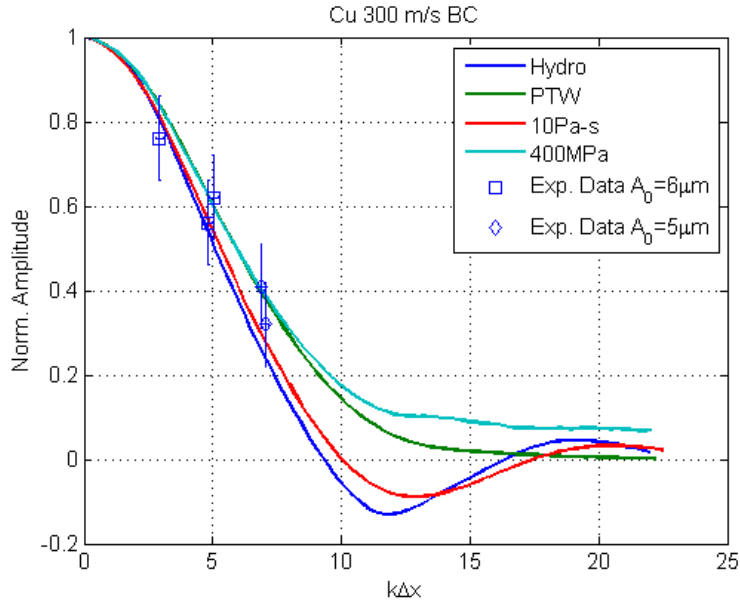


Figure 6.11: Experimental shock perturbation evolution versus simulations.

Results at larger $k\Delta x$ values are not included due to perturbation decay being dominated by the shock release wave [78]. We also show the results of ABAQUS simulations, with a 0.5 micron element size mesh (about 1/10 of initial perturbation amplitude to avoid phase shifts in Figure 6.11 plots), where a constant 300 m/s (equivalent to ~ 12 GPa) velocity was applied to a surface with a perfect sinusoidal modulation.

It is worth pointing out that using a sinusoidal perturbation to model experiments where a square wave was used is appropriate, because square vs sine perturbation simulations show only minor differences after an initial settling time of approximately half the fundamental mode, and analytically a single sinusoidal geometry is more clearly analyzed. A constant velocity condition was applied to show the decay behavior

qualitatively; simulations with release waves did not have an effect on results until the release wave reached the shock front [78]. All simulations used a Mie-Grüneisen equation of state with parameters from [162], but we compare inviscid and viscous fluid solutions to elastic perfectly-plastic and Preston-Tonks-Wallace (PTW) [162] materials possessing strength. PTW model parameters are from Table 5.2. For the viscous model a shear viscosity of 10 Pa-s was selected to best fit the shock front width (i.e., rise time) produced by the PTW model. The elastic perfectly-plastic model was given a yield stress of 400 MPa, which was the approximate average flow stress found in the shocked region of the PTW model simulations.

As can be seen in Figure 6.11 if we had experimental data for thicker samples (with longer laser pulses to prevent release waves from affecting shock perturbation decay) we would have been able to determine if the dominant deviatoric response was elastic or viscous, i.e., it is unlikely multiple material models could concurrently satisfy the shock front rise times and the shock front perturbation evolution at distances near the hydrodynamic inversion point.

Future experiments with shock perturbation evolution, with appropriate geometry and driving forces, i.e., Eqs. (6.3) and (6.4), would be helpful in clarifying dominant deviatoric behavior and therefore optimizing design and material parameters. The next section discusses some boundary and geometry details of the perturbation experiments.

6.1.4. Boundary and Geometry Effects

This section discusses the effect of a pressure boundary condition (as opposed to a rigid velocity boundary condition used in prior sections) and a flyer impact boundary

condition as in Figure 1.9 [95]. We also look at the effect of geometry that violates Eq. (6.3).

6.1.4.1. Pressure Boundary Condition

The boundary condition is simply an applied pressure. This is the same BC typical of ideal Richtmyer-Meshkov experiments. Analytical solutions for the hydrodynamic shock front perturbation evolution exists as reviewed in Section 1.3.1. and Section 1.4. (for ideal gas EOSs). Figure 6.12 shows the shock front evolution for two different geometries and various yield strengths.

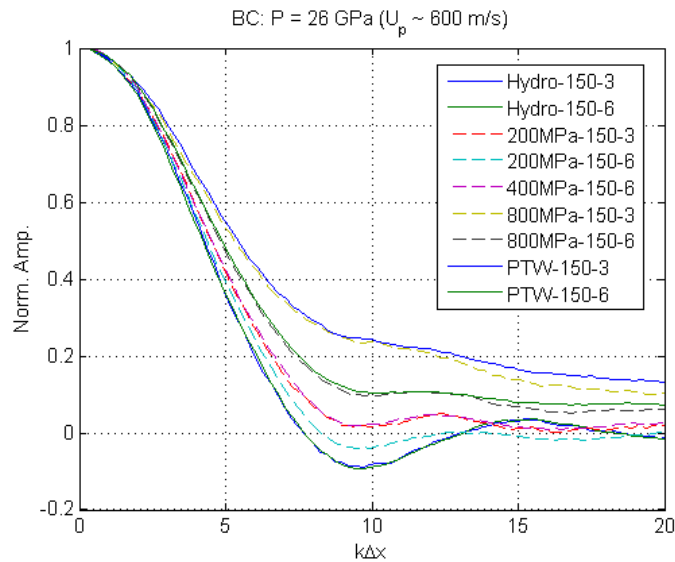


Figure 6.12: Shock front evolution with pressure BC. Comparison to rigid piston BC, see Figure 6.2, shows that the two BCs have similar effects on the shock front perturbation evolution.

Comparison to Figure 6.2 shows that the results are similar to the rigid piston velocity boundary condition with the largest differences occurring for materials with low effective yield strengths. In contrast the RM evolution would obviously be very sensitive to the BC (i.e., for the rigid piston BC you have no RM evolution).

6.1.4.2. Flyer Impact Boundary Condition

In this boundary condition a flat flyer of the same material as the perturbed sample impacts the perturbed face launching a perturbed shock into the sample as shown in Figure 1.9 [95]. This could be a simple experiment to perform and accurately simulated with FEA. However, as Figure 6.13 shows, the perturbation evolution does not appear to be as sensitive as the other BCs to the material strength (i.e., hydrodynamics dominate more) at moderate impact velocities/pressures. The peak shock front amplitude is also greater than the initial perturbation amplitude for weak to moderate shocks. Using simple geometry, the peak shock perturbation amplitude A_i is given by

$$\frac{A_i}{A_0} = \frac{(U_s - V_f)}{V_f} = \frac{C + (\frac{1}{2}s - 1)V_f}{V_f} \quad (6.9)$$

where A_0 is the initial free surface perturbation amplitude, V_f is the initial flyer velocity, and U_s is the shock velocity $U_s = C + sU_p = C + s(\frac{V_f}{2})$. Figure 6.13d shows that small

initial free surface perturbations (or large flyer velocities) show a good dependence on material strength but experimentally it may be hard to measure these perturbations.

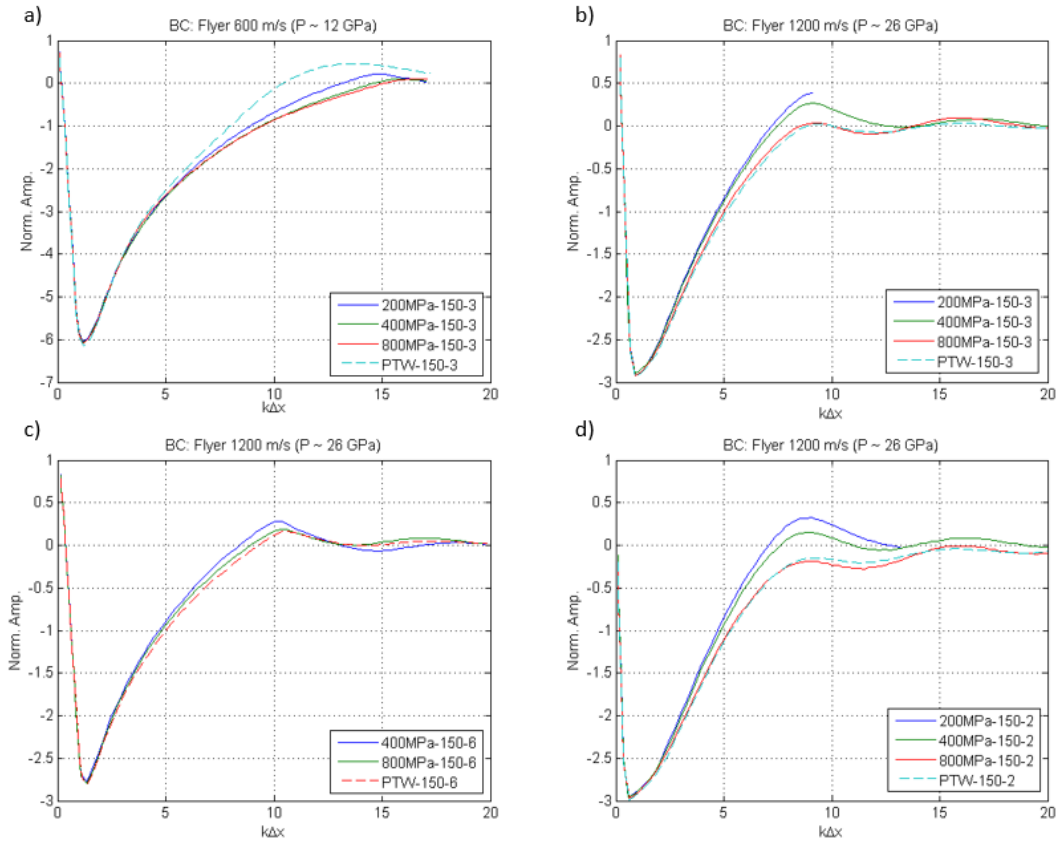


Figure 6.13: Shock perturbation evolution with flyer BC. Legend format of “strength-wavelength-initial perturbation amplitude”. Vertical axis is normalized with initial free surface perturbation amplitude A_0 (as has been done in all previous plots). Figures a) is with a flyer vel. of 600 m/s, while b) through d) are at 1200 m/s. Hydrodynamic simulation (no yield strength) was unstable numerically and is not shown, refinements to model are needed. Shock perturbation amplitude is greater than initial amplitude because shock speed is greater than flyer velocity.

6.1.4.3. Large Amplitude to Wavelength Geometry

At large shock perturbation amplitudes nonlinearities can cause the perturbation evolution to become less dependent on strength and more dependent on the hydrodynamics.

Figure 6.14 shows the evolution for an amplitude to wavelength ratio that violates Eq. (6.3), and as a result the behavior becomes less dependent on material strength (compare Figure 6.14 to Figure 6.2).

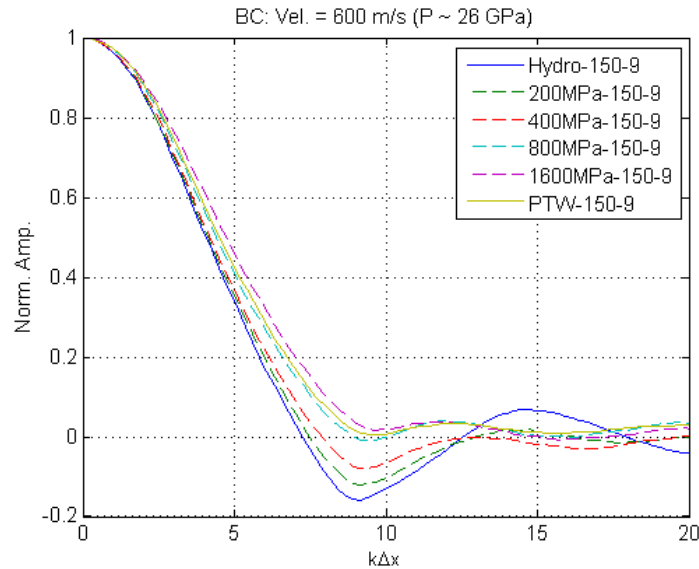


Figure 6.14: Shock front perturbation evolution for large amplitudes. Boundary condition is a constant velocity (rigid piston).

6.2. RM Evolution

This section discusses the effect strength and phase transformation has on the RM evolution of a bimaterial interface, and how this evolution can be used to characterize the high pressure phase strength of two phase materials. As was discussed in Section 1.2.4. , transient pressure perturbations establish a quasilinear perturbation growth rate (i.e., a constant perturbation velocity) that can be approximated with Richtmyer's impulsive model. Deviatoric strength opposes this growth rate and if the problem remains quasilinear the perturbation growth is arrested, otherwise nonlinear and usually unstable bubble and spikes form [66]. The deviatoric stress fields at the perturbation surface are similar to the

fields near the perturbed shock front so that RM growth scales with similar strength and geometry factors. RM growth is sensitive to the BC at the surface (e.g., uniform pressure) and insensitive to shock front perturbations after a short time (unless the shock is very strong [27]), while shock front perturbation evolution has the opposite dependency, i.e., dependent on BC at the surface for a short time, and sensitive to the shock front pressure perturbations which evolve in a more complex manner with deviatoric strength. Unless stated otherwise all simulations in this section use a 1 micron element length that produces a small amount of discretization error (<5%) but runs quickly. The boundary condition is a constant pressure applied to the perturbed surface.

6.2.1. Single Phase Materials (shock moves from vacuum to solid)

Piriz [68] developed a simple semi-analytical expression that captures the typical effect elastic-plastic materials has on the RM growth as was reviewed in Section 1.3.2.2. . His expression for the maximum change in perturbation amplitude was

$$\xi_m - \xi_0 \approx 0.29 \frac{\rho \dot{\xi}_0^2}{kY} \quad (6.10)$$

where ρ is the compressed density, ξ_m is the maximum perturbation amplitude (peak to valley distance divided by 2), and ξ_0 and $\dot{\xi}_0$ are the perturbation amplitude and perturbation velocity once the pressure perturbations near the interface have approximately vanished so that only deviatoric gradients remain [68,27]. If we approximate $\dot{\xi}_0$ with Richtmyer's impulsive approximation $\dot{\xi}_0 \approx k\xi_i U_p$ (Piriz used ABAQUS simulations to find $\dot{\xi}_0$ and ξ_0 which is not ideal for simple calculations) or use a form given by [27,31-33], let $\xi_0 = \xi_i + \Delta\xi_0$, and normalizing Eq. (6.10) with λ we get

$$\frac{\xi_m - \xi_i}{\lambda} \approx C(\rho U_p^2 2\pi) \frac{\xi_i^2}{\lambda^2 Y} + \frac{\Delta \xi_0}{\lambda} = C \left(\frac{\rho_0 U_s U_p^2 2\pi}{U_s - U_p} \right) \frac{\xi_i^2}{\lambda^2 Y} + \frac{\Delta \xi_0}{\lambda} \quad (6.11)$$

where ξ_i the initial perturbation amplitude, $\Delta \xi_0$ is the deflection at which pressure perturbations have vanished, λ is the perturbation wavelength, ρ_0 is the initial density, U_p is the mean particle velocity behind the shock (zero order term), C is a fitting factor, and Y is the effective material yield strength. So if we know an approximate value for C , then approximations for Y and $\Delta \xi_0$ can be found by plotting experimental data.

Equation (6.11) predicts that the wavelength normalized perturbation growth should scale with a term that is EOS dependent (term in parenthesis) and a geometry and material dependent term $\frac{\xi_i^2}{\lambda^2 Y}$, [66] used this normalization for Atwood numbers of -1. Alternatively, we could have normalized with ξ_i to obtain the inverse of the geometry/material factor we found in the shock perturbation discussion, both work well but Eq. (6.11) is preferred here because the perturbations become increasingly nonlinear as they grow so that the left hand side in Eq. (6.11) gives a measure for how far we have deviated from the linear perturbation assumption, in the shock perturbation problem the geometry actually becomes more linear at the shock front with time. Figure 6.15 shows Cu RM perturbation growth for several geometries and yield strengths, including a PTW model with the parameters in Table 5.2, at pressures of 26, 38.5, and 58 GPa (equivalent to U_p of 600, 830, and 1145 m/s respectively).

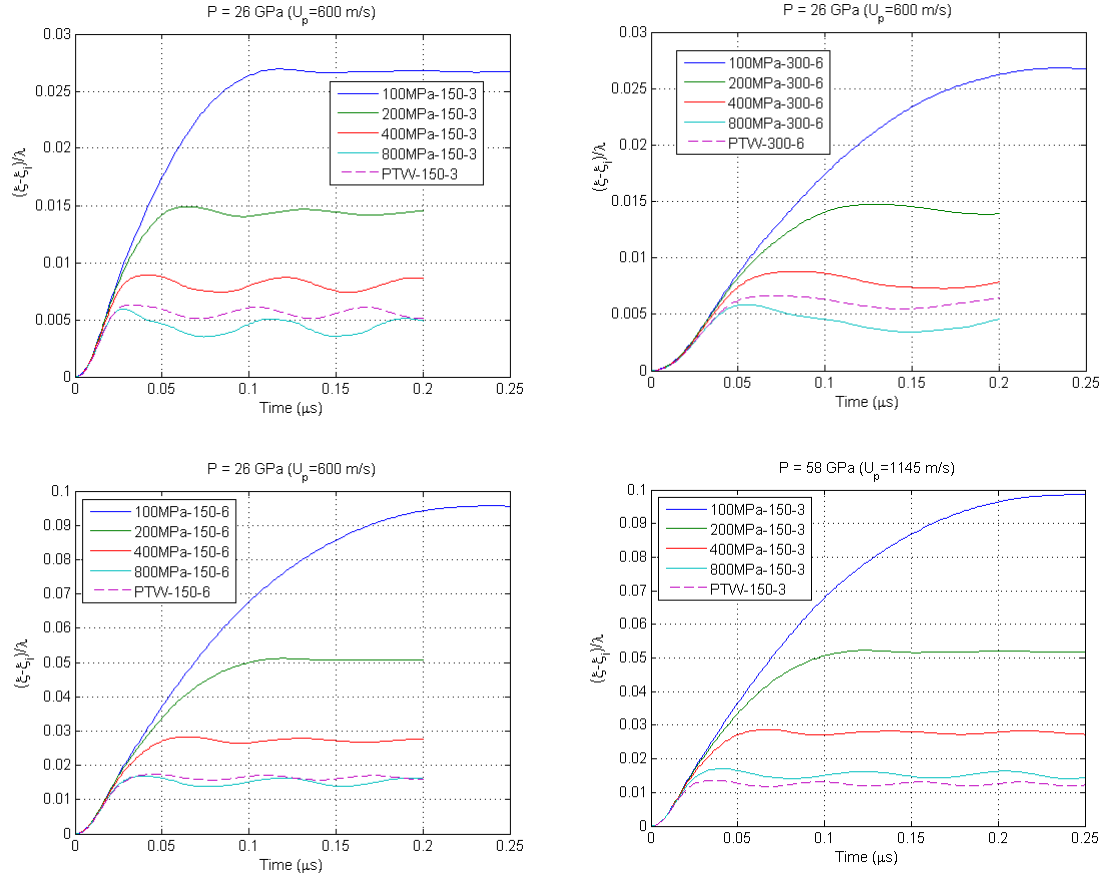


Figure 6.15: Single Phase RM evolution for $A=1$. Normalized displacement vs time for shock pressures of 26 and 58 GPa (U_p of 600 and 1145 m/s), with an Atwood number of 1. Legends are in format of “Yield – wavelength – initial amplitude.”

Figure 6.16 shows Figure 6.15 plots condensed as suggested by Eq. (6.11) where the y-axis is the simulation value and the x-axis is the RHS of Eq. (6.11). This plot includes an additional set of simulations for a wavelength and initial amplitude of 150 and 6 microns respectively for a shock pressure of 26 GPa, ran with yield strengths of 100, 200, 400, 800 MPa, and the PTW model. At 100 MPa an unstable growth occurs so it is not included in the figure. Figure 6.16 shows that even at large $\frac{\xi_m - \xi_i}{\lambda}$ ratios Eq. (6.11) holds well. To best fit all the data C becomes 0.24, which is partially explained due to Richtmyer’s impulsive

approximation overestimating the maximum deflection rate $\dot{\xi}_0$ by about 20% when we compare simulation values to the impulsive approximation.

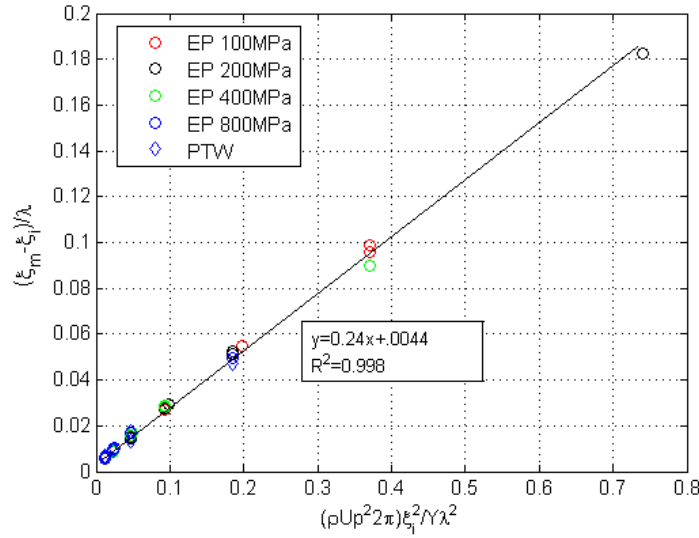


Figure 6.16: Maximum RM displacement. Maximum displacement of each curve in Figure 6.15 versus RHS of Eq. (6.11) without 0.29 factor. Note simulations in Figure 6.15 should fall into 1 of 7 point groups as predicted by Eq. (6.11). For the PTW simulation we calculated the x-axis value by assuming $Y \sim 800$ MPa. Figure shows simulation data agrees with Eq. (6.11) reasonably well.

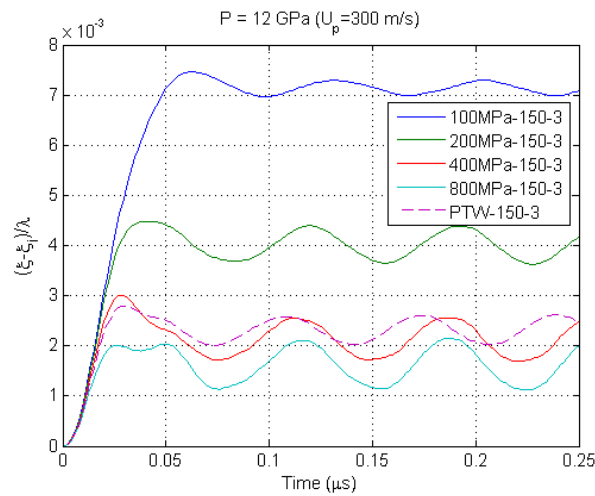


Figure 6.17: Simulations at low shock pressure of 12 GPa.

Figure 6.18 is representative of experimental data reduction to find an effective yield strength. Figure 6.19 shows plastic strain rate, Von Mises, and cumulative plastic strain at a time that is about 2 ns (about 10 % of total time to maximum deformation rate) after the maximum deformation rate $\dot{\xi}_0$. Figure 6.19 shows that the average effective yield stress predicted by Figure 6.16 matches the average contours seen in Figure 6.19. Despite the apparent wide range of strain rates and cumulative plastic strain the PTW response is rather insensitive as shown in Figure 6.20, where the small dashed square box more than encompasses all the strain rates and cumulative plastic strain shown in Figure 6.19.

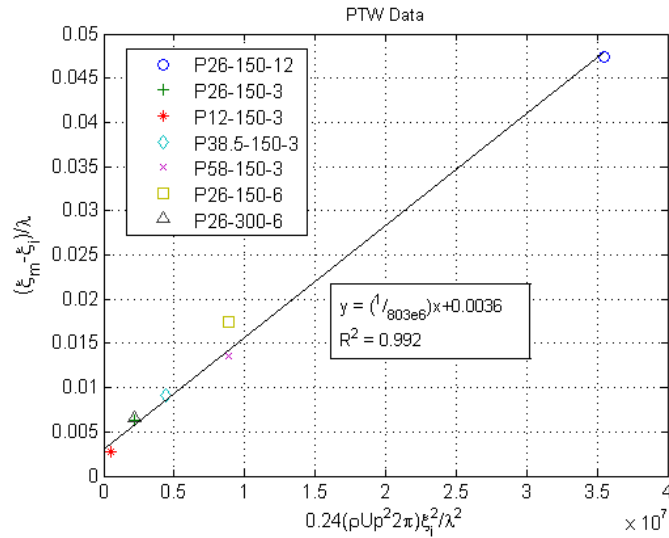


Figure 6.18: Consolidate PTW RM results versus RHS of Eq. (6.11), showing possible data reduction of experimental data. Slope of best fit line is inverse of effective yield strength (~ 803 MPa) which is the typical value found in simulations (~ 800 MPa, except at the low shock pressure of 12 GPa where the effective shear stress is closer to 400 MPa which is what the shock front perturbation simulations found also). Intercept of 0.0036 matches well with simulations that predict a normalized displacement at maximum perturbation deformation rate $\dot{\xi}_0/\lambda$ of about 0.0040 at a time of about 14 ns (for the 150 μm wavelength geometry, for the 300 μm it becomes 28 ns but the 0.0040 intercept is still correct).

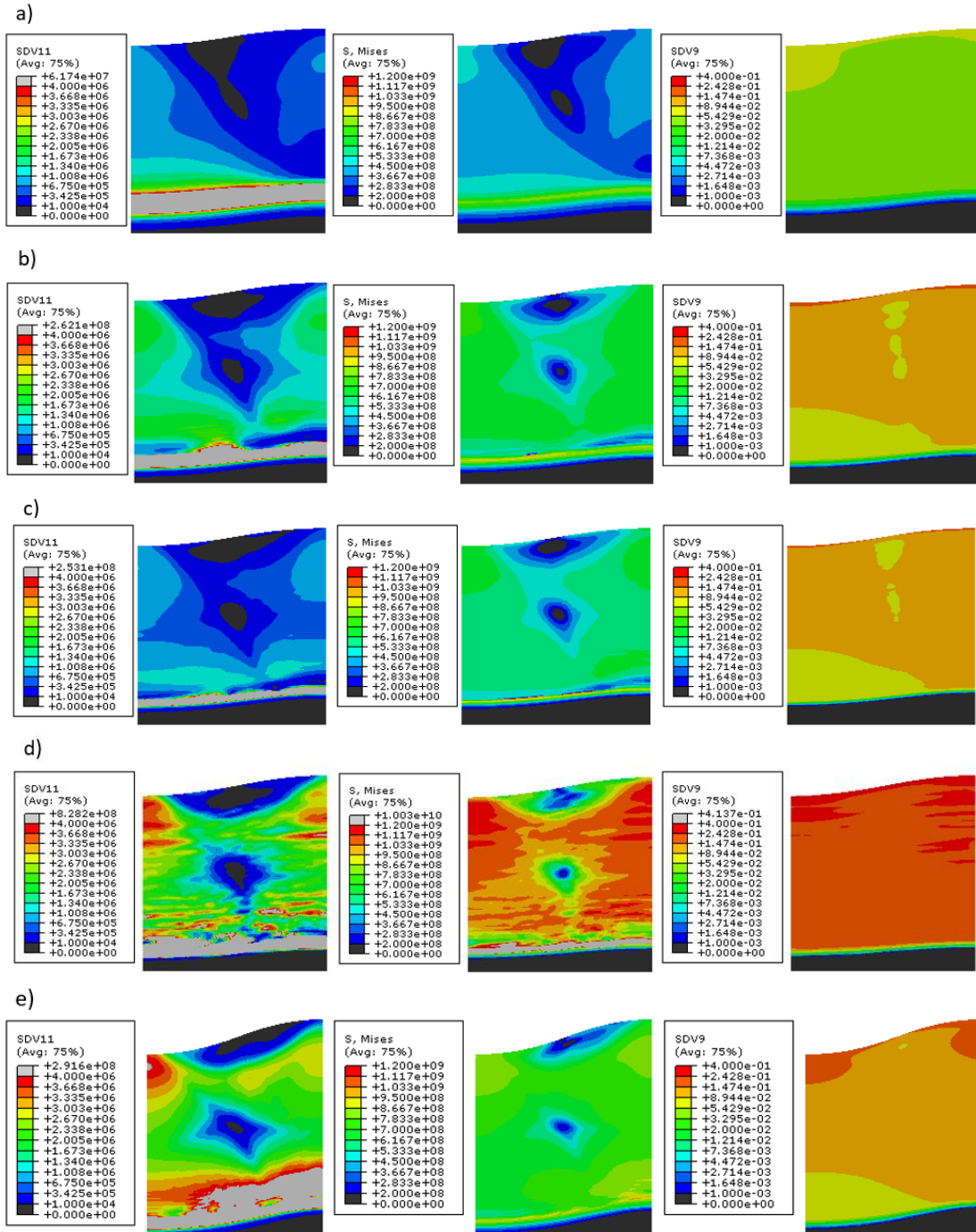


Figure 6.19: Simulation FEM contour results. Plastic strain rate, Von Mises, and plastic strain contours at a time ~ 2 ns after peak perturbation deformation rate for the PTW simulations. a) P12-150-3 (pressure-wavelength-amplitude), b) P26-150-3, c) P26-300-6, d) P58-150-3, and e) P26-150-6. Comparison with Figure 6.15 shows average Von Mises stress in b) through e) matches the effective yield stress predicted in Figure 6.15. The maximum deformation rate for the P26-300-6 and P26-150-3 is ~ 55 m/s, while for the P58-150-3 and P26-150-6 simulations the rate is ~ 115 m/s taken (values obtained from simulations), and at P12-150-3 it is ~ 25 m/s.

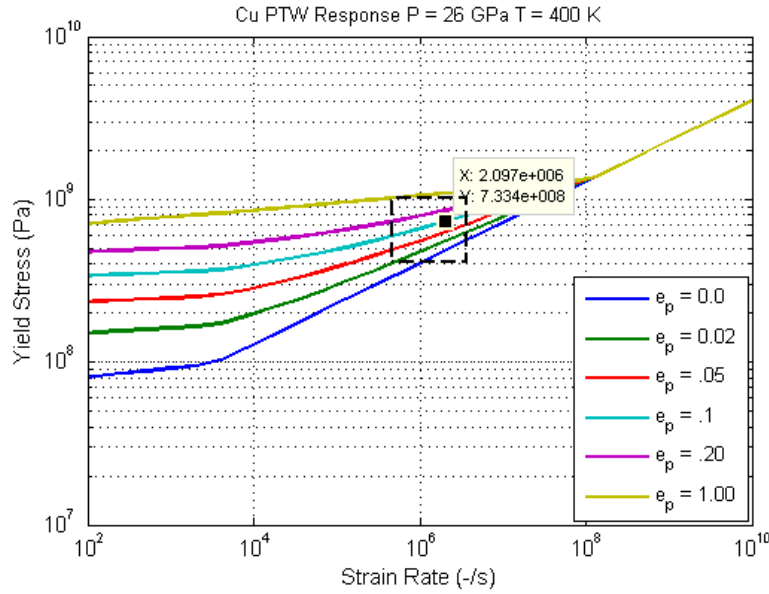


Figure 6.20: RM PTW strain rate domain. PTW response at a pressure of 26 GPa and temperature of 400 K (approximate temperature and pressure for Figure 6.19). Square box encompasses all the cumulative plastic strain and strain rates seen in Figure 6.19.

6.2.2. Single Phase Materials (shock moves from solid to vacuum)

The opposite limit is for a shock moving from a solid to a vacuum (Atwood number of -1). Typically, in this case the perturbation inverts and then grows at a quasilinear rate in the absence of deviatoric stresses. With deviatoric stress a semi-empirical equation similar to Eq. (6.10) exists [66]

$$\xi_{m,spike} \approx 0.24 \frac{\rho \dot{\xi}_{0,spike}^2}{kY} \quad (6.12)$$

where $\xi_{m,spike}$ is the maximum amplitude of the spike only, not the entire perturbation, and $\dot{\xi}_{0,spike}$ is the peak spike growth rate. Spikes were distinguished from bubbles by running simulations with flat samples to serve as a zero reference [66, 69].

Figure 6.21 and Figure 6.22 show the same shock pressures and geometries as in Figure 6.15 and Figure 6.17. In these figures negative y-values mean inversion did not

occur. Figure 6.23 shows the data consolidated as in Figure 6.16; better, more complicated fits are possible (such as Eq. (6.12)), we use the x-axis in Figure 6.23 for simplicity.

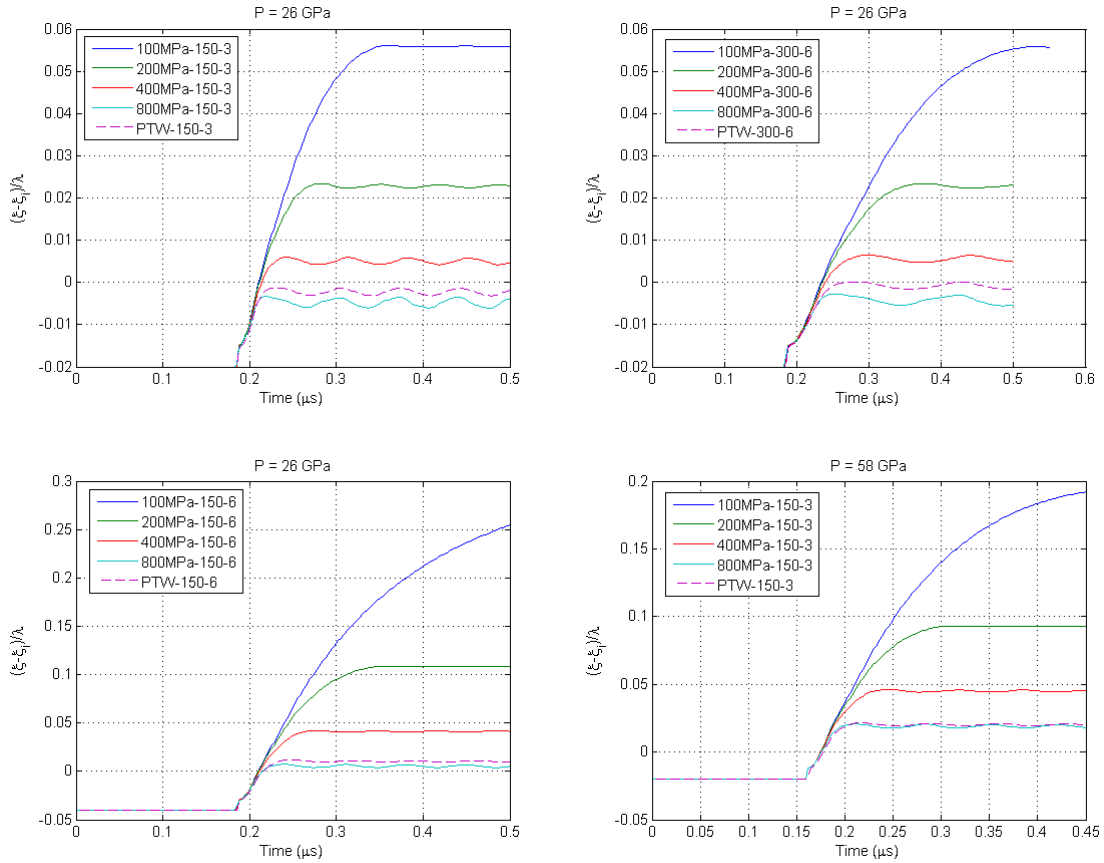


Figure 6.21: Cu RM evolution for $A = -1$. Normalized displacement vs time for shock pressures of 26 and 58 GPa (U_p of 600 and 1145 m/s), with an Atwood number of -1. Legends are in format of “Yield – wavelength – initial amplitude.” Negative y-axis values mean the perturbation has not inverted. Despite the significant difference in loading history the PTW model still has an effective yield strength of about 800 MPa as was found in Figure 6.15.

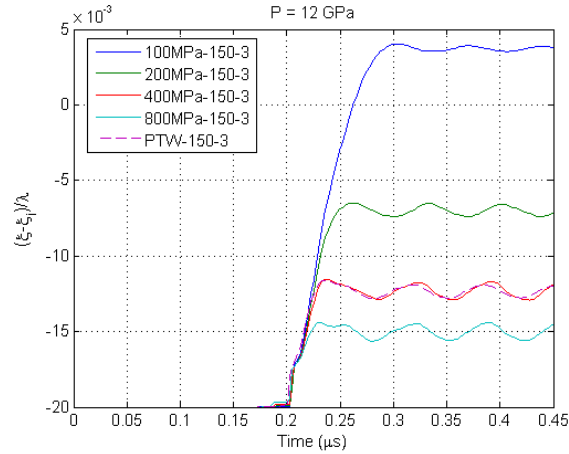


Figure 6.22: Simulations at low shock pressure of 12 GPa.

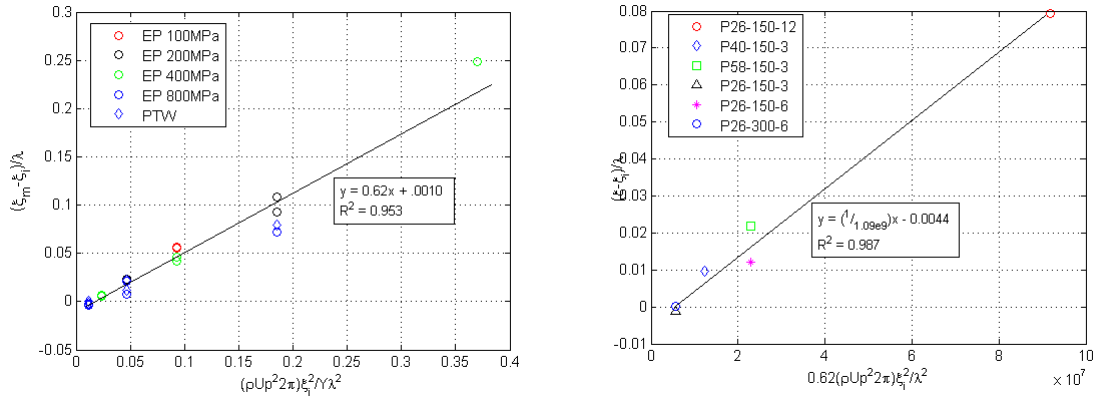


Figure 6.23: Maximum RM displacement in Cu RM A = -1 simulations. Maximum displacement of each curve in Figure 6.21 (in addition to some data at 150-12-P26 GPa) versus RHS of Eq. (6.11) without 0.29 factor. (left) For the PTW simulation we calculated the x-axis value by assuming $Y \sim 800$ MPa. (right) PTW data reduction estimates an effective PTW yield strength of 1.09 GPa which is about slightly larger than what simulations show.

The linear fit is not as convincing, likely due to the more complicated deformation history; since the perturbation first has to invert before growing. The maximum perturbation deformation rate $\dot{\xi}_0$ is about 80% larger in the A=-1 case than for the A=1 for the same shock pressure and geometry conditions (which agrees roughly with [66]). This

would explain the generally larger deformations seen for $A=-1$. Note that the higher deformation rate is largely dominated by the hydrodynamics and not a change in the deviatoric behavior. There is actually a larger deformation rate just as the shock reaches the valley (seen as the step displacement in Figure 6.21 plots), but this approaches zero as the shock reaches the perturbation peak, as shown in Figure 6.24. Figure 6.25 shows the plastic strain rate, von Mises stress, and cumulative plastic strain at a time 2 ns after the peak deformation rate $\dot{\xi}_0$.

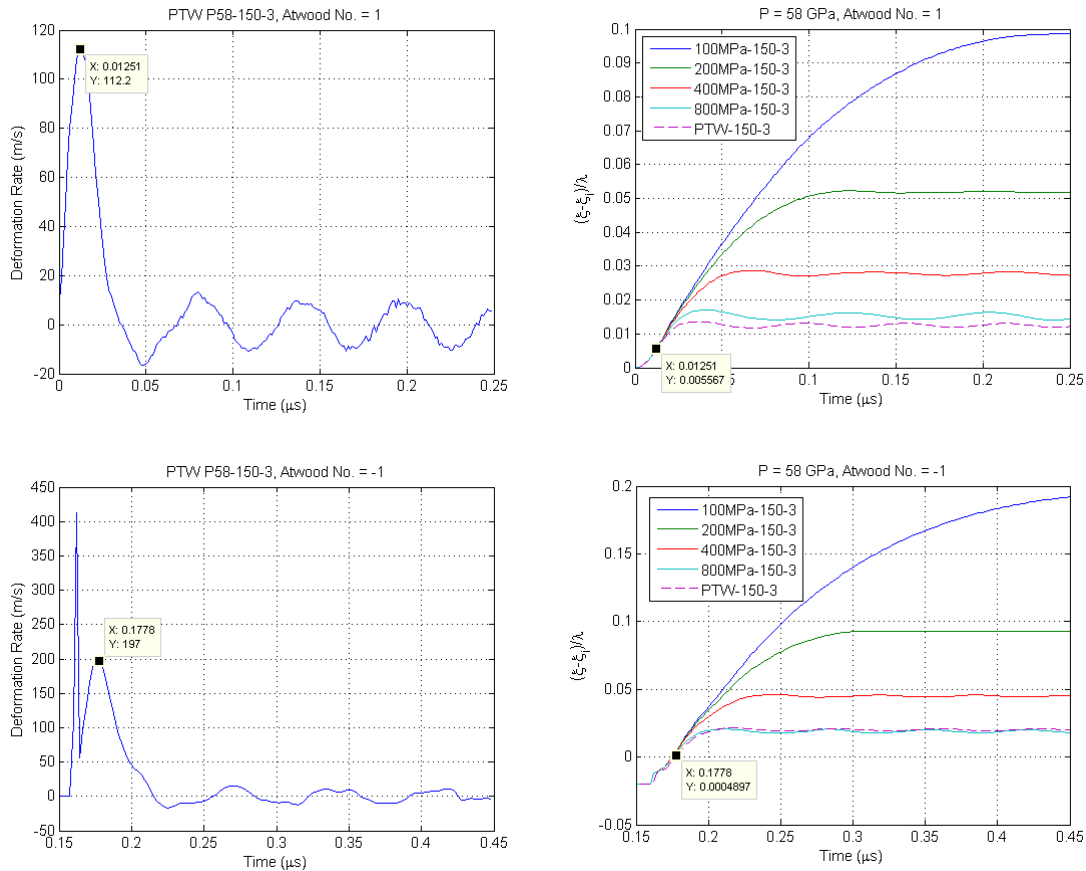


Figure 6.24: Maximum RM deformation rate. Deformation rate history $\dot{\xi}_0$ for a shock pressure of 58 GPa and perturbation amplitude and wavelength of 3 and 150 μm respectively. (left) Atwood number of 1, (right) Atwood Number of -1. Note peak deformation rate seen in $A=-1$ deformation rate plot (~ 400 m/s) is not accurate due to numerical differentiation error in the calculation. The short peak is when the shock first arrives at the valley of the deformation.

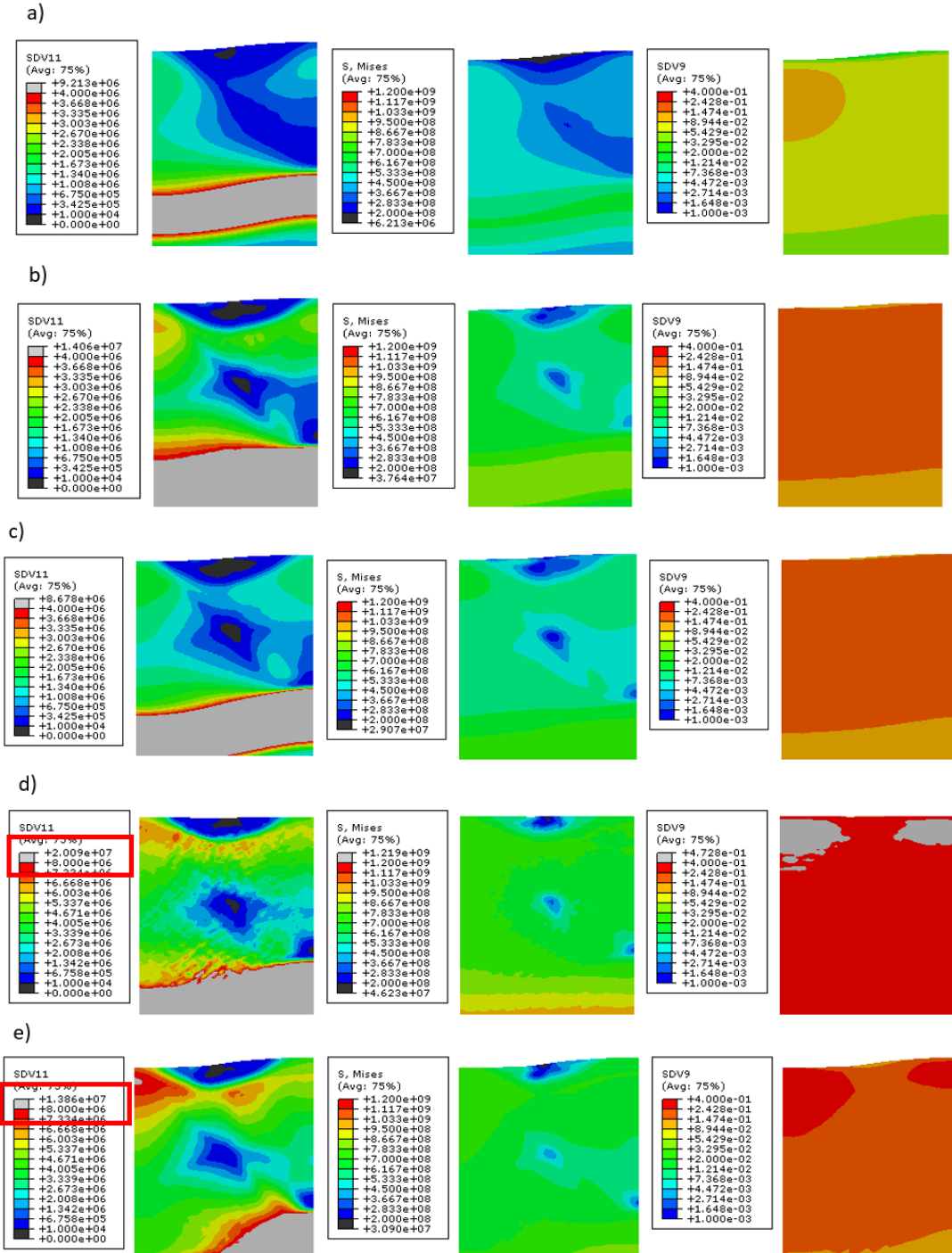


Figure 6.25: Simulation FEM contour results. Plastic strain rate, von Mises, and plastic strain contours at ~ 2 ns after peak perturbation deformation rate for the PTW simulations. a) P12-150-3 (pressure-wavelength-amplitude), b) P26-150-3, c) P26-300-6, d) P58-150-3, and e) P26-150-6. Comparison with Figure 6.21 shows average von Mises stress in b) through e) matches the effective yield stress predicted in Figure 6.21. The maximum $\dot{\xi}_0$ for P26-300-6 and P26-150-6 is ~ 102 m/s, while for P58-150-3 and P26-150-6 it is 200 and 222 m/s respectively (from simulations), and at P12-150-3 it is ~ 45 m/s.

Figure 6.15 and Figure 6.21 (perturbation evolution with time) and Figure 6.19 and Figure 6.25 (FEM contours after peak perturbation growth rate) show similar results in regards to the effective yield strength of about ~800 MPa. This is interesting because the loading scenario in the two cases is significantly different. In the $A = 1$ case there is a large amount of pressure induced strength due to the PTW strength pressure dependence, while in the $A = -1$ impact the pressure is approximately zero near the free surface however additional strength comes from more work hardening, higher plastic strain rates, and less adiabatic heating. However, both the $A=1$ and $A=-1$ RM evolutions provide valuable characterization data in different loading regimes, and assuming there equivalent based on these results would be premature.

6.2.3. Materials with Phase Transformation

6.2.3.1. Shock moves from Vacuum to Solid ($A=1$)

The RM evolution offers an approach to clearly characterize the high pressure phase strength. In shock front rise times, strength effects are not obvious due to the phase transformation occurring in the plastic wave leading up to the high pressure phase. Also at large pressures it is difficult to get accurate shock front rise times, since the shock front typically steepens drastically with pressure. However for RM evolutions with $A = 1$, the perturbation growth should occur well after complete phase transformation as suggested by the sub nanosecond transformation time found by [112], the results in Section 5.3.2. , and assuming this transformation rate applies to metals other than iron. Figure 6.26 and Figure 6.27 show the same study as that performed for the single phase copper. Figure 6.26 shows three PTW models, the model labeled “PTW” is the same as the “Belof” model

except the thermal activation region was moved up along the vertical axis by a factor of about 1.75 (see Table 5.2). The model labeled “Ph1Belof” has low pressure phase properties equal to the “Belof” model, and high pressure properties of the “PTW” model.

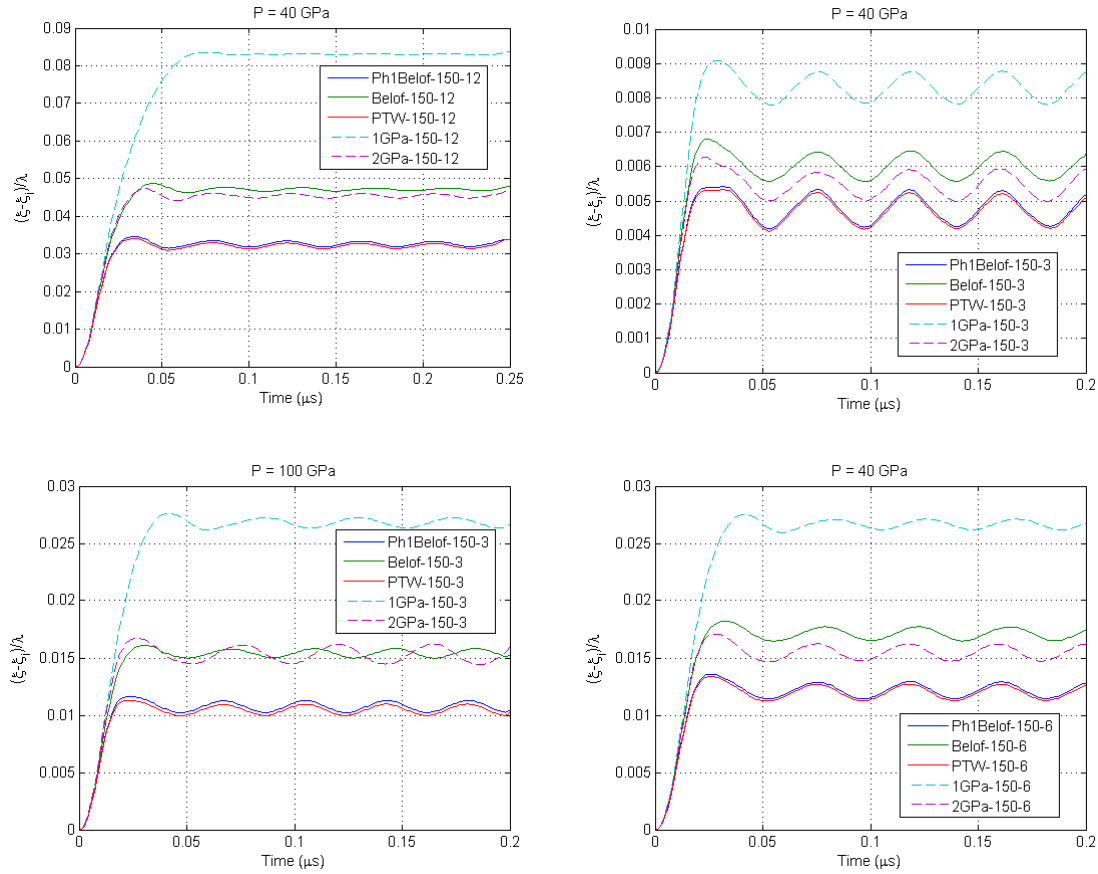


Figure 6.26: Iron RM evolution for $A = 1$. Normalized displacement vs time in format “strength model – wavelength – amplitude” for shock moving from vacuum to solid ($A=1$). PTW and Belof models have parameters from Table 5.2 and Ph1Belof has Belof parameters for low pressure phase and PTW parameters for high pressure phase. Note that low pressure phase parameters do not effect response, suggesting an RM experiment with $A = 1$ would be a good method for characterizing the high pressure strength. The shear modulus in the EP models was increased to 140 GPa to approximate the oscillation period of the PTW models (whose shear modulus has increased due to pressure dependence).

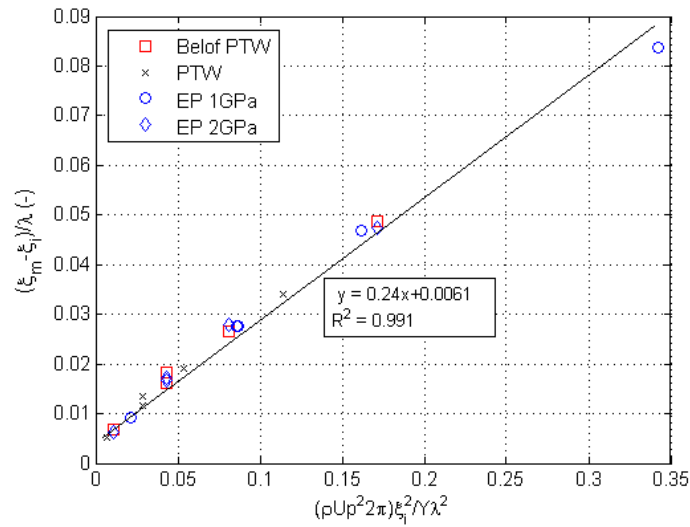


Figure 6.27: Maximum RM displacement for $A = 1$ for iron. Maximum displacement of each curve in Figure 6.26 versus RHS of Eq. (6.11) without 0.29 factor. Data in plot also includes simulation for P60-150-6 of each material. “Ph1Belof” is not plotted above. Same slope as in Cu simulations works well, i.e., $C = 0.24$. The “PTW” data was assigned an effective yield stress of 3 GPa, while the “Belof PTW” data was given an effective yield stress of 2 GPa for plotting purposes. Both values agreed with average values seen in simulation contours also.

The “Ph1Belof” model results are nearly identical to the “PTW” results suggesting the low pressure phase has no effect on the results and the RM instability test with $A = 1$ is a good technique for characterizing the high pressure phase strength. Figure 6.28 shows contour plots for some of the plots in Figure 6.26, while Figure 6.29 shows the PTW response for the same approximate temperature and pressure (at $P=40$ GPa). Note, as in the copper simulations, the strain rates seen in the iron perturbations are around $3e6$ to $2e7$ s^{-1} with the higher end for larger initial perturbations or driving pressures.

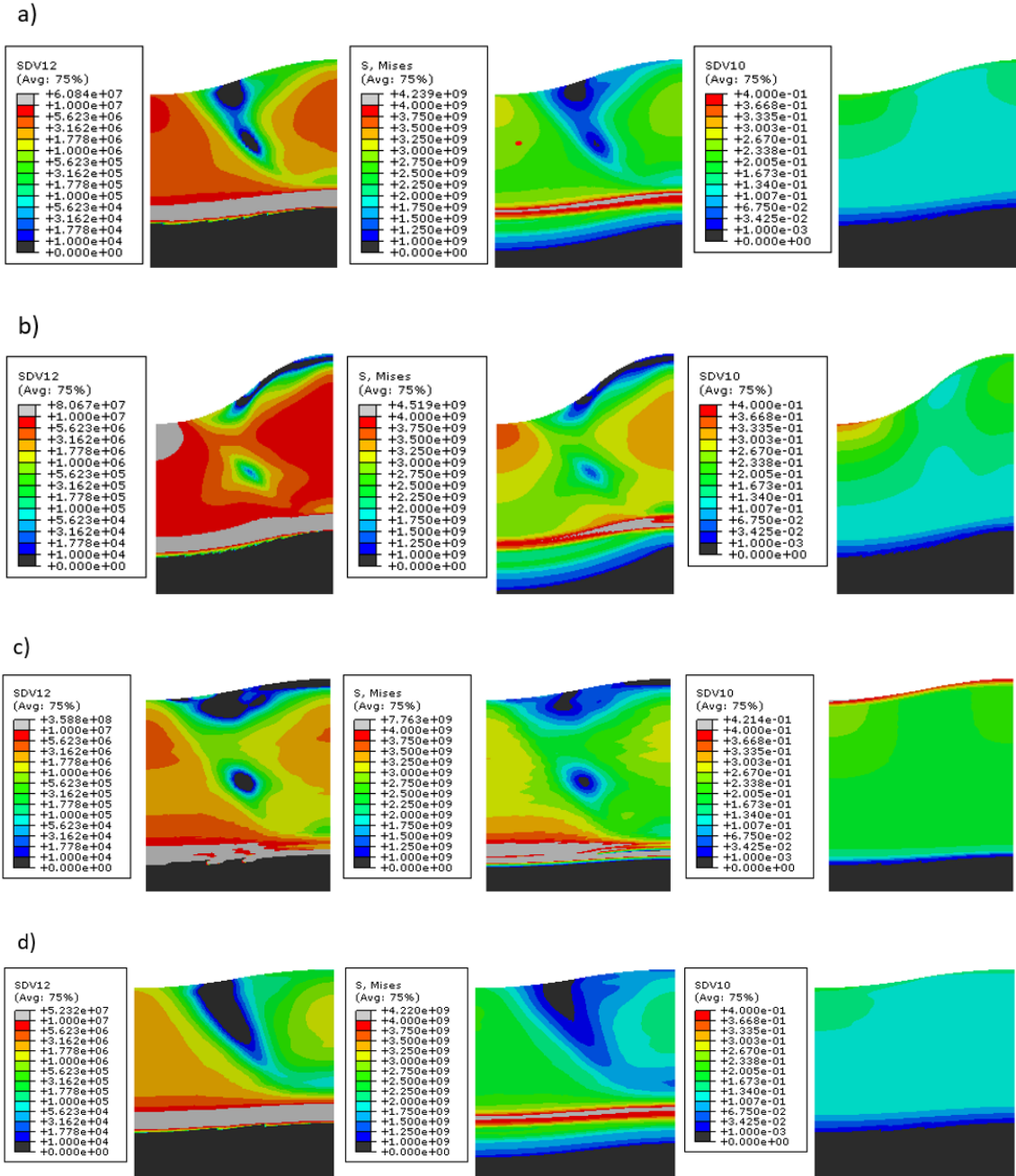


Figure 6.28: Simulation FEM contour results. Plastic strain rate, von Mises, and plastic strain contours at a time ~ 2 ns after peak perturbation deformation rate for the PTW simulations. a) P40-150-6 (pressure-wavelength-amplitude), b) P40-150-12, c) P100-150-3, d) P40-150-3. Comparison with Figure 6.27 shows average von Mises stress is near 3 GPa.

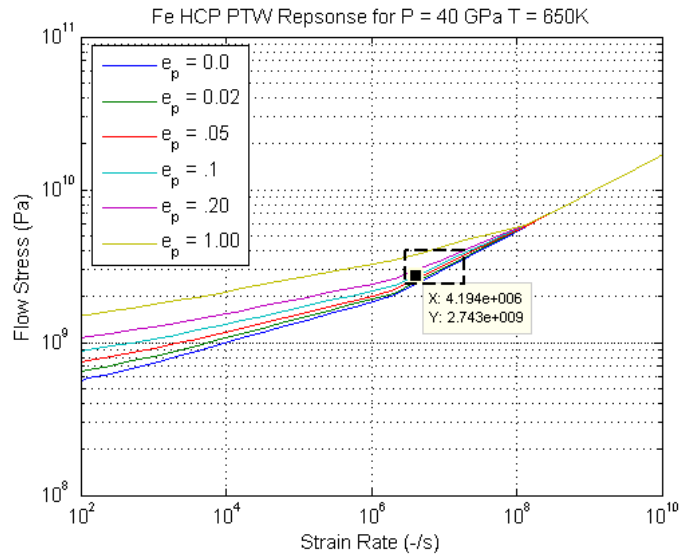


Figure 6.29: Iron HCP PTW response at $P = 40$ GPa and $T = 650$ K. Dashed box represents approximates strain rates and cumulative plastic strain seen in simulations for RM evolution with $A=1$. Strain rates are in the transition region of the PTW strength law.

6.2.3.2. Shock moves from Solid to Vacuum ($A=-1$)

A RM evolution with an Atwood number of -1 is not ideal for materials with a high pressure phase transformation. In the single phase material (e.g., Cu) a RM evolution with $A = -1$ was generally intuitive and while the data did not condense as well as the $A=1$ case it was still fairly well described by simple relations, and relatively simple simulations could easily describe the evolution. The benefit of the $A=-1$ case is the simulation boundary conditions can be executed with high confidence experimentally with a flyer-target setup. A disadvantage would be that high pressure strength would be difficult to infer since the vacuum interface drives the pressure to low values near the free surface; however, quality high strain rate data can still be gathered. Because of the low impedance interface the

deviatoric response for materials with a phase transformation appears to be a complicated function of both phases. Figure 6.30 shows the RM growth for three different PTW models.

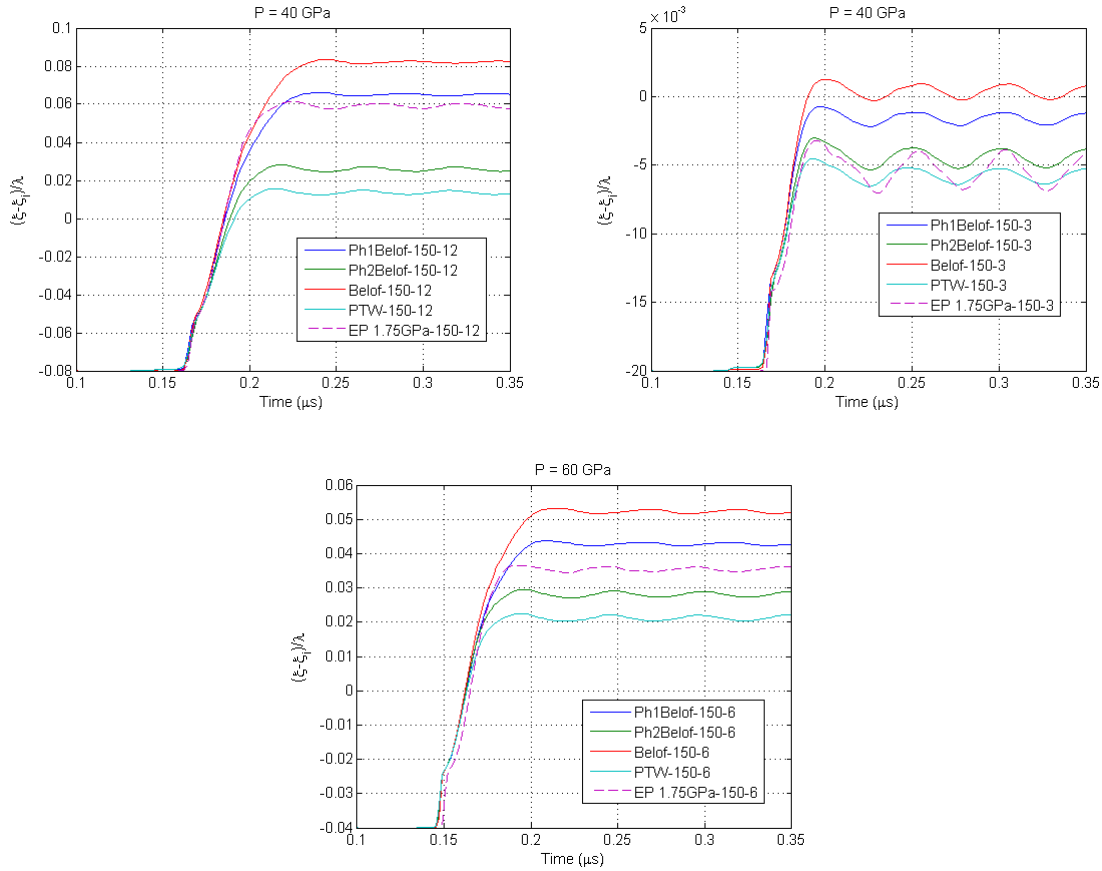


Figure 6.30: Iron RM evolution for $A = -1$. Normalized displacement vs time in format “strength model – wavelength – amplitude” for shock moving from solid to vacuum ($A = -1$). “PTW” and “Belof” parameters are from Table 5.2, and “Ph1Belof” and “Ph2Belof” have “Belof” (weak in comparison to “PTW”) low and high pressure phases respectively, with other phase equal to stronger “PTW” parameters. Note that, unlike the $A = 1$ case, deviatoric response of both phases is important in perturbation evolution, making it difficult to discern clearly the strength of the high pressure phase.

The model PTW parameters are from Table 5.2, the “Ph1Belof” model uses weaker parameters for the low pressure phase, “Ph2Belof” uses weaker parameters for the high pressure phase, “Belof” uses weaker parameters for both phases, and finally the “EP 1.75 GPa” model uses the mie-gruneisen parameters from the high pressure phase (simple

ABAQUS model) but a low pressure shear modulus. In order to characterize the high pressure phase strength with a $A=1$ RM evolution would require an accurate model for the low pressure strength and the phase transformation kinetics also.

In this chapter we looked at how shock front perturbations evolve with EOS parameters and deviatoric strength properties. It was found that the EOS determines how fast shock front perturbations decay, where the decay occurs faster for materials with a smaller shock wave speed to shocked sound speed ratio (isentropic sound speed behind shock). It is expected that materials with phase transformations will likely have the smallest ratios of similar materials (e.g., metals), due to the structure of a P - v Hugoniot that contains a volume collapsing phase transformation (see Figure 6.9). Tailoring of materials to capitalize on this fact may lead to improved designs in applications such as inertial confinement fusion (ICF), where perturbations at ablated surfaces of the capsule are fed-in, via shock front perturbations, to internal surfaces seeding/accelerating RT instability growth (see Section 1.3.2.1.). It was also discussed that single phase, and materials with phase transformations, could have similar decay properties (i.e., due to similar P - v Hugoniots at a particular point on the Hugoniot) but that materials with phase transformations will likely lead to less adiabatic heating since some energy is used for the phase transformation and not entirely wasted in irreversibilities. Depending on the application this could be a beneficial characteristic since heating typically reduces the strength of a material and therefore it's resistance to hydrodynamic instability growth.

Richtmyer-Meshkov growth was also reviewed for single phase materials and for materials with phase transformations. For single phase materials results similar to prior studies [66,68,69] were found, e.g., that complete modern strength models such as the PTW

model can in most cases be treated reasonably well with an effective yield strength at strain rates typically seen in instability evolution. This effective yield strength was also found to be the same effective strength that could be determined from the shock perturbation evolution experiments. However, simulations suggest the shock front perturbation experiments may be more attractive in some scenarios since the shock front perturbation experiments are not as dependent on boundary conditions (see Section 6.1.4.). The shock front perturbation experiments also have potential for determining deviatoric behavior (viscous or elastic) with simple changes to experimental parameters (see Section 6.1.3.). Accurate knowledge of the deviatoric behavior of materials is a critical parameter in instability evolution (e.g., Section 1.3.2.1.).

Determination of the high pressure deviatoric behavior was determined to be possible for Atwood numbers near $A=1$, which is the intuitive result. For much lower Atwood numbers, particularly for numbers close to $A=-1$, phase transformation kinetics and the deviatoric properties of the low pressure phase have a strong influence on experimental results, making it difficult to isolate the high pressure phase properties. Fortunately, as in the single phase material case, the shock front perturbation experiments show excellent promise as another method for determining the high pressure phase properties, since the perturbation evolution is most strongly affected by material properties behind the shock front, so that for a shock well into the high pressure phase those properties will be the high pressure phase properties. This could be a promising finding because RM experiments with $A=1$ are difficult to perform in comparison to experiments with $A=-1$ [202]. Optimization of the shock perturbation study, such as those being performed by [99] for granular materials, should be continued to further explore experimentally the

effectiveness of this method to determine high pressure phase material properties at large strain rates and pressures typical in hydrodynamic instability evolution. In summary the unique properties of a material with a phase transformation provides non trivial parameters that could be optimized for systems under large pressures and strain rates where instability evolution is a concern, and this work showed potential experimental setups to determine the deviatoric behavior of the high pressure stable phase that is difficult to assess with typical techniques such as 1D shock front rise-times or RM evolutions where $A=-1$.

7. CONCLUSIONS

The material models and predictive simulations developed in this work, when calibrated and validated to existing and experimental data post processed in this work, lead to the following observations and conclusions:

- Laser ablative loading of perturbed surfaces with thicknesses about equal or less than the perturbed surface wavelength produce clear perturbed shock front breakout signatures at the initially flat diagnostic surface (see Section 3.). The breakout of these perturbed shock fronts provides dynamic transient data that can be captured well with transient imaging displacement interferometry (TIDI) provided the displacements are small $\sim < 1 \mu\text{m}$, which is complimentary to other typical imaging techniques such as radiography.
- The displacement evolution of the free surface of the perturbed surface as the perturbed shock breaks out provides data for material model calibration; however, the data is sensitive to measurement errors.
- The perturbed shock breakout also provided a measure of the shock perturbation evolution when monitored with Line VISAR (as was done in this experiments for this work) which is useful for material model validation. A series of experiments with different sample thicknesses was used to confirm simulation predictions (see Section 6.1.3.). Unfortunately the laser pulse was too short to drive supported shocks for thicker samples, and release waves from the ablation surface invalidated our thicker samples in terms of experimental data to compare to simulations.
- Laser ablation of flat samples, while not unique, provided some calibration and validation data for Cu and Fe material models. The iron data, when combined with

- simulations, seemed to support experimental data on phase transformation kinetics from the literature indicating that shocks well over the ~ 13 GPa phase transformation (e.g., ~ 20 GPa or more) threshold have fast effective phase transformation time constants of less than 1 ns (see Section 5.3.2.).
- A phase aware crystal plasticity model was developed based on kinematic models from the literature. The effort was partially successful but produced volumetric errors upon phase reversal (high pressure phase to low pressure phase) that are not representative of physical results. An empirical factor was introduced to correct this error. Further analytical work and experimental validation data are necessary to make this model useful.
 - Cu simulation results, with models calibrated to 1-D flat sample data and some two dimensional data (see Section 5.4.), seem to suggest RM evolution is dominated by a narrow range of strain rates (about $5e5$ to $1e7$ s^{-1}) which is beyond the thermal activation region but below rates associated with phonon drag, i.e., the transition region of the PTW material law. The flow stress for these strain rates is affected by a number of state variables including temperature, pressure, and work hardening. Interestingly for most cases the flow stress could be well approximated by an elastic-plastic effective yield stress of about 800 MPa. This effective value would increase to about 1 GPa for large deformations (large initial amplitude to wavelength ratios), and decrease to about 400 MPa for weaker shocks ($\sim < 20$ GPa). RM evolution simulations with Atwood numbers of 1 and -1 showed similar effective yield stress values. This is surprising given that the for $A=1$ the perturbation growth is under large pressure and therefore pressure induced

strengthening; however, large amounts of adiabatic heating seemed to roughly cancel the pressure induced strengthening. Conversely for $A=-1$ the perturbations grow near a free surface so pressure induced strengthening largely absent, but so is adiabatic heating. Caution should be used, however, in extrapolating this observation to other materials as the observed behavior is dependent on material parameters (i.e., α_T , T_m , and α_P in Section 4.2.5.).

- Iron RM evolution results for $A=1$ confirmed the intuitive result that the high pressure phase dynamic response could be characterized well in the transition region of the PTW material law with little dependence on the low pressure phase and transformation kinetics. Although intuitive, it is still an important conclusion because typical 1-D shock front results are not very useful for characterizing the high pressure phase due to the high pressure plastic wave being affected by phase transformation kinetics in addition to the deviatoric properties we wish to characterize.
- Iron RM evolution results with $A=-1$ showed that the high pressure phase has a weak effect on the perturbation evolution, and is significantly affected by the low pressure phase properties. This is unfortunate because the $A=-1$ RM evolution with a flyer-target experiment can be modeled very accurately with numerical simulations. For an RM experiment with $A=-1$ to be useful in characterizing the high pressure deviatoric behavior a very accurate low pressure phase and phase transformation kinetic model would be needed.
- Significant work has been performed on the effect elastic-plastic strength has on shock front perturbation evolution. This work took existing analytical solutions for

hydrodynamic isentropic processes in gases and liquids and made small modifications necessary to make them applicable to metal equation of states. The analytical solutions were further improved by incorporating plastic strength that dominates the deviatoric behavior up to about shock front inversion. Both of these analytical solutions agreed well with simulation results and help to provide insight into fundamental relations such that increased elastic-plastic strength and/or increased perturbation wavelength delays shock front perturbation decay, the latter is the opposite effect seen in materials with linear viscosity; i.e., increased wavelength increases shock front decay in viscous materials. This wavelength dependence difference provides a simple experimental parameter to vary to differentiate between the underlying deviatoric behavior of the material.

- The analytical shock front perturbation evolution results also suggest the low shock velocity to compressed sound velocity ratio typical of materials with phase transformations might be a useful property in applications, since this characteristic results in shock front perturbations decaying faster and generating less heat (see Section 6.1.2.).
- Through simulations we showed PTW models can be validated in the transition region with shock perturbation evolution experiments and produce effective yield stress values in agreement with the RM evolution experiments for the $A=1$ case. This could be a significant result, since RM evolution with $A=1$ is much harder to perform than the typical $A=-1$ case.

8. FUTURE WORK

- It would be helpful to perform another series of experimental testing with more iron samples. Particularly sustained loading of the iron samples well above ($\sim >20$ GPa) the phase transformation pressure so that more data is available to calibrate a phase transformation kinetics model. Varying sample thicknesses would be useful, particular thick samples, in addition to thin samples, to confirm a phase transformation occurred by observing a two-wave shock front.
- Sustained loading of the perturbed iron samples (as well the copper samples), so that release waves do not invalidate the shock perturbation evolution data, would also be very useful for learning more about the deviatoric behavior of the high pressure phase and confirming the predictions of the simulations done in this work.
- Shock front perturbation evolution in solids as a tool to study dynamic strength in solids is relatively new, few researchers have done much work in this area. There are likely other novel experimental setups and diagnostics that could be developed to create shock perturbations and monitor the shock breakout. Unlike typical RT and RM experiments the diagnostics needed to measure the shock breakout, and hence the shock front perturbation amplitude, do not need to be very complicated making it a potentially attractive choice for many modest labs.
- On a personal note, it would be interesting to learn more about the details of ICF capsule design and how the unique properties of materials with phase transformations might play a role.

- More work is needed on the phase aware crystal plasticity model. The computational overhead, however, is large (e.g., computations scale with each additional variant considered whether the variant is active or not) and a detailed set of experimental data would be needed to calibrate and validate the model.

REFERENCES

- [1] A. Banerjee, M.J. Andrews, "3D Simulations to investigate initial condition effects on the growth of Rayleigh-Taylor mixing," *J. Heat and Mass Transfer*, 2009, 52:3906-3917.
- [2] C.D. Zhou, R. Betti, "Hydrodynamic relations for direct-drive fast-ignition and conventional inertial confinement fusion implosions," *Phy. Plas.*, 2007, 14:072703.
- [3] E.N. Loomis, S.R. Greenfield, R.P. Johnson, et. al., "Investigations into the seeding of instabilities due to x-ray preheat in beryllium-based inertial confinement fusion targets," *Phys. Of Plasmas*, 2010, 17:056308.
- [4] S. Atzeni, J. Meyer-ter-Vehn, "The Physics of Inertial Fusion: Beam Plasma Interaction, Hydrodynamics, Hot Dense Matter," Vol. 125. Oxford University Press, 2004.
- [5] N. Barton, J. Bernier, et. al., "A multiscale strength model for extreme loading conditions," *J. of App. Phys*, 2011, 109.
- [6] J.F. Barnes, P.J. Blewett, R.G. McQueen, "Taylor instability in solids," *J. App. Phys.*, 1974, 45:727-732.
- [7] A.R. Piriz, J.J. Lopez, O.D. Cortazar, "Rayleigh-Taylor instability in elastic solids," *Phys. Rev. E*, 2005, 72:056313.
- [8] E.N. Loomis, "LANL/ASU Summit on Richtmyer-Meshkov Strength Project," LANL, 2014, LA-UR-14-21052.
- [9] J. Nye, John Frederick, "Physical properties of crystals: their representation by tensors and matrices," Oxford university press, 1985.
- [10] R. Becker, "Effects of crystal plasticity on materials loaded at high pressures and strain rates," *Int. J. of Plas.*, 2004, 20:1983-2006.
- [11] T.J. Vogler, L.C. Chhabildas, "Strength behavior of materials at high pressures," *Int. J. of Impact Eng.*, 2006, 33:812-825.
- [12] H. Park, B.A. Remington, et. al., "Strong stabilization of the Rayleigh-Taylor instability by material strength at megabar pressure," *Physics of Plasmas*, 2010, 17.
- [13] G. Dimonte, C.E. Frerking, et. al., "Richtmyer-Meshkov instability with strong radiatively driven shocks," *Physics of Plasmas*, 1995, 3.

- [14] A.J. Mackinnon, P.K. Patel, et. al., "Proton radiography as an electromagnetic field and density perturbation diagnostic," *Review of Scientific Instruments*, 2004, 75:3531-3536.
- [15] S.R. Greenfield, J.L. Casson, A.C. Koskelo, "Nanosecond interferometric studies of surface deformations of dielectrics induced by laser irradiation," *SPIE*, 2002, 4065:557-566.
- [16] S.R. Greenfield, S.N. Luo, D.L. Paisley, "Transient Imaging Displacement Interferometry Applied to Shock Loading," *Shock Compression of Condensed Matter*, 2007, 955:1093-1096.
- [17] S.R. Greenfield, D.C. Swift, A.C. Koskelo, "Transient Interferometric Studies of Shocked Bicrystals," *Shock Compression of Condensed Matter*, 2003, 706:1269-1272.
- [18] K.T. Gahagan, D.S. Moore, D.J. Funk, "Ultrafast interferometric microscopy for laser-driven shock wave characterization," *J. App. Phys*, 2002, 92:3679-3682.
- [19] Celliers, P. M., D. K. Bradley, G. W. Collins, D. G. Hicks, T. R. Boehly, and W. J. Armstrong. "Line-imaging velocimeter for shock diagnostics at the OMEGA laser facility." *Review of scientific instruments*, 2004, 75: 4916-4929.
- [20] J. Boettger, D. Wallace, "Metastability and dynamics of the shock-induced phase transition in iron," *Phys Rev. B.*, 1997, 55:2840-2849.
- [21] Khalil, H. K. (1996). *Nonlinear Systems*. Prentice-Hall, New Jersey.
- [22] Piriz, A. R., Cela, J. L., Cortazar, O. D., "Tahir, N. A., & Hoffmann, D. H. H.. Rayleigh-Taylor instability in elastic solids," *Physical Review E*, 2005, 72(5), 056313.
- [23] S. Atzeni, J. Meyer-ter-Vehn, "The Physics of Inertial Fusion: Beam Plasma Interaction, Hydrodynamics, Hot Dense Matter," Vol. 125. Oxford University Press, 2004.
- [24] Piriz, A. R., JJ López Cela, and N. A. Tahir. "Rayleigh–Taylor instability in elastic-plastic solids," *J. App. Phys.*, 2009, 105:116101.
- [25] Frank W. M. (1999) "Fluid mechanics," McGraw-Hill, New York, NY, USA.
- [26] Ortega, A. López, et al. "Linearized Richtmyer-Meshkov flow analysis for impulsively accelerated incompressible solids." *Physical Review E*, 2010,81.6: 066305.
- [27] Wouchuk, Juan Gustavo, and Katsunobu Nishihara. "Asymptotic growth in the linear Richtmyer–Meshkov instability." *Physics of Plasmas*, 1997, 4:1028-1038.

- [28] Nishihara, K., et al. "Richtmyer–Meshkov instability: theory of linear and nonlinear evolution." *Philosophical Transactions of the Royal Society of London A: Mathematical, Physical and Engineering Sciences*, 2010, 368.1916: 1769-1807.
- [29] Richtmyer, Robert D. "Taylor instability in shock acceleration of compressible fluids." *Communications on Pure and Applied Mathematics*, 1960, 13.2: 297-319.
- [30] Yang, Yumin, Qiang Zhang, and David H. Sharp. "Small amplitude theory of Richtmyer–Meshkov instability." *Physics of Fluids*, 1994, 6.5: 1856-1873.
- [31] Wouchuk, J. G. "Growth rate of the linear Richtmyer-Meshkov instability when a shock is reflected." *Physical Review E*, 2001, 63.5: 056303.
- [32] Wouchuk, J. G. "Growth rate of the Richtmyer–Meshkov instability when a rarefaction is reflected." *Physics of Plasmas*, 2001, 8.6: 2890-2907.
- [33] Wouchuk, Juan Gustavo, and Katsunobu Nishihara. "Linear perturbation growth at a shocked interface." *Physics of Plasmas*, 1996, 3.10: 3761-3776.
- [34] Ishizaki, R., et al. "Instability of a contact surface driven by a nonuniform shock wave." *Physical Review E* 53.6 (1996): R5592.
- [35] Shigemori, K., et al. "Feed-out of rear surface perturbation due to rarefaction wave in laser-irradiated targets." *Physical review letters* 84.23 (2000): 5331.
- [36] Kane, J. O., et al. "Interface imprinting by a rippled shock using an intense laser." *Physical Review E* 63.5 (2001): 055401.
- [37] Betti, R., V. Lobatchev, and R. L. McCrory. "Feedout and Rayleigh-Taylor seeding induced by long wavelength perturbations in accelerated planar foils." *Physical review letters* 81.25 (1998): 5560.
- [38] Loomis, E. N., et al. "Investigations into the seeding of instabilities due to x-ray preheat in beryllium-based inertial confinement fusion targets a." *Physics of Plasmas* 17.5 (2010): 056308.
- [39] Velikovich, Alexander L. "Analytic theory of Richtmyer–Meshkov instability for the case of reflected rarefaction wave." *Physics of Fluids* 8.6 (1996): 1666-1679.
- [40] Velikovich, Alexander, and Lee Phillips. "Instability of a plane centered rarefaction wave." *Physics of Fluids* 8.4 (1996): 1107-1118.
- [41] Meshkov, E. E. "Instability of the interface of two gases accelerated by a shock wave." *Fluid Dynamics* 4.5 (1969): 101-104.

- [42] Benjamin, Robert F., and Joseph N. Fritz. "Shock loading a rippled interface between liquids of different densities." *The Physics of fluids* 30.2 (1987): 331-336.
- [43] Anderson, M. H., et al. "Shock tube investigation of hydrodynamic issues related to inertial confinement fusion." *Shock waves* 10.5 (2000): 377-387.
- [44] Brouillette, M., and R. Bonazza. "Experiments on the Richtmyer–Meshkov instability: Wall effects and wave phenomena." *Physics of Fluids* 11.5 (1999): 1127-1142.
- [45] Brouillette, Martin. "The richtmyer-meshkov instability." *Annual Review of Fluid Mechanics* 34.1 (2002): 445-468.
- [46] Dimonte, Guy, et al. "Richtmyer–Meshkov instability with strong radiatively driven shocks." *Physics of Plasmas* 3.2 (1996): 614-630.
- [47] Farley, David R., and Larry M. Logory. "Single-mode, nonlinear mix experiments at high Mach number using Nova." *The Astrophysical Journal Supplement Series* 127.2 (2000): 311.
- [48] Dimonte, Guy, et al. "A linear electric motor to study turbulent hydrodynamics." *Review of scientific instruments* 67.1 (1996): 302-306.
- [49] Goncharov, V. N. "Theory of the ablative Richtmyer-Meshkov instability." *Physical review letters* 82.10 (1999): 2091.
- [50] Aglitskiy, Y., et al. "Direct observation of mass oscillations due to ablative Richtmyer-Meshkov instability in plastic targets." *Physical review letters* 87.26 (2001): 265001.
- [51] Swegle, J. W., and Allen C. Robinson. "Acceleration instability in elastic-plastic solids. I. Numerical simulations of plate acceleration." *Journal of Applied Physics* 66.7 (1989): 2838-2858.
- [52] Barnes, John F., et al. "Taylor instability in solids." *Journal of Applied Physics* 45.2 (1974): 727-732.
- [53] Barnes, John F., et al. "Further experimentation on Taylor instability in solids." *Journal of Applied Physics* 51.9 (1980): 4678-4679.
- [54] Colvin, J. D., et al. "A model for instability growth in accelerated solid metals." *Journal of applied physics* 93.9 (2003): 5287-5301.
- [55] Robinson, Allen C., and J. W. Swegle. "Acceleration instability in elastic-plastic solids. II. Analytical techniques." *Journal of Applied Physics* 66.7 (1989): 2859-2872.

- [56] Sohn, Sung-Ik. "Effects of surface tension and viscosity on the growth rates of Rayleigh-Taylor and Richtmyer-Meshkov instabilities." *Physical Review E* 80.5 (2009): 055302.
- [57] Terrones, Guillermo. "Fastest growing linear Rayleigh-Taylor modes at solid/fluid and solid/solid interfaces." *Physical Review E* 71.3 (2005): 036306.
- [58] Dimonte, Guy. "Nonlinear evolution of the Rayleigh–Taylor and Richtmyer–Meshkov instabilities." *Physics of Plasmas* 6.5 (1999): 2009-2015.
- [59] Dimonte, Guy, Robert Gore, and Marilyn Schneider. "Rayleigh-Taylor instability in elastic-plastic materials." *Physical review letters* 80.6 (1998): 1212.
- [60] Edwards, J., et al. "Laser-driven plasma loader for shockless compression and acceleration of samples in the solid state." *Physical review letters* 92.7 (2004): 075002.
- [61] Smith, Raymond F., et al. "Stiff response of aluminum under ultrafast shockless compression to 110 GPa." *Physical review letters* 98.6 (2007): 065701.
- [62] Lorenz, K. Thomas, et al. "Accessing ultrahigh-pressure, quasi-isentropic states of matter a." *Physics of plasmas* 12.5 (2005): 056309.
- [63] Barton, N. R., and M. Rhee. "A multiscale strength model for tantalum over an extended range of strain rates." *Journal of Applied Physics* 114.12 (2013): 123507.
- [64] Austin, Ryan A., and David L. McDowell. "Parameterization of a rate-dependent model of shock-induced plasticity for copper, nickel, and aluminum." *International Journal of Plasticity* 32 (2012): 134-154.
- [65] Barton, Nathan R., Nicholas W. Winter, and John E. Reaugh. "Defect evolution and pore collapse in crystalline energetic materials." *Modelling and Simulation in Materials Science and Engineering* 17.3 (2009): 035003.
- [66] Dimonte, Guy, et al. "Use of the Richtmyer-Meshkov instability to infer yield stress at high-energy densities." *Physical review letters* 107.26 (2011): 264502.
- [67] Preston, Dean L., Davis L. Tonks, and Duane C. Wallace. "Model of plastic deformation for extreme loading conditions." *Journal of Applied Physics* 93.1 (2003): 211-220.
- [68] Piriz, Antonio R., et al. "Richtmyer-Meshkov instability in elastic-plastic media." *Physical Review E* 78.5 (2008): 056401.

- [69] Ortega, A. López, et al. "Numerical simulations of the Richtmyer-Meshkov instability in solid-vacuum interfaces using calibrated plasticity laws." *Physical Review E* 89.3 (2014): 033018.
- [70] Prime, Michael B., et al. "Using Richtmyer–Meshkov Instabilities to Estimate Metal Strength at Very High Rates." *Dynamic Behavior of Materials, Volume 1*. Springer International Publishing, 2016. 191-197.
- [71] Prime, Michael B., et al. "Estimation of metal strength at very high rates using free-surface Richtmyer–Meshkov Instabilities." *Journal of Dynamic Behavior of Materials* (2017): 1-14.
- [72] Buttler, W. T., et al. "Unstable Richtmyer-Meshkov growth of solid and liquid metals in vacuum." *Journal of Fluid Mechanics* 703 (2012): 60.
- [73] Peralta, Pedro, et al. "Grain orientation effects on dynamic strength of FCC multicrystals at low shock pressures: a hydrodynamic instability study." *Philosophical Magazine Letters* 95.2 (2015): 67-76.
- [74] Jensen, B. J., et al. "Jet formation in cerium metal to examine material strength." *Journal of Applied Physics* 118.19 (2015): 195903.
- [75] Ortega, A. López, et al. "Richtmyer–Meshkov instability for elastic–plastic solids in converging geometries." *Journal of the Mechanics and Physics of Solids* 76 (2015): 291-324.
- [76] Zaidel', P. M. "Shock wave from a slightly curved piston." *Journal of Applied Mathematics and Mechanics* 24.2 (1960): 316-327.
- [77] Briscoe, M. G., and A. A. Kovitz. "Experimental and theoretical study of the stability of plane shock waves reflected normally from perturbed flat walls." *Journal of Fluid Mechanics* 31.03 (1968): 529-546.
- [78] Wouchuk, J. G., and J. Lopez Cavada. "Spontaneous acoustic emission of a corrugated shock wave in the presence of a reflecting surface." *Physical Review E* 70.4 (2004): 046303.
- [79] Ishizaki, R., and K. Nishihara. "Propagation of a rippled shock wave driven by nonuniform laser ablation." *Physical review letters* 78.10 (1997): 1920.
- [80] Ishizaki, R., and K. Nishihara. "Model of hydrodynamic perturbation growth in the start-up phase of laser implosion." *Physical Review E* 58.3 (1998): 3744.
- [81] Bates, Jason W. "Initial-value-problem solution for isolated rippled shock fronts in arbitrary fluid media." *Physical Review E* 69.5 (2004): 056313.

- [82] Bates, J. W. "On the theory of a shock wave driven by a corrugated piston in a non-ideal fluid." *Journal of Fluid Mechanics* 691 (2012): 146-164.
- [83] D'yakov, S. P. "Shock wave stability." *Zh. Eksp. Teor. Fiz* 27.3 (1954): 288-295.
- [84] Kontorovich, V. M. "Concerning the stability of shock waves." *Soviet Phys. JETP* 6 (1958).
- [85] Bates, J. W. "Theory of the corrugation instability of a piston-driven shock wave." *Physical Review E* 91.1 (2015): 013014.
- [86] Kontorovich, V. M. "Reflection and refraction of sound by shock waves." *Akusticheskii. Zh* 5 (1959): 320-330.
- [87] Zaidel, R. M. "Development of perturbations in plane shock waves." *Journal of Applied Mechanics and Technical Physics* 8.4 (1967): 20-25.
- [88] Miller, Gregory H., and Thomas J. Ahrens. "Shock-wave viscosity measurement." *Reviews of modern physics* 63.4 (1991): 919.
- [89] Mineev, V. N., and E. V. Savinov. "Viscosity and melting point of aluminum, lead and sodium chloride subjected to shock compression." *Sov. Phys JETP* 25 (1967): 411-416.
- [90] Xiao-Juan, Ma, et al. "Shear viscosity of aluminum studied by shock compression considering elasto-plastic effects." *Chinese Physics B* 23.9 (2014): 096204.
- [91] Endo, T., et al. "Dynamic behavior of rippled shock waves and subsequently induced areal-density-perturbation growth in laser-irradiated foils." *Physical review letters* 74.18 (1995): 3608.
- [92] Sakharov, A. D., et al. "Experimental investigation of the stability of shock waves and the mechanical properties of substances at high pressures and temperatures." *Soviet Physics Doklady*. Vol. 9. 1965.
- [93] Mineev, Vladimir N., and Aleksandr I. Funtikov. "Viscosity measurements on metal melts at high pressure and viscosity calculations for the earth's core." *Physics-Uspekhi* 47.7 (2004): 671.
- [94] Mineev, Vladimir Nikolaevich, and Aleksandr Iosifovich Funtikov. "Measurements of the viscosity of iron and uranium under shock compression." *High temperature* 44.6 (2006): 941-949.
- [95] Fu-Sheng, Liu, et al. "Shear viscosity of aluminium under shock compression." *Chinese Physics Letters* 22.3 (2005): 747.

- [96] Xiao-Juan, Ma, et al. "Viscosity of aluminum under shock-loading conditions." Chinese Physics B 20.6 (2011): 068301.
- [97] Xiao-Juan, Ma, et al. "Shear viscosity of aluminum studied by shock compression considering elasto-plastic effects." Chinese Physics B 23.9 (2014): 096204.
- [98] Vogler, Tracy J. "Shock wave perturbation decay in granular materials." Journal of Dynamic Behavior of Materials 1.4 (2015): 370-387.
- [99] Vogler, Tracy, et al. Perturbation Decay Experiments on Granular Materials. No. SAND2016-2537C. Sandia National Laboratories (SNL-CA), Livermore, CA (United States), 2016.
- [100] M. Myers, "Dynamic Behavior of Materials," John Wiley and Sons, 1994.
- [101] J. Forbes, "Shock Wave Compression of Condensed Matter," Springer, 2012.
- [102] L. Barker, R. Hollenbach, "Shock wave study of the $\alpha \rightarrow \epsilon$ phase transition in iron," J. of App. Phys, 1974, 45:4872-4887.
- [103] G. Duvall, R. Graham, "Phase transitions under shock-wave loading," Rev. of Mod. Phys., 1977, 49:523-579.
- [104] A. Molinari, G. Ravichandran, "Fundamental structure of steady plastic shock waves in metals," J. of Appl. Phys., 2004, 95:1718-1732.
- [105] Wallace, Duane C. "Irreversible thermodynamics of overdriven shocks in solids." Physical Review B 24.10 (1981): 5597.
- [106] Wallace, Duane C. "Nature of the process of overdriven shocks in metals." Physical Review B 24.10 (1981): 5607.
- [107] J. Swegle, D. Grady, "Shock viscosity and the prediction of shock wave rise times," J. of Appl. Phys., 1985, 58:692-701.
- [108] J. Zukas, "Introduction to Hydrocodes," Elsevier, 2004.
- [109] R. Smith, J. Eggert, et. al., "High strain-rate plastic flow in Al and Fe," J. of Appl. Phys., 2011, 110.
- [110] M. Bastea, S. Bastea, R. Becker, "High Pressure phase transformation in iron under fast compression," App. Phys Letters, 2009, 95.
- [111] R. Smith, J. Eggert, et. al., "Time-dependence of the alpha to epsilon phase transformation in iron," J. of App. Phys., 2013, 114.

- [112] B. Jensen, G. Gray, R. Hixson, "Direct measurements of the $\alpha \rightarrow \epsilon$ transition stress and kinetics for shocked iron," *J. of Appl. Phys.*, 2009, 105.
- [113] J. Lloyd, J. Clayton, R. Becker, D. McDowell, "Plane wave simulation of elastic-viscoplastic single crystals," *J. Mech. Phys. Solids*, 2014, 69:14-32.
- [114] N. Barton, M. Rhee, "A multiscale strength model for tantalum over an extended range," *J. of App. Phys.*, 2013, 114.
- [115] L. Anand, M. Kothari, "A Computational Procedure for Rate-Independent Crystal Plasticity," *J. Mech. Phys. Solids*, 1996, 44:525-558.
- [116] R. Asaro, A. Needleman, "Texture Development and Strain Hardening in Rate Dependent Polycrystals," *Acta. Metall.*, 1985, 6:923-953.
- [117] R. McGinty, D. McDowell, "Multiscale Polycrystal Plasticity," *J. of Eng. Mat. Tech.*, 1999, 121:203-209.
- [118] T. Wu, J. Bassani, C. Laird, "Latent hardening in single crystals I. Theory and experiments," *Proc. R. Soc. Lond. A*, 1991, 435:1-19.
- [119] J. Bassani, T. Wu., "Latent hardening in single crystals II. Analytical characterization and predictions," *Proc. R. Soc. Lond. A*, 1991, 435:21-41.
- [120] J. Bassani, "Single crystal hardening," *Appl. Mech. Rev.*, 1990, 43:320-327.
- [121] R. Armstrong, F. Zerilli, "High rate straining of tantalum and copper," *J. Phys. D: Appl. Phys.*, 2010, 43.
- [122] R.W. Armstrong, W. Arnold, F. Zerilli, "Dislocation Mechanics of Shock-Induced Plasticity," *Met. Mat. Trans.*, 2007, 38:2605-2610.
- [123] R. Austin, D. McDowell, "A dislocation-based constitutive model for viscoplastic deformation of fcc metals at very high strain rates," *Int. J. of Plas.*, 2011, 27:1-24.
- [124] J. Lloyd, J. Clayton, R. Becker, D. McDowell, "Plane wave simulation of elastic-viscoplastic single crystals," *J. Mech. Phys. Solids*, 2014, 69:14-32.
- [125] R. Clifton, "Dynamic Plasticity," *J. of App. Mech.*, 1983, 50:941-952.
- [126] U. Kocks, A. Argon, M. Ashby, "Thermodynamics and Kinetics of Slip," *Prog. Mater. Sci.*, 19, Pergamon Press, 1975.
- [127] J. Jordan, C. Siviour, et. al., "Strain rate-dependent mechanical properties of OFHC copper," *J. Maer. Sci.*, 2013, 48:7134-7141.

- [128] Steinberg, D. J., S. G. Cochran, and M. W. Guinan. "A constitutive model for metals applicable at high-strain rate." *Journal of Applied Physics* 51.3 (1980): 1498-1504.
- [129] Steinberg, D. J., and C. M. Lund. "A constitutive model for strain rates from 10⁻⁴ to 10⁶ s⁻¹." *Journal of Applied Physics* 65.4 (1989): 1528-1533.
- [130] N. Barton, A. Arsenlis, M. Rhee, et. al., " A multi-scale model with phase transformation," *Shock Compression of Condensed Matter*, 2012, 1426:1513-1516.
- [131] J.L. Belof, R.M. Cavallo, et. al. "Rayleigh-Taylor Strength Experiments of the Pressure Induced Phase Transition in Iron," LLNL-PROC-492911, 2011.
- [132] Mikaelian, Karnig O. "Shock-induced interface instability in viscous fluids and metals." *Physical Review E* 87.3 (2013): 031003.
- [133] J. Poirier, "Introduction to the Physics of the Earth's Interior," Cambridge Univ. Press, 2000.
- [134] O. Heuze, "Building of State with Numerous Phase Transitions - Applications to Bismuth," *Shock Compression of Condensed Matter*, 2005, 212-215.
- [135] Segletes, Steven B. An Analysis on the Stability of the Mie-Gruneisen Equation of State for Describing the Behavior of Shock-Loaded Materials. No. BRL-TR-3214. ARMY BALLISTIC RESEARCH LAB ABERDEEN PROVING GROUND MD, 1991.
- [136] D. Wallace, "Statistical Physics of Crystals and Liquids," World Scientific, 2002.
- [137] C. Greef, D. Trinkle, R. Albers, "Shock-induced $\alpha \rightarrow \omega$ transition in titanium," *J. App. Phys.*, 2001, 90:2221-2226.
- [138] J. Boettger, D. Wallace, "Metastability and dynamics of the shock-induced phase transition in iron," *Phys Rev. B.*, 1997, 55:2840-2849.
- [139] R. Abeyaratne, J. Knowles, "A continuum model of a thermoelastic solid capable of undergoing phase transitions," *J. Mech. Phys. Solids*, 1993, 41:541-571.
- [140] R. Abeyaratne, J. Knowles, "Evolution of Phase Transitions a Continuum Theory," Cambridge, 2006.
- [141] D. Luscher, C. Bronkhorst, C. Alleman, "A model for finite-deformation nonlinear thermomechanical response of single crystal copper under shock conditions," *J. Mech. Phys. Solids*, 2013, 61:1877-1894.

- [142] N. Barton, D. Benson, R. Becker, "Crystal level continuum modelling of phase transformations: the $\alpha \rightarrow \epsilon$ transformation in iron," *Model. Simul. Mater. Sci. Eng.*, 2005, 13:707-731.
- [143] Christian, J. W. "Theory of Transformations in Metals and Alloys." Part1, 2nd Edition, PergamonPress, Oxford, 1975.
- [144] M. Knudson, Y. Gupta, "Transformation kinetics for the shock wave induced phase transition in cadmium sulfide crystals," *J. App. Phys.*, 91:9561-9571.
- [145] P. Debenedetti, "When a phase is born," *Nature*, 2006, 441:168-169.
- [146] V. Levitas, A. Idesman, G. Olson, E. Stein, "Numerical modelling of martensitic growth in an elastoplastic material," *Phil. Mag. A.*, 2002, 82:429-462.
- [147] Jensen, Brian J., G. T. Gray III, and Robert S. Hixson. "Direct measurements of the α - ϵ transition stress and kinetics for shocked iron." *Journal of Applied Physics* 105.10 (2009): 103502.
- [148] G. Ghosh, G. Olson, "Kinetics of FCC \rightarrow BCC heterogeneous martensitic nucleation-I. The critical driving force for athermal nucleation," *Acta Metall. Mater.*, 1994, 42:3361-3370.
- [149] Q. Zuo, E. Harstad, F. Addessio, C. Greeff, "A model for plastic deformation and phase transformations of zirconium under high-rate loading," *Model. Simul. Mater. Sci. Eng.*, 2006, 14:1465-1484.
- [150] F. Addessio, Q. Zuo, T. Mason, "Model for high-strain-rate deformation of uranium-niobium alloys," *J. App. Phys.*, 2003, 93:9644-9654.
- [151] B. Clements, J. Yeon, N. Plohr, F. Addessio, "Dynamically driven phase transformations in heterogeneous materials I. Theory and microstructure considerations," *J. Appl. Phys.*, 2006, 100.
- [152] K. Bhattacharya, "Microstructure of Martensite why it forms and how it gives rise to the shape-memory effect," Oxford, 2003.
- [153] E. Patoor, A. Eberhardt, M. Berveiller, "Micromechanical Modelling of Superelasticity in Shape Memory Alloys," *J. Phys.*, 1996, 6:277-292.
- [154] P. Thamburaja, L. Anand, "Polycrystalline shape-memory materials: effect of crystallographic texture," *J. Mech. and Phys. Solids*, 2001, 49:709-737.
- [155] S. Merkel, H. Wenk, P. Gillet, H. Mao, "Deformation of polycrystalline iron up to 30 GPa and 1000K," *Phys. of Earth and Plan. Int.*, 2004, 145:239-251.

- [156] L. Miyagi, M. Kunz, et. al., "In situ phase transformation and deformation of iron at high pressure and temperature," *J. App. Phys.*, 2008, 104.
- [157] N. Bargen, R. Boehler, "Effect of Non-Hydrostaticity on the $\alpha \rightarrow \epsilon$ Transition of Iron," *High Pressure Research*, 1990, 6:133-140.
- [158] S. Aubry, M. Fago, M. Ortiz, "A constrained sequential-lamination algorithm for the simulation of sub-grid microstructure in martensitic materials," *Comp. Methods Appl. Mech. Eng.*, 2003, 192:2823-22843.
- [159] K. Caspersen, A. Lew, M. Ortiz, E. Carter, "Importance of Shear in the bcc-to-hcp Transformation in Iron," *Phys Rev. Letters*, 2004, 93.
- [160] Luo, S. N., et al. "Laser-induced shock waves in condensed matter: some techniques and applications." *High Pressure Research* 24.4 (2004): 409-422.
- [161] de Rességuier, Thibaut, and Martine Hallouin. "Effects of the $\alpha - \epsilon$ phase transition on wave propagation and spallation in laser shock-loaded iron." *Physical Review B* 77.17 (2008): 174107.
- [162] Loomis, E., et al. "High-resolution measurements of shock behavior across frictional Be/Cu interfaces." *Journal of Applied Physics* 117.18 (2015): 185906.
- [163] Opie, S., Loomis, E., Peralta, P., et al. "Strength and Viscosity Effects on Perturbed Shock Front Stability in Metals." *Physical Review Letters* 118.19 (2017): 195501.
- [164] Furnish, Michael D. LineVISAR: a fringe-trace data analysis program. Tech. Rep. SAND2014-1632, Sandia National Laboratories, 2014.
- [165] Takeda, Mitsuo, Hideki Ina, and Seiji Kobayashi. "Fourier-transform method of fringe-pattern analysis for computer-based topography and interferometry." *JosA* 72.1 (1982): 156-160.
- [166] Ghiglia, Dennis C., and Mark D. Pritt. Two-dimensional phase unwrapping: theory, algorithms, and software. Vol. 4. New York: Wiley, 1998. Matlab Code available at : <http://www.mathworks.com/matlabcentral/fileexchange/29497-goldsteinunwrap2d-r1>
- [167] Oppenheim, Alan V. Discrete-time signal processing. Pearson Education, 1999.
- [168] Jain, A., and S. R. Agnew. "Modeling the temperature dependent effect of twinning on the behavior of magnesium alloy AZ31B sheet." *Materials Science and Engineering: A* 462.1 (2007): 29-36.
- [169] Dunne, Fionn, and Nik Petrinic. Introduction to computational plasticity. Oxford University Press on Demand, 2005.

- [170] Andrews, D. J. "Equation of state of the alpha and epsilon phases of iron." *Journal of Physics and Chemistry of Solids* 34.5 (1973): 825-840.
- [171] Andrews, D. J. "Calculation of mixed phases in continuum mechanics." *Journal of Computational Physics* 7.2 (1971): 310-326.
- [172] Greeff, C. W., et al. "Modeling dynamic phase transitions in Ti and Zr." *AIP Conference Proceedings*. Eds. Michael D. Furnish, Yogendra M. Gupta, and Jerry W. Forbes. Vol. 706. No. 1. AIP, 2004.
- [173] Kerley, Gerald I. "A new multiphase equation of state for iron." *AIP Conference Proceedings*. Eds. S. C. Schmidt, et al. Vol. 309. No. 1. AIP, 1994. (see also SAND93-0027)
- [174] De Ressaiguiet, T., and M. Hallouin. "Interaction of two laser shocks inside iron samples." *Journal of Applied Physics* 90.9 (2001): 4377-4384.
- [175] Heuzé, Olivier. "Building of equations of state with numerous phase transitions—application to bismuth." *AIP Conference Proceedings*. Eds. Michael D. Furnish, et al. Vol. 845. No. 1. AIP, 2006.
- [176] ABAQUS, ABAQUS Documentation, 2012, Dassault Systèmes, Providence, RI, USA.
- [177] H. Xiao, O. T. Bruhns, A. Myers, "Existence and uniqueness of the integrable-exactly hypoelastic equation $\dot{\tau} = \lambda(\text{tr}D)I + 2\mu D$ and its significance to finite elasticity," *Acta Mech.*, 1999, 138:31-50.
- [178] A. Meyers, H. Xiao, O Bruhns, "Elastic Stress Ratchetting and Corotational Stress Rates," *Technische Mechanik*, 2003, 23:92-102.
- [179] R. Lin, "Numerical study of consistency of rate constitutive equations with elasticity at finite deformation," *Int. J. Num. Meth. Eng.*, 2003, 55:1053-1077.
- [180] J. C. Simo, K. S. Pister, "Remarks on Rate Constitutive Equations for Finite Deformation Problems: Computational Implications," *Comp. Meth. App. Mech. Eng.*, 1984, 46:201-215.
- [181] N.R. Barton, J. Knap, A. Arsenlis, et. al., "Embedded polycrystal plasticity and adaptive sampling," *Int. J. Plas.*, 2008, 24:242-266.
- [182] P.M. Pinsky, M. Ortiz, K.S. Pister, "Numerical Integration of Rate Constitutive Equations in Finite Deformation Analysis," *Comp Meth. App. Mech. Eng.*, 1983, 40:137-158.

- [183] Z.P. Bazant, J. Vorel, "Energy-Conservation Error Due to Green-Naghdi Objective Stress Rate in Commercial Finite-Element Codes and Its Compensation," *J. App. Mech.*, 2014, 81:021008.
- [184] R. A. Lebensohn, P. A. Turner, et. al., "Calculation of intergranular stresses based on a large-strain viscoplastic self-consistent polycrystal model," *Mod. Simul. Mater. Sci.*, 1998, 6:447-465.
- [185] X. Ling, M. Horstemeyer, G. Potirniche, "On the numerical implementation of 3D rate-dependent single crystal plasticity formulations," *Int. J. for Num. Meth. in Eng.*, 2004, 63:548-568.
- [186] Zel'dovich, Yakov Boris, and Yu P. Raizer. *Physics of shock waves and high-temperature hydrodynamic phenomena*. Dover Publ., 2002.
- [187] Hofmeister, A. M., and H. K. Mao. "Pressure derivatives of shear and bulk moduli from the thermal Grüneisen parameter and volume-pressure data." *Geochimica et Cosmochimica Acta* 67.6 (2003): 1215-1235.
- [188] K. Bhattacharya, "Microstructure of Martensite why it forms and how it gives rise to the shape-memory effect," Oxford, 2003.
- [189] Caspersen, Kyle J., et al. "Importance of shear in the bcc-to-hcp transformation in iron." *Physical review letters* 93.11 (2004): 115501.
- [190] Merkel, Sébastien, et al. "Deformation of polycrystalline iron up to 30GPa and 1000K." *Physics of the Earth and Planetary Interiors* 145.1 (2004): 239-251.
- [191] Miyagi, Lowell, et al. "In situ phase transformation and deformation of iron at high pressure and temperature." *Journal of applied physics* 104.10 (2008): 103510.
- [192] Smith, C. Stanley, and C. M. Fowler. "Further metallographic studies on metals after explosive shock." *Response of Metals to High Velocity Deformation* 9 (1961): 309.
- [193] Loomis, Eric. *The Effect of Grain Boundaries on the Deformation Mechanisms of Nickel Aluminide During Laser-induced Shock Loading*. 2005.
- [194] Wallace, Duane C. "Irreversible thermodynamics of overdriven shocks in solids." *Physical Review B* 24.10 (1981): 5597.
- [195] Wallace, Duane C. "Nature of the process of overdriven shocks in metals." *Physical Review B* 24.10 (1981): 5607.

- [196] Lindl, John. "Development of the indirect-drive approach to inertial confinement fusion and the target physics basis for ignition and gain." *Physics of plasmas* 2.11 (1995): 3933-4024.
- [197] de Rességuier, Thibaut, and Martine Hallouin. "Effects of the α - ϵ phase transition on wave propagation and spallation in laser shock-loaded iron." *Physical Review B* 77.17 (2008): 174107.
- [198] Prime, Michael B., et al. *Cyclic Plasticity under Shock Loading in an HCP Metal*. No. LA-UR-12-22056. Los Alamos National Laboratory (LANL), 2012.
- [199] Wang, C. H., W. Hu, and J. P. G. Sawyer. "Explicit numerical integration algorithm for a class of non-linear kinematic hardening model." *Computational Mechanics* 26.2 (2000): 140-147.
- [200] Peterson, J. L., et al. "The effects of early time laser drive on hydrodynamic instability growth in National Ignition Facility implosions." *Physics of Plasmas* 21.9 (2014): 092710.
- [201] Parker, W. J., et al. "Flash method of determining thermal diffusivity, heat capacity, and thermal conductivity." *Journal of applied physics* 32.9 (1961): 1679-1684.
- [202] Prime, M. B., et al. "Using growth and arrest of Richtmyer-Meshkov instabilities and Lagrangian simulations to study high-rate material strength." *Journal of Physics: Conference Series*. Vol. 500. No. 11. IOP Publishing, 2014.
- [203] Potteiger, L. A. "Explosive Hardening of Iron and Low-Carbon Steel," No. 1950. NAVAL WEAPONS LAB DAHLGREN VA, 1964.

APPENDIX A

IRON VARIANTS

```

%=====
%Define transform U
%=====
c_over_a = 1.603;
gamma = c_over_a/((8/3)^.5);
U11 = 3/(4*2^.5)+gamma/2;
U12 = -3/(4*2^.5)+gamma/2;
U22 = 3/(4*2^.5)+gamma/2;
U33 = 3^.5/2;
%General BCC to HCP transformation (G=I, H=I)
U = [U11 U12 0;U12 U22 0;0 0 U33];
%=====
%HCP Variant (Gi*U*Gi')
%=====
G1 = eye(3,3);
G2 = [0 -1 0;1 0 0;0 0 1];
G3 = [1 0 0;0 0 -1;0 1 0];
G4 = G3*G2;
G5 = [0 0 -1;0 1 0;1 0 0];
G6 = G5*G2;
%=====
%for BCC variant i ((H*G*U^-1*G'*H')*(G*U*G'))
%(1) first using BCC symmetry transform to HCP,
%(2) then using HCP symmetry rotate,
%(3) then apply reverse BCC to HCP transform of (1)
%=====
%for BCC variant 1
H1 = eye(3,3);
%for BCC variant 2
H2 = [cos(pi/4) -sin(pi/4) 0;sin(pi/4) cos(pi/4) 0;0 0 1]* ...
      [1 0 0;0 cos(pi/3) -sin(pi/3);0 sin(pi/3) cos(pi/3)]*....
      [cos(pi/4) -sin(pi/4) 0;sin(pi/4) cos(pi/4) 0;0 0 1]';
%for BCC variant 3
H3 = [cos(pi/4) -sin(pi/4) 0;sin(pi/4) cos(pi/4) 0;0 0 1]* ...
      [1 0 0;0 cos(-pi/3) -sin(-pi/3);0 sin(-pi/3) cos(-pi/3)]*....
      [cos(pi/4) -sin(pi/4) 0;sin(pi/4) cos(pi/4) 0;0 0 1]';
%for BCC variant 4
H4 = G2*H2*G2';
%for BCC variant 5
H5 = G2*H3*G2';
%for BCC variant 6
H6 = G3*H2*G3';
%for BCC variant 7
H7 = G3*H3*G3';
%for BCC variant 8
H8 = G4*H2*G4';
%for BCC variant 9
H9 = G4*H3*G4';
%for BCC variant 10
H10 = G5*H2*G5';
%for BCC variant 11
H11 = G5*H3*G5';
%for BCC variant 12
H12 = G6*H2*G6';
%for BCC variant 13
H13 = G6*H3*G6';

```

```

%=====
% DEFORMATION GRADIENTS FOR ALL VARIANTS
%=====
%BCC 1
Fbcc_1=(H1*G1*U^-1*G1'*H1')*(G1*U*G1');
%BCC2
Fbcc_2=(H2*G1*U^-1*G1'*H2')*(G1*U*G1');
%BCC3
Fbcc_3=(H3*G1*U^-1*G1'*H3')*(G1*U*G1');
%BCC4
Fbcc_4=(H4*G2*U^-1*G2'*H4')*(G2*U*G2');
%BCC5
Fbcc_5=(H5*G2*U^-1*G2'*H5')*(G2*U*G2');
%BCC6
Fbcc_6=(H6*G3*U^-1*G3'*H6')*(G3*U*G3');
%BCC7
Fbcc_7=(H7*G3*U^-1*G3'*H7')*(G3*U*G3');
%BCC8
Fbcc_8=(H8*G4*U^-1*G4'*H8')*(G4*U*G4');
%BCC9
Fbcc_9=(H9*G4*U^-1*G4'*H9')*(G4*U*G4');
%BCC10
Fbcc_10=(H10*G5*U^-1*G5'*H10')*(G5*U*G5');
%BCC11
Fbcc_11=(H11*G5*U^-1*G5'*H11')*(G5*U*G5');
%BCC12
Fbcc_12=(H12*G6*U^-1*G6'*H12')*(G6*U*G6');
%BCC13
Fbcc_13=(H13*G6*U^-1*G6'*H13')*(G6*U*G6');

%HCP1
Fhcp_1=G1*U*G1';
%HCP2
Fhcp_2=G2*U*G2';
%HCP3
Fhcp_3=G3*U*G3';
%HCP4
Fhcp_4=G4*U*G4';
%HCP5
Fhcp_5=G5*U*G5';
%HCP6
Fhcp_6=G6*U*G6';

```

APPENDIX B

SHOCK FRONT PERTURBATION EVOLUTION


```

clear all
%=====
% SYMBOLIC MANIPULATION
%=====
syms delta z w k v sigma
syms s rho rho0 c beta
syms Sy
%----Miller S and CapLambda, eqn (61)
S = [-1  z  -1;...
      z  -1  w;...
      z  -1  -w];
CapLambda = [-z*k  0  0;...
              0  k*(beta^2*z-w)/(1-beta^2)  0;...
              0  0  k*(beta^2*z+w)/(1-beta^2)];

%----u0, Miller eqn (42) w Sy term
syms xiHat xi0
u0 = [ -(sigma-1)*(1+delta)/(sigma*(1-delta))*(xi0-s*xiHat);...
       -k*v*(sigma-1)*xiHat + k*Sy/(rho*v)*xiHat;...
       2*(sigma-1)/(sigma*(1-delta))*(xi0-s*xiHat)];
u0 = subs(u0,s,k*v*z);

%----my g, Miller eqn (53d)
syms c1 Sy Cx Cy
g = [-1/(rho*v^2)*beta^2/(1-beta^2)*Cx/3^.5*Sy/z;...
      1/(rho*v^2)*Cy/3^.5*Sy/z;...
      1/(rho*v^2)*1/(1-beta^2)*Cx/3^.5*Sy/z];

%----int(expm(-CapLambda*p)dt,0,inf), from Miller eqn (65)
intExpmsg = CapLambda^-1*S*g;

%----Miller eqn (65)
Su0 = S*u0;

%----Su0+intExpmsg, Miller eqn (65)
temp = Su0+intExpmsg;

%----solve for xiHat/xi0, by setting temp(3)=0 and dividing by xi0
%first argument is (Su0+intExpmsg)[3]=0, solve this for xiHat
temp_xiHat = solve(temp(3),xiHat);
xiHat_div_xi0 = 1/xi0*temp_xiHat;
xiHat_div_xi0 = simplify(xiHat_div_xi0);
pretty(xiHat_div_xi0)

%----bring back Laplace variable s
xiHat_div_xi0 = subs(xiHat_div_xi0,w,(beta^2*z^2+1-beta^2)^.5);
xiHat_div_xi0 = subs(xiHat_div_xi0,z,s/(k*v));

%=====
% REPLACE SYMBOLIC VARIABLES WITH VALUES
%=====
%----material and geometry parameters
Up = 600; %m/s
s0 = 1.5; %-
C0 = 3933; %m/s
gamma = 2.12; %-

```

```

rho0 = 8960; %kg/m^3
Sy = 400e6; %Pa
k = 2*pi/(150e-6); %1/m
xi0 = 6e-6; %m

%----calculations
Us = C0 + s0*Up; %m/s
delta = (Us-s0*Up)/(Us+s0*Up); %-
v = Us-Up; %m/s
eta = Up/Us; %=1-rho0/rho => rho0/rho=1-eta
rho = rho0/(1-eta); %kg/m^3
c = ( (1-eta)^2/(1-s0*eta)^3*C0^2*(1+s0*eta*(1-gamma*eta)) )^.5; %m/s
Cx=2; %fitting constant in strength approximation
Cy=1; %fitting constant in strength approximation
sigma = rho/rho0;
beta = v/c;
xiHat_div_xi0_temp = subs(xiHat_div_xi0);

%----turn into function handle
xiHat_div_xi0_temp = matlabFunction(xiHat_div_xi0_temp);

%----apply numerical inverse Laplace and get solution
time = 0:1e-9:120e-8;
%xAxis_Hydro = time*(k*v);
xAxis= time*(k*Us);
%norm_amp = talbot_inversion(xiHat_div_xi0_temp, time)';
norm_amp = euler_inversion(xiHat_div_xi0_temp, time)';

%=====
% PLOT
%=====
figure('name','Shock Front Evolution')
plot(xAxis,norm_amp)
axis([0 20 -.2 1.000000002])
xlabel('k*Us*t')
ylabel('Norm. Amp.')
grid

```

```

%=====
function ilt = euler_inversion(f_s, t, M)
%=====
% ilt = euler_inversion(f_s, t, [M])
%
% Returns an approximation to the inverse Laplace transform of function
% handle f_s eval. at each value in t (1xn) using the Euler method as
% summarized in the source below.
%
% This implementation is coarse; use euler_inversion_sym for better
% precision. Further, please see example_inversions.m for examples.
%
% f_s: Handle to function of s
% t:   Times at which to evaluate the inverse Laplace transform of f_s
% M:   Optional, number of terms to sum for each t (64 is a good guess);
%       highly oscillatory functions require higher M, but this can grow
%       unstable; see test_talbot.m for an example of stability.
%
% Abate, Joseph, and Ward Whitt. "A Unified Framework for Numerically
% Inverting Laplace Transforms." INFORMS Journal of Computing, vol. 18.4
% (2006): 408-421. Print.
%
% The paper is also online:
%http://www.columbia.edu/~ww2040/allpapers.html.
%
% Tucker McClure
% Copyright 2012, The MathWorks, Inc.
%---Make sure t is n-by-1.
    if size(t, 1) == 1
        t = t';
    elseif size(t, 2) > 1
        error('Input times, t, must be a vector.');
```

end

```

%---Set M to 64 if user didn't specify an M.
    if nargin < 3
        M = 32;
    end
%---Vectorized Talbot's algorithm
    bnml = @(n, z) prod((n-(z-(1:z)))./(1:z));
    xi = [0.5, ones(1, M), zeros(1, M-1), 2^-M];
    for k = 1:M-1
        xi(2*M-k + 1) = xi(2*M-k + 2) + 2^-M * bnml(M, k);
    end
    k = 0:2*M; % Iteration index
    beta = M*log(10)/3 + 1i*pi*k;
    eta = (1-mod(k, 2)*2) .* xi;
%---Make a mesh so we can do this entire calc. across all k for all
% given times without a single loop (it's faster this way).
    [beta_mesh, t_mesh] = meshgrid(beta, t);
    eta_mesh = meshgrid(eta, t);

%---Finally, calc. the inverse Laplace transform for each given time.
    ilt = 10^(M/3)./t ...
        .* sum(eta_mesh .* real(arrayfun(f_s, beta_mesh./t_mesh)), 2);

end
```